frontiers | Research Topics

Next generation staging in head and neck cancers

Edited by
N. Gopalakrishna Iyer, Narayana Subramaniam and Cesare Piazza

Published in
Frontiers in Oncology

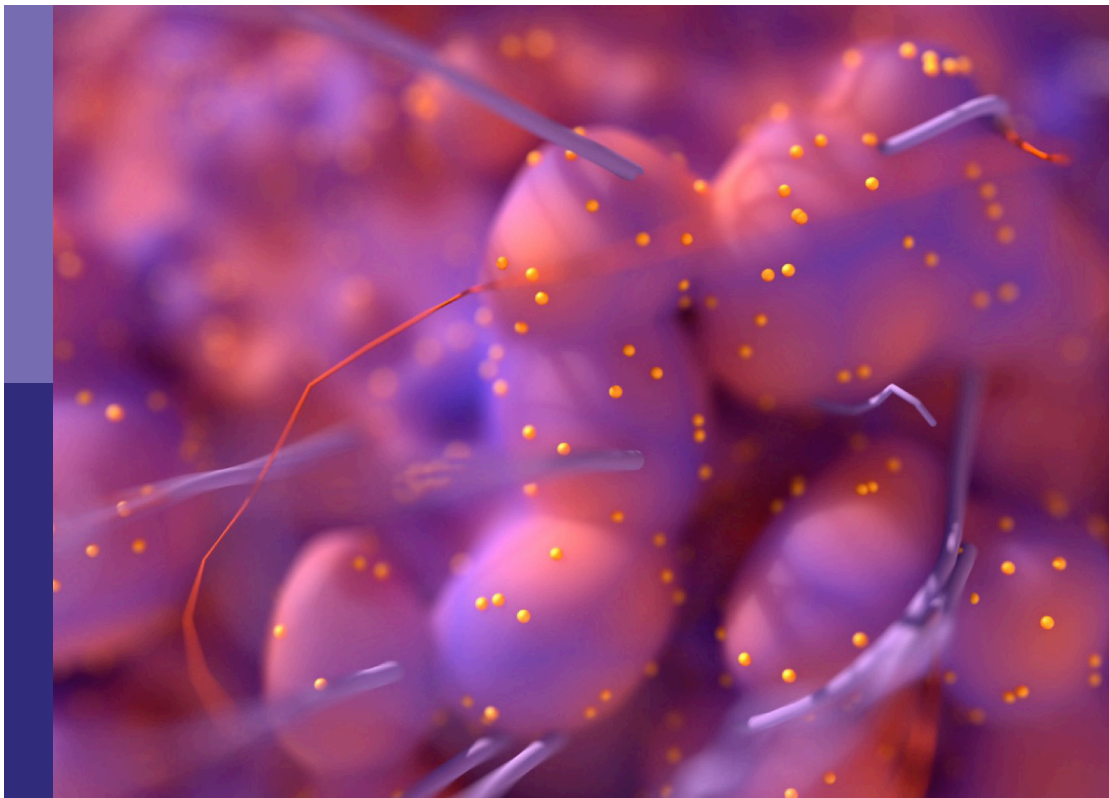

ISSN 1664-8714
ISBN 978-2-83251-172-5
DOI 10.3389/978-2-83251-172-5

About Frontiers

Frontiers is more than just an open access publisher of scholarly articles: it is a pioneering approach to the world of academia, radically improving the way scholarly research is managed. The grand vision of Frontiers is a world where all people have an equal opportunity to seek, share and generate knowledge. Frontiers provides immediate and permanent online open access to all its publications, but this alone is not enough to realize our grand goals.

Frontiers journal series

The Frontiers journal series is a multi-tier and interdisciplinary set of open-access, online journals, promising a paradigm shift from the current review, selection and dissemination processes in academic publishing. All Frontiers journals are driven by researchers for researchers; therefore, they constitute a service to the scholarly community. At the same time, the *Frontiers journal series* operates on a revolutionary invention, the tiered publishing system, initially addressing specific communities of scholars, and gradually climbing up to broader public understanding, thus serving the interests of the lay society, too.

Dedication to quality

Each Frontiers article is a landmark of the highest quality, thanks to genuinely collaborative interactions between authors and review editors, who include some of the world's best academicians. Research must be certified by peers before entering a stream of knowledge that may eventually reach the public - and shape society; therefore, Frontiers only applies the most rigorous and unbiased reviews. Frontiers revolutionizes research publishing by freely delivering the most outstanding research, evaluated with no bias from both the academic and social point of view. By applying the most advanced information technologies, Frontiers is catapulting scholarly publishing into a new generation.

What are Frontiers Research Topics?

Frontiers Research Topics are very popular trademarks of the *Frontiers journals series*: they are collections of at least ten articles, all centered on a particular subject. With their unique mix of varied contributions from Original Research to Review Articles, Frontiers Research Topics unify the most influential researchers, the latest key findings and historical advances in a hot research area.

Find out more on how to host your own Frontiers Research Topic or contribute to one as an author by contacting the Frontiers editorial office: frontiersin.org/about/contact

Next generation staging in head and neck cancers

Topic editors

N. Gopalakrishna Iyer — National Cancer Centre Singapore, Singapore
Narayana Subramaniam — Sri Shankara Cancer Research Foundation, India
Cesare Piazza — University of Brescia, Italy

Citation

Iyer, N. G., Subramaniam, N., Piazza, C., eds. (2023). *Next generation staging in head and neck cancers*. Lausanne: Frontiers Media SA.
doi: 10.3389/978-2-83251-172-5

Table of contents

frontiers | Frontiers in Oncology

TYPE Editorial
PUBLISHED 14 December 2022
DOI 10.3389/fonc.2022.1106125

OPEN ACCESS

EDITED AND REVIEWED BY
Andreas Dietz,
Leipzig University, Germany

*CORRESPONDENCE
N Gopalakrishna Iyer
gopaliyer@singhealth.com.sg
Narayana Subramaniam
narayana.subramaniam@gmail.com

SPECIALTY SECTION
This article was submitted to Head and Neck Cancer, a section of the journal Frontiers in Oncology

RECEIVED 23 November 2022
ACCEPTED 05 December 2022
PUBLISHED 14 December 2022

CITATION
Iyer NG, Subramaniam N and Piazza C (2022) Editorial: Next generation staging in head and neck cancers. *Front. Oncol.* 12:1106125. doi: 10.3389/fonc.2022.1106125

Editorial: Next generation staging in head and neck cancers

N. Gopalakrishna Iyer[1]*, Narayana Subramaniam[2]* and Cesare Piazza[3]

[1]Department of Head and Neck Surgery, Singapore General Hospital and National Cancer Centre, Singapore and Duke National University of Singapore (NUS) Medical School, Singapore, Singapore, [2]Head and Neck Oncology, Sri Shankara Cancer Hospital and Research Centre, Bengaluru, India, [3]Unit of Otorhinolaryngology – Head and Neck Surgery, ASST Spedali Civili of Brescia, Department of Surgical and Medical Specialties, Radiological Sciences and Public Health, University of Brescia, School of Medicine, Brescia, Italy

KEYWORDS

staging, radiomics, biomarkers, molecular markers, prognosis, squamous cell carcinoma, head and neck cancer

Editorial on the Research Topic
Next generation staging in head and neck cancers

Despite numerous advances in treatment, head and neck squamous cell carcinoma (HNSCC) has remained an important cause of cancer-related morbidity and mortality the world over. Until 2017, when the 8th Edition of the TNM staging system of the Union for International Cancer Control/American Joint Committee on Cancer was released, staging had remained relatively unchanged for decades. The new staging system acknowledged the role of depth of invasion in oral cancer, as well as prognostic determinants in HPV-positive oropharyngeal tumors and virus-related (including HPV and EBV-associated) unknown primaries (1), representing its intention to evolve from a population-based staging system to a more 'personalized' approach. Even with these improvements, conventional TNM staging has been found to have drawbacks difficult to be addressed (2). While TNM staging is focused on prediction of overall survival using well-established, historical criteria, there have been constant attempts at improving it by incorporating pathologic, radiologic, genomic, and other biomarkers. This serves several purposes: to improve precision and accuracy in existing staging systems, to sub-stratify patients within a stage to predict survival more accurately, and to identify those who are candidates for treatment escalation through clinical trials and other novel therapeutic strategies.

In the quest to improve the present staging system, there is an almost reflexive instinct to improve it by increasing the number of parameters included and, thus, the inherent complexity of the overall process, but this approach is not without drawbacks. In fact, it results in increased heterogeneity of staging, across geographies and institutions, which are difficult to account for (3). As the complexity and number of parameters

included increase, there is inevitably also a parallel reduction of the inter-observer agreement. This, in turn, impacts the overall reliability of the staging system itself. Herein lies the challenge: how do we improve staging methodology to reflect our better understanding of the disease, while maintaining its simplicity, applicability, and reproducibility? The answer to this question, we believe, is probably nuanced. As our knowledge and understanding of the tumor behavior and biology improve, the TNM staging needs to reflect this; however, staging, by nature, needs to be simple, easy to understand and apply, and standardized across the world. As we consider tumor-related as well as patient-related factors that better prognosticate survival, it becomes important to understand the context in which they need to be applied. Parameters with a strong prognostic relevance which are universally applicable features, easy to be interpreted with little to no inter-observer variability are suitable for incorporation into staging, while others are likely to be better suited for a nomogram or a decision-making tool, which may help guide treatment decisions.

Next-generation HNSCC staging represents the understanding of the role that novel markers are likely to play in the diagnosis and treatment of such a dismal disease. Patient-specific models allow incorporating these factors into prognostication and treatment planning; in other cancers, like breast and prostate, these have become a common part of practice, while in HNSCC they have not yet become widely accepted. In the era of personalized medicine, this is even more relevant. Studies which incorporate molecular or genomic data into therapeutic decisions are unlikely to accrue the same number of patients as a traditional phase III clinical trial due to financial and other logistical hurdles, however the value they add cannot be discounted. It is important to be able to incorporate this newer data, as it appears, into practice to improve the quality of decision making, even if the number of patients studied is low. We are proud to present this issue, which is a good representation of such an expanding body of literature. The articles in this special issue cover novel clinical parameters, radiomics, and molecular markers that help predict survival, treatment response or improve prognostication, which continue to remain a pressing need in the treatment of patients with HNSCC.

Author contributions

All authors listed have made a substantial, direct, and intellectual contribution to the work and approved it for publication.

Conflict of interest

The authors declare that the research was conducted in the absence of any commercial or financial relationships that could be construed as a potential conflict of interest.

Publisher's note

References

1. Amin MB, Greene FL, Edge SB, Compton CC, Gershenwald JE, Brookland RK, et al. The eighth edition AJCC cancer staging manual: Continuing to build a bridge from a population-based to a more "personalized" approach to cancer staging. *CA Cancer J Clin* (2017) 67(2):93–9. doi: 10.3322/caac.21388

2. Subramaniam N, Murthy S, Balasubramanian D, Low TH, Vidhyadharan S, Clark JR, et al. Adverse pathologic features in T1/2 oral squamous cell carcinoma classified by the American joint committee on cancer eighth edition and implications for treatment. *Head Neck* (2018) 40(10):2123–8. doi: 10.1002/hed.25168

3. Subramaniam N, Clark JR, Goldstein D, de Almeida J, Abdalaty AH, Balasubramanian D, et al. Geographical heterogeneity in the American joint committee on cancer oral cancer staging and prognostic implications. *Oral Oncol* (2021) 113:105122. doi: 10.1016/j.oraloncology.2020.105122

frontiers in Oncology

ORIGINAL RESEARCH
published: 23 March 2022
doi: 10.3389/fonc.2022.870544

Preoperative Prediction of Malignant Transformation of Sinonasal Inverted Papilloma Using MR Radiomics

Yang Yan[1†], Yujia Liu[2,3†], Jianhua Tao[1], Zheng Li[1], Xiaoxia Qu[1], Jian Guo[1] and Junfang Xian[1]*

[1] Department of Radiology, Beijing Tongren Hospital, Capital Medical University, Beijing, China, [2] School of Artificial Intelligence, University of Chinese Academy of Sciences, Beijing, China, [3] Chinese Academy of Sciences Key Laboratory of Molecular Imaging, Institute of Automation, Chinese Academy of Sciences, Beijing, China

OPEN ACCESS

Edited by:
Cesare Piazza, University of Brescia, Italy

Reviewed by:
Vittorio Rampinelli, University of Brescia, Italy
Marco Ferrari, University of Padua, Italy
Alberto Schreiber, ASST Spedali Civili Brescia, Italy

***Correspondence:**
Junfang Xian
cjr.xianjunfang@vip.163.com

[†]These authors have contributed equally to this work and share first authorship

Specialty section:
This article was submitted to Head and Neck Cancer, a section of the journal Frontiers in Oncology

Received: *07 February 2022*
Accepted: *28 February 2022*
Published: *23 March 2022*

Citation:
Yan Y, Liu Y, Tao J, Li Z, Qu X, Guo J and Xian J (2022) Preoperative Prediction of Malignant Transformation of Sinonasal Inverted Papilloma Using MR Radiomics. Front. Oncol. 12:870544. doi: 10.3389/fonc.2022.870544

Purpose: Accurate preoperative prediction of the malignant transformation of sinonasal inverted papilloma (IP) is essential for guiding biopsy, planning appropriate surgery and prognosis of patients. We aimed to investigate the value of MRI-based radiomics in discriminating IP from IP-transformed squamous cell carcinomas (IP-SCC).

Methods: A total of 236 patients with IP-SCC (n=92) or IP (n=144) were enrolled and divided into a training cohort and a testing cohort. Preoperative MR images including T1-weighted, T2-weighted, and contrast enhanced T1-weighted images were collected. Radiomic features were extracted from MR images and key features were merged into a radiomic model. A morphological features model was developed based on MR morphological features assessed by radiologists. A combined model combining radiomic features and morphological features was generated using multivariable logistic regression. For comparison, two head and neck radiologists were independently invited to distinguish IP-SCC from IP. The area under the receiver operating characteristics curve (AUC) was used to assess the performance of all models.

Results: A total of 3948 radiomic features were extracted from three MR sequences. After feature selection, we saved 15 key features for modeling. The AUC, sensitivity, specificity, and accuracy on the testing cohort of the combined model based on radiomic and morphological features were respectively 0.962, 0.828, 0.94, and 0.899. The diagnostic ability of the combined model outperformed the morphological features model and also outperformed the two head and neck radiologists.

Conclusions: A combined model based on MR radiomic and morphological features could serve as a potential tool to accurately predict IP-SCC, which might improve patient counseling and make more precise treatment planning.

Keywords: inverted papilloma (IP), squamous cell carcinoma, sinonasal cancer, radiomics, magnetic resonance imaging

INTRODUCTION

Inverted papilloma (IP) is an uncommon sinonasal epithelial neoplasm accounting for 0.5% to 4.0% of all primary sinonasal neoplasms (1), and it is characterized by aggressive behavior, high recurrence rate, and a 7% to 10% possibility of malignant transformation into squamous cell carcinoma (IP-SCC) (2). The incidence of IP associated with the synchronously or metachronous SCC is reported from 2% to 53% (2–5), in which synchronous SCC accounts for approximately 55%–70% (2, 5, 6). Therefore, it is essential for precision diagnosis and treatment as well as prognosis to accurately predict IP-SCC preoperatively (3, 7, 8). However, it is very difficult to diagnose IP-SCC preoperatively due to similarity in clinical presentation and imaging findings with IP (9).

Local biopsy based on endoscopy is the most common surveillance technique (10). However, it is difficult for surgeons to inspect areas in the sinus that are not easily seen, and the accuracy of biopsies may be affected by sampling errors (11). Some studies have found that pain, epistaxis, and recurrence are the clinical presentations of malignant transformation of IP (12–14). However, these clinical presentations could also be found in IP patients, and sample sizes of IP-SCC in these studies are relatively small (5).

CT and MRI have also been used to distinguish IP-SCC from IP. Although IP-SCC on CT scan can show significantly higher bone destruction (13), this finding is quite nonspecific because IP may also have aggressive bone destruction (15, 16). So far, MRI has more promise in detecting malignant transformation. Convoluted cerebriform pattern (CCP) has been proved as a classical and reliable MRI feature of IP (17–19). Several studies have reported that focal loss of CCP may indicate malignant transformation of IP (18, 20, 21). Recently, some studies have attempted to predict IP-SCC using the loss of CCP combined with MR morphological features associated with malignancy, and achieved high specificity, but the sensitivity was unsatisfactory (9, 22). This is mainly because designation of CCP is relatively subjective and may be affected by radiologists' misinterpretation, particularly when evaluating smaller tumors (9). Therefore, it is necessary to develop a more objective form of image analysis.

Radiomics is a novel technique which extracts large-scale quantitative features from medical images and constructs machine learning models based on these features (23–26). Radiomics has been widely used in cancer screening, diagnosis, treatment, and outcome prediction (27–30). Recently, Ramkumar et al. (31) found that MRI-based texture analysis had the potential to differentiate SCC from IP. However, there is no study investigating the application of radiomics to the differentiation of IP and IP-transformed squamous cell carcinomas.

Therefore, this study aimed to investigate the value of MRI-based radiomics in discriminating sinonasal IP from IP-transformed squamous cell carcinomas, and to improve the accuracy of preoperative diagnosis of IP-SCC.

Abbreviations: IP, Inverted papilloma; IP-SCC, Inverted papilloma-transformed squamous cell carcinomas; CCP, Convoluted cerebriform pattern; T1WI, T1-weighted images; T2WI, T2-weighted images; CE-T1WI, Contrast-enhanced T1-weighted images; ROI, Regions of interest; ICC, intra-class correlation coefficient; mRMR, Minimum redundancy maximum relevance; SVM, Support vector machine; ROC, The area under the receiver operating characteristic; AUC, The area under the receiver operating characteristic curves; CI, confidence interval.

MATERIALS AND METHODS

Patients

This retrospective study has been approved by our institutional review board and the informed consents were waived. The medical records of pathologically proven IP or IP-SCC patients who underwent surgery at Beijing Tongren Hospital were retrospectively reviewed between January 2008 and December 2019. Recurrent tumors were included in the study. Patients were required to have a contrast-enhanced head and neck MRI within 3 weeks before surgical resection. Patients were excluded if they had chemotherapy or radiation therapy. In addition, patients were further excluded if the maximum diameter of the tumor was smaller than 1.5 cm on axial MR slices to ensure that enough radiomics features could be extracted. Finally, 236 patients with IP-SCC (n=92) or IP (n=144) were included in the study. The patients were randomly divided into a training cohort (n=157) and a testing cohort (n=79) at a ratio of 2:1 (**Figure 1**).

Demographic and clinical data were collected from enrolled patients, including gender, age, tumor location, and history of IP resection.

Image Data Acquisition

All MR images were obtained with 3.0 T MR scanners (Ingenia; Philips Healthcare, Amsterdam, The Netherlands; or GE Signa HDxt, GE Healthcare, Milwaukee, USA; or GE Discovery 750, GE Healthcare, Milwaukee, USA) using an 8-channel head coil. The MR protocol included axial fast spin-echo (FSE) T1-weighted images (T1WI), FSE T2-weighted images (T2WI), and fat-saturated contrast enhanced T1WI (CE-T1WI). Contrast-enhanced T1-weighted images (CE-T1WI) were obtained after the intravenous bolus injection of 0.1 mL/kg gadopentetate dimeglumine. The detailed parameters for MR images acquisition are shown in **Table S1**.

Images Segmentation

A head and neck radiologist (Y.Y.) segmented the Region of Interest (ROIs) of tumor for all of the patients using ITK-SNAP software (www.itksnap.org). For each MR sequence, the slice with the largest tumor area and its adjacent slices were selected and the outline of the tumor was delineated. In order to check the intra-reader agreement of tumor segmentation, we randomly selected 30 patients and segmented the ROI again by another radiologist (JH.T.). The intra-class correlation coefficient (ICC) was calculated to measure the robustness of the radiomic features.

Feature Selection and Radiomic Model Construction

Before feature selection, all MR images were normalized and resampled using B-spline interpolation to 1mm×1mm×1mm in order to compensate for scanner-dependent variability in image intensity. Detailed process shown in **Supplementary A1**. A total

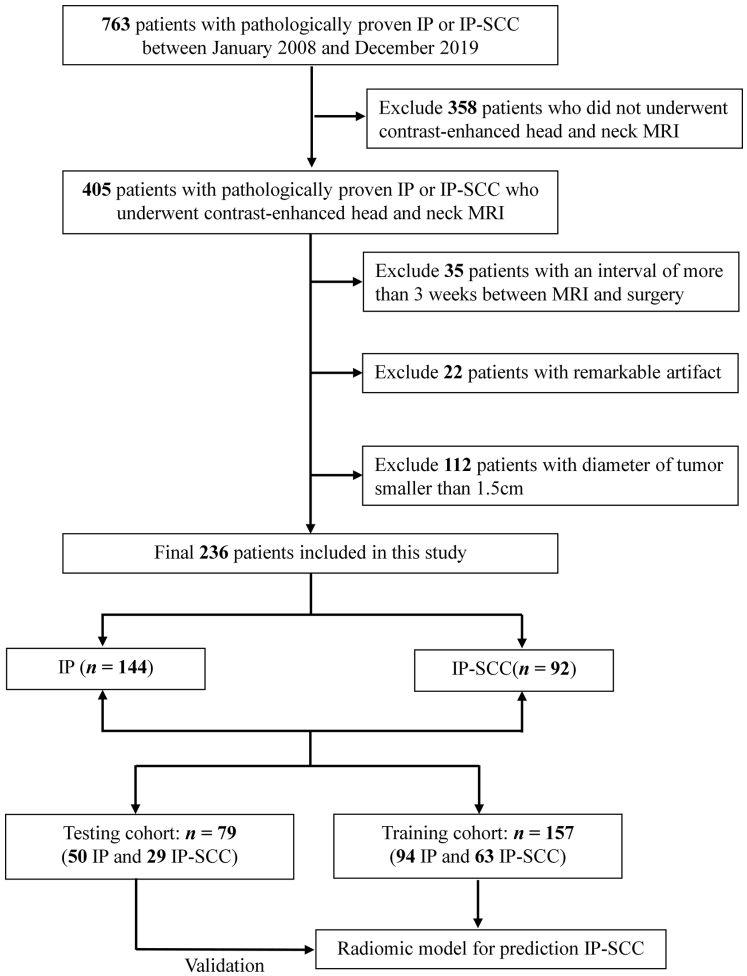

FIGURE 1 | Flow diagram shows the procedure of data selection for prediction of malignant transformation of inverted papilloma. IP, inverted papilloma; IP-SCC, inverted papilloma–transformed squamous cell carcinoma.

of 1316 radiomic features were extracted from each MR sequence using Pyradiomics (https://pyradiomics.readthedocs.io). For each ROI, the shape, intensity (first order statistics), and textural features were calculated and normalized by the z-score method (29, 32). Then, we respectively constructed three single-sequence radiomic signatures (T1WI, T2WI, and CE-T1WI) using corresponding sequence images.

The building process of each single-sequence signature was as follows: (1) we retained features that were significantly associated with IP-SCC in a univariable analysis; (2) the features with good robustness (ICC>0.75) were reserved for further analysis (33); (3) the minimum redundancy maximum relevance (mRMR) method was used to rank the radiomic features with mutual information. The top five features were selected as the final radiomic features; (4) the radiomic signatures were generated using logistic regression based on the five features.

We further combined the three single-sequence radiomic signatures to construct a radiomic model using multivariable logistic regression.

Morphological Model and Combined Model Construction

The morphological features assessment was performed independently by two head and neck radiologists (Y.Y. 5 years of clinical experience and JH.T. 10 years of clinical experience, respectively) who were blinded to histopathology and clinical information. Morphological features included cranial base invasion, orbit invasion, soft tissue invasion in the maxillofacial area, internal necrosis of the tumor, and loss of a convoluted cerebriform pattern (CCP). We designated a CCP as alternating hyperintense and hypointense bands in the solid components of the tumor on T2WI or CE-T1WI. The loss of CCP was categorized as partial, total, and no loss of CCP (9, 34). Cohen's kappa interrater reliability score was calculated to measure the inter-group agreement of the two radiologists' assessments for the morphological features.

For the morphological model, we first selected the morphological features that were of significant relevance to IP-SCC. Then, based on significant features, we respectively used

two classifiers, including logistic regression and support vector machine (SVM), to construct and save the one with better diagnosis ability as a morphological model.

Finally, we built a combined model that embedded the radiomic model and morphological model. Linear regression was used for the merging of the two models.

Model Validation and Comparison

The performances of the prediction models were assessed using the receiver operating characteristic (ROC) curve and area under the curve (AUC) with a 95% confidence interval (CI). The sensitivity, specificity, and accuracy were also calculated for further evaluation. The calibration curves were applied to modify and reduce the bias of the models. Furthermore, the performance of the constructed models in this study were evaluated by a 5-fold cross-validation setup.

For comparison, a senior and junior head and neck radiologist (Y.Y. and JH.T.) were invited to independently diagnose IP-SCC *via* MR images. Both of the radiologists were blinded to the histopathology during the diagnosis process.

All of the images were scanned by three MR scanners (Philips Ingenia; GE Signa HDxt; GE Discovery 750). Stratified analysis was used to check whether the models were affected by different MR scanners.

Statistical Analysis

The chi-square test and two-tailed *t* tests were used to calculate univariate analyses for categorical and continuous variables, respectively. $P<0.05$ was considered statistically significance. Radiomic feature standardization, selection and model building were performed using the Python (version: 3.7). The radiomic features with ICC > 0.75 were regarded as having good robustness and stability. ROC analysis was used to evaluate the diagnostic performances of models and radiologist assessment [95% confidence intervals (CIs), specificity, and sensitivity were also calculated]. The DeLong test was performed to compare the diagnostic performance of models. The statistical analyses were performed with R software (version: 3.6) and Python (version: 3.7).

RESULTS

Clinical and Morphological Characteristics

There were 157 patients in the training cohort (94 IPs and 63 IP-SCCs). The remaining 79 patients were allocated into the testing cohort (50 IPs and 29 IP-SCCs). As shown in **Table 1**, the average ages of patients for IP-SCC and IP were 57.4 and 51.6 years, respectively ($P = 0.001$). There was no difference in sex and prior IP resection between IP-SCC and IP. The maxillary sinus was a more common tumor site in IPs than IP-SCCs ($P <0.001$); the frontal sinus was a more common tumor site in IP-SCCs than IPs ($P < 0.001$).

The Cohen's kappa interrater reliability score calculated for five MR morphological features assessed by two radiologists were over 0.8, reflecting a strong agreement (**Table S2**) (35). As shown in **Table 2**, there were five features that were significantly associated with IP-SCC in the training cohort including cranial base invasion ($P = 0.001$), orbit invasion ($P <0.001$), soft tissue invasion in the maxillofacial area ($P = 0.003$), internal necrosis of the tumor ($P = 0.003$), and loss of a convoluted cerebriform pattern ($P < 0.001$). All of these features were also significant in the testing cohort.

TABLE 1 | Demographics and Clinical Characteristics.

	IP-SCC (n = 92)	IP (n = 144)	P
Age, years (mean ± SD)	57.4 ± 13.6	51.6 ± 11.8	0.001
Sex, *n* (%)			0.070
Male	72 (78.3)	97 (67.4)	
Female	20 (21.7)	47 (32.6)	
Tumor location*, *n* (%)			
Nasal cavity	54 (58.7)	100 (69.4)	0.091
Maxillary sinus	55 (59.8)	126 (87.5)	<0.001
Ethmoid sinus	40 (43.5)	55 (38.2)	0.419
Sphenoid sinus	4 (4.3)	3 (2.1)	0.322
Frontal sinus	22 (23.9)	10 (6.9)	<0.001
Prior IP resection, *n* (%)			0.604
Yes	39 (42.4)	66 (45.8)	
No	53 (57.6)	78 (54.2)	

**Multiple locations of tumors were counted separately.*

IP, inverted papilloma; IP-SCC, inverted papilloma–transformed squamous cell carcinoma.

Reproducibility and Feature Selection

A total of 3948 features (1316 features per MR sequence) were extracted from the tumor ROIs. After the univariable analysis, we selected 701, 757, and 748 features with a significant difference from T1WI, T2WI, and CET1WI, respectively. There were 580 (82.8%), 714 (94.4%), and 645 (86.2%) features showing good consistency and robustness from T1WI, T2WI and CE-T1WI sequences, respectively. For each sequence, we finally selected five key features to construct a radiomic signature. **Table S3** shows those key features in the three sequences.

Diagnostic Performances of Radiomic and Morphological Models

The performances of the three single-sequence signatures are shown in **Table S4**. In the validation cohort, the AUC of the CE-T1WI-signature (AUC = 0.931) surpassed the T1WI-signature (AUC = 0.857) and T2WI-signature (AUC = 0.886).

A radiomic model was constructed by fusing a T1WI-signature, T2WI-signature, and CE-T1WI-signature. As shown in **Table 3**, the radiomic model had good ability in discriminating IP-SCC from IP. In the testing cohort, the AUC of the radiomic model (AUC = 0.940) was better than the three single-sequence signatures.

We chose SVM classifier to construct morphological features model containing five morphological features. The morphological features model reached accuracy of 0.796 and 0.823 in training and testing cohorts, respectively (**Table 3**).

Diagnostic Performances of the Combined Model and Comparison With Radiologists

The ROC curves of the radiomic model, and combined model are shown in **Figure 2**. The quantitative indices of the models are

TABLE 2 | Morphological features of patients in training and Testing cohorts.

	Training cohort (n=157)			Testing cohort (n=79)		
	IP-SCC (n = 63)	IP (n = 94)	P	IP-SCC (n = 29)	IP (n = 50)	P
Internal necrosis of the tumor, *n* (%)			0.002			0.007
Absent	39 (61.9)	79 (84)		19(65.5)	45 (90)	
Present	24 (38.1)	15 (16)		10(34.5)	5 (10)	
Orbit invasion, *n* (%)			<0.001			<0.001
Absent	40 (63.5)	90 (95.7)		19(65.5)	50 (100)	
Present	23 (36.5)	4 (4.3)		10(34.5)	0 (0)	
Cranial base invasion, *n* (%)			0.001			0.020
Absent	53 (84.1)	93 (98.9)		26 (89.7)	50 (100)	
Present	10 (15.9)	1 (1.1)		3(10.3)	0(0)	
Soft tissue invasion in the maxillofacial area, *n* (%)			0.001			<0.001
Absent	49 (77.8)	89 (94.7)		21 (72.4)	50(100)	
Present	14 (22.2)	5 (5.3)		8 (27.6)	0 (0)	
Loss of CCP, *n* (%)			<0.001			<0.001
Absent	26 (41.3)	83 (88.3)		9 (31)	45 (90)	
Partial	27 (42.8)	10 (10.6)		8 (27.6)	5 (10)	
Total	10 (15.9)	1 (1.1)		12 (41.4)	0 (0)	

IP, inverted papilloma; IP-SCC, inverted papilloma–transformed squamous cell carcinoma; CCP, convoluted cerebriform pattern.

TABLE 3 | The Performance of Models in Training and Testing cohorts.

Model	AUC (95%CI)	SEN	SPE	ACC	TP	FN	FP	TN
Morphological features model								
Training cohort	—	0.667	0.883	0.796	42	21	11	83
Testing cohort	—	0.690	0.9	0.823	20	9	5	45
Radiomic model								
Training cohort	0.954 (0.926-0.982)	0.857	0.883	0.873	54	9	11	83
Testing cohort	0.940 (0.888-0.992)	0.793	0.92	0.873	23	6	4	46
Combined model								
Training cohort	0.957 (0.928-0.987)	0.889	0.915	0.904	56	7	8	86
Testing cohort	0.962 (0.927-0.997)	0.828	0.94	0.899	24	5	3	47
Senior radiologist								
Training cohort	—	0.571	0.947	0.796	36	27	5	89
Testing cohort	—	0.517	0.980	0.810	15	14	1	49
Junior radiologist								
Training cohort	—	0.492	0.904	0.739	31	32	9	85
Testing cohort	—	0.448	0.960	0.772	13	16	2	48

AUC, area under the curve; CI, confidence interval; SEN, Sensitivity; SPE, Specificity; ACC, Accuracy; TP, True Positive; FN, False Negative; FP, False Positive; TN, True Negative.

shown in **Table 3**. The AUC, sensitivity, specificity, and accuracy on the test cohort of the combined model were respectively 0.962, 0.828, 0.94, and 0.899. The sensitivity, specificity, and accuracy of the combined model surpassed morphological features model.

We also randomly divided the dataset into five parts. After 5-fold cross-validation, we noticed that the AUCs of combined model range from 0.964-0.9790 in training cohort and 0.932-0.985 in testing cohort. The average AUC of combined model (training cohort:0.971; testing cohort: 0.951) surpassed than that of other models (**Table S5**). As shown in **Figure 3**, the calibration curves demonstrated that the predicted results of the combined model were in good agreement with the actual results.

We also compared the performance of the two head and neck radiologists and the combined model (**Figure 4**). As shown in **Table 3**, the combined model had better accuracy (0.899) and sensitivity (0.828) than the two radiologists in the testing cohort. The specificity of the combined model was similar to the two radiologists. This indicated that the combined model could diagnose more patients with IP-SCC, while avoiding missed diagnoses.

Impact of Different MR Scanners on the Models

In the stratified analysis, all patients were divided into three subgroups according to different MR scanners (Philips Ingenia; GE Signa HDxt; GE Discovery 750). From **Table S6**, we found that the radiomics features in the model performed well in different scanners. As shown in **Figure 5**, there was no significant difference in the performance of the combined model among the three MR scanners ($P \geq 0.249$).

DISCUSSION

Accurate prediction of the malignant transformation of IP has long been a focus of clinical concern and challenge (1, 5).

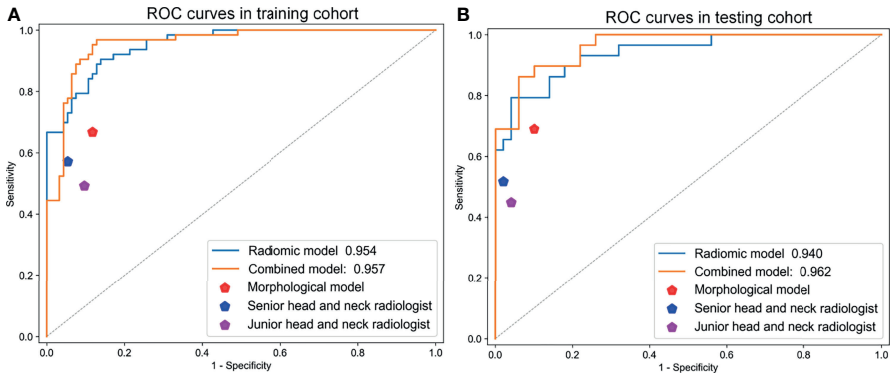

FIGURE 2 | The ROC curves of the radiomic model, morphological features model, and combined model in **(A)** training and **(B)** testing cohorts.

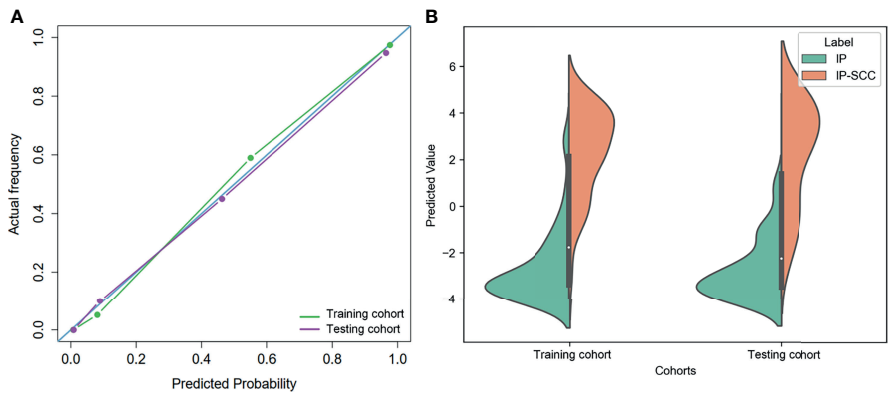

FIGURE 3 | **(A)** The calibration curves of the combined model in training and testing cohorts. **(B)** Distribution of the combined model predicted values in training and testing cohorts.

As malignant tumors require more extensive surgical resection and adjuvant treatment, preoperatively prediction of the malignant transformation of IP is critical for improving patient counseling and planning precise treatment (3).

In this retrospective study, we developed a combined model based on MR radiomic features and morphological features to discriminate IP-SCC from IP. The results showed that the combined model had excellent diagnostic accuracy, which performed better than the radiomic model and morphological model. Moreover, the combined model outperformed the two head and neck radiologists, demonstrating the potential clinical value of the model.

In previous studies, many researchers found that the loss of a convoluted cerebriform pattern (CCP) was a significant MRI feature for predicting IP-SCC (18, 20–22, 34). Yan et al. (9) previously evaluated 35 IP-SCC patients and found that 60% of patients had a complete loss of CCP. In the study of Zhang et al. (22), the sensitivity and specificity of loss of CCP for predicting IP-SCC were 73.4% and 85.4%, respectively. In our study, the loss of CCP was found in 61.9% (57/92) of IP-SCC patients and 11.1% (16/144) of IP patients. These studies suggested that it is not sufficient for differentiating IP-SCC from IP only by the presence or absence of CCP. The potential possibility of interpretive error increases, particularly when a small focus of SCC exists within a large benign IP and cannot be recognized because of the presence of CCP (22, 36).

In terms of evaluating the intrinsic appearance of a tumor, radiomics has a strong ability of feature extraction and texture analysis. It can provide incremental benefits when the radiologists' visual recognition ability reaches its limit, and can comprehensively extract and analyze the internal fine structure of the tumor (37–39). In the current study, the best 15 radiomic features that could discriminate IP-SCC from IP included 13 texture features, 1 shape feature, and 1 intensity feature. Among them, the texture features which reflect gray-level nonuniformity had higher values in IP-SCC, which may be explained by a higher heterogeneity of the images. Accurately assessing the heterogeneity of a small region would be the key to detecting focal malignant transformation in IP (31).

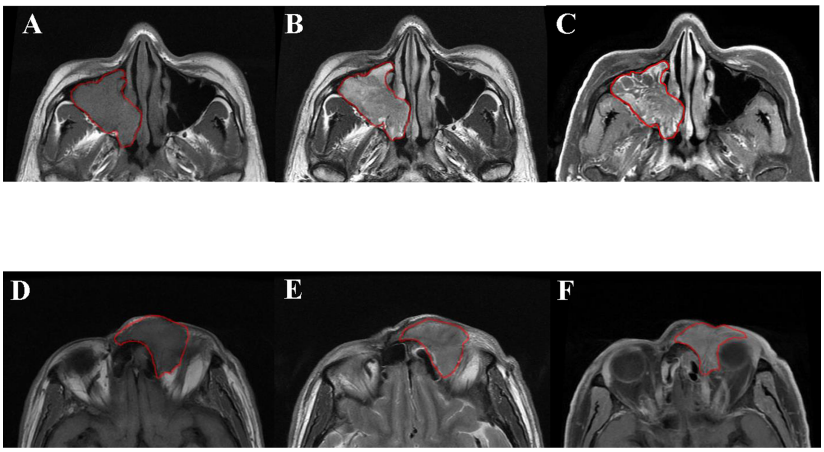

FIGURE 4 | Patient 1: axial T1WI **(A)**, axial T2WI **(B)**, and axial contrast-enhanced T1WI **(C)**. A 48-year-old man was pathologically diagnosed as inverted papilloma in the right nasal cavity and maxillary sinus, with severe epithelial atypical hyperplasia and carcinogenesis. The presence of convoluted cerebriform pattern and absence of extra-sinonasal involvement led to a misclassification as benign by the two radiologists, whereas the radiomic model well-classified it as malignant. Patient 2: axial T1WI **(D)**, axial T2WI **(E)**, and axial contrast-enhanced T1WI **(F)**. A68 year-old man was pathologically diagnosed as an inverted papilloma in the left frontal sinus and, with squamous cell carcinoma in some areas. In this case, orbital invasion was a key feature of malignancy easily seen by radiologists. The two radiologists well-classified the case as malignant, whereas the radiomic model misclassified it as benign.

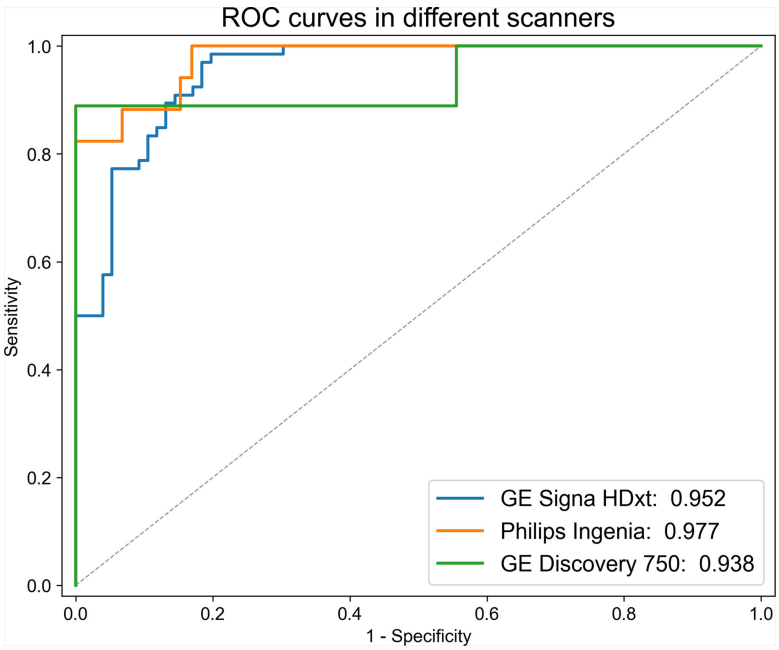

FIGURE 5 | ROC curves of the combined model in different MR scanners. There was no significant difference in the performance of the combined model among the three MR scanners.

Interestingly, radiomics could also extract useful features from images that may be ignored by the human eyes. The study of Ramkumar et al. (31) found that the texture features extracted from non-enhanced T1WI could be used to distinguish IP from SCC. To our best knowledge, the value of T1WI in distinguishing malignant transformation of IP has not receive attention. Therefore, our study selected radiomic features from T1WI, T2WI, and CE-T1WI images to avoid missing key

features. The results showed that the key radiomic features of these three sequences had good diagnostic performances. The features in the CE-T1WI sequence showed the best diagnostic performance. In this study, we fused the radiomic features from the three sequences together to construct a radiomic model, which has a powerful ability to identify IP-SCC.

However, the radiomic model we constructed was meant to supplement radiologists' diagnostic abilities rather than compete with them. In clinics, the diagnosis is based on the synthesis of all available data, including not only the intrinsic appearance of tumor, but also the imaging features of the peritumoral environment, such as the invasion and destruction of the tumor in the surrounding tissues (31). Therefore, five MR morphological features assessed by radiologists were analyzed in this study, these features were significantly different between IP and IP-SCC. Among them, cranial base invasion, orbit invasion, and soft tissue invasion in the maxillofacial area reflect the involvement of peritumoral tissues, whereas these features were not common in IP-SCCs of our study. Some malignancies of this study, including 29 cases of pathologically confirmed carcinoma *in situ*, did not show obvious aggressiveness, leading to the high specificity but unsatisfactory sensitivity of diagnostic results by the two head and neck radiologists who give results based on these morphological features.

The model based on morphological features performed worse than the radiomic model, the combined model (the combination of radiomic model and morphological feature model) performed better than the other two models. This indicated that the combined model might improve the limit of ignoring the peritumoral environment produced by radiomic model, and would bring an icing on the cake effect.

Our study had some limitations. First, we did not include diffusion weighted images. It has been reported that the apparent diffusion coefficient (ADC) value can also distinguish IP-SCC from IP (9). However, if malignant transformation occurs as a small focus, the mean ADC value cannot represent IP-SCC in the background of IP (34), which may require a histogram analysis of ADC values for the whole tumor (34). Second, we included inverted papilloma-transformed squamous cell carcinoma as much as possible to develop a robust model, the current study included 105 recurrent patients, which may decrease the quality of data. But we have not found any difference in radiomic features between the recurrent tumors and primary tumors. The outcomes of a previous treatment (scar, hyperostosis, iatrogenic anatomical changes) could influence the radiological interpretation. However, scar and hyperostosis identified by MR images may not be totally consistent with histopathological results, so they are not evaluated in the current study, which my influence the performance of the model. We will investigate them in the future. Third, although the radiomic model can distinguish IP-SCC from IP, it cannot accurately pinpoint which regions develop malignant transformation within the tumor, further prospective studies were required to ensure that the histopathological analysis results can be accurately synchronized and corresponded with MR images (31). The goal of the next step for radiomics should be to assist diagnosis by highlighting the most suspicious regions of malignant transformation. Forth, the rate of SCC in inverted papillomas (39%) is higher than the trends reported in the literature, which may bring bias to the assessment of the diagnostic performance of the model. Our hospital is one of the best hospitals in otorhinolaryngology in China, many patients with IP-SCC seek treatment at our hospital, so the rate of SCC in inverted papillomas in higher than trends reported in the literature. We will validate and optimize the model using multicenter data in the future.

In conclusion, we constructed a combined model based on MR radiomic features and morphological features to discriminate IP-SCC from IP. The model could serve as a potential tool to assist clinicians for an accurate and noninvasive diagnosis of the malignant transformation in IP patients, which might improve patient counseling and help to make more precise treatment planning for IP-SCC.

DATA AVAILABILITY STATEMENT

The raw data supporting the conclusions of this article will be made available by the authors, without undue reservation.

ETHICS STATEMENT

The studies involving human participants were reviewed and approved by The Ethics Review Committee of Beijing Tongren Hospital. Written informed consent for participation was not required for this study in accordance with the national legislation and the institutional requirements.

AUTHOR CONTRIBUTIONS

YY, YL, and JX designed and supervised the study. YY, ZL, and JG collected the clinical data, MR images, and histopathological results. YY, YL, and JT processed the clinical and images data. YY, YL, and XQ performed the statistical analysis. YY and YL drafted and revised the manuscript. All authors contributed to the article and approved the submitted version.

FUNDING

This work was supported by the National Key R&D Program of China (2017YFA0205200, 2017YFC1308700, 2017YFA0700401, 2017YFC1309100), National Natural Science Foundation of China (82022036, 91959130, 81971776, 81771924, 62027901, 81930053, 81227901), Beijing Natural Science Foundation (L182061), Strategic Priority Research Program of the Chinese Academy of Sciences (XDB 38040200), Chinese Academy of Sciences under Grant (GJJSTD20170004 and QYZDJ-SSW-JSC005), Project of High-Level Talents Team Introduction in Zhuhai City (Zhuhai HLHPTP201703), Youth Innovation Promotion Association CAS (2017175), Beijing Municipal

Administration of Hospitals'Ascent Plan (DFL20190203), Beijing Municipal Administration of Hospitals Clinical Medicine Development of Special Funding Support (ZYLX201704), and High Level Health Technical Personnel of Bureau of Health in Beijing (2014-2-005).

SUPPLEMENTARY MATERIAL

The Supplementary Material for this article can be found online at: https://www.frontiersin.org/articles/10.3389/fonc.2022.870544/full#supplementary-material

REFERENCES

1. Melroy CT, Senior BA. Benign Sinonasal Neoplasms: A Focus on Inverting Papilloma. *Otolaryngol Clin North Am* (2006) 39(3):601–17. doi: 10.1016/j.otc.2006.01.005
2. Mirza S, Bradley PJ, Acharya A, Stacey M, Jones NS. Sinonasal Inverted Papillomas: Recurrence, and Synchronous and Metachronous Malignancy. *J Laryngol Otol* (2007) 121(9):857–64. doi: 10.1017/S002221510700624X
3. Lawson W, Kaufman MR, Biller HF. Treatment Outcomes in the Management of Inverted Papilloma: An Analysis of 160 Cases. *Laryngoscope* (2003) 113(9):1548–56. doi: 10.1097/00005537-200309000-00026
4. Lesperance MM, Esclamado RM. Squamous Cell Carcinoma Arising in Inverted Papilloma. *Laryngoscope* (1995) 105(2):178–83. doi: 10.1288/00005537-199502000-00013
5. Long C, Jabarin B, Harvey A, Ham J, Javer A, Janjua A, et al. Clinical Evidence Based Review and Systematic Scientific Review in the Identification of Malignant Transformation of Inverted Papilloma. *J Otolaryngol Head Neck Surg* (2020) 49(1):25. doi: 10.1186/s40463-020-00420-x
6. Anari S, Carrie S. Sinonasal Inverted Papilloma: Narrative Review. *J Laryngol Otol* (2010) 124(7):705–15. doi: 10.1017/S0022215110000599
7. Liang QZ, Li DZ, Wang XL, Huang H, Xu ZG, Wu YH. Survival Outcome of Squamous Cell Carcinoma Arising From Sinonasal Inverted Papilloma. *Chin Med J (Engl)* (2015) 128(18):2457–61. doi: 10.4103/0366-6999.164929
8. Li Y, Wang C, Wang R, He S, Feng L, Ma H, et al. Survival Outcomes and Prognostic Factors of Squamous Cell Carcinomas Arising From Sinonasal Inverted Papillomas: A Retrospective Analysis of 120 Patients. *Int Forum Allergy Rh* (2019) 9(11):1367–73. doi: 10.1002/alr.22400
9. Yan CH, Tong C, Penta M, Patel VS, Palmer JN, Adappa ND, et al. Imaging Predictors for Malignant Transformation of Inverted Papilloma. *Laryngoscope* (2019) 129(4):777–82. doi: 10.1002/lary.27582
10. Peng R, Thamboo A, Choby G, Ma Y, Zhou B, Hwang PH. Outcomes of Sinonasal Inverted Papilloma Resection by Surgical Approach: An Updated Systematic Review and Meta-Analysis. *Int Forum Allergy Rhinol* (2019) 9(6):573–81. doi: 10.1002/alr.22305
11. Han MW, Lee BJ, Jang YJ, Chung YS. Clinical Value of Office-Based Endoscopic Incisional Biopsy in Diagnosis of Nasal Cavity Masses. *Otolaryngol Head Neck Surg* (2010) 143(3):341–7. doi: 10.1016/j.otohns.2010.05.019
12. Sham CL, Lee DL, van Hasselt CA. Tong MC. A Case-Control Study of the Risk Factors Associated With Sinonasal Inverted Papilloma. *Am J Rhinol Allergy* (2010) 24(1):e37–40. doi: 10.2500/ajra.2010.24.3408
13. Miyazaki T, Haku Y, Yoshizawa A, Iwanaga K, Fujiwara T, Mizuta M, et al. Clinical Features of Nasal and Sinonasal Inverted Papilloma Associated With Malignancy. *Auris Nasus Larynx* (2018) 45(5):1014–9. doi: 10.1016/j.anl.2018.02.009
14. Yasumatsu R, Nakashima T, Sato M, Nakano T, Kogo R, Hashimoto K, et al. Clinical Management of Squamous Cell Carcinoma Associated With Sinonasal Inverted Papilloma. *Auris Nasus Larynx* (2017) 44(1):98–103. doi: 10.1016/j.anl.2016.04.004
15. Chawla A, Shenoy J, Chokkappan K, Chung R. Imaging Features of Sinonasal Inverted Papilloma: A Pictorial Review. *Curr Probl Diagn Radiol* (2016) 45(5):347–53. doi: 10.1067/j.cpradiol.2015.10.004
16. Som PM, Lawson W, Lidov MW. Simulated Aggressive Skull Base Erosion in Response to Benign Sinonasal Disease. *Radiology* (1991) 180(3):755–9. doi: 10.1148/radiology.180.3.1871290
17. Yousem DM, Fellows DW, Kennedy DW, Bolger WE, Kashima H, Zinreich SJ. Inverted Papilloma: Evaluation With MR Imaging. *Radiology* (1992) 185(2):501–5. doi: 10.1148/radiology.185.2.1410362
18. Ojiri H, Ujita M, Tada S, Fukuda K. Potentially Distinctive Features of Sinonasal Inverted Papilloma on MR Imaging. *AJR Am J Roentgenol* (2000) 175(2):465–8. doi: 10.2214/ajr.175.2.1750465
19. Fang G, Lou H, Yu W, Wang X, Yang B, Xian J, et al. Prediction of the Originating Site of Sinonasal Inverted Papilloma by Preoperative Magnetic Resonance Imaging and Computed Tomography. *Int Forum Allergy Rhinol* (2016) 6(12):1221–8. doi: 10.1002/alr.21836
20. Maroldi R, Farina D, Palvarini L, Lombardi D, Tomenzoli D, Nicolai P. Magnetic Resonance Imaging Findings of Inverted Papilloma: Differential Diagnosis With Malignant Sinonasal Tumors. *Am J Rhinol* (2004) 18(5):305–10. doi: 10.1177/194589240401800508
21. Jeon TY, Kim H, Chung S, Dhong H, Kim HY, Yim YJ, et al. Sinonasal Inverted Papilloma: Value of Convoluted Cerebriform Pattern on MR Imaging. *Am J Neuroradiol* (2008) 29(8):1556–60. doi: 10.3174/ajnr.A1128
22. Zhang L, Fang G, Yu W, Yang B, Wang C, Zhang L. Prediction of Malignant Sinonasal Inverted Papilloma Transformation by Preoperative Computed Tomography and Magnetic Resonance Imaging. *Rhinology* (2020) 58(3):248–56. doi: 10.4193/Rhin19.240
23. Lambin P, Rios-Velazquez E, Leijenaar R, Carvalho S, van Stiphout RG, Granton P, et al. Radiomics: Extracting More Information From Medical Images Using Advanced Feature Analysis. *Eur J Cancer* (2012) 48(4):441–6. doi: 10.1016/j.ejca.2011.11.036
24. Lambin P, Leijenaar RTH, Deist TM, Peerlings J, de Jong EEC, van Timmeren J, et al. Radiomics: The Bridge Between Medical Imaging and Personalized Medicine. *Nat Rev Clin Oncol* (2017) 14(12):749–62. doi: 10.1038/nrclinonc.2017.141
25. Bi WL, Hosny A, Schabath MB, Giger ML, Birkbak NJ, Mehrtash A, et al. Artificial Intelligence in Cancer Imaging: Clinical Challenges and Applications. *CA Cancer J Clin* (2019) 69(2):127–57. doi: 10.3322/caac.21552
26. Dong D, Tang L, Li Z, Fang M, Gao J, Shan X, et al. Development and Validation of an Individualized Nomogram to Identify Occult Peritoneal Metastasis in Patients With Advanced Gastric Cancer. *Ann Oncol* (2019) 30(3):431–8. doi: 10.1093/annonc/mdz001
27. Zhang F, Zhong LZ, Zhao X, Dong D, Yao JJ, Wang SY, et al. A Deep-Learning-Based Prognostic Nomogram Integrating Microscopic Digital Pathology and Macroscopic Magnetic Resonance Images in Nasopharyngeal Carcinoma: A Multi-Cohort Study. *Ther Adv Med Oncol* (2020) 12:431380840. doi: 10.1177/1758835920971416
28. Dong D, Fang MJ, Tang L, Shan XH, Gao JB, Giganti F, et al. Deep Learning Radiomic Nomogram can Predict the Number of Lymph Node Metastasis in Locally Advanced Gastric Cancer: An International Multicenter Study. *Ann Oncol* (2020) 31(7):912–20. doi: 10.1016/j.annonc.2020.04.003
29. Dong D, Zhang F, Zhong LZ, Fang MJ, Huang CL, Yao JJ, et al. Development and Validation of a Novel MR Imaging Predictor of Response to Induction Chemotherapy in Locoregionally Advanced Nasopharyngeal Cancer: A Randomized Controlled Trial Substudy (NCT01245959). *BMC Med* (2019) 17(1):190. doi: 10.1186/s12916-019-1422-6
30. He B, Dong D, She Y, Zhou C, Fang M, Zhu Y, et al. Predicting Response to Immunotherapy in Advanced Non-Small-Cell Lung Cancer Using Tumor Mutational Burden Radiomic Biomarker. *J Immunother Cancer* (2020) 8(2):e000550. doi: 10.1136/jitc-2020-000550
31. Ramkumar S, Ranjbar S, Ning S, Lal D, Zwart CM, Wood CP, et al. MRI-Based Texture Analysis to Differentiate Sinonasal Squamous Cell Carcinoma From Inverted Papilloma. *Am J Neuroradiol* (2017) 38(5):1019–25. doi: 10.3174/ajnr.A5106
32. Liu Y, Fan H, Dong D, Liu P, He B, Meng L, et al. Computed Tomography-Based Radiomic Model at Node Level for the Prediction of Normal-Sized Lymph Node Metastasis in Cervical Cancer. *Transl Oncol* (2021) 14(8):101113. doi: 10.1016/j.tranon.2021.101113
33. Li Q, Liu YJ, Dong D, Bai X, Huang QB, Guo AT, et al. Multiparametric MRI Radiomic Model for Preoperative Predicting WHO/ISUP Nuclear Grade of

Clear Cell Renal Cell Carcinoma. *J Magn Reson Imaging* (2020) 52(5):1557–66. doi: 10.1002/jmri.27182
34. Suh CH, Lee JH, Chung MS, Xu XQ, Sung YS, Chung SR, et al. MRI Predictors of Malignant Transformation in Patients With Inverted Papilloma: A Decision Tree Analysis Using Conventional Imaging Features and Histogram Analysis of Apparent Diffusion Coefficients. *Korean J Radiol* (2021) 22(5):751–8. doi: 10.3348/kjr.2020.0576
35. Landis JR, Koch GG. The Measurement of Observer Agreement for Categorical Data. *Biometrics* (1977) 33(1):159–74. doi: 10.2307/2529310
36. Wang X, Zhang Z, Chen X, Li J, Xian J. Value of Magnetic Resonance Imaging Including Dynamic Contrast-Enhanced Magnetic Resonance Imaging in Differentiation Between Inverted Papilloma and Malignant Tumors in the Nasal Cavity. *Chin (Engl)* (2014) 127(9):1696–701. doi: 10.3760/cma.j.issn.0366-6999.20132409
37. Zhu Y, Man C, Gong L, Dong D, Yu X, Wang S, et al. A Deep Learning Radiomics Model for Preoperative Grading in Meningioma. *Eur J Radiol* (2019) 116:128–34. doi: 10.1016/j.ejrad.2019.04.022
38. Li J, Dong D, Fang M, Wang R, Tian J, Li H, et al. Dual-Energy CT-Based Deep Learning Radiomics can Improve Lymph Node Metastasis Risk Prediction for Gastric Cancer. *Eur Radiol* (2020) 30(4):2324–33. doi: 10.1007/s00330-019-06621-x
39. Li Z, Li H, Wang S, Dong D, Yin F, Chen A, et al. MR-Based Radiomics Nomogram of Cervical Cancer in Prediction of the Lymph-Vascular Space Invasion Preoperatively. *J Magn Reson Imaging* (2019) 49(5):1420–6. doi: 10.1002/jmri.26531

Conflict of Interest: The authors declare that the research was conducted in the absence of any commercial or financial relationships that could be construed as a potential conflict of interest.

Publisher's Note: All claims expressed in this article are solely those of the authors and do not necessarily represent those of their affiliated organizations, or those of the publisher, the editors and the reviewers. Any product that may be evaluated in this article, or claim that may be made by its manufacturer, is not guaranteed or endorsed by the publisher.

frontiers | Frontiers in Oncology

ORIGINAL RESEARCH
published: 08 April 2022
doi: 10.3389/fonc.2022.841262

Predicting the Proliferation of Tongue Cancer With Artificial Intelligence in Contrast-Enhanced CT

Ting-Guan Sun[1†], *Liang Mao*[1,2†], *Zi-Kang Chai*[1], *Xue-Meng Shen*[1] *and Zhi-Jun Sun*[1,2*]

[1] *The State Key Laboratory Breeding Base of Basic Science of Stomatology (Hubei-MOST) and Key Laboratory of Oral Biomedicine, Ministry of Education, School and Hospital of Stomatology, Wuhan University, Wuhan, China,* [2] *Department of Oral Maxillofacial-Head Neck Oncology, School and Hospital of Stomatology, Wuhan University, Wuhan, China*

Tongue squamous cell carcinoma (TSCC) is the most common oral malignancy. The proliferation status of tumor cells as indicated with the Ki-67 index has great impact on tumor microenvironment, therapeutic strategy making, and patients' prognosis. However, the most commonly used method to obtain the proliferation status is through biopsy or surgical immunohistochemical staining. Noninvasive method before operation remains a challenge. Hence, in this study, we aimed to validate a novel method to predict the proliferation status of TSCC using contrast-enhanced CT (CECT) based on artificial intelligence (AI). CECT images of the lesion area from 179 TSCC patients were analyzed using a convolutional neural network (CNN). Patients were divided into a high proliferation status group and a low proliferation status group according to the Ki-67 index of patients with the median 20% as cutoff. The model was trained and then the test set was automatically classified. Results of the test set showed an accuracy of 65.38% and an AUC of 0.7172, suggesting that the majority of samples were classified correctly and the model was stable. Our study provided a possibility of predicting the proliferation status of TSCC using AI in CECT noninvasively before operation.

Keywords: tongue cancer, artificial intelligence, convolutional neural networks, proliferation, bioinformatics

OPEN ACCESS

Edited by:
Narayana Subramaniam, Sri Shankara Cancer Research Foundation, India

Reviewed by:
Marco Mascitti, Marche Polytechnic University, Italy
Giuseppe Troiano, University of Foggia, Italy

***Correspondence:**
Zhi-Jun Sun
sunzj@whu.edu.cn

[†]*These authors have contributed equally to this work*

Specialty section:
This article was submitted to Head and Neck Cancer, a section of the journal Frontiers in Oncology

Received: *22 December 2021*
Accepted: *14 March 2022*
Published: *08 April 2022*

Citation:
Sun T-G, Mao L, Chai Z-K, Shen X-M and Sun Z-J (2022) Predicting the Proliferation of Tongue Cancer With Artificial Intelligence in Contrast-Enhanced CT. Front. Oncol. 12:841262. doi: 10.3389/fonc.2022.841262

INTRODUCTION

Tongue squamous cell carcinoma (TSCC) is the most common oral malignancy with increasing prevalence, and the 5-year survival rate is approximately 56.3% in China (1, 2). As a type of cancer, its fundamental trait is the ability to sustain proliferation (3), which relates closely to the tumor microenvironment. Tumors can produce mutations with neoantigens constantly during proliferation, influencing patients' response to chemotherapy and immune checkpoint inhibitors (4). Therefore, with the advent of immunotherapy in cancer therapy, accurate prediction of the proliferation status is of great significance to the subsequent clinical strategy making.

Among the biomarkers correlated to the proliferation, the most frequently used one is the percentage of Ki-67 expression, quantified by the Ki-67 index. Ki-67 is a DNA-binding protein located in the nucleus, and is only expressed in the proliferation phase with a short half-life (5). High expression of the Ki-67 suggests active cell proliferation, and may lead to tumor invasion, lymph node metastasis, and poor prognosis (6–8). OSCC patients with higher Ki-67 expression had better

response to radiosensitivity (9). In renal cancer, researchers found that Ki-67 could be a promising target for target therapy (10). In breast cancer, the Ki-67 index was considered as an indicator to monitor patient's treatment effect to chemotherapy (11). However, the present procedure to acquire the Ki-67 index is biopsy-based immunohistochemical (IHC) staining (12). Not only is it invasive and time-consuming, its result is also greatly affected by the quality of the biopsy (13). Therefore, obtaining proliferation status by noninvasive methods before operation is important for the multi-disciplinary treatment of TSCC.

Compared to traditional biopsy-based IHC that only reflects parts of tumor, radiological images have the advantage of involving the entire tumor information in a non-invasive manner, avoiding the influence of tumor heterogeneity (14). Recently, artificial intelligence (AI) has shown outstanding performance in quantifying and analyzing patterns of tumor phenotypes on radiographic images with bioinformatics tools to build pathoclinical relevant models (15, 16). However, the capability of the AI model to noninvasively predict the proliferation status of TSCC using radiological images remains unclear. Therefore, in this study, our purpose is to develop and validate a classifier based on a relatively mature convolutional neural network (CNN) model: Inception-Resnet-V2 (17), and use it to predict the proliferation status of TSCC through contrast-enhanced CT (CECT). We adapted our CNN model to single CT slide of TSCC and hypothesized that by learning to detect subtle patterns, our model can build a bridge between CT images and proliferation status of TSCC.

MATERIALS AND METHODS

Study Population

The data of the patients with TSCC in this experiment are collected from the Hospital of Stomatology, Wuhan University from August 2012 to July 2021. All the procedures were done following the Declaration of Helsinki guidelines and the protocol was ratified by the Institutional Medical Ethics Committee of School and Hospital of Stomatology, Wuhan University (2018LUNSHENZIA28).

Exclusion criteria were as follows:

- Patients without CECT images;
- Patients without Ki-67 staining;
- Artifacts caused by metal prostheses, implants, and titanium plate more than 50% in the lesion area;
- Patients with nonprimary tumor;
- Lesion is too small to be noticed in CECT.

There were 1,390 patients diagnosed with TSCC in the Hospital of Stomatology, Wuhan University from August 2012 to July 2021. At present, we found 179 patients who met our requirements. All the included TSCC patients underwent primary surgery. The patients were randomly divided into a training set, a validation set, and a test set (**Figure 1A**).

Immunohistochemistry of Ki-67 and Scoring

Immunohistochemistry (IHC) was established as previously described (18). Briefly, 4-μm-thick paraffin sections were deparaffinized in xylene and rehydrated *via* step-gradient ethanol. Antigen retrieval was operated with ethylenediaminetetraacetic acid, and the endogenous peroxidase was blocked by 3% hydrogen peroxide. After blocking with goat serum at 37°C for 1 h, sections were incubated with anti-human Ki-67 (clone: MXR002; RMA-0731, MXB Biotechnologies, China) with a dilution of 1:400 at a 4°C refrigerator overnight. Then, secondary biotin-labeled antibody and avidin-biotin-peroxidase reagent were used to incubate the sections at 37°C for 20 min each in order. Lastly, DAB kit (DAB-0031 MXB Biotechnologies, China) was applied for staining. The Ki-67 index was reported independently by the Department of Pathology in the Hospital of Stomatology, Wuhan University, without seeing patients' CECT.

CT Acquisition and Image Processing

All the CECT images in this study were obtained from a brightspeed 16-slice multi-slice CT machine (GE Healthcare, Milwaukee, WI) in the Hospital of Stomatology, Wuhan University (120 kV, 300 mA, slice thickness of 0.6 mm, pitch of 1.75:1, matrix of 512 × 512). The contrast agent is iopromide (Ultravist®300 Bayer AG, China), with a concentration of 300 mg/ml, 1.5–2.0 ml/kg.

To better process our data and reduce the computation cost, we converted the original CT files from DCM to PNG. The pixels of images were still 512 × 512 × 3, because besides the tongue, other unnecessary parts of the head in the CT images would disturb the judgment of CNN and bring unnecessary calculation. We then cut the majority of the noise parts out and only kept those images with lesion for the next step. After cutting, the size of the images was 180 × 180 × 3; only 12.36% of the original data remained (**Figure 1C**).

Code Availability and CNN Training

The computer used in this study included an Intel i7 1070 4.20 GHz CPU with 16 GB DDR4 Memory and an NVIDIA GeForce GTX 1070 8 GB GPU. The programming language for neural network structure is tensorflow2.2 available on an open-source software pycharm 2021.1.1.

The model based on the Inception-Resnet-V2 network was built with the structures shown in **Figure 2**. It consisted of 9 parts: the Input layer, the Stem layer, 3 Inception-resnet layers (Inception-resnet A, Inception-resnet B, and Inception-resnet C), 2 Reduction layers (Reduction A and Reduction B), the Average-pooling layer, and the Fully-connected layer (19). The input was the processed CT images with a size of 180 × 180 × 3. In addition, we also applied transfer learning to train our model on a large dataset on ImageNet in order to tackle the problem of limited dataset. With weights model adjusted properly, the pre-trained model can extract features and retrieve information from data automatically, and learn advanced abstract representations of data.

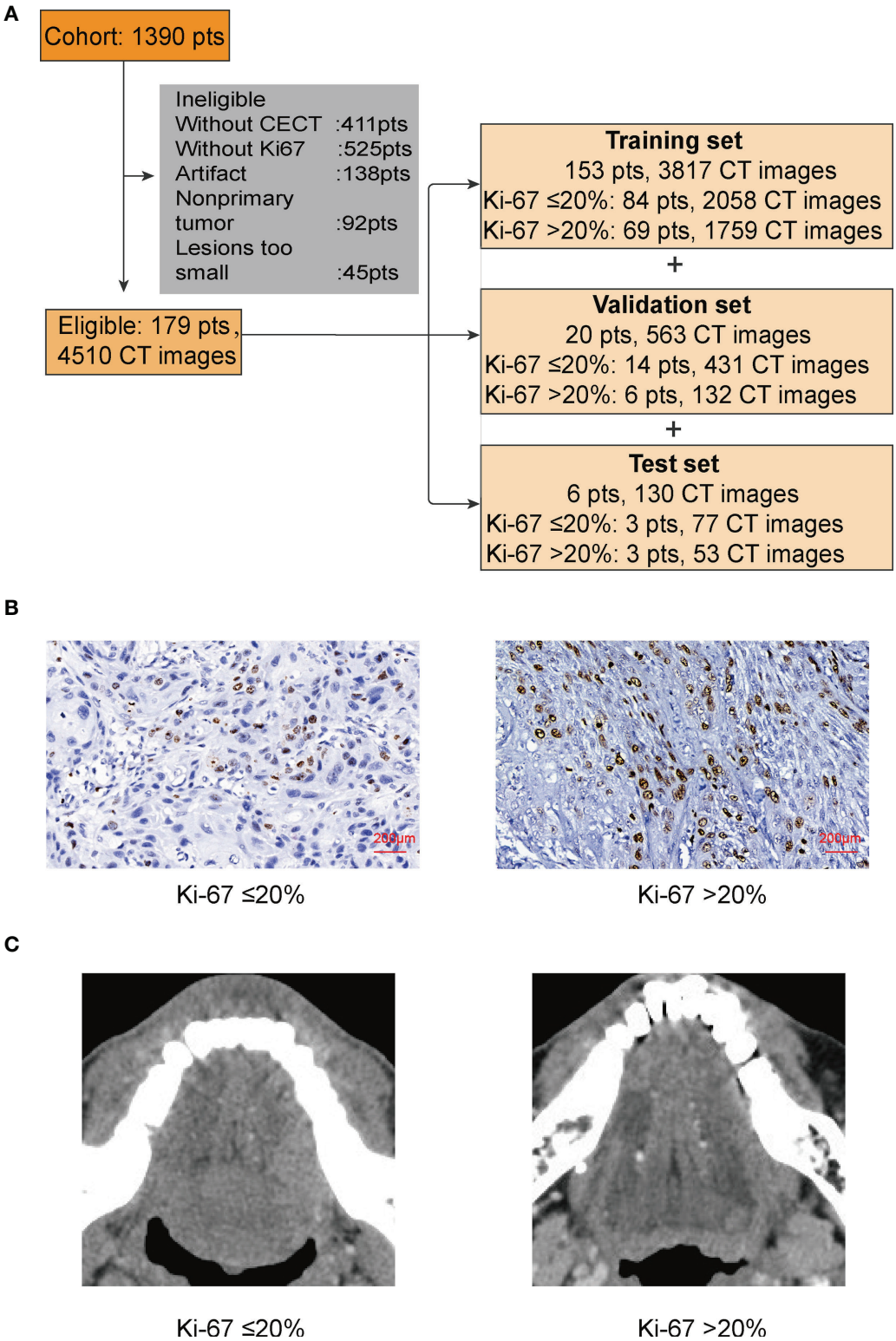

FIGURE 1 | **(A)** In this study, patients (pts) were randomly divided into a training set, a validation set, and a test set. **(B)** IHC of Ki-67. We used 20% as the cutoff to divide our patients into two groups: low proliferation status with Ki-67 ≤ 20%; high proliferation status with Ki-67 >20%. **(C)** The lesion part of TSCC in CECT.

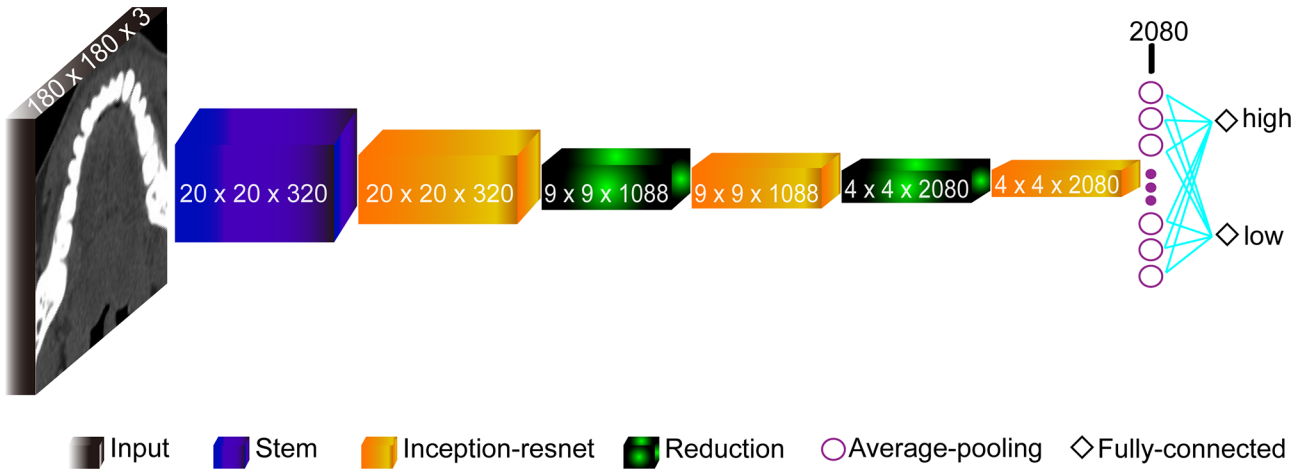

FIGURE 2 | The structure of the Inception-Resnet-V2 network model.

Statistical Analysis and Evaluation Metrics

$$\text{Accuracy} = \frac{\text{TP+TN}}{\text{TP+TN + TP+FN}}$$

$$\text{Sensitivity} = \frac{\text{TP}}{\text{TP+FN}}$$

$$\text{Specificity} = \frac{\text{TN}}{\text{TN+FP}}$$

(TP: true positive, FP: false positive, TN: true negative, FN: false negative)

We used accuracy, loss, sensitivity, specificity, the receiver operating characteristic (ROC) curve, and AUC to assess the performance of our model. For statistical analysis, we regarded low proliferation as positive and high proliferation as negative. For the analysis of clinical and pathologic features, χ^2 test, Fisher's exact test, and Mann–Whitney U test ($p < 0.05$) were performed using SPSS (IBM® SPSS® version 20 for Windows). This study was done following the TRIPOD reporting guidelines (**Supplementary Table 1**) (20).

RESULTS

Patient Cohort and Ki-67 Immunostaining

From August 2012 to July 2021, a total of 1,390 patients were diagnosed with TSCC in the Hospital of Stomatology, Wuhan University. We collected data of 179 patients with TSCC meeting our criteria. We used pTNM classification in this study following the 8th edition of the AJCC staging standard (21). The median age was 53 years (range, 26–87), and gender ratio (male:female) was 119:60. There were 39 cases with excellent differentiation, 98 cases with moderate differentiation, and 42 cases with poor differentiation. There were 62 cases with tumor at the T1 stage, 81 cases with tumor at the T2 stage, and 36 cases with tumor at the T3 or T4 stage. Seventy-five patients were diagnosed with lymph node metastasis (**Table 1**).

There is no explicit standard cutoff of Ki-67 index to divide TSCC into high and low proliferation status. In order to obtain a more balanced dataset, the median 20% (range, 0–80%) was used as the cutoff in this study (**Figure 1B**) (22). There were 56.4% of cases considered as low proliferation status (Ki-67 index ≤ 20%) and 43.6% of cases considered as high proliferation status. We connected proliferation status of TSCC with patients' clinicopathological parameters, such as age, gender, T stage of tumor, lymph node metastasis, and tumor differentiation. Results in **Table 1** shows no difference in gender ratio, T stage of tumor, and lymph node metastasis with proliferation status. However, difference existed between proliferation status and age ($p = 0.012$), and between proliferation status and differentiation ($p < 0.001$).

Predictive Power of the CNN Model

In this experiment, we used CECT of patients with TSCC to train an Inception-ResNet-V2 network model. The training was stopped after 20 epochs because the results were flattening. The performance of our model in the training set and the validation set is shown in **Figure 3**. Our model performed best in the 19th epoch shown in **Figure 3F**. We then used the trained model to predict the test set with an accuracy of 65.38% (**Figure 4A**) and an AUC of 0.7172 (**Figure 4B**).

DISCUSSION

Uncontrolled proliferation is the most fundamental feature of cancers (3). It has a great impact on the immune microenvironment and immunotherapy by creating more mutations with neoantigens and damaging the function of

TABLE 1 | Clinicopathological parameters and proliferation status.

	Proliferation		*p*-value
	High	Low	
Sex			
Male	51	68	0.785^{ns}
Female	27	33	
Age			
Median (range)	54 (26–87)	52 (28–74)	0.012*
Differentiation			
Well	10	29	<0.001***
Moderate	39	59	
Poor	29	13	
T stage			
T1	27	35	0.792^{ns}
T2	37	44	
T3+T4	14	22	
Lymph node metastasis			
Negative	40	65	0.078^{ns}
Positive	38	36	

*$p < 0.05$, ***$p < 0.001$, ns, not significant.*

T cells to help tumor escape immunity (4, 23, 24). A recent work also showed that PD-L1 expression was associated with a higher Ki-67 index in pituitary adenomas (25). On the other hand, patients with high proliferative oral cancers have higher recurrence risk after surgery, which is a potential indicator for extensive surgery and neck dissection (26, 27). Therefore, the proliferation status and Ki-67 index can help us develop therapeutic strategies, predict the therapy response, and observe the treatment effect.

In this study, we found that high proliferation status was associated with poor differentiation and old age of patients with TSCC, which are predictive factors of poor prognosis (28). However, the proliferation status showed no difference in T stage and lymph node metastasis in our study. On the contrary, Liu et al. came out with a different conclusion that the Ki-67 index had predictive value of lymph node metastasis in head and neck squamous cell carcinoma (29). The difference in results could be attributed to our different sample sizes, grouping cutoffs, and statistical methods. A recent study suggested that the expression of Ki-67 was strongly connected with tumor size and survival of patients (22).

The predictive results of our experiment proved that the CNN model was capable to predict the proliferation status of TSCC, with an accuracy of 65.38% and an AUC of 0.7172 in the test set, suggesting that the majority of our samples were classified correctly and the model was stable. Compared to radiomics, CNN is a more powerful model in processing data with grid patterns, especially images. Its spatial hierarchy enables it to automatically and adaptively learn features indistinguishable by human eyes from low-level patterns to high-level patterns. Accordingly, manual annotation is not considered indispensable, which makes prediction more efficient (30). Compared to other networks, Xie et al. found that the Inception-ResNet-V2 network could extract much more informative features from CT images of breast cancer (19). CECT can indicate the blood supply of tumor through the enhancement of blood vessels; therefore, it works well in reflecting soft tissue and providing inner information of tumor (31). Yoshiko Ariji et al. used CNN to assess the cervical lymph node metastasis of patients with oral cancer, acquiring an accuracy of 78.2% in their study (32). Indeed, MRI is superior to CT for imaging soft tissue. However, compared to MRI, CT has advantages of lower price, shorter inspection times, and less contraindications, especially for patients with dental artifacts (33). In some studies, CECT outperforms MRI in detecting neck metastasis and assessment of tumor depth of invasion in oral cancer (34, 35). Hence in TSCC, CECT is used more widely than MRI, which makes the research of CECT in TSCC more meaningful. In this study, all the CT images were obtained from the same CT machine, which could reduce bias of different machines.

Still, there remained several limitations in this study. First the rather small size of our study sample is a main issue. In the present study, only 179 patients and 4,510 CT images are involved. In a similar study of lung cancer, Fu et al. conducted radiomics to predict the Ki-67 expression of 282 patints with lung cancers, reaching an accuracy of 79.8% (36). We attributed the main reason to the size of our dataset, because when the sample size is small and asymmetrical, results of the AI model would come with bias, especially in the medical field (37, 38). Second, in the present study, only one model was used for analysis. The capability of other models needs further exploration. Third, we only used CECT in this study; patient's clinical information was not involved. Patient's clinical information such as age is correlated to the proliferation of TSCC, which we believe could assist the model to predict. Therefore, we considered this study as a preliminary exploratory study on the relationship between radiological images and the proliferation of TSCC. Further studies with an increased sample size and that involve more clinical information to improve the performance and universality of the AI model need to be conducted.

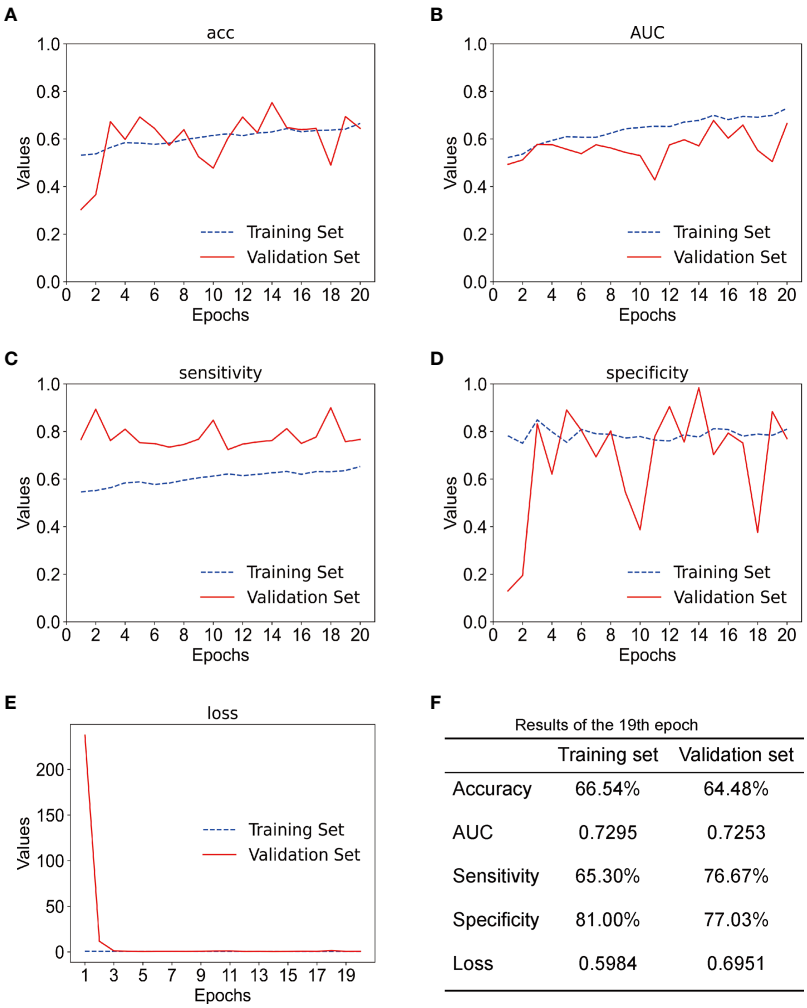

	Training set	Validation set
Accuracy	66.54%	64.48%
AUC	0.7295	0.7253
Sensitivity	65.30%	76.67%
Specificity	81.00%	77.03%
Loss	0.5984	0.6951

FIGURE 3 | **(A)** The accuracy of training set and the validation set; acc stands for accuracy. **(B)** The AUC of the training set and the validation set. **(C)** The sensitivity of training set and validation set. **(D)** The specificity of the training set and the validation set. **(E)** The loss of the training set and the validation set. **(F)** Results of the training set and the validation set in the 19th epoch.

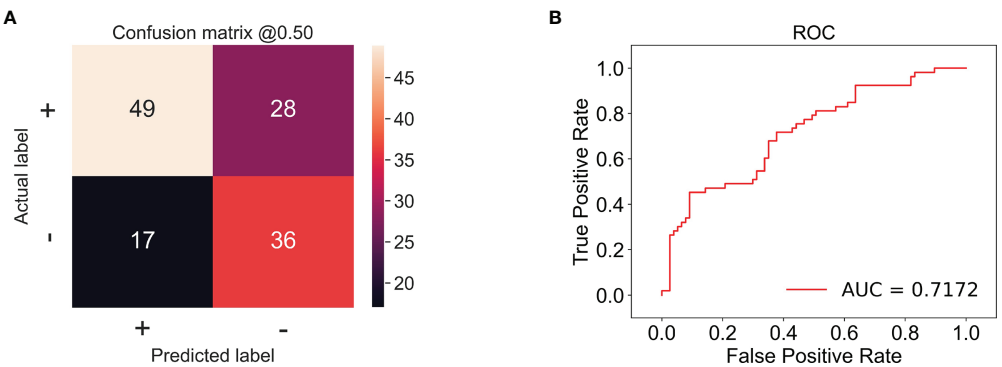

FIGURE 4 | **(A)** The confusion matrix of the test set; the accuracy was 65.38%. + stands for low proliferation status. - stands for high proliferation status. The number in the matrix stands for CT amounts. **(B)** The receiver operating characteristic (ROC) example of the test set; the AUC is 0.7172.

In conclusion, the present study provides a new way to establish the relationship between medical images and the pathological proliferation status of TSCC. To advance ideas on noninvasive and multidisciplinary integrative medicine, more researches are needed to reflect on the pathological features of cancer using AI.

DATA AVAILABILITY STATEMENT

The datasets presented in this article are not readily available because we want to protect the interest of the patients. Requests to access the datasets should be directed to Z-JS, sunzj@whu.edu.cn.

ETHICS STATEMENT

The studies involving human participants were reviewed and approved by the Institutional Medical Ethics Committee of School and Hospital of Stomatology, Wuhan University (2018LUNSHENZIA28). The patients/participants provided their written informed consent to participate in this study.

AUTHOR CONTRIBUTIONS

T-GS and LM, contributed to conception, design, data acquisition, analysis, and interpretation, and drafted and critically revised the manuscript. Z-KC and X-MS contributed to data acquisition and data interpretation, and drafted and critically revised the manuscript. Z-JS contributed to conception, design, data analysis and interpretation, and drafted and critically revised the manuscript. All authors contributed to the article and approved the submitted version.

FUNDING

This work was supported by the National Natural Science Foundation of China 82072996 and 82103333, and the Fundamental Research Funds for the Central Universities (2042021kf0174 and 2042021kf0216).

ACKNOWLEDGMENTS

The authors appreciate Prof. Zhang Jiali and the staff in the Department of Pathology, and Zhi-Yuan Xiong and Hai-Yan Qi from the information center in Hospital of Stomatology, Wuhan University.

SUPPLEMENTARY MATERIAL

The Supplementary Material for this article can be found online at: https://www.frontiersin.org/articles/10.3389/fonc.2022.841262/full#supplementary-material

REFERENCES

1. Du M, Nair R, Jamieson L, Liu Z, Bi P. Incidence Trends of Lip, Oral Cavity, and Pharyngeal Cancers: Global Burden of Disease 1990-2017. *J Dent Res* (2020) 99:143–51. doi: 10.1177/0022034519894963
2. Chen SW, Zhang Q, Guo ZM, Chen WK, Liu WW, Chen YF, et al. Trends in Clinical Features and Survival of Oral Cavity Cancer: Fifty Years of Experience With 3,362 Consecutive Cases From a Single Institution. *Cancer Manag Res* (2018) 10:4523–35. doi: 10.2147/CMAR.S171251
3. Hanahan D, Weinberg RA. Hallmarks of Cancer: The Next Generation. *Cell* (2011) 144:646–74. doi: 10.1016/j.cell.2011.02.013
4. McGranahan N, Furness AJ, Rosenthal R, Ramskov S, Lyngaa R, Saini SK, et al. Clonal Neoantigens Elicit T Cell Immunoreactivity and Sensitivity to Immune Checkpoint Blockade. *Science* (2016) 351:1463–9. doi: 10.1126/science.aaf1490
5. Scholzen T, Gerdes J. The Ki-67 Protein: From the Known and the Unknown. *J Cell Physiol* (2000) 182:311–22. doi: 10.1002/(SICI)1097-4652(200003)182:3<311::AID-JCP1>3.0.CO;2-9
6. Szentkuti G, Danos K, Brauswetter D, Kiszner G, Krenacs T, Csako L, et al. Correlations Between Prognosis and Regional Biomarker Profiles in Head and Neck Squamous Cell Carcinomas. *Pathol Oncol Res* (2015) 21:643–50. doi: 10.1007/s12253-014-9869-4
7. Fischer CA, Jung M, Zlobec I, Green E, Storck C, Tornillo L, et al. Co-Overexpression of P21 and Ki-67 in Head and Neck Squamous Cell Carcinoma Relative to a Significantly Poor Prognosis. *Head Neck* (2011) 33:267–73. doi: 10.1002/hed.21440
8. Lopes VKM, Jesus AS, Souza LL, Miyahara LAN, Guimaraes DM, Pontes HAR, et al. Ki-67 Protein Predicts Survival in Oral Squamous Carcinoma Cells: An Immunohistochemical Study. *Braz Oral Res* (2017) 31:e66. doi: 10.1590/1807-3107BOR-2017.vol31.0066
9. Freudlsperger C, Freier K, Hoffmann J, Engel M. Ki-67 Expression Predicts Radiosensitivity in Oral Squamous Cell Carcinoma. *Int J Oral Maxillofac Surg* (2012) 41:965–9. doi: 10.1016/j.ijom.2012.04.014
10. Yang C, Zhang J, Ding M, Xu K, Li L, Mao L, et al. Ki67 Targeted Strategies for Cancer Therapy. *Clin Transl Oncol* (2018) 20:570–5. doi: 10.1007/s12094-017-1774-3
11. Schmid P, Pinder SE, Wheatley D, Macaskill J, Zammit C, Hu J, et al. Phase II Randomized Preoperative Window-Of-Opportunity Study of the PI3K Inhibitor Pictilisib Plus Anastrozole Compared With Anastrozole Alone in Patients With Estrogen Receptor-Positive Breast Cancer. *J Clin Oncol* (2016) 34:1987–94. doi: 10.1200/JCO.2015.63.9179
12. Choi SB, Park JM, Ahn JH, Go J, Kim J, Park HS, et al. Ki-67 and Breast Cancer Prognosis: Does It Matter if Ki-67 Level Is Examined Using Preoperative Biopsy or Postoperative Specimen?. *Breast Cancer Res Treat* (2022) 192:343–52. doi: 10.1007/s10549-022-06519-1
13. Bello IO, Wennerstrand PM, Suleymanova I, Siponen M, Qannam A, Nieminen P, et al. Biopsy Quality Is Essential for Preoperative Prognostication in Oral Tongue Cancer. *APMIS* (2021) 129:118–27. doi: 10.1111/apm.13104
14. Ilhan B, Lin K, Guneri P, Wilder-Smith P. Improving Oral Cancer Outcomes With Imaging and Artificial Intelligence. *J Dent Res* (2020) 99:241–8. doi: 10.1177/0022034520902128
15. Tian P, He B, Mu W, Liu K, Liu L, Zeng H, et al. Assessing PD-L1 Expression in non-Small Cell Lung Cancer and Predicting Responses to Immune Checkpoint Inhibitors Using Deep Learning on Computed Tomography Images. *Theranostics* (2021) 11:2098–107. doi: 10.7150/thno.48027
16. Iwatate Y, Hoshino I, Yokota H, Ishige F, Itami M, Mori Y, et al. Radiogenomics for Predicting P53 Status, PD-L1 Expression, and Prognosis With Machine Learning in Pancreatic Cancer. *Br J Cancer* (2020) 123:1253–61. doi: 10.1038/s41416-020-0997-1

17. Al-Masni MA, Kim DH, Kim TS. Multiple Skin Lesions Diagnostics *via* Integrated Deep Convolutional Networks for Segmentation and Classification. *Comput Methods Programs BioMed* (2020) 190:105351. doi: 10.1016/j.cmpb.2020.105351
18. Sun ZJ, Zhang L, Hall B, Bian Y, Gutkind JS, Kulkarni AB. Chemopreventive and Chemotherapeutic Actions of mTOR Inhibitor in Genetically Defined Head and Neck Squamous Cell Carcinoma Mouse Model. *Clin Cancer Res* (2012) 18:5304–13. doi: 10.1158/1078-0432.CCR-12-1371
19. Xie J, Liu R, Luttrell JT, Zhang C. Deep Learning Based Analysis of Histopathological Images of Breast Cancer. *Front Genet* (2019) 10:80. doi: 10.3389/fgene.2019.00080
20. Collins GS, Reitsma JB, Altman DG, Moons KG. Transparent Reporting of a Multivariable Prediction Model for Individual Prognosis or Diagnosis (TRIPOD): The TRIPOD Statement. *BMJ* (2015) 350:g7594. doi: 10.1136/bmj.g7594
21. Amin MB, Edge SB, Greene FL, Byrd DR, Brookland RK, Washington MK, et al. *AJCC Cancer Staging Manual. Book*. Chicago: Springer International Publishing (2018).
22. Gadbail AR, Sarode SC, Chaudhary MS, Gondivkar SM, Tekade SA, Yuwanati M, et al. Ki67 Labelling Index Predicts Clinical Outcome and Survival in Oral Squamous Cell Carcinoma. *J Appl Oral Sci* (2021) 29:e20200751. doi: 10.1590/1678-7757-2020-0751
23. Hegde PS, Chen DS. Top 10 Challenges in Cancer Immunotherapy. *Immunity* (2020) 52:17–35. doi: 10.1016/j.immuni.2019.12.011
24. Sugiura A, Rathmell JC. Metabolic Barriers to T Cell Function in Tumors. *J Immunol* (2018) 200:400–7. doi: 10.4049/jimmunol.1701041
25. Wang PF, Wang TJ, Yang YK, Yao K, Li Z, Li YM, et al. The Expression Profile of PD-L1 and CD8(+) Lymphocyte in Pituitary Adenomas Indicating for Immunotherapy. *J Neurooncol* (2018) 139:89–95. doi: 10.1007/s11060-018-2844-2
26. Wangsa D, Ryott M, Avall-Lundqvist E, Petersson F, Elmberger G, Luo J, et al. Ki-67 Expression Predicts Locoregional Recurrence in Stage I Oral Tongue Carcinoma. *Br J Cancer* (2008) 99:1121–8. doi: 10.1038/sj.bjc.6604633
27. Freudlsperger C, Rohleder SE, Reinert S, Hoffmann J. Predictive Value of High Ki-67 Expression in Stage I Oral Squamous Cell Carcinoma Specimens After Primary Surgery. *Head Neck* (2011) 33:668–72. doi: 10.1002/hed.21502
28. Argiris A, Li Y, Forastiere A. Prognostic Factors and Long-Term Survivorship in Patients With Recurrent or Metastatic Carcinoma of the Head and Neck. *Cancer* (2004) 101:2222–9. doi: 10.1002/cncr.20640
29. Liu M, Lawson G, Delos M, Jamart J, Ide C, Coche E, et al. Predictive Value of the Fraction of Cancer Cells Immunolabeled for Proliferating Cell Nuclear Antigen or Ki67 in Biopsies of Head and Neck Carcinomas to Identify Lymph Node Metastasis: Comparison With Clinical and Radiologic Examinations. *Head Neck* (2003) 25:280–8. doi: 10.1002/hed.10218
30. Yamashita R, Nishio M, Do RKG, Togashi K. Convolutional Neural Networks: An Overview and Application in Radiology. *Insights Imaging* (2018) 9:611–29. doi: 10.1007/s13244-018-0639-9
31. Yan Y, Sun X, Shen B. Contrast Agents in Dynamic Contrast-Enhanced Magnetic Resonance Imaging. *Oncotarget* (2017) 8:43491–505. doi: 10.18632/oncotarget.16482
32. Ariji Y, Fukuda M, Kise Y, Nozawa M, Yanashita Y, Fujita H, et al. Contrast-Enhanced Computed Tomography Image Assessment of Cervical Lymph Node Metastasis in Patients With Oral Cancer by Using a Deep Learning System of Artificial Intelligence. *Oral Surg Oral Med Oral Pathol Oral Radiol* (2019) 127:458–63. doi: 10.1016/j.oooo.2018.10.002
33. Tsai LL, Grant AK, Mortele KJ, Kung JW, Smith MP. A Practical Guide to MR Imaging Safety: What Radiologists Need to Know. *Radiographics* (2015) 35:1722–37. doi: 10.1148/rg.2015150108
34. de Souza Figueiredo PT, Leite AF, Barra FR, Dos Anjos RF, Freitas AC, Nascimento LA, et al. Contrast-Enhanced CT and MRI for Detecting Neck Metastasis of Oral Cancer: Comparison Between Analyses Performed by Oral and Medical Radiologists. *Dentomaxillofac Radiol* (2012) 41:396–404. doi: 10.1259/dmfr/57281042
35. Waech T, Pazahr S, Guarda V, Rupp NJ, Broglie MA, Morand GB. Measurement Variations of MRI and CT in the Assessment of Tumor Depth of Invasion in Oral Cancer: A Retrospective Study. *Eur J Radiol* (2021) 135:109480. doi: 10.1016/j.ejrad.2020.109480
36. Fu Q, Liu SL, Hao DP, Hu YB, Liu XJ, Zhang Z, et al. CT Radiomics Model for Predicting the Ki-67 Index of Lung Cancer An Exploratory Study. *Front Oncol* (2021) 11:743490. doi: 10.3389/fonc.2021.743490
37. Shin HC, Roth HR, Gao M, Lu L, Xu Z, Nogues I, et al. Deep Convolutional Neural Networks for Computer-Aided Detection: CNN Architectures, Dataset Characteristics and Transfer Learning. *IEEE Trans Med Imaging* (2016) 35:1285–98. doi: 10.1109/TMI.2016.2528162
38. Schwendicke F, Samek W, Krois J. Artificial Intelligence in Dentistry: Chances and Challenges. *J Dent Res* (2020) 99:769–74. doi: 10.1177/0022034520915714

Conflict of Interest: The authors declare that the research was conducted in the absence of any commercial or financial relationships that could be construed as a potential conflict of interest.

frontiers | Frontiers in Oncology

ORIGINAL RESEARCH
published: 20 April 2022
doi: 10.3389/fonc.2022.869895

Multiphase Dual-Energy Spectral CT-Based Deep Learning Method for the Noninvasive Prediction of Head and Neck Lymph Nodes Metastasis in Patients With Papillary Thyroid Cancer

Dan Jin[1†], Xiaoqiong Ni[1†], Xiaodong Zhang[1†], Hongkun Yin[2], Huiling Zhang[2], Liang Xu[1], Rui Wang[1] and Guohua Fan[1]*

[1] Department of Radiology, Second Affiliated Hospital of Soochow University, Suzhou, China, [2] Department of Advanced Research, Infervision Medical Technology Co., Ltd, Beijing, China

OPEN ACCESS

Edited by:
Cesare Piazza,
University of Brescia, Italy

Reviewed by:
Marco Ravanelli,
University of Brescia, Italy
Wen Zeng,
Zhongnan Hospital of Wuhan University, China

***Correspondence:**
Guohua Fan
fangh22@126.com

[†]These authors have contributed equally to this work and share first authorship

Specialty section:
This article was submitted to Head and Neck Cancer, a section of the journal Frontiers in Oncology

Received: *05 February 2022*
Accepted: *21 March 2022*
Published: *20 April 2022*

Citation:
Jin D, Ni X, Zhang X, Yin H, Zhang H, Xu L, Wang R and Fan G (2022) Multiphase Dual-Energy Spectral CT-Based Deep Learning Method for the Noninvasive Prediction of Head and Neck Lymph Nodes Metastasis in Patients With Papillary Thyroid Cancer. Front. Oncol. 12:869895. doi: 10.3389/fonc.2022.869895

Purpose: To develop deep learning (DL) models based on multiphase dual-energy spectral CT for predicting lymph nodes metastasis preoperatively and noninvasively in papillary thyroid cancer patients.

Methods: A total of 293 lymph nodes from 78 papillary thyroid cancer patients who underwent dual-energy spectral CT before lymphadenectomy were enrolled in this retrospective study. The lymph nodes were randomly divided into a development set and an independent testing set following a 4:1 ratio. Four single-modality DL models based on CT-A model, CT-V model, Iodine-A model and Iodine-V model and a multichannel DL model incorporating all modalities (Combined model) were proposed for the prediction of lymph nodes metastasis. A CT-feature model was also built on the selected CT image features. The model performance was evaluated with respect to discrimination, calibration and clinical usefulness. In addition, the diagnostic performance of the Combined model was also compared with four radiologists in the independent test set.

Results: The AUCs of the CT-A, CT-V, Iodine-A, Iodine-V and CT-feature models were 0.865, 0.849, 0.791, 0.785 and 0.746 in the development set and 0.830, 0.822, 0.744, 0.739 and 0.732 in the testing set. The Combined model had outperformed the other models and achieved the best performance with AUCs yielding 0.890 in the development set and 0.865 in the independent testing set. The Combined model showed good calibration, and the decision curve analysis demonstrated that the net benefit of the Combined model was higher than that of the other models across the majority of threshold probabilities. The Combined model also showed noninferior diagnostic capability compared with the senior radiologists and significantly outperformed the junior

radiologists, and the interobserver agreement of junior radiologists was also improved after artificial intelligence assistance.

Conclusion: The Combined model integrating both CT images and iodine maps of the arterial and venous phases showed good performance in predicting lymph nodes metastasis in papillary thyroid cancer patients, which could facilitate clinical decision-making.

Keywords: thyroid cancer, dual-energy CT (DECT), lymph nodes metastasis, multiphase, deep learning

INTRODUCTION

Approximately 30%-80% of patients with papillary thyroid cancer (PTC) have cervical lymph nodes (LNs) metastasis, especially to the lateral neck (1, 2). Recognizing the presence of metastatic LNs is pivotal for determining a correct therapeutic strategy for patients and is beneficial to the clinical command and prognosis evaluation of PTC. At present, there are many ways to evaluate the benign and malignant status of LNs in patients with PTC. Although the 2015 American Thyroid Association (ATA) guidelines consider preoperative ultrasonography (US) the preferred technique for the assessment of LNs status in PTC patients (3), this technique has deficiencies when evaluating LNs at low cervical levels, such as the retropharyngeal area and upper mediastina, and depends heavily on the clinical experience of the operator. Computed tomography (CT) can compensate for the above partial defects by relying on excellent tissue and spatial resolution. However, the subjective nature of morphologic criteria such as node size, degree and pattern of enhancement, necrosis, and extranodal extension for visually evaluating whether cervical LNs are benign or metastatic results in diminished reproducibility and objectivity, especially for small LNs without specific morphological features.

With the widespread application of dual-energy spectral CT (DECT) called gemstone spectral imaging (GSI), some studies have found that CT image features with higher spatial resolution and energy spectrum parameters provided by DECT can be conducive to the detection and evaluation of LNs status in PTC (4). Several studies have suggested that the slope of the spectral Hounsfield unit curve (λ^{HU}), the normalized iodine concentration (NIC), and the normalized effective atomic number are effective parameters for diagnosing LNs metastasis in patients with PTC (1, 4, 5)

In recent years, artificial intelligence (AI) based on deep learning (DL) has been a frontier computational method that simulates brain structures connecting a large number of neurons, can complete image-recognition tasks in a short time without subjective assessment and includes nonvisual image details, which have a high-dimensional association with clinical issues (6–8). Theoretically, the combination of dual-energy CT and deep learning methods may potentially improve the preoperative predictive performance for LNs metastasis in patients with PTC.

The purpose of our study was to investigate the usefulness of DL models based on multiphase DECT for predicting LNs metastasis in patients with PTC and to compare them with radiologists' assessments.

MATERIALS AND METHODS

Patient Enrollment

The study was approved by the institutional review board of our hospital, and the requirement for informed consent was waived. Dual-energy spectral CT images of papillary thyroid cancer patients from April 2018 to December 2020 were retrospectively collected. The inclusion criteria were as follows: 1) preoperative dual-energy CT was performed within two weeks before surgery; 2) patients underwent lymphadenectomy, and the tumor metastasis of lymph nodes was pathologically confirmed. The exclusion criteria were as follows: 1) patients had received any anti-cancer treatment before surgery; 2) patients had suffered from other cancer at the same time; 3) low CT image quality or lymph nodes less than 5mm.

Ultimately, a total of 117 lymph nodes with tumor metastasis and 176 lymph nodes without tumor metastasis from 78 patients were enrolled in this study. The patient enrollment flowchart is shown in **Figure 1**. These lymph nodes were divided into a development set (140 nonmetastatic and 94 metastatic) and an independent testing set (36 nonmetastatic and 23 metastatic) at a ratio of 4:1 using computer-generated random numbers.

Acquisition of CT Images

All patients underwent dual-energy CT examinations in gemstone spectral imaging (GSI) mode (GE Discovery CT750 HD scanner; GE Healthcare, Princeton, NJ, USA). DECT scans were from the skull base to the aortic arch level and in the head-foot direction. The DECT scan parameters were as follows: 64×0.625-mm detector collimation; 0.8-sec tube rotation time; 0.984 pitch; 1.25-mm-thick sections; 1.5-mm-thick section increments; rapid switching of high (140 kVp) and low (80 kVp) tube voltages; 360-mA tube current. For contrast-enhanced scans, patients were injected with 1.6 mL/kg of nonionic iodinated contrast medium (300 mg I/mL) by a pump injector at a rate of 3.5 mL/s into the antecubital vein. Images of arterial and venous phases were performed after 25- and 55-sec delays, respectively.

Iodine maps of both arterial and venous phases at a 1.5-mm slice thickness can be autogenerated by DECT.

Pathological Diagnosis of Lymph Nodes Metastasis

In this study, we adopted the labeling method of LNs imaging and pathological subregion comparison proposed by Park et al. (9). According to the LNs location standard established by the American Joint Committee on Cancer (AJCC), cervical LNs are divided into I-VII regions (10). The final histopathologic reports of

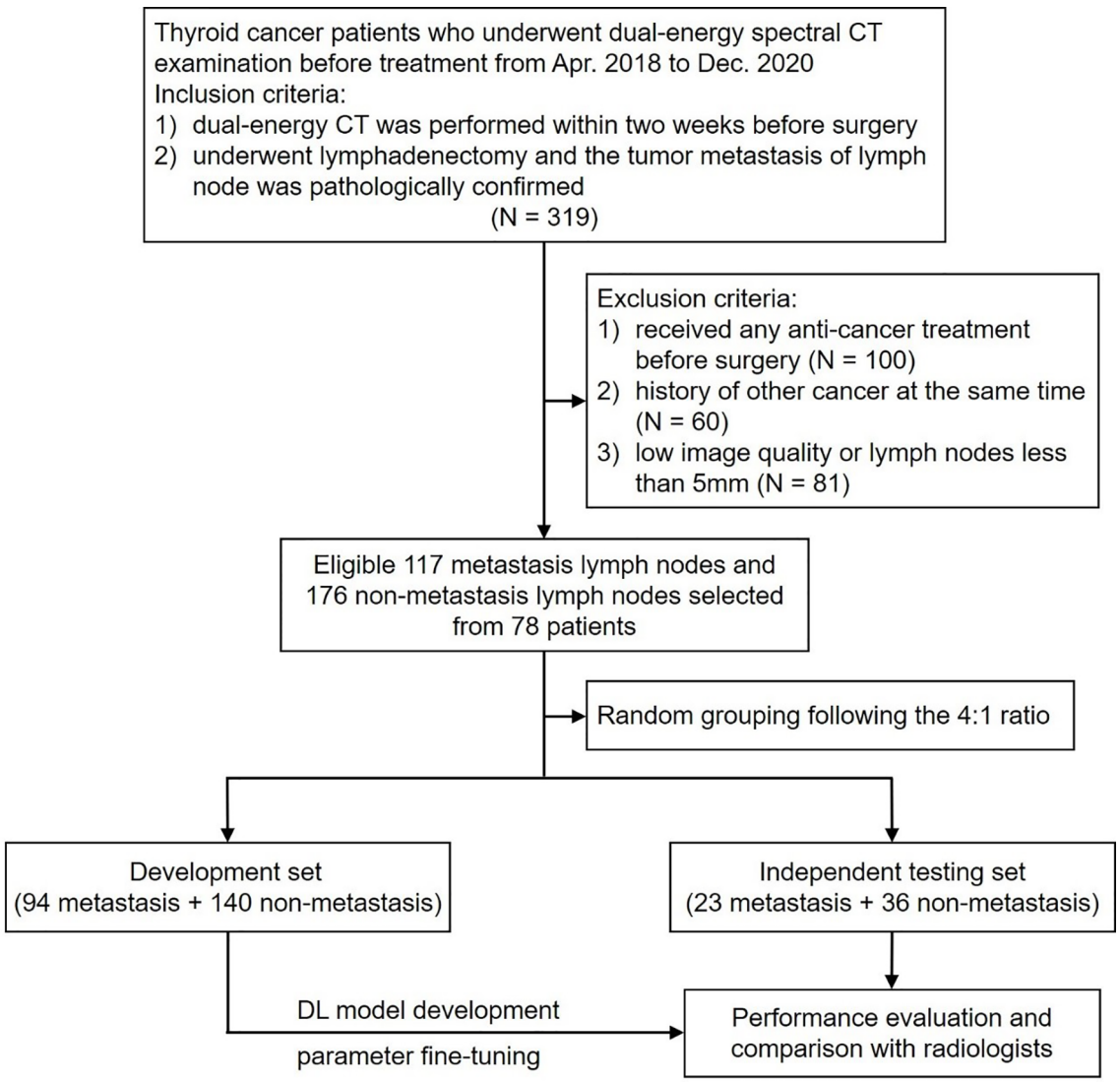

FIGURE 1 | Flowchart of patient enrollment and study design.

the surgical neck dissection samples served as the reference standard for nodal metastasis. After obtaining the numbers of metastatic and nonmetastatic LNs in each region, DECT images were compared by a radiologist with 10 years of experience in head and neck radiology. If pathological results showed metastasis in all LNs in a subregion, the LNs seen in the image area were marked as metastatic LNs. If the pathological results showed no metastasis in any of the LNs in a subregion, the LNs seen in the imaging region were marked as nonmetastatic LNs. In addition, if there were both metastatic and nonmetastatic LNs in the subregion, the levels with mixed LNs were ruled out in further research.

Qualitative Analysis of Lymph Nodes and Development of the CT-Feature Model

Eight morphological CT features of the lymph nodes from CT images were analyzed by two radiologists with 12 and 10 years of experience in head and neck imaging, including size, shape, margin, degree of enhancement, pattern of enhancement, calcification, cystic change, and extra-nodal extension. Size was determined by using the maximal short axis diameter. Degree of enhancement was assessed based on the neighboring muscle. Uniformity of enhancement was evaluated based on the arterial phase. Fuzzy boundaries and/or invasion into contiguous structures were deemed as extra-nodal extension (11). A third senior radiologist with more than 10 years of experience was consulted for the final decision if disagreements occurred. All radiologists were not aware of the pathological results.

The differences of CT image features were assessed in the development set through multivariate analysis using stepwise selection logistic regression. Only the CT image features with $p < 0.05$ were selected to build the CT-feature model.

Segmentation of Lymph Nodes

The lymph nodes were manually segmented on both arterial phase and venous phase CT images, and the iodine maps shared the same segmentations with the corresponding CT images. Three-dimensional segmentation was performed by a radiologist with more than 10 years of experience, and the region of interest (ROI) was manually drawn freehand strictly within the border of lymph nodes on each slice of the CT images using ITK-SNAP software (v3.8.0, http://www.itksnap.org). The cystic change, necrosis, and calcification regions were carefully excluded to obtain a more homogenized dataset (12). All the ROIs were confirmed by another senior radiologist with more than 20 years of experience in head and neck imaging. Both radiologists were blind to the pathological results.

Data Pretreatment for the DL Models

Before the development of the DL models, each manually labeled ROI was transformed and defined as follows: (i) a three-dimensional (3D) patch of 96*96*16 pixels containing the cropped lymph nodes region, whose size was determined based on the largest ROI; (ii) tumor masks, in which non-lesion areas were left padded with zero, were manually labeled pixelwise; and (iii) the pathologically identified label of tumor metastasis.

Owing to the limited amount of training data, we also used data augmentation approaches, including flipping (perpendicular to the x and y axes), random rotation (90, 180, and 270 degrees perpendicular to the z axis), and random brightness contrast (80%, 90%, 110% and 120%) in the development set. After data augmentation, the sample size increased to 10 times that of the original, yielding a total of 2340 samples for the development of the DL models.

Development of the Deep Learning Models

The MobileNetV2 network was used as the backbone structure of the DL model due to the faster calculation speed than other classic neural networks (e.g., IncePtionV3 and VGG16) while maintaining similar accuracy and greatly simplifying the number of parameters, which reduces the risk of overfitting for small sample sizes. In addition, the original MobilenetV2 model was entered into a 3D version according to the data characteristics in this study. More details about the modification of the 3D MobileNetV2 network were presented in the **Supplementary Data**. Two kinds of DL models were proposed in this study: a single-channel neural network for each modality of the DECT images (arterial phase CT images, venous phase CT images, arterial iodine maps and venous iodine maps) and a multichannel neural network that integrated four modalities of the DECT images (**Figure 2**).

Therefore, a total of five DL models were proposed in our study: four single-modality DL models based on arterial phase CT images (CT-A model), venous phase CT images (CT-V model), arterial iodine maps (Iodine-A model) and venous iodine maps (Iodine-V model), and a multichannel DL model using ROIs from all modalities as input (Combined model).

To improve the robustness of the model and achieve better performance, transfer learning methods were also applied. The neural networks used in this study were first pretrained on natural images from The ImageNet natural image dataset and were then pretrained on multiple medical image datasets from The Cancer Imaging Archive (TCIA) database.

The proposed DL models were trained based on the binary cross-entropy loss function, which is commonly used for classification tasks. Adam was used as the optimizer in the training stage owing to its fast convergence and weight-dependent learning rate. The initial learning rate and the weight decay were set to 0.0001 and 0.01, respectively. The minibatch size was set to 24, and the dropout rate was set to 0.5. The weight parameters of the initialized hidden layer were randomly allocated, and other parameters were set as default. During model development, 5-fold cross-validation was applied to avoid overfitting, and the weighted ensemble method was applied to integrate a weighted average result from those cross-validation models. The training was stopped when the loss function was stable. The relationship between the model efficiency (AUC) and the cross-entropy loss function index at each epoch during the model development process is presented in **Figure 3**.

The supervised training process of the DL models was performed on the InferScholar platform version 3.5 (InferVision, China) with a Core i7-7700 K central processing unit (Intel, Santa Clara, Calif), 32 GB memory, and a GeForce GTX 2070 graphics processing unit (NVIDIA, Santa Clara, Calif). Python 3.6.8 (https://www.python.org) and the Mxnet 1.5.0 framework for neural networks (https://mxnet.incubator.apache.org) were used to construct the DL models. The code of the DL models was available at https://github.com/Sarah-huiling/DL_ThyroidLymphNode.git.

Performance Evaluation of the Predictive Models

The discriminative efficacy of the DL models was evaluated by receiver operating characteristic (ROC) analysis with respect to the area under the curve (AUC). In addition, the sensitivity, specificity, positive predictive value (PPV) and negative predictive value (NPV) of each model were also calculated under the optimal threshold according to the maximum Youden index (13).

Calibration and Decision Curve Analysis

The consistency between the predicted metastasis probability and actual metastasis rate was evaluated through calibration curves using the 1,000 bootstrapping resamples method, and the Hosmer–Lemeshow test was conducted to assess the goodness-of-fit of the predictive models in both the development and independent testing sets (14). Decision curve analysis (DCA) was used to assess the clinical utility of the predictive models by estimating the net benefits for a range of threshold probabilities in the independent testing set (15).

Performance Comparison Between Artificial Intelligence (AI) and the Radiologists

We used the independent testing set to compare the diagnostic performance of the AI (the combined model) with that of 4 radiologists (2 senior radiologists with 15 and 12 years of experience and 2 junior radiologists with 4 and 5 years of experience). To evaluate the actual impact of the DL model in

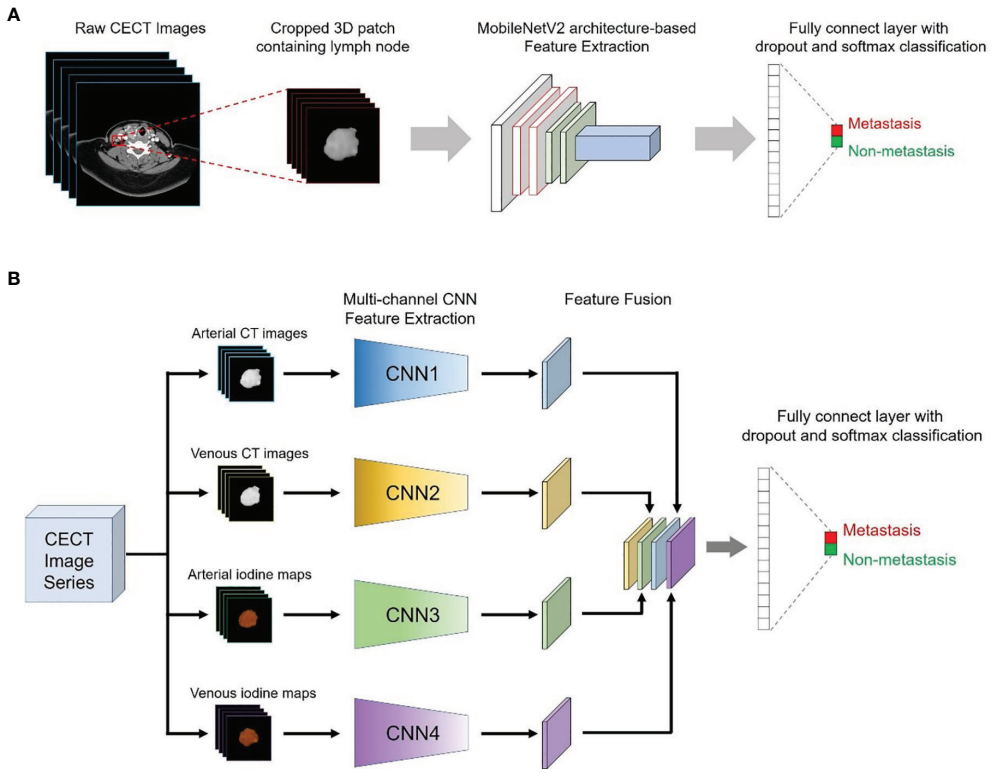

FIGURE 2 | Conceptual architecture of the single-modality DL model **(A)** and the multichannel DL model integrating all ROIs from the CT images and iodine maps **(B)**.

clinical practice, all radiologists first diagnosed the lymph nodes in the independent testing set independently, and they were asked to diagnose the same lymph nodes again with AI assistance after a washout period of 4 weeks. All the radiologists were aware that the cases in the independent testing set had undergone biopsy or surgery, but they were blinded to the pathological reports.

Statistical Analysis

Statistical analyses were performed using SPSS software (version 23.0) and MedCalc software (version 20.0). Continuous variables were compared by Student's t-test or the Mann–Whitney U test, and categorical variables were compared by the chi-square test or Fisher's exact test, where appropriate. The difference between two AUCs of different models was compared with Delong's test (16) or the Hanley-McNeil test (17), where appropriate. The weighted kappa value was used to assess the interobserver agreement of the two radiologists. The calibration curve was plotted using the "rms" package, and the decision curve was plotted using the "rmda" package. A two-sided $p < 0.05$ was considered statistically significant.

RESULTS

Patient Characteristics

A total of 319 patients from April 2018 to December 2020 in our hospital were initially recruited. According to the inclusion and exclusion criteria, 22 men (mean age, 40.9 ± 14.6 years) and 56 women (mean age, 40.7 ± 11.9 years) were enrolled in the study. There was no significant difference in the prevalence of lymph nodes metastasis (chi-square test, $p = 0.868$) between the development set (40.2%, 94/234) and the independent testing set (39.0%, 23/59).

Analysis of the CT Image Features

As shown in **Table 1**, the CT image features were compared between nonmetastatic and metastatic lymph nodes in the development set and independent testing set. Shape, enhancement degree and enhancement pattern were selected through multivariate logistic regression analysis (**Supplementary Table 1**), and the prediction value of the CT-feature model was calculated using following formula:

$$\begin{aligned}\text{Prediction value} &= -1.5411 + 1.08356 \times \text{Shape}(\text{Regular} = 0, \text{Irregular} = 1) \\ &\quad + 1.19649 \times \text{Enhancement pattern}(\text{Homogeneous} \\ &= 0, \text{Heterogeneous} \\ &= 1) + 0.90834 \\ &\quad \times \text{Enhancement degree}(\text{Mild} - \text{moderate} = 0, \text{Strong} = 1).\end{aligned}$$

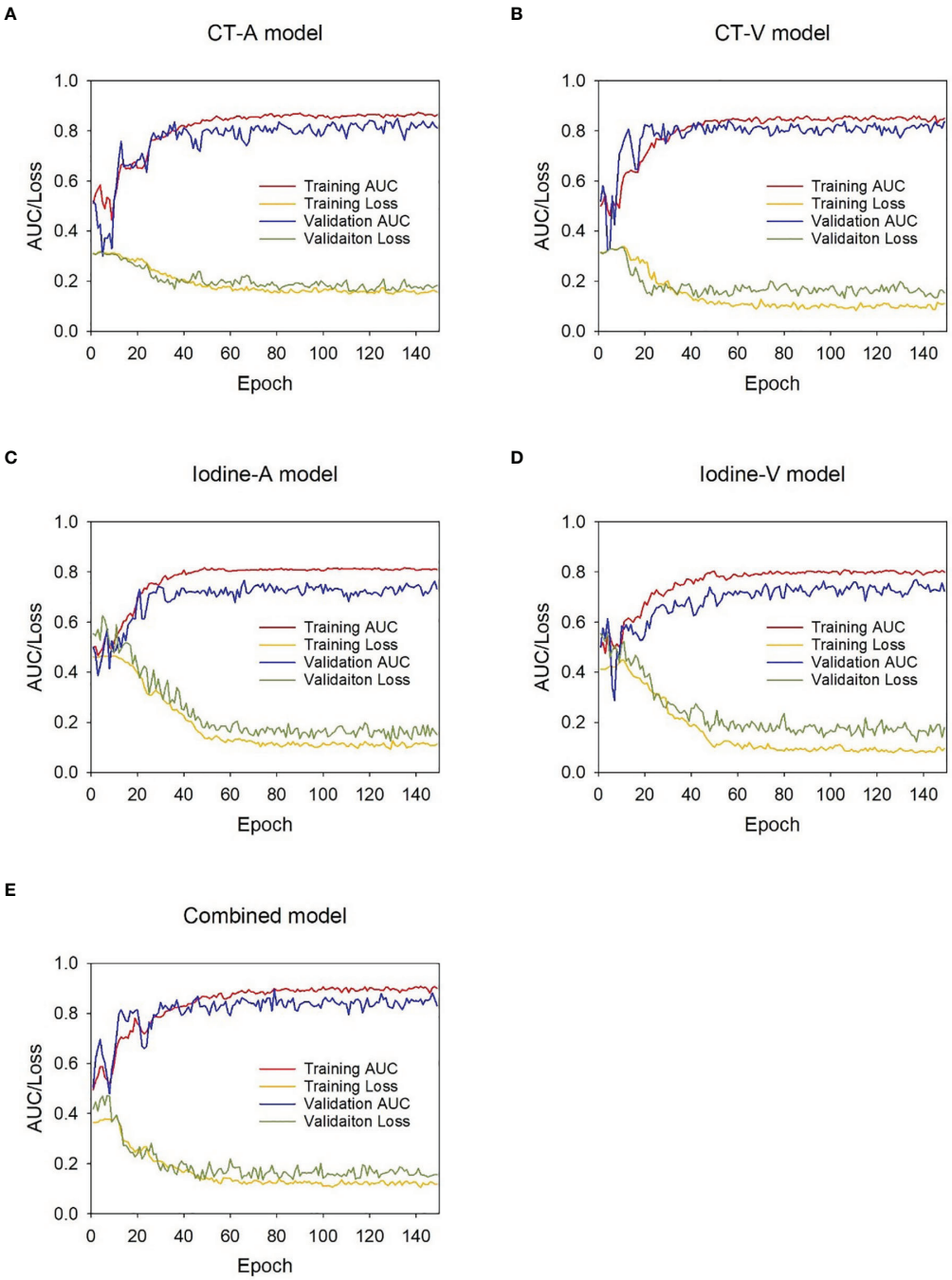

FIGURE 3 | AUC-loss curve of the DL models during development stage. **(A)** CT-A model, **(B)** CT-V model, **(C)** Iodine-A model, **(D)** Iodine-V model ,**(E)** Combined model.

Performance Evaluation of the Predictive Models

The ROC analysis of the predictive models in the development and independent testing sets was shown in **Figure 4**. The AUCs of the CT-feature model were 0.746 (95% CI, 0.685~0.800) in the development set and 0.732 (95% CI, 0.601~0.839) in the independent testing set. The CT-A, CT-V, Iodine-A, and Iodine V models achieved AUCs of 0.865 (95% CI, 0.814~0.906), 0.849 (95% CI, 0.797~0.892), 0.791 (95% CI, 0.733~0.841) and 0.785 (95% CI, 0.727~0.836) in the development set, and the AUCs of these models were 0.830 (95% CI, 0.709~0.915), 0.822 (95% CI, 0.701~0.910), 0.744 (95% CI, 0.614~0.849) and 0.739 (95% CI, 0.608~0.845) in the testing set, respectively. In general, the CT image-based models showed

TABLE 1 | Comparison of CT image features between no-metastatic and metastatic lymph nodes.

CT image features	Development set			Independent testing set		
	Nonmetastatic (n=140)	Metastatic (n=94)	*p*	Nonmetastatic (n=36)	Metastatic (n=23)	*p*
Size			*0.549*			*0.735*
5~10 mm	109	70		25	15	
>10 mm	31	24		11	8	
Shape			*<0.001*			*0.250*
Regular	117	55		27	14	
Irregular	23	39		9	9	
Margin			*0.075*			*0.071*
Clear	115	68		27	12	
Unclear	25	26		9	11	
Enhancement degree			*<0.001*			*0.006*
Mild-moderate	94	36		21	5	
Strong	46	58		15	18	
Enhancement pattern			*<0.001*			*0.006*
Homogeneous	112	45		27	9	
Heterogeneous	28	49		9	14	
Calcification			*0.005*			*0.010*
Yes	3	10		0	4	
No	137	84		36	19	
Cystic change			*<0.001*			*0.313*
Yes	0	14		1	2	
No	140	80		35	21	
Extra-nodal extension			*0.001*			*0.207*
Yes	0	7		0	1	
No	140	87		36	22	

higher performance than the iodine map-based models; Only one group was significantly different (CT-A model *vs*. Iodine-A model, p = 0.043 in the development set), with no significant differences seen in the remaining three groups (CT-A model *vs*. Iodine-A model, p = 0.151 in the independent testing set; CT-V model *vs*. Iodine-V model, p = 0.074 in the development set and p = 0.273 in the independent testing set). There were no significant differences between the arterial phase image-based models and venous phase image-based models (CT-A model *vs*. CT-V model, p = 0.655 in the development set and p = 0.870 in the independent testing set; Iodine-A model *vs*. Iodine-V model, p = 0.889 in the development set and p = 0.957 in the independent testing set).

The Combined model, incorporating both arterial and venous phase CT images and the corresponding iodine maps, showed the highest accuracy in predicting lymph nodes metastasis, with AUCs achieving 0.890 (95% CI, 0.842~0.927) in the development set and 0.865 (95% CI, 0.751~0.940) in the independent testing set. The AUCs of the Combined model were significantly higher than those of the Iodine-A model (p = 0.007), Iodine-V model (p = 0.004) and CT-feature model (p < 0.001) in the development set. Although not statistically significant, the Combined model showed better performance than the CT-A model (p = 0.427) and CT-V (p = 0.225) in the development set and all the other predictive models in the independent testing set (p = 0.096 *vs*. the CT-feature model, p = 0.330 *vs*. the CT-A model, p = 0.237 *vs*. the CT-V model, p = 0.074 *vs*. the Iodine-A model, p = 0.085 *vs*. the Iodine-V model). The detailed sensitivity, specificity, PPV and NPV of these models in the development set and the independent testing set are summarized in **Tables 2**, **3** respectively. In addition, subsequent ROC analysis according to the size of lymph nodes (5~10 mm or >10mm) was performed (**Supplementary Figure 1**), and the performance of the Combined model was consistent across lymph node size (**Supplementary Table 2**).

Calibration and Clinical Utility Analysis

The Combined model showed good consistency between the predicted lymph nodes metastasis probability and the actual metastasis rate in both the development and independent testing sets (**Figure 5**). The calibration curve suggested no significant deviation from an ideal fitting, with the nonsignificant statistic of the Hosmer–Lemeshow test achieving p = 0.070 and 0.803 in the development and independent testing sets, respectively.

The decision curve analysis for the DL models in the independent testing set indicated that the Combined model showed a higher overall net benefit in differentiating metastatic LNs from nonmetastatic LNs than other single-modality DL models, which demonstrated the superiority of the Combined model compared with other models in terms of clinical usefulness (**Figure 6**).

Comparison of the Combined Model and Radiologists in the Independent Testing Set

Although not statistically significant, the Combined model achieved a higher AUC than senior radiologist #1 (p = 0.180) and senior radiologist #2 (p = 0.262), while it significantly outperformed the two junior radiologists (both p values < 0.05) in the independent testing set. All radiologists benefited from AI assistance, with the AUCs of the two senior radiologists increasing from 0.760 to 0.830 (p = 0.359) and 0.780 to 0.838

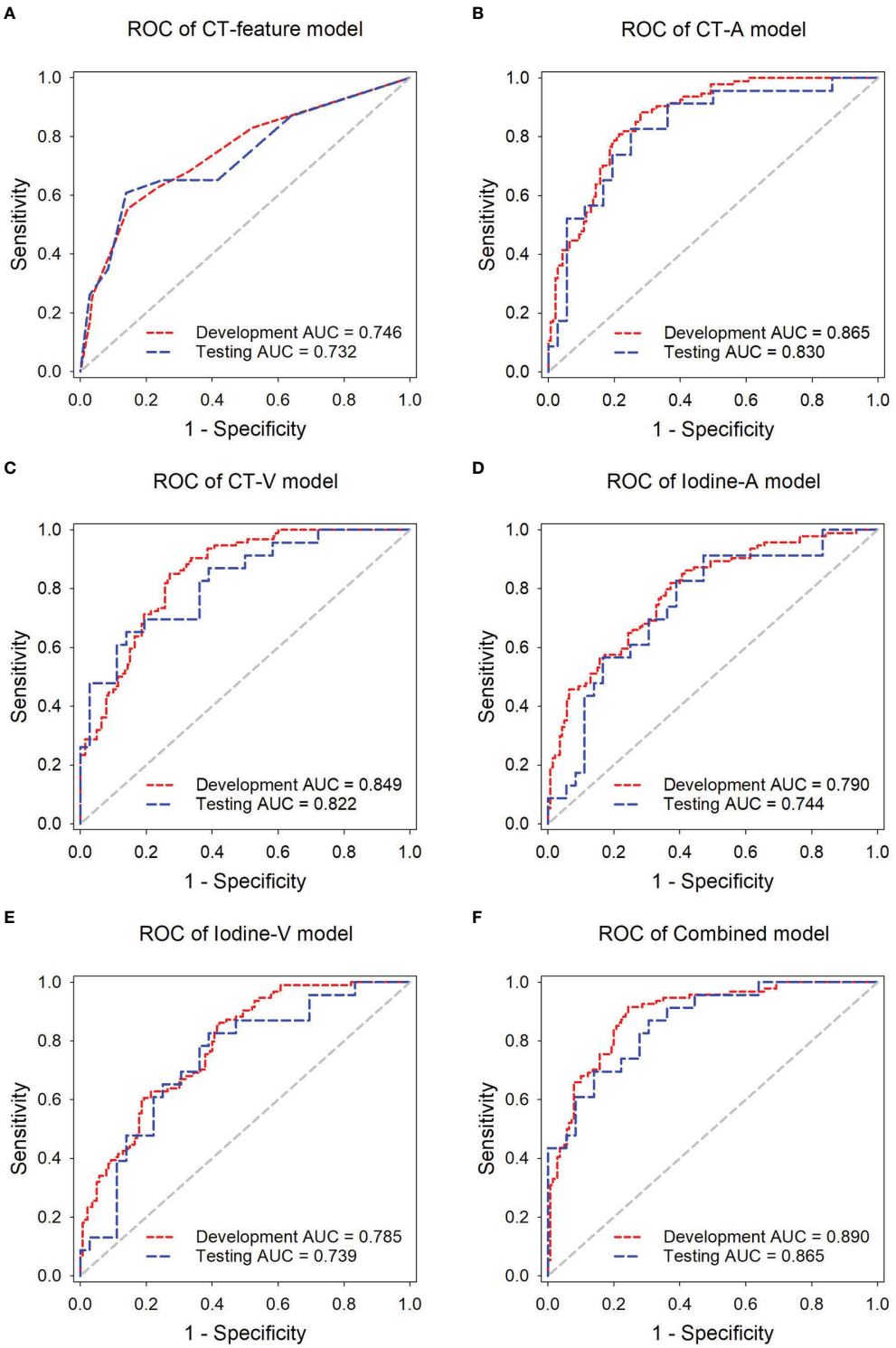

FIGURE 4 | ROC analysis of the predictive models in the development and independent testing sets. ROC curves of the **(A)** CT-feature model, **(B)** CT-A model, **(C)** CT-V model, **(D)** Iodine-A model **(E)** Iodine-V model, and **(F)** Combined model in the delelopment and testing sets, respectively.

TABLE 2 | Performance comparison of different models in the development set.

Model	AUC (95% CI)	*p-value*	Threshold	Sensitivity	Specificity	PPV	NPV
CT-feature	0.746 (0.685~0.800)	*<0.001*	>0.3753	55.3%	85.7%	72.2%	74.1%
CT-A	0.865 (0.814~0.906)	*0.427*	>0.4518	88.3%	72.1%	68.0%	90.2%
CT-V	0.849 (0.797~0.892)	*0.225*	>0.4202	85.1%	72.9%	67.8%	87.9%
Iodine-A	0.791 (0.733~0.841)	*0.007*	>0.3491	81.9%	62.9%	59.7%	83.8%
Iodine-V	0.785 (0.727~0.836)	*0.004*	>0.4097	86.2%	57.9%	57.9%	86.2%
Combined	0.890 (0.842~0.927)	*reference*	>0.4239	91.5%	75.7%	71.7%	93.0%

TABLE 3 | Performance comparison of different models in the independent testing set.

Model	AUC (95% CI)	*p-value*	Threshold	Sensitivity	Specificity	PPV	NPV
CT-feature	0.732 (0.601~0.839)	*0.096*	>0.6248	60.9%	86.1%	73.7%	77.5%
CT-A	0.830 (0.709~0.915)	*0.330*	>0.3818	82.6%	75.0%	67.9%	87.1%
CT-V	0.822 (0.701~0.910)	*0.237*	>0.6009	65.2%	86.1%	75.0%	79.5%
Iodine-A	0.744 (0.614~0.849)	*0.074*	>0.3785	91.3%	52.8%	55.3%	90.5%
Iodine-V	0.739 (0.608~0.845)	*0.085*	>0.3473	82.6%	61.1%	57.6%	84.6%
Combined	0.865 (0.751~0.940)	*reference*	>0.4387	87.0%	69.4%	64.5%	89.3%

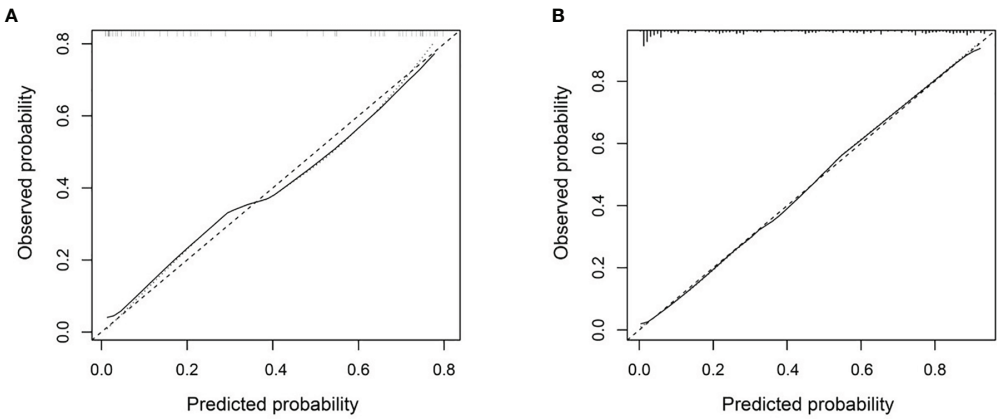

FIGURE 5 | Calibration curve of the Combined model in the development set **(A)** and the independent testing set **(B)**. The X axis and Y axis represent the predicted lymph nodes metastasis probability and the actual metastasis rate, respectively. A closer fit to the diagonal gray dash line represents a better prediction.

(p = 0.335). The AUCs of the two junior radiologists also increased from 0.669 to 0.810 (p = 0.020) and 0.709 to 0.802 (p = 0.258), respectively. In addition, the interobserver agreement between the two junior radiologists also improved after AI assistance, with a weighted kappa of 0.334 (95% CI, 0.104~0.564) increasing to 0.593 (95% CI, 0.387~0.798). The results of the ROC analysis are presented in **Figure 7**, and the detailed sensitivity, specificity, PPV, NPV, and AUC are summarized in **Table 4**.

DISCUSSION

In this study, we developed five deep learning models based on multiphase dual-energy spectral CT to predict lymph nodes metastasis preoperatively and noninvasively in papillary thyroid cancer patients. Using the independent testing set, our study showed that the combined DL model possessed superior diagnostic capability compared to that of the other four single-modality DL models, with AUCs of 0.865. Meanwhile, the combined DL model showed high diagnostic efficacy across the size of LNs with AUCs achieving 0.845,0.898 in LNs of 5-10mm and >10mm, respectively. Although not statistically significant, we found that single-modality DL models based on the arterial phase achieved a better sensitivity and diagnostic performance whether CT images or iodine maps were used. The results were consistent with previously published studies, and these studies considered that arterial phase CT could highlight the difference between metastatic and benign LNs because tumor angiogenesis and recruitment of capsular vessels increased tumor perfusion in metastatic LNs (18).

The thyroid gland is the main organ with the capacity for iodine intake in the human body, and metastatic LNs from PTC can take up iodine. In addition, increased tumor vascularity in metastatic LNs may contribute to an increase in iodine uptake (1, 19). Hence, the utilization of iodine maps for the evaluation of

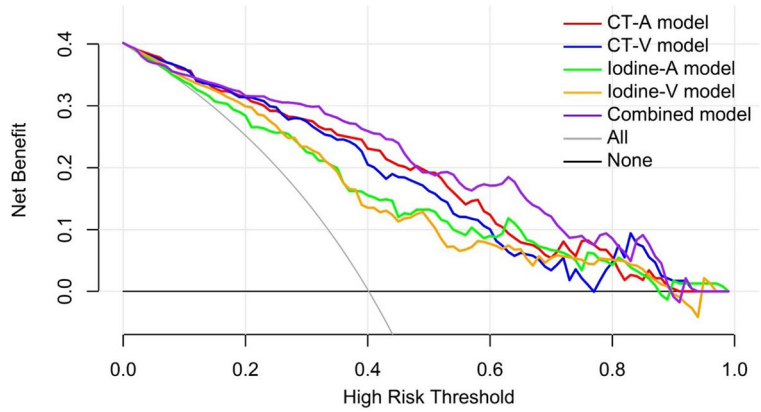

FIGURE 6 | Decision curve analysis for the predictive models in the independent testing set. The gray line and black line represented situations in which all lymph nodes were metastatic and no lymph nodes were free of cancer, respectively.

metastatic LNs from PTC has certain advantages. However, the results from our study showed inconsistency with the above theory, which found that the iodine map-based models were not better than the CT image-based models, regardless of arterial phase or venous phase. The reasons for the inconsistency of the results may be that although iodine maps can highlight the difference of iodine intake in tissues, it is inferior to conventional CT image in the display of morphological features, such as boundary and internal structure. Nevertheless, the DL models based on iodine maps exhibited relatively high sensitivity (91.3% of the iodine-A model, 82.6% of the iodine-V model) in the independent testing set.

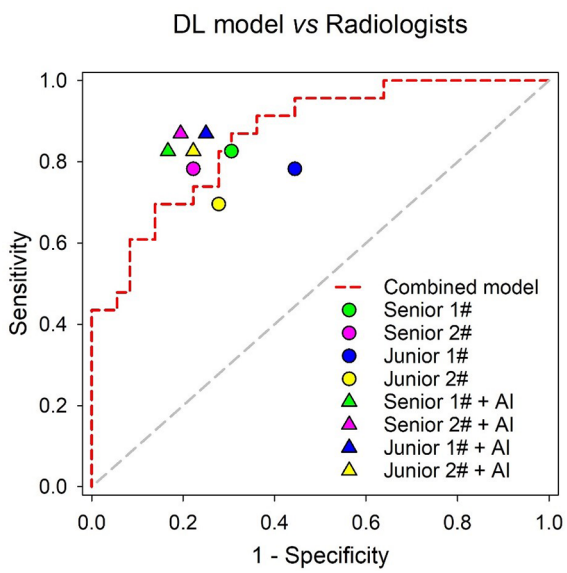

FIGURE 7 | Performance comparison of the Combined model and radiologists in the independent testing set.

The conventional approach to diagnose metastatic cervical LNs is according to the morphologic characteristics of the nodes, including size or shape, central necrosis or cystic degeneration, degree and pattern of enhancement and extra-nodal extension (20). This approach is not only controversial but also challenging, especially for unskilled radiologists. The current studies could not come to an agreement. Zhou et al. indicated that morphological features larger than 10 mm in size, with irregular shape, unclear margins, strong enhancement, heterogeneous enhancement, and extra-nodal extension were highly suggestive of metastatic LNs (19). However, Liu et al. reported that the degree and pattern of enhancement were only valuable indicators for differentiating LNs status (1). Moreover, a study from J.E. Park et al. reported that the method for the detection of cervical LNs using morphologic characteristics had relatively low sensitivity, with a value of only 46.8% (9).Our study found that the degree and pattern of enhancement and calcification showed significant differences both in development and independent testing set. but, the shape, cystic change, and extra-nodal extension showed significant differences only in development set. The reasons for the results may be that the sample size of independent testing set was not large enough to reflect the difference. The result also manifested that evaluating LNs by the morphological features was controversial. In addition, our study found the Combined model had better performance than the CT-feature model but there was significant difference only in the development set. This reason may be that the CT features were evaluated by senior radiologists, and the Combined model did not include CT-feature model, which was in accordance with the result of comparison between the Combined model and the senior radiologists.

The results of this study showed that the Combined model significantly outperformed two junior radiologists (both p values < 0.05) and showed noninferior diagnostic capability compared with the senior radiologists in the independent testing set. Notably, our study found that all radiologists benefited from AI assistance, the junior radiologists received more help from AI assistance than the junior radiologists, and the interobserver

TABLE 4 | Comparison of the diagnostic efficiency between the Combined model and the radiologists (with or without AI assistance) in the independent testing set.

	AUC (95% CI)	*p-value*	Sensitivity	Specificity	PPV	NPV
Senior Radiologist 1	0.760 (0.631~0.862)	*0.180*	82.6%	69.4%	63.3%	86.2%
Senior Radiologist 2	0.780 (0.653~0.878)	*0.262*	78.3%	77.8%	69.2%	84.8%
Junior Radiologist 1	0.669 (0.534~0.786)	*0.021*	78.3%	55.6%	52.9%	90.0%
Junior Radiologist 2	0.709 (0.576~0.820)	*0.043*	69.6%	72.2%	61.5%	78.9%
Senior Radiologist 1 + AI	0.830 (0.709~0.915)	*0.532*	82.6%	83.3%	76.0%	88.2%
Senior Radiologist 2 + AI	0.838 (0.718~0.921)	*0.680*	87.0%	80.6%	74.1%	90.6%
Junior Radiologist 1 + AI	0.810 (0.687~0.900)	*0.438*	87.0%	75.0%	69.0%	90.0%
Junior Radiologist 2 + AI	0.802 (0.678~0.894)	*0.202*	82.6%	77.8%	70.4%	87.5%
Combined model *	0.865 (0.751~0.940)	*reference*	87.0%	69.4%	64.5%	89.3%

**The sensitivity, specificity, PPV and NPV of the Combined model were calculated under the optimal cut-off point. (threshold = 0.4387) when compared with that of the radiologists.*

agreement between the two junior radiologists significantly increased from a kappa of 0.334 to 0.593. Our findings were consistent with those of the recent work by Lee et al., which demonstrated that deep learning-based computer-aided diagnosis could help resident physicians gain confidence in diagnosis, improve diagnostic accuracy and increase overall confidence levels for CT diagnosis of cervical LNs metastasis from thyroid cancer using a large clinical cohort (21).

Some limitations of this study should be noted. First, our dataset was obtained from a single center, and all patients underwent unified contrast-enhanced CT protocols, which can cause biases. Further study will require a larger sample size from multiple centers to validate our results and increase their repeatability. Second, the deep learning model was not combined with clinical data, which should be incorporated in further studies. Third, this study only excluded lymph nodes less than 5mm to avoid a partial volume effect. However, malignant nodes smaller than 5 mm are often encountered. Further studies need to improve the ability of LNs segmentation to include smaller lymph nodes, which will be better able to reflect reality.

In conclusion, a Combined model integrating both CT images and iodine maps of the arterial and venous phases showed good performance in predicting lymph nodes metastasis in thyroid cancer patients, which could facilitate clinical decision-making.

DATA AVAILABILITY STATEMENT

The raw data supporting the conclusions of this article will be made available by the authors, without undue reservation.

ETHICS STATEMENT

This study was approved by the Institutional Ethics Committee of the Second Affiliated Hospital of Soochow University, and the written informed consent requirement was waived.

AUTHOR CONTRIBUTIONS

DJ, XN, and XZ have contributed equally to this work and share first authorship. DJ, XN, and XZ: collected and analyzed the data, plotted tables, and wrote this article. HY: analyzed the results. HZ: suggested Deep Learning approaches. LX: provided medical advice. RW: collected and analyzed the data. GF: designed and implemented the work and provided medical advice. All authors contributed to manuscript revision, read, and approved the submitted version.

FUNDING

This work was supported by the Suzhou Science & Technology Innovation Project (Grant No. ZHYLYB 2021001).

SUPPLEMENTARY MATERIAL

The Supplementary Material for this article can be found online at: https://www.frontiersin.org/articles/10.3389/fonc.2022.869895/full#supplementary-material

REFERENCES

1. Liu X, Ouyang D, Li H, Zhang R, Lv Y, Yang A, et al. Papillary Thyroid Cancer: Dual-Energy Spectral CT Quantitative Parameters for Preoperative Diagnosis of Metastasis to the Cervical Lymph Nodes. *Radiology* (2015) 275 (1):167–76. doi: 10.1148/radiol.14140481
2. Kim E, Park JS, Son KR, Kim JH, Jeon SJ, Na DG. Preoperative Diagnosis of Cervical Metastatic Lymph Nodes in Papillary Thyroid Carcinoma: Comparison of Ultrasound, Computed Tomography, and Combined Ultrasound With Computed Tomography. *Thyroid* (2008) 18(4):411–8. doi: 10.1089/thy.2007.0269
3. Haugen BR, Alexander EK, Bible KC, Doherty GM, Mandel SJ, Nikiforov YE, et al. 2015 American Thyroid Association Management Guidelines for Adult Patients With Thyroid Nodules and Differentiated Thyroid Cancer: The American Thyroid Association Guidelines Task Force on Thyroid Nodules and Differentiated Thyroid Cancer. *Thyroid* (2016) 26(1):1–133. doi: 10.1089/thy.2015.0020
4. Wu YY, Wei C, Wang CB, Li NY, Zhang P, Dong JN. Preoperative Prediction of Cervical Nodal Metastasis in Papillary Thyroid Carcinoma: Value of Quantitative Dual-Energy CT Parameters and Qualitative Morphologic Features. *AJR Am J Roentgenol* (2021) 216(5):1335–43. doi: 10.2214/AJR.20.23516
5. Zou Y, Zhang H, Li W, Guo Y, Sun F, Shi Y, et al. Prediction of Ipsilateral Lateral Cervical Lymph Node Metastasis in Papillary Thyroid Carcinoma: A Combined Dual-Energy CT and Thyroid Function Indicators Study. *BMC Cancer* (2021) 21(1):221. doi: 10.1186/s12885-021-07951-0
6. Hosny A, Parmar C, Quackenbush J, Schwartz LH, Aerts H. Artificial Intelligence in Radiology. *Nat Rev Cancer* (2018) 18(8):500–10. doi: 10.1038/s41568-018-0016-5

7. Zhou LQ, Wu XL, Huang SY, Wu GG, Ye HR, Wei Q, et al. Lymph Node Metastasis Prediction From Primary Breast Cancer Us Images Using Deep Learning. *Radiology* (2020) 294(1):19–28. doi: 10.1148/radiol.2019190372
8. Parmar C, Barry JD, Hosny A, Quackenbush J, Aerts H. Data Analysis Strategies in Medical Imaging. *Clin Cancer Res* (2018) 24(15):3492–9. doi: 10.1158/1078-0432.CCR-18-0385
9. Park JE, Lee JH, Ryu KH, Park HS, Chung MS, Kim HW, et al. Improved Diagnostic Accuracy Using Arterial Phase CT for Lateral Cervical Lymph Node Metastasis From Papillary Thyroid Cancer. *AJNR Am J Neuroradiol* (2017) 38(4):782–8. doi: 10.3174/ajnr.A5054
10. Robbins KT, Clayman G, Levine PA, Medina J, Sessions R, Shaha A, et al. Neck Dissection Classification Update: Revisions Proposed by the American Head and Neck Society and the American Academy of Otolaryngology-Head and Neck Surgery. *Arch Otolaryngol Head Neck Surg* (2002) 128(7):751–8. doi: 10.1001/archotol.128.7.751
11. Zhao Y, Li X, Li L, Wang X, Lin M, Zhao X, et al. Preliminary Study on the Diagnostic Value of Single-Source Dual-Energy CT in Diagnosing Cervical Lymph Node Metastasis of Thyroid Carcinoma. *J Thorac Dis* (2017) 9 (11):4758–66. doi: 10.21037/jtd.2017.09.151
12. Moltz JH, Bornemann L, Kuhnigk J-M, Dicken V, Peitgen E, Meier S, et al. Advanced Segmentation Techniques for Lung Nodules, Liver Metastases, and Enlarged Lymph Nodes in CT Scans. *IEEE J Select Topics Signal Process* (2009) 3(1):122–34. doi: 10.1109/JSTSP.2008.2011107
13. Youden WJ. Index for Rating Diagnostic Tests. *Cancer* (1950) 3(1):32–5. doi: 10.1002/1097-0142(1950)3:1<32::AID-CNCR2820030106>3.0.CO;2-3
14. Finazzi S, Poole D, Luciani D, Cogo PE, Bertolini G. Calibration Belt for Quality-Of-Care Assessment Based on Dichotomous Outcomes. *PloS One* (2011) 6(2):e16110. doi: 10.1371/journal.pone.0016110
15. Vickers AJ, Elkin EB. Decision Curve Analysis: A Novel Method for Evaluating Prediction Models. *Med Decis Mak* (2006) 26(6):565–74. doi: 10.1177/0272989X06295361
16. DeLong ER, DeLong DM, Clarke-Pearson DL. Comparing the Areas Under Two or More Correlated Receiver Operating Characteristic Curves: A Nonparametric Approach. *Biometrics* (1988) 44(3):837–45. doi: 10.2307/2531595
17. Kloos RT, Ringel MD, Knopp MV, Hall NC, King M, Stevens R, et al. Phase II Trial of Sorafenib in Metastatic Thyroid Cancer. *J Clin Oncol* (2009) 27 (10):1675–84. doi: 10.1200/JCO.2008.18.2717
18. Ying M, Bhatia KS, Lee YP, Yuen HY, Ahuja AT. Review of Ultrasonography of Malignant Neck Nodes: Greyscale, Doppler, Contrast Enhancement and Elastography. *Cancer Imaging* (2014) 13(4):658–69. doi: 10.1102/1470-7330.2013.0056
19. Zhou Y, Su GY, Hu H, Ge YQ, Si Y, Shen MP, et al. Radiomics Analysis of Dual-Energy CT-Derived Iodine Maps for Diagnosing Metastatic Cervical Lymph Nodes in Patients With Papillary Thyroid Cancer. *Eur Radiol* (2020) 30(11):6251–62. doi: 10.1007/s00330-020-06866-x
20. Sun J, Li B, Li CJ, Li Y, Su F, Gao QH, et al. Computed Tomography Versus Magnetic Resonance Imaging for Diagnosing Cervical Lymph Node Metastasis of Head and Neck Cancer: A Systematic Review and Meta-Analysis. *Onco Targets Ther* (2015) 8:1291–313. doi: 10.2147/OTT.S73924
21. Lee JH, Ha EJ, Kim D, Jung YJ, Heo S, Jang YH, et al. Application of Deep Learning to the Diagnosis of Cervical Lymph Node Metastasis From Thyroid Cancer With CT: External Validation and Clinical Utility for Resident Training. *Eur Radiol* (2020) 30(6):3066–72. doi: 10.1007/s00330-019-06652-4

Conflict of Interest: HY and HZ were employed by Infervision Medical Technology Co., Ltd, Beijing, China.

The remaining authors declare that the research was conducted in the absence of any commercial or financial relationships that could be construed as a potential conflict of interest.

frontiers | Frontiers in Oncology

ORIGINAL RESEARCH
published: 11 May 2022
doi: 10.3389/fonc.2022.870055

FAT1 Upregulates in Oral Squamous Cell Carcinoma and Promotes Cell Proliferation *via* Cell Cycle and DNA Repair

Ting Lan[1†], Qi Ge[1†], Ke Zheng[2†], Li Huang[3], Yuxiang Yan[1], Lixin Zheng[4], Youguang Lu[1,5] and Dali Zheng[1*]*

[1] Fujian Key Laboratory of Oral Diseases, Fujian Biological Materials Engineering and Technology Center of Stomatology, School and Hospital of Stomatology, Fujian Medical University, Fuzhou, China, [2] Department of Pathology, The First Affiliated Hospital of Fujian Medical University, Fuzhou, China, [3] Department of Dentistry, The First Affiliated Hospital of Fujian Medical University, Fuzhou, China, [4] School of Mathematics, Georgia Institute of Technology, Atlanta, GA, United States, [5] Department of Preventive Dentistry, School and Hospital of Stomatology, Fujian Medical University, Fuzhou, China

OPEN ACCESS

Edited by:
Amanda Psyrri,
University General Hospital Attikon, Greece

Reviewed by:
Elena Vagia,
University General Hospital Attikon, Greece
Paola Massimi,
International Centre for Genetic Engineering and Biotechnology, Italy

***Correspondence:**
Dali Zheng
dalizheng@fjmu.edu.cn
Youguang Lu
fjlyg63@fjmu.edu.cn

[†]These authors have contributed equally to this work

Specialty section:
This article was submitted to Head and Neck Cancer, a section of the journal Frontiers in Oncology

Received: 05 February 2022
Accepted: 23 March 2022
Published: 11 May 2022

Citation:
Lan T, Ge Q, Zheng K, Huang L, Yan Y, Zheng L, Lu Y and Zheng D (2022) FAT1 Upregulates in Oral Squamous Cell Carcinoma and Promotes Cell Proliferation via Cell Cycle and DNA Repair. Front. Oncol. 12:870055. doi: 10.3389/fonc.2022.870055

Objective: Previous studies have revealed that FAT atypical cadherin 1 (FAT1) plays a tumor-suppressive or oncogenic role in a context-dependent manner in various cancers. However, the functions of FAT1 are ambiguous in tumorigenesis owing to inconsistent research in oral squamous cell carcinoma (OSCC). The present study aimed at gaining an insight into the role of FAT1 in the tumor genesis and development.

Methods: The expression, mutant, and survival data analyses were done using data from The Cancer Genome Atlas (TCGA), the Gene Expression Omnibus (GEO), and the Clinical Proteomic Tumor Analysis Consortium (CPTAC) database, verified with clinical samples *via* real-time polymerase chain reaction (qRT-PCR), Western blot (WB), and immunohistochemical (IHC) staining. OSCC cells transfected with siRNA were employed for *in vitro* assessment in cell proliferation, apoptosis, and migration ability in appropriate ways. The underlying mechanism was explored by RNA sequencing after FAT1 silencing.

Results: Overall, FAT1 significantly increased in OSCC with a poor prognosis outcome. The *in vitro* experiment showed the promoting effect of FAT1 in the proliferation and migration of OSCC cells. FAT1 can also inhibit both the early and late apoptosis of OSCC cells. RNA-sequencing analysis of FAT1 silencing revealed that the cell cycle, DNA replication, and some core genes (MCM2, MCM5, CCNE1 SPC24, MYBL2, KIF2C) may be the potential mechanism in OSCC.

Conclusions: FAT1 may act as an oncogene in OSCC with potential mechanism influencing the cell cycle and DNA repair.

Keywords: Fat1, OSCC, cell proliferation, TCGA, RNA-seq

INTRODUCTION

Oral squamous cell carcinoma (OSCC), a subset of head and neck squamous cell carcinoma (HNSC), is always lethal. Mainly based on stage and anatomic location, the current standard therapy for OSCC consists of surgery and radiation therapy, which are generally recommended for the approximately 30% to 40% of individuals in the early-stage disease (stage I or II) (1). Like all solid tumors, OSCCs are thought to be initiated through a series of genetic alterations (2). Integrated genomic analysis has identified FAT1 as an additional driver gene, which has been detected mutant in several large-scale exome sequencing projects, frequently in esophageal squamous cell carcinoma (ESCC) and OSCC (3, 4). FAT1 (FAT atypical cadherin 1) is a member of the vertebrate Fat cadherin family, which comprised FAT1, FAT2, FAT3, and FAT4 genes (5). First isolated from the T-leukemia cell line J6, FAT1 is located on human chromosome 4q35.2, consists of 27 exons, and encodes proteins with a single transmembrane domain, 34 extracellular cadherin repeats, and laminin G-like and epidermal growth factor (EGF)-like domains (5, 6). FAT1 is widely expressed in many fetal tissues whereas it is downregulated or disappears in most adult tissues, indicating that FAT1 may play a role in development (7).

However, compared to the ample studies and information available of FAT1 over the past two decades, the role of FAT1 in tumor initiation and progression has been conflicting. Morris et al. identified FAT1 as a candidate tumor-suppressor gene which is able to suppress cancer cell growth by binding β-catenin and antagonizing its nuclear localization in glioblastoma (GBM) (8). Similarly, in breast cancer, it has been reported that the loss of FAT1 was associated with progression, aggressive behavior, poor prognosis, and cyclin-dependent kinase (CDK) 4/6 inhibitor resistance through the Hippo signaling pathway (9, 10). The expression of FAT1, as the transcriptional target of E2F1, was frequently downregulated in ESCC tissues and inhibited proliferation, adhesion, and invasion through the MAPK signaling pathway (11, 12). Yu et al. suggested that a low FAT1 expression was associated with poor prognosis in children with medulloblastoma and acted on the WNT signaling pathway to inhibit cell proliferation (13). On the other hand, FAT1 functions as an oncogene in many other cancers. FAT1 was shown to be aberrantly expressed in pediatric patients with acute leukemia, whereas hematopoietic progenitors from healthy donors lacked the FAT1 expression. FAT1 expression was also correlated with a more mature leukemic immunophenotype (14, 15). Furthermore, FAT1, reported as a new glypican-3 (GPC3)-interacting protein, appeared as a relevant mediator of hypoxia and growth receptor signaling to critical tumorigenic pathways with a higher expression in HCC (16, 17).

In regard to head and neck cancers, Lin et al. reported that a lower FAT1 expression was correlated with poor disease-free survival, and they proved that FAT1 suppressed the migration and invasion capability of the SCC25, FaDu, HSC3, OECM-1, and OC4 HNSC cell lines, not changing the cell proliferation (18). Martin et al. supported that the FAT1 intracellular domain (ICD) interacted with and facilitated the assembly of the core Hippo signaling complex as upstream of Yes-associated protein 1 (YAP1). Inactivation mutations and genomic alterations in FAT1 resulted in HNSC by activating YAP1 to suppress the HIPPO signaling pathway and promoted the proliferation (19). Interestingly, Hsu et al.'s findings contradicted those of Lin et al., and they cautiously attributed to tumor heterogeneity and/or cohort constitution, similar to the studies of GBM in which the expression level depended on the grade of cancerous cells (20–22).

In this study, we aimed to comprehensively analyze the expression of FAT1 and its effect on OSCC as well as some exploration of mutations which may cause gene expression changes. In addition, we silenced FAT1 to evaluate the effects on cell death and survival, proliferation, and migration in two OSCC cells. Finally, RNA sequencing (RNA-seq) was performed to investigate the gene expression profile upon FAT1 knockdown. FAT1 was thus considered to be a potential target for the development of molecular therapeutic strategies to improve the prognosis of OSCC.

MATERIALS AND METHODS

Data Preparation From Public Database and Statistical Analysis

RNA-seq (HTSeq-FPKM), mutation, and corresponding clinical data were downloaded from The Cancer Genome Atlas (TCGA) HNSC project in March 2020 using the R package TCGAbiolinks (23). The transcriptome data were log10-transformed for comparison. The R package maftools was utilized to analyze and visualize the somatic condition of HNSC patients from TCGA (24). The GSE6631, GSE37991, GSE30784, and GSE10300 datasets were retrieved from the Gene Expression Omnibus (GEO) database (https://www.ncbi.nlm.nih.gov/geo/). Raw data were examined within normalization and log2 transformation, and then the gene probes were annotated to explore the FAT1 expression level. Kaplan–Meier (KM) survival analysis was undertaken to compare the overall survival of different groups of patients *via* the R package survival and survminer (determined the optimal cutpoint), and P-values were calculated using the log-rank test. The COSMIC database (https://cancer.sanger.ac.uk/cosmic) was used to determine the occurrence of FAT1 mutation variants.

Processed mass spectrometry data of HNSC were downloaded from the Clinical Proteomic Tumor Analysis Consortium (CPTAC) Data Portal (https://cptac-data-portal.georgetown.edu/), a 108 human papilloma virus (HPV)-negative HNSC cohort. After plus 10, raw data were converted into log10. Data used in this publication were generated by the Clinical Proteomic Tumor Analysis Consortium (NCI/NIH).

All statistical analyses and visualizations were performed using R (version 4.0.1) or GraphPad Prism (version 6.01). For comparisons, Student's t-test, Mann–Whitney U-test, Fisher's exact test, or chi-square test was used when appropriate and $P < 0.05$ was considered statistically significant for all tests.

Clinical HNSC Specimens

This study was approved by the Institutional Review Board of Fujian Medical University School and Hospital of Stomatology

(Approval Number: FMUSS-18-004). Samples and clinical information were collected as described (25). The patient clinicopathologic characteristics included age, sex, tumor stage, differentiation degree, metastasis status, depth of invasion, extra extension, and perineural invasion. Patient death was mainly caused by carcinoma recurrence or metastasis. Another 33 paired fresh samples were collected to quantify the FAT1 mRNA expression, and we confirmed 8 pairs at the protein level.

Total RNA Isolation and Quantitative Reverse Transcription Polymerase Chain Reaction

Total RNA was extracted from tissue samples using NucleoZOL Reagent (Takara, Dalian, China) according to the manufacturer's protocol, and cDNA was synthesized from 1 μg of total RNA using a PrimeScript® 1st strand cDNA Synthesis Kit (Takara, Dalian, China) in a final reaction volume of 20 μl. Quantitative RT-PCR was performed using SYBR Premix Ex Taq (Takara, Dalian, China) with primers listed in **Table 1**. The expression levels were normalized to the GAPDH mRNA level for each sample obtained from parallel assays, and the data were analyzed according to the relative 2^ (-ΔΔCt) method.

IHC Staining

The tissue microarrays and immunohistochemistry were performed as previously described (25). Antigen retrieval was performed with EDTA buffer (pH 8.0) using a high-temperature and high-pressure antigen repair method. The slides were incubated with a primary antibody, polyclonal rabbit anti-human FAT1 (1:500; ab190242, Abcam, Cambridge, MA, USA), for 3 h at 25°C. Secondary antibodies were applied for 20 min at 25°C. All cases were reviewed and scored independently by two senior pathologists without knowledge of the clinical characteristics. The immunoreactivity intensity was scored in the following four categories: 0 (no staining), 1+ (weak staining), 2+ (moderate staining), and 3+ (strong staining). The immunoscore was obtained by multiplying (3*x% + 2*x% + 1*x% = total score) the percentage of positively stained tumor cells (0%–100%) by the corresponding immunostaining intensity (0 to 3+) to obtain a value ranging from 0 to 300. An immunoscore of 150 was set as the cutoff point for negative or positive expression (26), while another cutoff value was used in subsequent survival analyses determined by the R package survminer.

Western Blot Assay

Using RIPA (Beyotime, China), after specific treatments, HN6 and HN30 cells were collected and lysed. After the protein concentrations was determined by the BCA method (Beyotime, Shanghai, China), the lysates were diluted into 5× SDS buffer to a 1× SDS final concentration and then heated for 10 min at 100°C. Proteins were separated on 4%–12% SDS-PAGE gels and electrophoresed at 30-V constant voltage overnight to polyvinylidene fluoride (PVDF) membranes. Blots were blocked with 5% BSA in TBST at room temperature for 1 h and then incubated overnight at 4°C with a primary antibody against FAT1 (1:1,000; ab190242, Abcam) and actin (1:1,000; ab179467, Abcam), followed by a horseradish peroxidase–conjugated secondary antibody for 1 h at room temperature. The membranes were washed thrice with TBST. Finally, they were visualized with Pierce™ Enhanced Chemiluminescence (ECL) Western Blotting Substrate (Beyotime, China) and imaged with a densitometer for semi-quantification of the signal intensity and later analyzed with the NIH ImageJ software (https://imagej.nih.gov/ij/download.html). The experiment was repeated three times.

Cell Lines and Culture

The HN6 and HN30 cell lines were bought from the Cell Bank of the Institute of Biochemistry and Cell Biology, Chinese Academy of Sciences (Shanghai, China). Cells were cultured under the conditions provided by the supplier.

Small Interfering RNA Transfection

Small interfering RNA (siRNA) logos against human FAT1 (siFAT1-1, synthesized as follows: sense: 5′-GCACCACAAUUUCGAGCAATT-3′, antisense: 5′-UUGCUCGAAAUUGUGGUGCTT-3′; siFAT1-2, synthesized as follows: 5′-GCACGUGUGUUGUCGACAATT-3′, antisense: 5′-UUGUCGACAACACACGUGCTT-3′) and a scrambled siRNA used as negative control (NC, synthesized as

TABLE 1 | The primers for qRT-PCR in the current study.

Gene	Forward	Reverse
GAPDH	5′-GGTGTGAACCATGAGAAGTATGA-3′	5′-GAGTCCTTCCACGATACCAAAG-3′
FAT1	5′-GCACCTGTTGGTTCATTGGTAA-3′	5′-AATAATGGGAGGTCGATTCACG-3′
MCM2	5′-ACCCGAAGCTCAACCAGATG-3′	5′-ATAGTCCCGCAGATGGATGC-3′
MCM5	5′-TCGTCAAGGATGAGCACAATG-3′	5′-TCACTCGGCAGTAGGCAATA-3′
CCNE1	5′-CTGGATGTTGACTGCCTTGAAT-3′	5′-TCTCTATGTCGCACCACTGAT-3′
CD83	5′-CTGCTGCTGGCTCTGGTTAT-3′	5′-CAGTTCTGTCTTGTGAGGAGTCA-3′
SPC24	5′-GCTGCGAGAGATCCTCACCAT-3′	5′-TGGCCTTCAGACGGGTGT-3′
MYBL2	5′-GCTGGCATCGAACTCATCAT-3′	5′-GCTTCACATCCTCATCCACAAT-3′
KIF2C	5′-GATGGAAGCCTGCTCTAACG-3′	5′-AGTCTGGTCCTTGCTGTATGA-3′
SUV39H1	5′-GTGGATGCCGCCTACTATGG-3′	5′-CGCTCGTCAAGGTTGTCTATG-3′
UHRF1	5′-CCAACCACTACGGACCCATC-3′	5′-ACTAGGGAGTACGCTCCGTC-3′
PERP	5′-TACTCAGCGCCATCGCCTTC-3′	5′-TCTTGGGAGCATTTCCACCAC-3′
TPM4	5′-GGAAGAGGCTGACCGCAAAT-3′	5′-TTAGTTCAGACACCTCCGCAC-3′
GANAB	5′-CGGCGGTCTTCAGAATGTATG-3′	5′-TGTTGCCAGAGAATGAGAATCG-3′
EMC6	5′-CCTGGATTATTGCCGGACCTC-3′	5′-AGGCGAGCAGGTAGAAGATG-3′

follows: sense: 5′-UUCUCCGAACGUGUCACGUTT-3′, antisense: 5′-ACGUGACACGUUCGGAGAATT-3′) were purchased from GenePharma (GenePharma, Shanghai, China). Cells were transfected with siRNAs with Lipofectamine RNAiMAX (Cat. 13778075, Invitrogen, Carlsbad, CA, USA) according to the manufacturer's instructions. On the following day, cells were harvested for quantitative reverse transcription polymerase chain reaction (qRT-PCR), Western blot analysis, and other assays.

Cell Proliferation Analysis

After transfection for 24 h, cells were collected from the interference group and NC group and then reseeded in 96-well plates at a density of 4,000 cells/well with 3 replicate wells per group. Cell Counting Kit-8 (Dojindo, Kumamoto, Japan) was employed to quantitatively evaluate cell viability every 24 h for 6 days. The absorbance was measured at 450 nm in a microplate reader (Pharmacia Biotech, Piscataway, NJ, USA). The experiment was performed in triplicate and repeated three times.

Clone Formation Assay

After transfection for 24 h, cells were collected from the interference group and NC group and then reseeded in 6-well plates with 4,000 cells per well. Three duplicate wells were performed for each group. The plates were incubated at 37°C for 14 days and stained with crystal violet. They were then air-dried, and the numbers of clones were calculated. The experiment was performed in triplicate and repeated three times.

Cell Cycle Assay

After transfection for 48 h, cells from the gene silencing group and NC group were harvested and washed three times with precooled PBS and then treated with 70% ethanol for at 4°C at least overnight. Then the cells were washed three times with PBS and resuspended in 500 μl PI/RNase Staining Buffer (550825, BD Biosciences, Franklin Lakes, NJ, USA) according to the manufacturer's instructions. Cell cycle status was tested using a BD Accuri C6 flow cytometer (BD Biosciences) and analyzed by FlowJo software. The experiment was repeated three times.

Cell Apoptosis Analysis With Annexin V-FITC/PI

After transfection for 48 h, cells were collected by trypsinization and centrifuged with supernatant at 1,500×g for 5 min. After being resuspended and incubated at 37°C for 30 min, the cells were washed three times with 4°C PBS and resuspended in 100 μl 1× binding buffer. 5 μl Annexin V-FITC and 5 μl propidium iodide (PI) solution (YF® 488 Annexin V and PI Apoptosis Kit, US Everbright, Suzhou, China) were then added to stain the cells under darkness for 15 min. The apoptosis rate was measured by a BD Accuri C6 flow cytometer (BD Biosciences). Single-stained and unstained cells were used as a control. The experiment was repeated three times.

The Sphere-Forming Assay

After transfection for 24 h, cells were dissociated to produce single-cell suspensions and were seeded in 96-well ultralow-attachment plates (Corning, Tewksbury, MA, USA) at a density of 800 cells/well. They were cultured in mTeSR medium (STEMCELL Technologies, Vancouver, Canada). After incubation for 1–2 weeks, tumorspheres were photographed under a microscope (×50 magnification) and the number was determined. The experiment was performed in triplicate and repeated three times.

Migration Assay

After transfection for 24 h, using a 24-well plate, we seeded 5×10^4 cells for HN6 and 3×10^5 cells for HN30 into the upper chamber of the insert (8-μm pore size, BD Biosciences, USA) containing FBS-free media, while the lower chamber contained 10% FBS-supplemented media. After incubation for 24 h for HN6 and 48 h for HN30, the chambers were stained with crystal violet and non-invaded cells in the upper surface were removed with sterile cotton swipes. Then, the average number of invaded cells was determined and photographed under a microscope (×200 magnification), from at least five non-overlapping visual fields selected randomly. The experiment was repeated three times.

Wound Healing Assay

After transfection for 24 h, cells were reseeded in 12-well plates and until cell monolayers were cultured, scratched by manually scraping off cells with a sterile yellow pipette tip. All the wound sizes were verified to be of similar width in the beginning. The images of cell migration were observed and captured at the 18- and 32-h time-points afterward under a ×50 microscope magnification (Olympus, Tokyo, Japan) and later analyzed with the NIH ImageJ software (https://imagej.nih.gov/ij/download.html). The experiment was repeated three times.

RNA Sequencing and Analysis

After transfection for 24 h, cells were harvested and the total RNA extracted using NucleoZOL Reagent (Takara, Dalian, China) according to the manufacturer's protocol. RNA-sequencing libraries were constructed with FAT1 knockdown (siFAT1-1 and siFAT1-2) and the control group in two HN6 and HN30, repeated two biological times. RNA-seq was performed by Berry Genomics company. Briefly, RNA integrity was evaluated using NanoDrop 2000 or an Agilent 2100 Bioanalyzer. All included samples had RNA concentrations >40 ng/μl, and a total amount of >2 μg with an RNA integrity number (RIN) ≥6.5 was subjected to subsequent analyses. The library preparations were sequenced on an Illumina NovaSeq 6000 platform, and 150-bp paired-end reads were generated. Raw reads were processed using custom scripts, and ploy-N-containing reads, PCR duplications, and low-quality reads were removed to obtain clean reads, which were then mapped to the hg38 genome. R package Limma-voom was used for the differential expression analysis. Abs ($\log_2$ fold change) >1.00 and P-value <0.05 were used as criteria to classify differentially expressed genes (DEGs) (27). Gene Set Enrichment Analysis (GSEA) based on the ordered list of all genes according to the log2 fold change (log2FC) value, Gene Ontology (GO) functional enrichment analyses, and Kyoto Encyclopedia of Genes and Genomes (KEGG) pathway analyses were performed by the R

package clusterProfiler (28). Cancer hallmark definitions were downloaded from GSEA/MSigDB 6.2 (http://www.broadinstitute.org/gsea/msigdb). The STRING database (https://string-db.org/) was used to produce protein–protein interaction networks (PPI) and the enrichment analyses based on DEGs, and the networks was visualized *via* Cytoscape 3.9. P-value < 0.05 was set as a significant enrichment criterion.

RESULTS

High FAT1 mRNA Expression Level in OSCC Correlates With Poor Prognosis

Because of the controversial roles of FAT1 reported in different malignancies also in HNSC, we first evaluated in TCGA database to figure out its expression pattern. Data from HNSC samples (n = 502) revealed a significantly higher expression level of FAT1 in comparison with the adjacent normal tissues (n = 44; P < 0.0001). According to the Kaplan–Meier survival analysis, the survival rate was dramatically lower in FAT1 high expression group patients (P = 0.003). The results between OSCC samples (n = 330, the main subtype of HNSC) and adjacent normal tissues (n = 32) showed the same trend. Furthermore, FAT1 exhibited moderate classification ability between the tumor tissues and normal tissues lesion types with an AUC = 0.78 in HNSC and an AUC = 0.804 in OSCC (**Figures 1A, B**). Together, these results provided important insights into the potential capacity of FAT1 as a biomarker. Then, we analyzed further data from more than one region derived from the GEO database. Also, FAT1 was upregulated in tumor samples from two independent tumor and non-tumor pair-wise data sources (GSE6631 with HNSCs and GSE37991 with OSCCs; P < 0.0001, P < 0.001) and another set with 167 OSCCs and 45 normal oral tissues (GSE30784; P < 0.0001). Through the GEO cohort (GSE10300 with HNSC) with clinical data (recurrence-free survival), we could see that a higher expression of FAT1 based on the median was associated with a poor overall survival (P = 0.042 in RFS, **Figure 1C**). We also validated the FAT1 expression level with RNAs extracted from OSCC tissues and their matched normal tissues by quantitative real-time PCR (**Figure 1D**). Consistently, they showed statistically higher expression levels of FAT1 (P < 0.0001). Taken together, our findings demonstrated that a high FAT1 expression occurred in HNSC and OSCC, which was associated with poor patient survival and may play an oncogenic role in OSCC.

High FAT1 Protein Expression Level in OSCC Associated With Adverse Clinicopathological Features

To study the clinical significance and protein expression level of FAT1 in OSCC, we next examined 122 tissues by IHC. The expression levels of FAT1 were evaluated independently at the tumor center and the invasion front, which was defined as the tumoral advancing edge. FAT1 gave a positive staining in 62.6% (67/107) tumor front samples, 55.1% (65/118) tumor center samples, and 0.3% (3/116) normal tissues. FAT1 was detected mainly in the cytoplasm of squamous carcinoma cell (weak staining in the region of squamous pearl formation), and normal oral mucosa specimens displayed positivity mainly in sporadic cells of basal layers. The proportion of FAT1-positive tumor front and tumor center samples was significantly higher than that in non-cancerous samples (P < 0.0001). Kaplan–Meier survival analysis demonstrated that a high expression of FAT1 indicated a poor prognosis of OSCC, but the differences did not reach statistical significance (P = 0.33 in tumor center, P = 0.51 in tumor front; **Figure 2A**). The FAT1 expression of tumor front was significantly or nearly related with age (P = 0.0379), metastasis (P = 0.0063), tumor bunding (P = 0.0168), and perineural invasion (P = 0.0535) while the FAT1 expression of tumor center was significantly or nearly related with age (P = 0.0114) and differentiation (P = 0.0203) and metastasis (P = 0.0532). Statistical significance was not found in gender, tumor stage, depth of invasion (DOI), or extranodal extension (ENE) (**Table 2**). What emerged from the IHC results here was that FAT1 exhibited a high expression localized in the cytoplasm and was associated with the adverse clinicopathological features in OSCC. In addition, protein expression levels of FAT1 were determined in a cohort of 109 head and neck tumors and 70 normal head and neck tissue samples in the CPTAC database, consistently, which was upregulated in HNSC tissues (P < 0.0001). Moreover, we observed the FAT1 expression presenting an elevated trend in progressing tumor stages but not significantly. Interestingly, the FAT1 expression significantly increased in stage IV compared with that in low disease stages (P < 0.05). The results between OSCC samples (including lips and oral cavity, n = 53, a main subtype of HNSC) and adjacent normal tissues (n = 25) showed the same trend. The FAT1 expression increased in stage III and stage IV with a trend that approached statistical significance with P = 0.069 and P = 0.053. Likewise, we attempted AUC analysis at the protein level, also confirming a prominence in its diagnostic value (AUC = 0.79 in HNSC and AUC = 0.829 in OSCC) (**Figures 2B, C**). The protein expression level of FAT1 in 8 paired OSCC tissues was further verified *via* Western blotting (P < 0.001; **Figure 2D**).

Analysis of FAT1 Mutations in Combined With TCGA HNSC and OSCC Tissues

Mutations of oncogenes or tumor-suppressor genes often result in deregulation of the expression of these genes themselves, such as TP53. For illustrative purposes, bioinformatics analysis of the FAT1 mutational profile in TCGA HNSC cohort (n = 508) were performed, and the results generated that the most mutated driver genes in HNSC included TP53, TTN, FAT1, CDKN2A, and MUC16 (**Figure 3A**). The 22% (114/508) alterations of FAT1 in HNSC were investigated, and most of those were missense or nonsense mutation, frameshift, or splice site, occurring mostly in the cadherin domains (**Figure 3B**). We evaluated the effect of altered FAT1 mutants and demonstrated that compared to the FAT1 wild-type group, the FAT1 mutant group conferred a significantly lower FAT1 expression level but not a specific survival correlation (P < 0.0001; **Figure 3C**). The results between wild-type samples (n = 235) and FAT1 mutant samples (n = 86) showed the same trend in OSCC (**Figure 3D**).

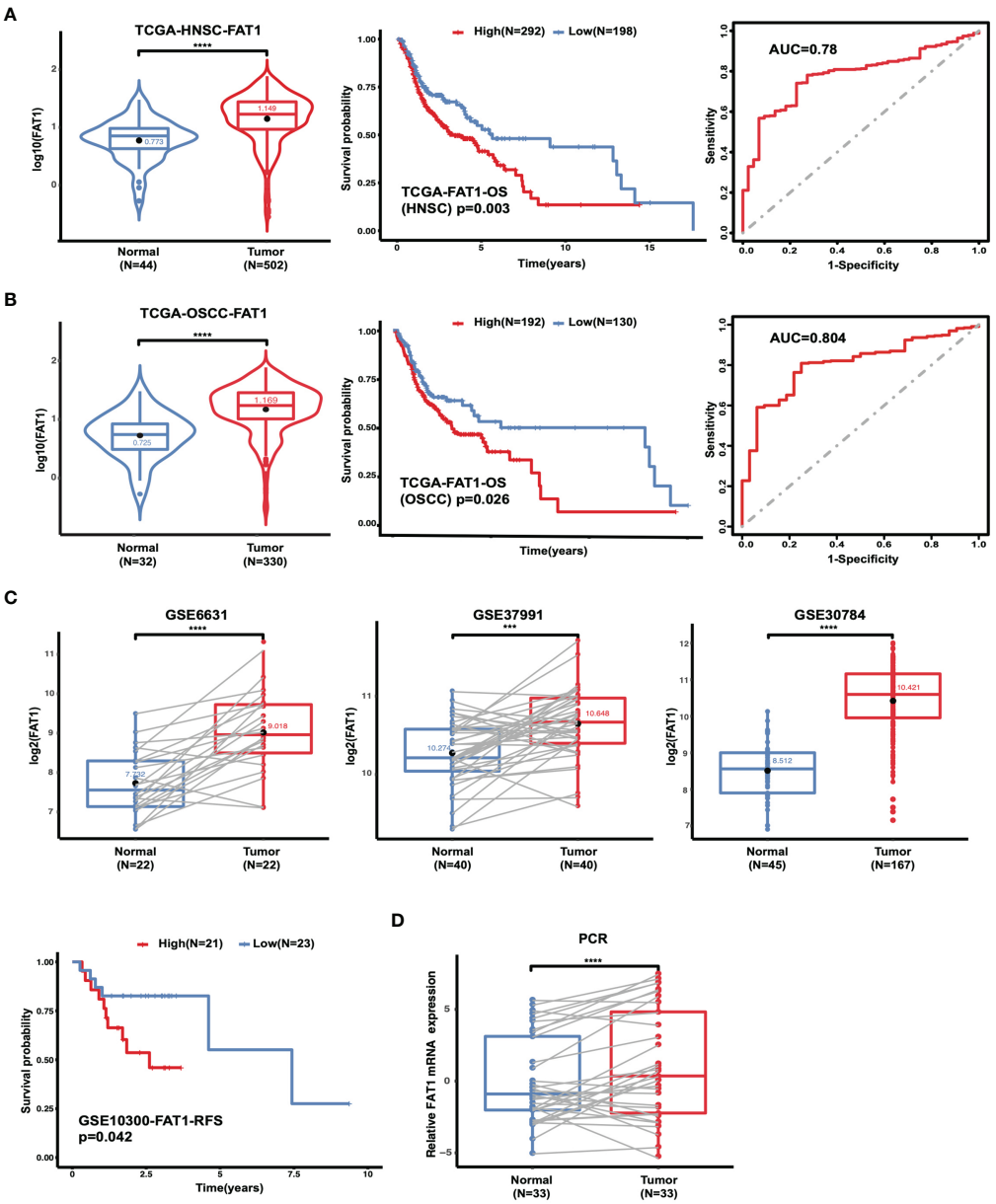

FIGURE 1 | The FAT1 mRNA level is upregulated in HNSC and OSCC, and a higher FAT1 expression level is associated with shorter overall survival. **(A)** FAT1 mRNA expression status between normal tissues and tumor tissues in HNSC from TCGA (boxplot and violin plot); Kaplan–Meier survival curve of overall survival time in HNSC from TCGA; areas under the curve (AUCs) of the ability to discriminate normal tissues and tumor tissues by the FAT1 mRNA level in HNSC from TCGA. **(B)** FAT1 mRNA expression status between normal tissues and tumor tissues in OSCC from TCGA (boxplot and violin plot); Kaplan–Meier survival curve of overall survival time in OSCC from TCGA; areas under the curve (AUCs) of the ability to discriminate normal tissues and tumor tissues by FAT1 mRNA level in OSCC from TCGA. OSCC is the main subtype of HNSC (including the sites of mouth, cheek mucosa, tongue, hard plate, lip, and gum). **(C)** FAT1 mRNA expression status in paired tumor and non-tumor pair-wise data sources (GSE6631 and GSE37991) and another GSE30784 set (boxplot). Kaplan–Meier survival curve of recurrence-free survival time in HNSC from GSE10300. **(D)** FAT1 mRNA expression status in clinical samples (boxplot). ***P < 0.001; ****P < 0.0001.

Then, the next section of the survey was concerned with FAT1 mutation in OSCC tissues. Simultaneously, based on the COSMIC mutation database, no hotspot region was observed for FAT1 mutations in HNSC, so we selected 4 most frequent mutation sites (404, 614, 1,662, 3,554) detected in multiple cancers, which may have implications for protein function, to be validated by Sanger sequencing (**Figures 3E, F**). However, we inspected a high FAT1 mutation ratio in OSCC tissues but also in matched adjacent normal tissues and leukocyte DNA of normal individuals (**Table 3**). What is more, no significant association was detected between the candidate variants and FAT1 expression level in OSCC tissues ($P > 0.05$), but we could

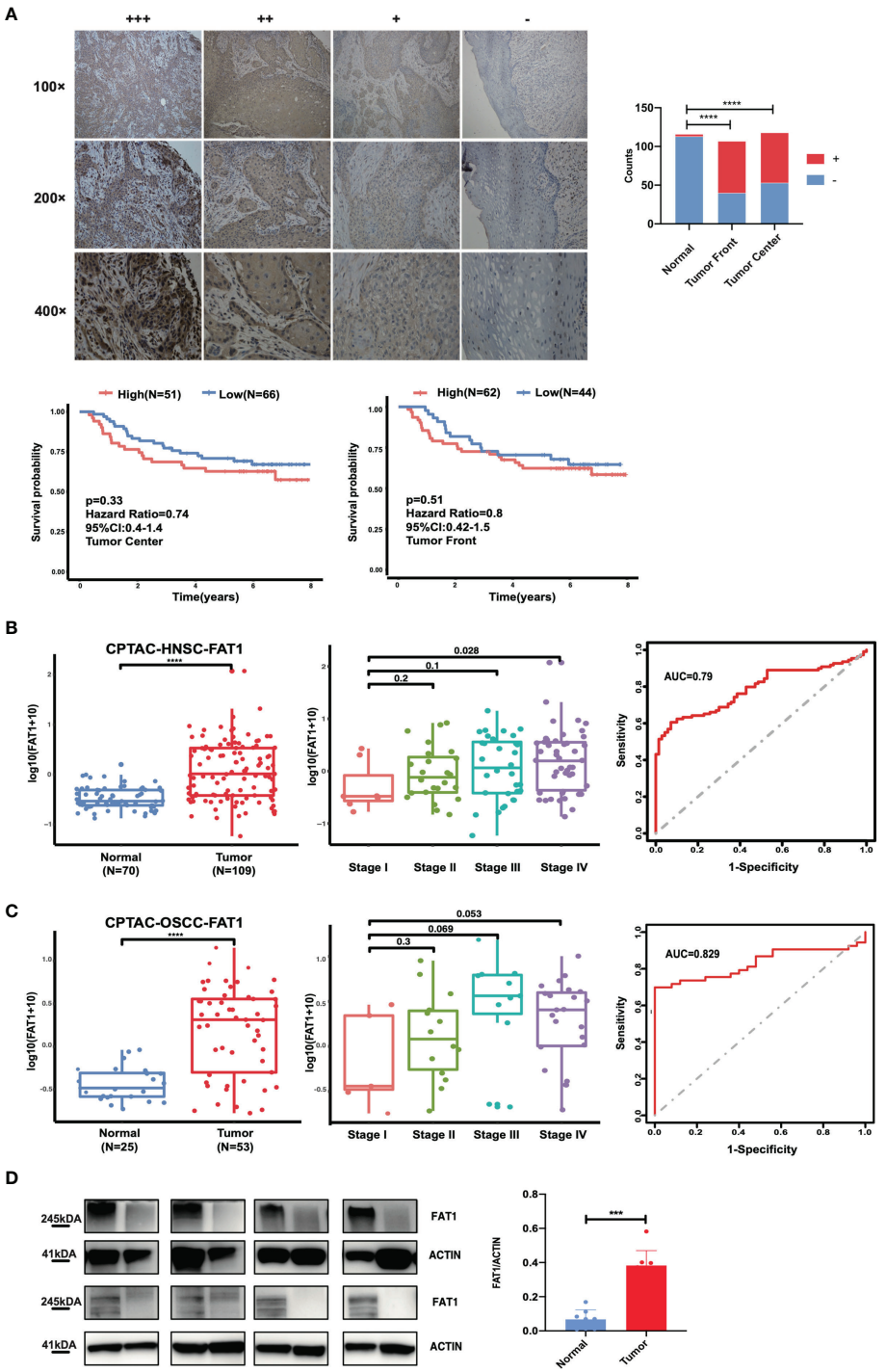

FIGURE 2 | FAT1 protein levels are upregulated in HNSC and OSCC tissues. **(A)** Left: Representative immunohistochemical staining images of normal and tumor tissues (magnification at ×100, ×200, ×400). FAT1 localization appears as brown staining in the cytoplasm. Right: histogram of the proportion of the FAT4 staining levels among the tumor front, tumor center, and adjacent normal samples and Kaplan–Meier survival analysis of patients with high and low levels of FAT1 protein expression by immunohistochemical staining levels. A high FAT1 expression exhibited poor survival but not significantly ($P > 0.05$). **(B)** FAT1 protein expression status between normal tissues and tumor tissues in HNSC from CPTAC (boxplot); FAT1 protein expression status among high stage and stage I tumor tissues in HNSC from CPTAC (boxplot); areas under the curve (AUCs) of the ability to discriminate normal tissues and tumor tissues by the FAT1 protein level in HNSC from CPTAC. **(C)** FAT1 protein expression status between normal tissues and tumor tissues in OSCC from CPTAC (boxplot); FAT1 protein expression status among high stage and stage I tumor tissues in OSCC from CPTAC (boxplot); areas under the curve (AUCs) of the ability to discriminate normal tissues and tumor tissues by the FAT1 protein level in OSCC from CPTAC. **(D)** FAT1 protein expression status in clinical samples (bar plot). ***$P < 0.001$; ****$P < 0.0001$.

TABLE 2 | Expression levels of FAT1 in OSCC samples with different clinical and pathological characteristics.

Characteristics	Tumor center				Tumor front			
	Cases	FAT1+	FAT1-	P value	cases	FAT1+	FAT1-	P value
Tumor	118	65	53	<0.0001	107	67	40	<0.0001
Normal	116	3	113	****	116	3	113	****
Gender	117				106			
Female	37	20	17	0.8245	32	20	12	0.9209
Male	80	45	35		74	47	27	
Age	117				106			
Less than 55	53	35	18	0.0379	44	34	10	0.0114
55 and up	64	30	34	*	62	33	29	*
Tumor stage	116				105			
T1	16	7	9	0.7127	17	9	8	0.1758
T2	34	18	16		31	16	15	
T3	21	12	9		17	11	6	
T4	45	27	18		40	30	10	
Differentiation	117				106			
Poorly	11	9	2	0.1914	11	10	1	0.0203
Moderately	70	36	34		64	34	30	*
Highly	36	20	16		31	23	8	
Metastasis	117				106			
Yes	76	35	41	0.0063	71	40	31	0.0532
No	41	30	11	**	35	27	8	
Depth of invasion	100				90			
above median	50	30	20	0.4214	44	30	14	0.124
less than median	50	25	25		46	23	23	
Extranodal extension	96				86			
Negative	78	41	37	0.2106	71	42	29	0.8025
Positive	18	13	5		15	10	5	
Perineural invasion	102				92			
Negative	63	30	33	0.0535	57	30	27	0.1173
Positive	39	27	12		35	25	10	
Tumor budding	102				92			
Negative	78	38	40	0.0168	72	40	32	0.1898
Positive	24	19	5	*	20	15	5	

*$P < 0.05$; **$P < 0.01$; ****$P < 0.0001$.

observe a decreasing FAT1 level trend in the FAT1 404, 614, and 1,662 mutated group (**Figure 3G**). Our results of mutation failed to identify the association between candidate sites and FAT1 expression level. They may be four SNP loci.

Downregulation of FAT1 Suppresses Proliferation, Stemness and Cell Cycle, and Promoted Cell Apoptosis in OSCC Cells

To explore potential FAT1 functions in OSCC, we conducted a loss-of-function study using two small interfering RNAs to knock down FAT1 in the HN6 and HN30 cell lines *in vitro*. Compared with the negative control siRNA group, RT-qPCR and Western blots determined the downregulated FAT1 expression in both mRNA and protein levels in the two-siRNA group (siFAT1-1 and siFAT1-2) (**Figures 4A, B**). First, we applied CCK-8 and colony formation assays to evaluate the functional effects of FAT1 alterations on cell growth. The results revealed that cell proliferation was suppressed after FAT1 silencing in both cell lines (**Figures 4C, D**). Meanwhile, the downregulation of FAT1 promoted OSCC cell apoptosis, including early apoptosis and late apoptosis (**Figure 4E**), and an increase in proportion in the G0/G1 phase accompanied by a decrease in proportion in the S phase was observed, hindering G1/S progression (**Figure 4F**). Due to the observation of the trend of significant inhibition of growth, we hypothesize that FAT1 expression contributes to the maintenance of OSCC CSCs. With tumorsphere assay, the self-renewal capability of HN30 was found to be suppressed after the knockdown of FAT1 (**Figure 4G**) while HN6 itself lacked the sphere-forming ability. Taken together, these results demonstrated that FAT1 may act as a tumor suppressor in OSCC.

FAT1 Increases Cell Migration *In Vitro*

We next examined whether FAT1 could impact the migration of OSCC cells. Taking advantage of the transwell assay, the results showed that FAT1 knockdown decreased the migrated cell numbers (**Figure 5A**). The results of the wound-healing assay displayed that, 18 h after scratching, the blank areas in the negative control were wider than in the interfering group and after 32 h, the negative control cells almost healed, while there were wide areas in the interfering group (**Figure 5B**). Thus, we validated that knockdown of FAT1 prevented OSCC cell migration.

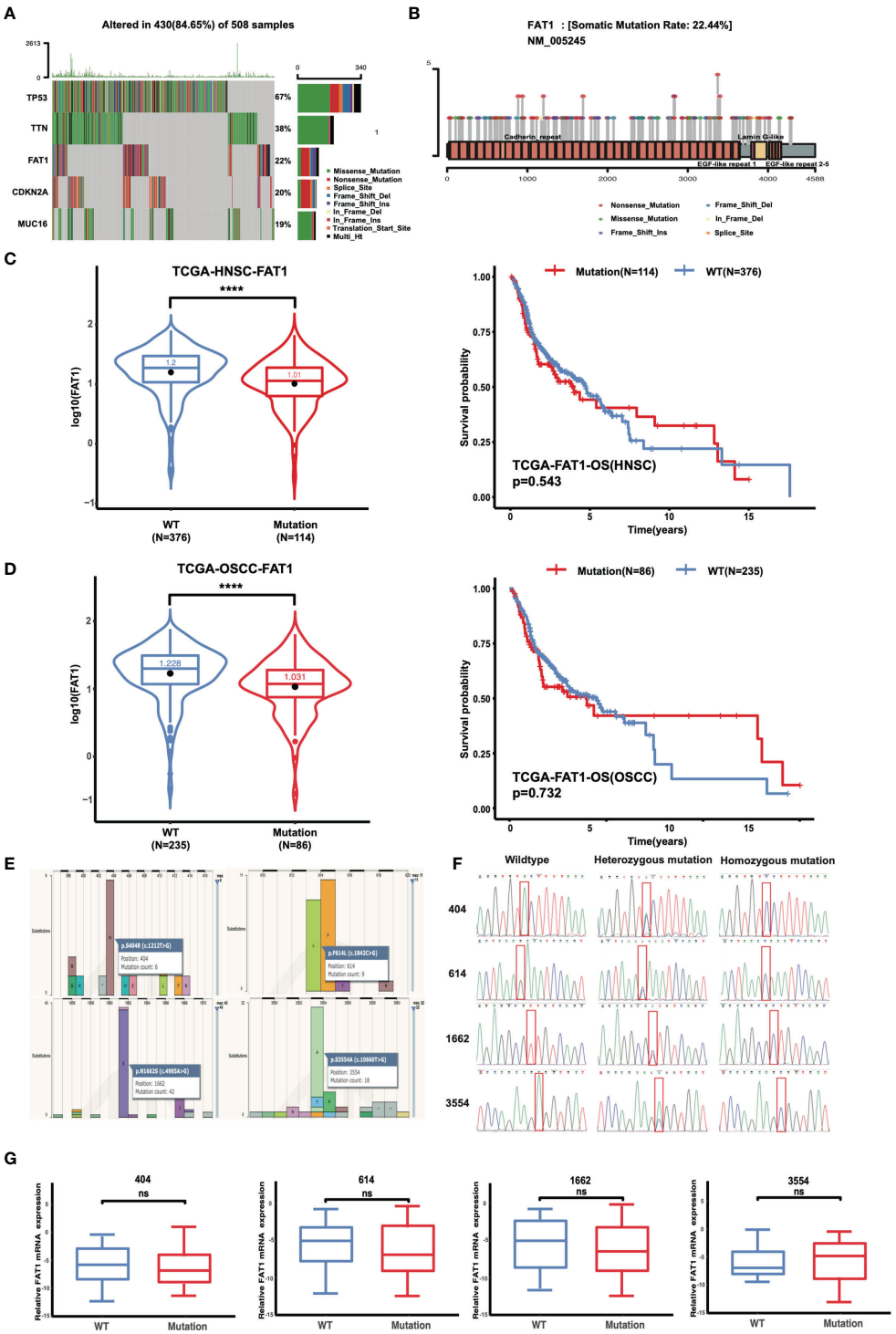

FIGURE 3 | FAT1 exhibits high genetic alterations in HNSC and FAT1 mutation status and the affection of the FAT1 expression. **(A)** FAT1 was a highly mutated gene (22%) in HNSC. **(B)** Frequency of FAT1 mutation sites in HNSC. **(C)** FAT1 mRNA expression status between FAT1 wild-type and FAT1 mutation tumor tissues in HNSC from TCGA (boxplot and violin plot); Kaplan–Meier survival curve of OS time between in HNSC FAT1 wild-type and FAT1 mutation tumor tissues from TCGA. **(D)** FAT1 mRNA expression status between FAT1 wild-type and FAT1 mutation tumor tissues in OSCC from TCGA (boxplot and violin plot); Kaplan–Meier survival curve of OS time between in OSCC FAT1 wild-type and FAT1 mutation tumor tissues from TCGA. **(E)** Four chosen sites of the FAT1 from all types of cancers in COSMIC online. **(F)** Representative image of Sanger confirmation of four variant sites. **(G)** Relative FAT1 mRNA expression status between FAT1 wild-type and FAT1 variants tumor tissues in clinical samples according to four variants sites (boxplot). ns, $P > 0.05$; ****$P < 0.0001$.

TABLE 3 | FAT1 mutation status among OSCC tissues, matched adjacent normal tissues, and leukocyte DNA of normal individuals.

Sample	Case	FAT1-404			FAT1-614			FAT1-1662			FAT1-3554		
UCSC		ACT(-)			GAA(-)			GTT(-)			AGA(-)		
Mutant		CCT(-)			CAA(-)			GCT(-)			AGC(-)		
Mutant(aa)		S404R			F614L			N1662S			S3554A		
		A/A	A/C	C/C	G/G	G/C	C/C	T/T	T/C	C/C	A/A	A/C	C/C
Tumor	58	32	24	2	10	32	16	18	29	11	10	22	25
Adjacent normal	58	31	25	2	10	32	16	18	31	8	10	23	25
Healthy control	26	17	7	2	7	14	5	5	16	5	2	9	16

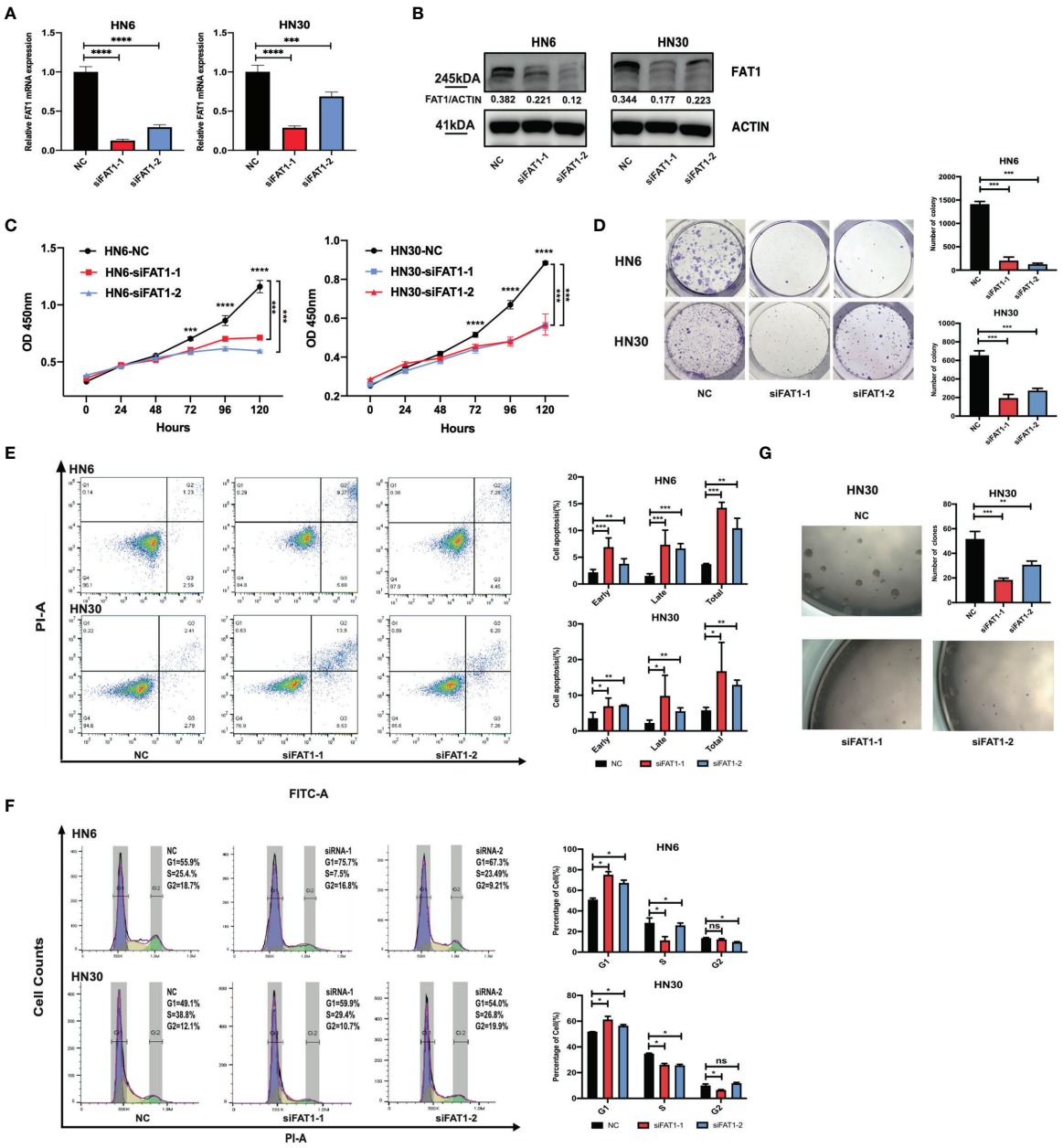

FIGURE 4 | Downregulation of FAT1 impairs OSCC proliferation, cell cycle, and stemness, and promoted cell apoptosis. FAT1 knockdown by siFAT1-1 and siFAT1-2 in both HN6 and HN30 was confirmed by qPCR **(A)** and Western blot **(B)**. FAT1 knockdown by siFAT1-1 and siFAT1-2 inhibited HN6 and HN30 cell proliferation *via* CCK8 analysis **(C)** and clone formation **(D)**, facilitated cell both early and late apoptosis **(E)**, promoted cell cycle arrest **(F)**, and suppressed the tumorsphere formation of HN30 **(G)**. *P < 0.05; **P < 0.01; ***P < 0.001; ****P < 0.0001; ns, not significant.

RNA Sequencing Indicates That FAT1 Plays an Important Role in Cell Proliferation and Activated Pathways

To delineate transcriptomic changes after suppression of FAT1 in OSCC oncogenesis, RNA sequencing was performed after FAT1 knockdown (siFAT1-1 and siFAT1-2) compared to the control group (NC) in two OSCC cells; the raw data have been deposited in the NCBI gene expression omnibus (GEO) under accession no. GSE196138 (https://www.ncbi.nlm.nih.gov/geo/query/acc.cgi?acc=GSE196138). After bioinformatic analysis, volcano plots were used to assess the variation in gene expression (**Figure 6A**). Totally, 472 differentially expressed genes were confirmed, comprising 289 upregulated and 183 downregulated using the thresholds P < 0.05 and abs (log2 fold

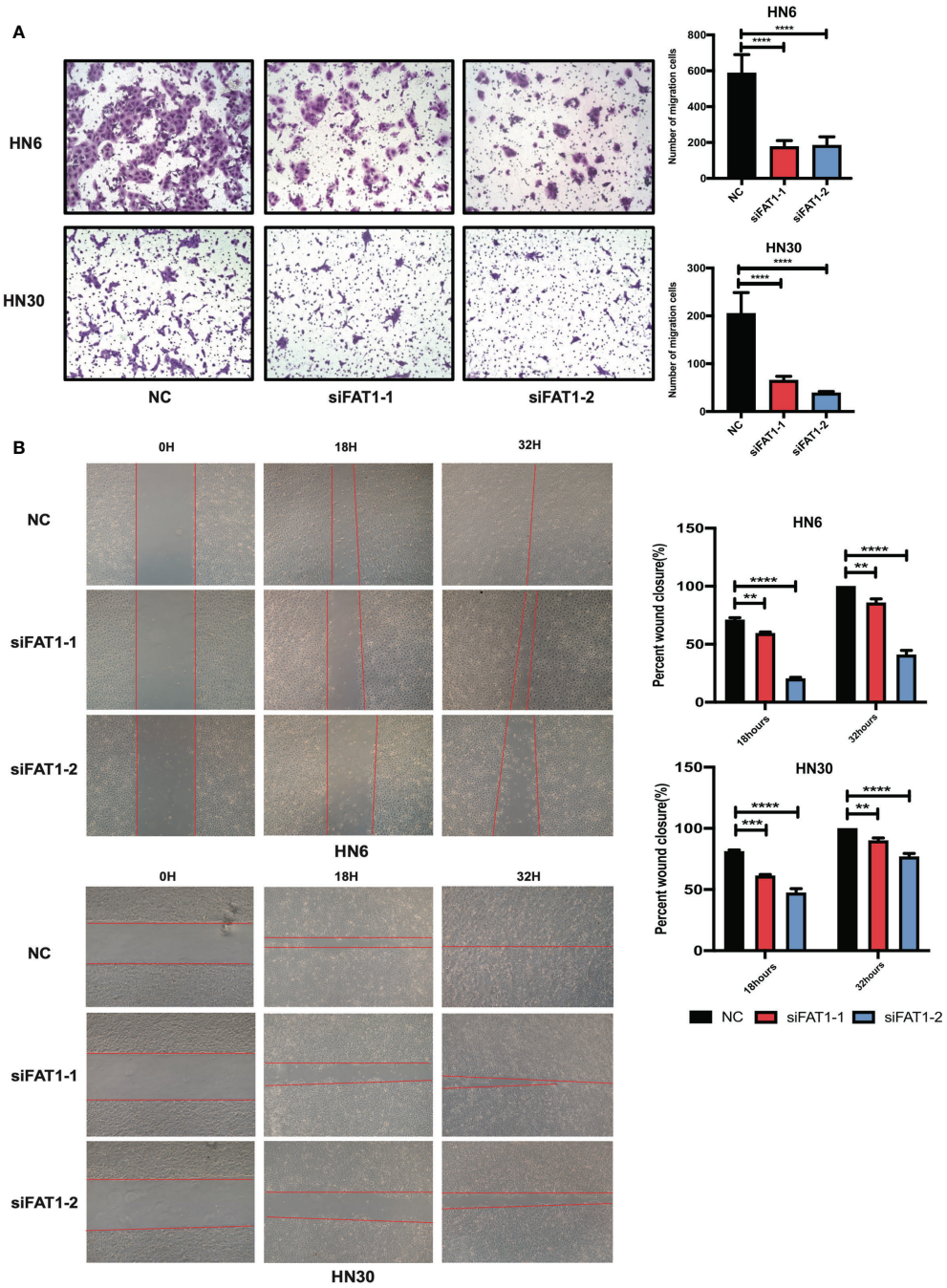

FIGURE 5 | Downregulation of FAT1 impairs migration ability of OSCC. Knockdown by siFAT1-1 and siFAT1-2 inhibited HN6 and HN30 cells migration *via* transwell chambers without Matrigel **(A)** and wound healing migration assays **(B)**. **P < 0.01; ***P < 0.001; ****P < 0.0001.

change)> 1 *via* Limma-voom methods. The heat map consisted of DEGs revealed tight clustering, separating the FAT1 KD group and the normal control group in both two cell lines into two distinct clusters (**Figure 6B**). We then performed gene-set enrichment analysis in an order of decreasing log2 fold change as a ranked gene list of all genes. Consistent with our observations *in vitro*, GO analysis reflected that the affected genes by FAT1 knockdown were involved most significantly in cell death, survival, and proliferation. We showed 5 most significantly enriched terms (according to q values or NES) from the cellular component (CC), biological process (BP), and molecular function (MF; **Figure 6C**). Kyoto Encyclopedia of Genes and Genomes analysis revealed that in addition to the signaling pathways associated with cell growth similar to the above, FAT1 KD suppressed the TNF, NF-kappa B, and IL-17 signaling pathway (**Figure 6D**). Moreover, we conducted a GSEA analysis using the hallmark gene set from the Molecular Signatures Database (mSigDB, http://software.broadinstitute.org/gsea/index.jsp) and observed that E2F targets, G2M checkpoint, TNFA signaling up NFKB, DNA repair, mitotic spindle, IL6 JAK STAT3 signaling, IL2 STAT5 signaling, and MYC targets V1 were negatively correlated with FAT1 expression (**Figure 6E**), corroborating our above findings. To validate the RNA-seq data, 13 DEGs, including 8 genes (MCM2, MCM5, CCNE1, CD83, SPC24, MYBL2, KIF2C, SUV39H1) involved in E2F targets, G2M checkpoint, TNFA signaling up NFKB, IL2 STAT5 signaling, and MYC targets V1 as core enrichment and other 5 randomly selected genes (UHRF1, PERP, TPM4, GANAB, EMC6), were determined *via* qRT-PCR analysis. The change trends were consistent with those detected *via* transcriptome sequencing (**Figure 6F**). PPI network constriction was serviced to visualize DEG protein–protein interactions. The different sizes of the nodes represented the degree of the node in the PPI network. In the network, we visualized them with different sizes of the nodes and the label represents the degree of the node of the top 30 genes which contain at least 19 nodes with related interaction genes. Blue nodes mean downregulation level while red nodes represent upregulation level (**Figure 7A**). Similarly, the enriched terms in the Gene Ontology were mainly related to the cell cycle and replication (**Figure 7B**). We focused on six hub DEGs with more than 19 nodes also involved in the pathway signaling mentioned above and determined *via* qRT-PCR analysis. The expression of MCM2, MCM5, CCNE1 SPC24, MYBL2, and KIF2C was significantly upregulated in OSCC samples (**Figure 7C**). These results implicated FAT1 as a factor mediating the growth characteristics of OSCC cells.

DISCUSSION

Oral squamous cell carcinoma is a major subset of head and neck squamous cell carcinoma, which is one of the most common malignant tumors globally with a high rate of genetic heterogeneity, resulting in loss-of-function mutations in tumor-suppressor genes and activation of oncogenes (29, 30). The studies from Morris et al. showed that the recurrent somatic mutation of FAT1 was detected in several cancer types and FAT1 mutation could result in promotion of WNT signaling in GBM pointing FAT1 to act as a tumor suppressor. There were 6 heterozygous mutations in head and neck squamous cell carcinoma (4 of 60; 6.7%), but they did not evaluate the function in OSCC cells (8). Nakaya et al. reported that FAT1 was homozygously deleted in 80% of primary oral cancer cases and FAT1 mRNA expression was repressed because of homozygous deletion and/or promoter CpG hypermethylation (31, 32). Non-synonymous FAT1 mutations have been linked to better prognosis in HPV-negative HNSC patients (33). Lin et al. reported that FAT1 mRNA and protein expression was downregulated or absent compared with that in normal oral mucosal epithelial cells in HNSC cell lines (SCC25, OECM1, FaDu, HSC3, SAS, and OC3) (18). However, research results from Hsu et al. demonstrated that FAT1 could promote the process of the tumor (22). Hence, in the present research, we first checked the expression levels of FAT1 comprehensively. Both the data from clinical specimens and the data from the public database (TCGA, GEO, and CPTAC) indicated that the expression of FAT1 was upregulated in HNSC and OSCC in both mRNA and protein levels and a high FAT1 expression level correlated with poor prognosis. In the IHC assay, we observed an upregulation of FAT1 in tumor tissues, but the survival difference did not reach statistical significance. The positive FAT1 staining which resulted for these parameters was associated with age, differentiation, metastasis, and tumor budding, indicating that FAT1 has potential for clinical pathologic diagnosis. Through AUC, both FAT1 mRNA and protein levels performed well in distinguishing tumor and normal tissues (AUC = 0.78). These results indicate that FAT1 is closely related with the neoplasia and development of HNSC and OSCC.

To advance the understanding of HNSC, the CPTAC program, which has been publicly available in 2020, has performed a comprehensive integrated proteogenomic characterization of a 109 human papilloma virus (HPV)-negative HNSC cohort (34). FAT1 is one of the most frequently mutated genes in this cohort, in which truncating mutations account for >70% of all FAT1 mutations, in sharp contrast to other cancer types. However, none of the previous studies, which have linked FAT1 mutations to the WNT and HIPPO pathways, were supported by this cohort (8, 19). Instead, an investigation of the mutually exclusive relationship between FAT1 truncating mutations and 11q13.3 amplifications revealed their functional convergence on dysregulated actin dynamics, underlying poor prognosis of tumors with these genetic aberrations (35). We also explored FAT1 protein expression levels in this cohort. FAT1 was expressed remarkably high in tumor tissues compared to normal tissues and in stage IV compared to stage I tumor tissues in the whole cohort ($P < 0.01$). Focusing on OSCCs (53/109), FAT1 protein expression was upregulated remarkably and increased in stage III and stage IV with a trend that approached statistical significance with $P = 0.069$ and $P = 0.053$. The FAT1 protein level also performed well in distinguishing tumor and normal tissues in HNSC and OSCC (AUC = 0.79 and 0.829).

Lin et al. performed multiplex polymerase chain reaction-based next-generation sequencing to indicate that approximately

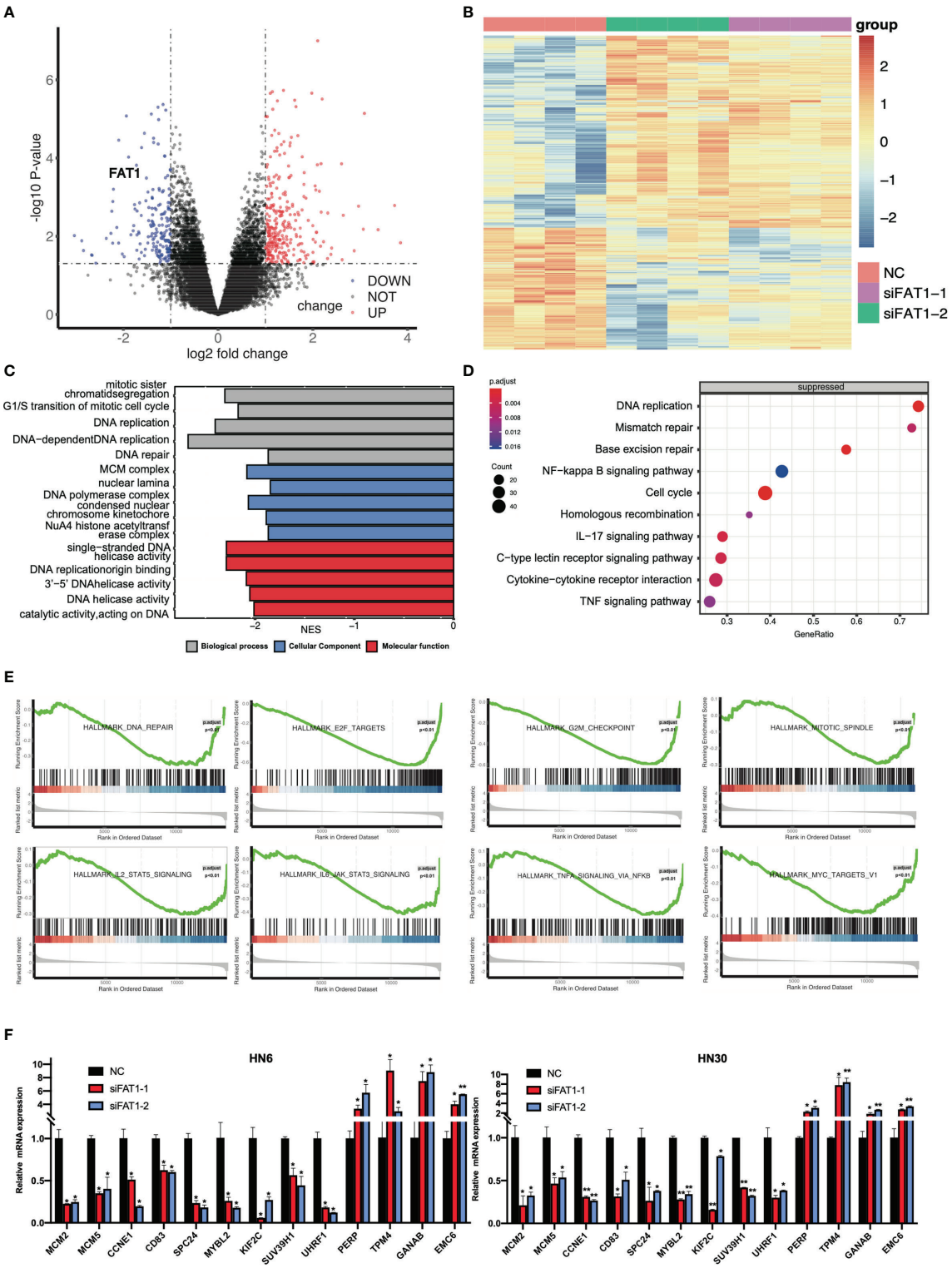

FIGURE 6 | Results of the RNA sequencing analysis and validation of DEGs. **(A)** Volcano plots of the data from RNA-seq analysis by the Limma-voom R package, presenting the differences between NC and FAT1-KD groups and plotting the log2(fold change) versus the –log10(adjusted P-value). 472 differentially expressed genes (DEGs) were confirmed, comprising 289 upregulated (red dots) and 183 downregulated (blue dots) using the thresholds $P < 0.05$ and abs (log2 fold change)> 1. **(B)** Heat map of the DEGs. **(C)** Suppressed enriched GO terms (BP, CC, and MF). **(D)** Suppressed enriched KEGG terms. **(E)** Gene set enrichment analysis (GSEA) plots of the major enriched hallmark pathway. **(F)** Validation of DEGs of RNA-seq results through quantitative PCR. *$P < 0.05$; **$P < 0.01$.

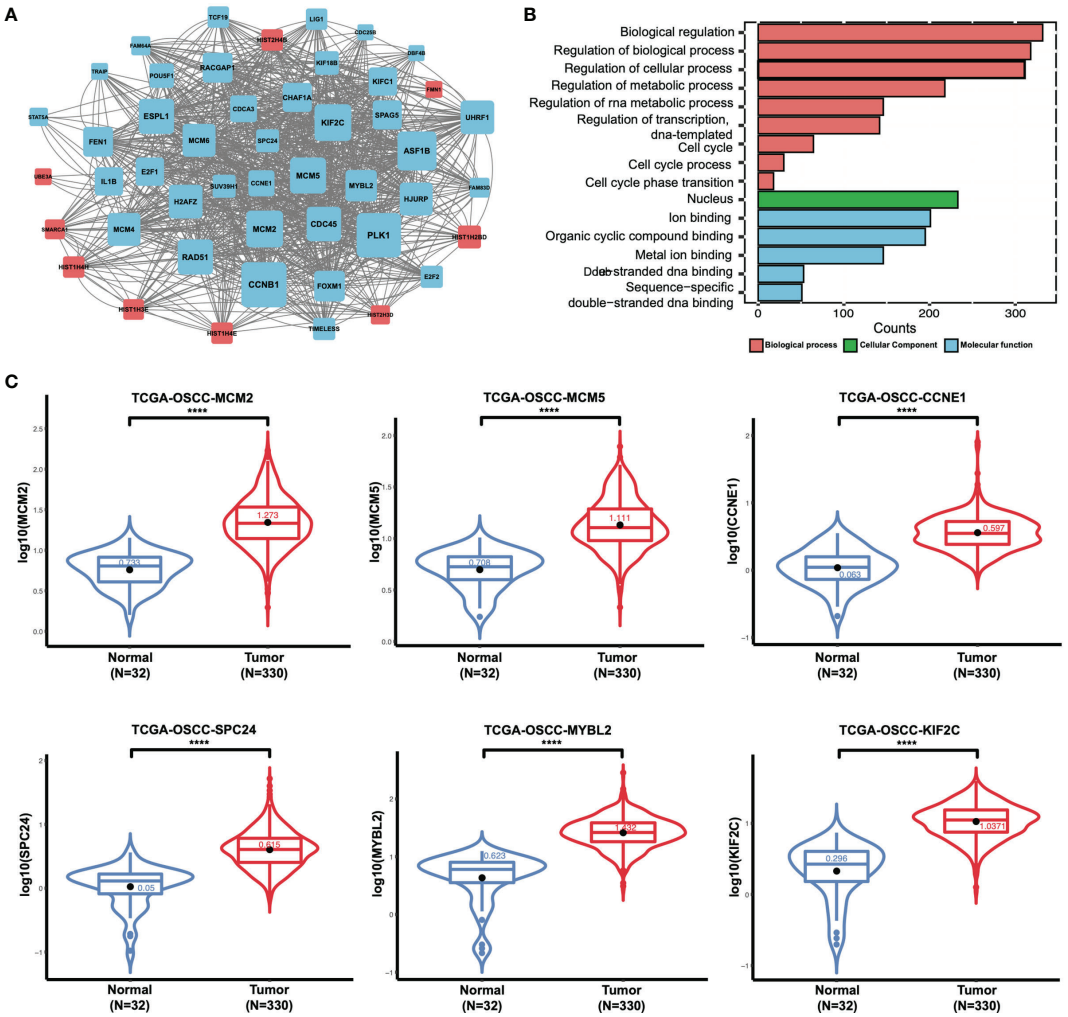

FIGURE 7 | Results of the RNA sequencing analysis and validation of DEGs. **(A)** Protein–protein interactive network of DEGs with nodes >19 and their related proteins. The different sizes of the nodes represented the degree of the node specific in the PPI network. Blue nodes mean downregulation level while red nodes represent upregulation level. **(B)** Enriched GO terms of DEGs (BP, CC, and MF). **(C)** MCM2, MCM5, CCNE1 SPC24, MYBL2, and KIF2C mRNA expression status between normal tissues and tumor tissues in OSCC from TCGA (boxplot and violin plot). ****P < 0.0001.

29% of HNSC patients harbored damaging non-synonymous FAT1 mutations, which could be prognostic indicators (18). Martin et al. conducted a pan-cancer analysis and recognized only FAT1 to be significantly mutated (19). Moreover, in a recent newly genomic analysis, FAT1 has also been identified (an early-onset OTSCC cohort, which was diagnosed before the age of 50 years, and a novel buccal mucosal cancer cell line "GBC035" derived from non-tobacco users) (36, 37). We explored FAT1 mutation status in TCGA HNSC and OSCC and demonstrated that FAT1 mutation did correlate with reduced mRNA levels but not survival outcomes in both HPV+ and HPV- patients. For 404, 614, 1,662, and 3,554, the four FAT1 hot mutation sites in all types of cancers in the COSMIC database, we observed a high mutation ratio in clinical OSCC tissues but also in matched adjacent normal tissues and leukocyte DNA of normal individuals.

Next, knocking down the FAT1 expression showed that downregulated FAT1 could inhibit tumor formation and progression by inhibiting cell proliferation, stemness, and cell cycle and promoting the apoptosis. Furthermore, the ability of migration was suppressed by FAT1 silencing. The analysis of RNA-seq constructed by FAT1 knockdown (siFAT1-1 and siFAT1-2) compared to the control group supported FAT1 as a factor mediating the growth characteristics of OSCC cells through DNA repair, cell cycle, DNA repair, and other signaling pathways, which were pivotal mechanisms influencing cell proliferation, cycle, apoptosis, and migration. GSEA analyses reflect processes or pathways affected by FAT1 downregulation, e.g., those related to cellular proliferation (E2F targets, G2M checkpoint, TNFA signaling up NFKB, mitotic spindle, IL6 JAK STAT3 signaling, IL2 STAT5 signaling, and MYC targets) and the DNA damage responses. We further focused on six of the most important DEGs

(MCM2, MCM5, CCNE1 SPC24, MYBL2, KIF2C), which were involved in the above pathway that may exert a regulatory function in OSCC with a significant upregulation expression level in TCGA as well as the hub genes in the PPI network with DEGs. Their downregulation with FAT1 silencing was proved by qPCR. As a result, additional focus on the molecular mechanism of the six hub genes in OSCC is warranted. However, it still lacked experimental exploration of assumed FAT1-related genes to validate our speculations. The study of Lin et al. disagreed with ours, and we carefully attributed this to the genetic heterogeneity that reflected the complicated constitution of different HNSC cells (18). Otherwise, our findings of FAT1, partly corroborated by data of HSC-3 and SAS of Hsu et al., showed two human squamous carcinomas of the tongue cells which exhibited high lymph node metastasis potential and poor differentiation status (38). Hsu et al. found that FAT1 played a role in the regulation of oral carcinogenesis and cisplatin resistance through deregulation of the LRP5/WNT2/GSS signaling axis (22). Therefore, our current study provided a reason for FAT1 to jump out of its classic role as a tumor suppressor by featuring its oncogenic properties mainly *via* cellular proliferation and repair.

CONCLUSIONS

In summary, we illuminated that FAT1 was upregulated in OSCC and correlated with a poor survival and disease progression. No relationship was observed between the variants of these loci (404, 614, 1,662, and 3,554) and tumorigenesis or FAT1 expression. We found that FAT1 could promote OSCC cell proliferation, cell cycle, and migration and inhibit cell apoptosis in an *in vitro* experiment. RNA-seq analysis of FAT1 silencing revealed that the cell cycle, DNA replication, and some core genes (MCM2, MCM5, CCNE1 SPC24, MYBL2, KIF2C) may be the potential mechanisms in OSCC, which was consistent with the *in vitro* phenotype experiments. Therefore, these findings provided new insight into the role of FAT1 as an oncogene and its more potential mechanisms.

DATA AVAILABILITY STATEMENT

The datasets presented in this study can be found in online repositories. The names of the repository/repositories and accession number(s) can be found as follows: https://www.ncbi.nlm.nih.gov/geo/query/acc.cgi?acc=GSE196138.

ETHICS STATEMENT

The studies involving human participants were reviewed and approved by Fujian Medical University School and Hospital of Stomatology. The patients/participants provided their written informed consent to participate in this study.

AUTHOR CONTRIBUTIONS

DZ and YL presented the study concepts. TL, DZ, and YL designed this study. TL, QG, KZ, LH, and YY were in charge of the data acquisition. TL, QG, and KZ controlled the quality of data and algorithms. TL, QG, and LZ analyzed and interpreted the data. TL, LZ, and DZ performed the statistical analysis. TL, LZ, and DZ wrote the first draft of the manuscript. All authors contributed to the manuscript revision and read and approved the submitted version.

FUNDING

This work was supported by the National Natural Sciences Foundation of China (grant number 81872186), grants from Joint Funds for the Innovation of Science and Technology, Fujian province (grant number: 2019Y9112), Natural Sciences Foundation of Fujian Province (grant number: 2019J01318), and scientific research funding of the School and Hospital of Stomatology, Fujian Medical University (grant number: 2018KQYJ01). The funding bodies had no role in the design of the study and collection, analysis, and interpretation of data and in writing of the manuscript.

SUPPLEMENTARY MATERIAL

The Supplementary Material for this article can be found online at: https://www.frontiersin.org/articles/10.3389/fonc.2022.870055/full#supplementary-material

REFERENCES

1. Adelstein D, Gillison ML, Pfister DG, Spencer S, Adkins D, Brizel DM, et al. NCCN Guidelines Insights: Head and Neck Cancers, Version 2. 2017. *J Natl Compr Cancer Netw* (2017) 15(6):761–70. doi: 10.6004/jnccn.2017.0101
2. Leemans CR, Braakhuis BJM, Brakenhoff RH. The Molecular Biology of Head and Neck Cancer. *Nat Rev Cancer* (2010) 11(1):9–22. doi: 10.1038/nrc2982
3. Campbell KM, Lin T, Zolkind P, Barnell EK, Skidmore ZL, Winkler AE, et al. Oral Cavity Squamous Cell Carcinoma Xenografts Retain Complex Genotypes and Intertumor Molecular Heterogeneity. *Cell Rep* (2018) 24 (8):2167–78. doi: 10.1016/j.celrep.2018.07.058
4. Kalu NN, Mazumdar T, Peng S, Shen L, Sambandam V, Rao X, et al. Genomic Characterization of Human Papillomavirus-Positive and -Negative Human Squamous Cell Cancer Cell Lines. *Oncotarget* (2017) 8(49):86369–83. doi: 10.18632/oncotarget.21174
5. Sadeqzadeh E, de Bock CE, Thorne RF. Sleeping Giants: Emerging Roles for the Fat Cadherins in Health and Disease. *Medicinal Res Rev* (2013) 34(1):190–221. doi: 10.1002/med.21286
6. Dunne J, Hanby AM, Poulsom R, Jones TA, Sheer D, Chin WG, et al. Molecular Cloning and Tissue Expression of FAT, the Human Homologue of the Drosophila Fat Gene That Is Located on Chromosome 4q34–Q35 and Encodes a Putative Adhesion Molecule. *Genomics* (1995) 30(2):207–23. doi: 10.1006/geno.1995.9884
7. Yaoita E, Kurihara H, Yoshida Y, Inoue T, Matsuki A, Sakai T, et al. Role of Fat1 in Cell-Cell Contact Formation of Podocytes in Puromycin Aminonucleoside Nephrosis and Neonatal Kidney. *Kidney Int* (2005) 68(2):542–51. doi: 10.1111/j.1523-1755.2005.00432.x

8. Morris LGT, Kaufman AM, Gong Y, Ramaswami D, Walsh LA, Turcan Ş, et al. Recurrent Somatic Mutation of FAT1 in Multiple Human Cancers Leads to Aberrant Wnt Activation. *Nat Genet* (2013) 45(3):253–61. doi: 10.1038/ng.2538
9. Li Z, Razavi P, Li Q, Toy W, Liu B, Ping C, et al. Loss of the FAT1 Tumor Suppressor Promotes Resistance to CDK4/6 Inhibitors *via* the Hippo Pathway. *Cancer Cell* (2018) 34(6):893–905.e8. doi: 10.1016/j.ccell.2018.11.006
10. Wang L, Lyu S, Wang S, Shen H, Niu F, Liu X, et al. Loss of FAT1 During the Progression From DCIS to IDC and Predict Poor Clinical Outcome in Breast Cancer. *Exp Mol Pathol* (2016) 100(1):177–83. doi: 10.1016/j.yexmp.2015.12.012
11. Wang Y, Wang G, Ma Y, Teng J, Wang Y, Cui Y, et al. FAT1, a Direct Transcriptional Target of E2F1, Suppresses Cell Proliferation, Migration and Invasion in Esophageal Squamous Cell Carcinoma. *Chin J Cancer Res* (2019) 31(4):609–19. doi: 10.21147/j.issn.1000-9604.2019.04.05
12. Lu Y, Wang Z, Zhou L, Ma Z, Zhang J, Wu Y, et al. FAT1 and PTPN14 Regulate the Malignant Progression and Chemotherapy Resistance of Esophageal Cancer Through the Hippo Signaling Pathway. *Anal Cell Pathol* (2021) 2021:1–9. doi: 10.1155/2021/9290372
13. Yu J, Li H. The Expression of FAT1 Is Associated With Overall Survival in Children With Medulloblastoma. *Tumori J* (2016) 103(1):44–52. doi: 10.5301/tj.5000570
14. De Bock CE, Ardjmand A, Molloy TJ, Bone SM, Johnstone D, Campbell DM, et al. The Fat1 Cadherin Is Overexpressed and an Independent Prognostic Factor for Survival in Paired Diagnosis–Relapse Samples of Precursor B-Cell Acute Lymphoblastic Leukemia. *Leukemia* (2011) 26(5):918–26. doi: 10.1038/leu.2011.319
15. Neumann M, Seehawer M, Schlee C, Vosberg S, Heesch S, von der Heide EK, et al. FAT1 Expression and Mutations in Adult Acute Lymphoblastic Leukemia. *Blood Cancer J* (2014) 4(6):e224. doi: 10.1038/bcj.2014.44
16. Valletta D, Czech B, Spruss T, Ikenberg K, Wild P, Hartmann A, et al. Regulation and Function of the Atypical Cadherin FAT1 in Hepatocellular Carcinoma. *Carcinogenesis* (2014) 35(6):1407–15. doi: 10.1093/carcin/bgu054
17. Meng P, Zhang Y-F, Zhang W, Chen X, Xu T, Hu S, et al. Identification of the Atypical Cadherin FAT1 as a Novel Glypican-3 Interacting Protein in Liver Cancer Cells. *Sci Rep* (2021) 11(1):40. doi: 10.1038/s41598-020-79524-3
18. Lin S-C, Lin L-H, Yu S-Y, Kao S-Y, Chang K-W, Cheng H-W, et al. FAT1 Somatic Mutations in Head and Neck Carcinoma Are Associated With Tumor Progression and Survival. *Carcinogenesis* (2018) 39(11):1320–30. doi: 10.1093/carcin/bgy107
19. Martin D, Degese MS, Vitale-Cross L, Iglesias-Bartolome R, Valera JLC, Wang Z, et al. Assembly and Activation of the Hippo Signalome by FAT1 Tumor Suppressor. *Nat Commun* (2018) 9(1):2372. doi: 10.1038/s41467-018-04590-1
20. Dikshit B, Irshad K, Madan E, Aggarwal N, Sarkar C, Chandra PS, et al. FAT1 Acts as an Upstream Regulator of Oncogenic and Inflammatory Pathways, *via* PDCD4, in Glioma Cells. *Oncogene* (2012) 32(33):3798–808. doi: 10.1038/onc.2012.393
21. Madan E, Dikshit B, Gowda SH, Srivastava C, Sarkar C, Chattopadhyay P, et al. FAT1 Is a Novel Upstream Regulator of HIF1α and Invasion of High Grade Glioma. *Int J Cancer* (2016) 139(11):2570–82. doi: 10.1002/ijc.30386
22. Hsu TN, Huang CM, Huang CS, Huang MS, Yeh CT, Chao TY, et al. Targeting FAT1 Inhibits Carcinogenesis, Induces Oxidative Stress and Enhances Cisplatin Sensitivity Through Deregulation of LRP5/WNT2/GSS Signaling Axis in Oral Squamous Cell Carcinoma. *Cancers* (2019) 11(12):1883. doi: 10.3390/cancers11121883
23. Colaprico A, Silva TC, Olsen C, Garofano L, Cava C, Garolini D, et al. TCGAbiolinks: An R/Bioconductor Package for Integrative Analysis of TCGA Data. *Nucleic Acids Res* (2015) 44(8):e71. doi: 10.1093/nar/gkv1507
24. Anand M, De-Chen L, Yassen A, Christoph P, Phillip KH. Maftools: Efficient and Comprehensive Analysis of Somatic Variants in Cancer. *Genome Res* (2018) 28(11):1747–56. doi: 10.1101/gr.239244.118
25. Zheng K, Lan T, Li G, Huang L, Chen Y, Su BH, et al. Evaluated Expression of CELSR3 in Oral Squamous Cell Carcinoma Is Associated With Perineural Invasion and Poor Prognosis. *Oral Surg Oral Med Oral Pathol Oral Radiol* (2021) S2212-4403(21)00714-8. doi: 10.1016/j.oooo.2021.10.016
26. Cappuzzo F, Hirsch FR, Rossi E, Bartolini S, Ceresoli GL, Bemis L, et al. Epidermal Growth Factor Receptor Gene and Protein and Gefitinib Sensitivity in Non–Small-Cell Lung Cancer. *J Natl Cancer Institute* (2005) 97(9):643–55. doi: 10.1093/jnci/dji112
27. Ritchie ME, Phipson B, Wu D, Hu Y, Law CW, Shi W, et al. Limma Powers Differential Expression Analyses for RNA-Sequencing and Microarray Studies. *Nucleic Acids Res* (2015) 43(7):e47. doi: 10.1093/nar/gkv007
28. Wu T, Hu E, Xu S, Chen M, Guo P, Dai Z, et al. ClusterProfiler 4.0: A Universal Enrichment Tool for Interpreting Omics Data. *Innovation* (2021) 2(3):100141. doi: 10.1016/j.xinn.2021.100141
29. Kemmer JD, Johnson DE, Grandis JR. Leveraging Genomics for Head and Neck Cancer Treatment. *J Dental Res* (2018) 97(6):603–13. doi: 10.1177/0022034518756352
30. Alsahafi E, Begg K, Amelio I, Raulf N, Lucarelli P, Sauter T, et al. Clinical Update on Head and Neck Cancer: Molecular Biology and Ongoing Challenges. *Cell Death Dis* (2019) 10(8):540. doi: 10.1038/s41419-019-1769-9
31. Katoh M. Function and Cancer Genomics of FAT Family Genes. *Int J Oncol* (2012) 41(6):1913–8. doi: 10.3892/ijo.2012.1669
32. Nakaya K, Yamagata HD, Arita N, Nakashiro K, Nose M, Miki T, et al. Identification of Homozygous Deletions of Tumor Suppressor Gene FAT in Oral Cancer Using CGH-Array. *Oncogene* (2007) 26(36):5300–8. doi: 10.1038/sj.onc.1210330
33. Kim KT, Kim B-S, Kim JH. Association Between FAT1 Mutation and Overall Survival in Patients With Human Papillomavirus-Negative Head and Neck Squamous Cell Carcinoma. *Head Neck* (2016) 38(S1):E2021–9. doi: 10.1002/hed.24372
34. Mertins P, Tang LC, Krug K, Clark DJ, Gritsenko MA, Chen L, et al. Reproducible Workflow for Multiplexed Deep-Scale Proteome and Phosphoproteome Analysis of Tumor Tissues by Liquid Chromatography–Mass Spectrometry. *Nat Protoc* (2018) 13(7):1632–61. doi: 10.1038/s41596-018-0006-9
35. Huang C, Chen L, Savage SR, Eguez RV, Dou Y, Li Y, et al. Proteogenomic Insights Into the Biology and Treatment of HPV-Negative Head and Neck Squamous Cell Carcinoma. *Cancer Cell* (2021) 39(3):361–9. e16. doi: 10.1016/j.ccell.2020.12.007
36. Campbell BR, Chen Z, Faden DL, Agrawal N, Li RJ, Hanna GJ, et al. The Mutational Landscape of Early- and Typical-Onset Oral Tongue Squamous Cell Carcinoma. *Cancer* (2020) 127(4):544–53. doi: 10.1002/cncr.33309
37. Vipparthi K, Patel AK, Ghosh S, Das S, Das C, Das K, et al. Two Novel Cell Culture Models of Buccal Mucosal Oral Cancer From Patients With No Risk-Habits of Tobacco Smoking or Chewing. *Oral Oncol* (2021) 113:105131. doi: 10.1016/j.oraloncology.2020.105131
38. Matsui T, Ota T, Ueda Y, Tanino M, Odashima S. Isolation of a Highly Metastatic Cell Line to Lymph Node in Human Oral Squamous Cell Carcinoma by Orthotopic Implantation in Nude Mice. *Oral Oncol* (1998) 34(4):253–6. doi: 10.1016/S1368-8375(98)80003-1

Conflict of Interest: The authors declare that the research was conducted in the absence of any commercial or financial relationships that could be construed as a potential conflict of interest.

frontiers | Frontiers in Oncology

ORIGINAL RESEARCH
published: 16 May 2022
doi: 10.3389/fonc.2022.870935

A Clinical-Radiomics Nomogram Based on the Apparent Diffusion Coefficient (ADC) for Individualized Prediction of the Risk of Early Relapse in Advanced Sinonasal Squamous Cell Carcinoma: A 2-Year Follow-Up Study

*Naier Lin†, Sihui Yu†, Mengyan Lin†, Yiqian Shi, Wei Chen, Zhipeng Xia, Yushu Cheng and Yan Sha**

Department of Radiology, Eye & ENT Hospital, Shanghai Medical College, Fudan University, Shanghai, China

OPEN ACCESS

Edited by:
Narayana Subramaniam, Sri Shankara Cancer Research Foundation, India

Reviewed by:
Xiaofeng Tao, Shanghai Jiao Tong University, China
Zhongxiang Ding, Zhejiang University, China

***Correspondence:**
Yan Sha
yanshavip@yeah.net

†These authors have contributed equally to this work

Specialty section:
This article was submitted to Head and Neck Cancer, a section of the journal Frontiers in Oncology

Received: *07 February 2022*
Accepted: *19 April 2022*
Published: *16 May 2022*

Citation:
Lin N, Yu S, Lin M, Shi Y, Chen W, Xia Z, Cheng Y and Sha Y (2022) A Clinical-Radiomics Nomogram Based on the Apparent Diffusion Coefficient (ADC) for Individualized Prediction of the Risk of Early Relapse in Advanced Sinonasal Squamous Cell Carcinoma: A 2-Year Follow-Up Study. Front. Oncol. 12:870935. doi: 10.3389/fonc.2022.870935

Purpose: To develop and validate a nomogram model combining radiomic features and clinical characteristics to preoperatively predict the risk of early relapse (ER) in advanced sinonasal squamous cell carcinomas (SNSCCs).

Methods: A total of 152 SNSCC patients (clinical stage III-IV) who underwent diffusion-weighted imaging (DWI) were included in this study. The training cohort included 106 patients assessed at the headquarters of our hospital using MR scanner 1. The testing cohort included 46 patients assessed at the branch of our hospital using MR scanner 2. Least absolute shrinkage and selection operator (LASSO) regression was applied for feature selection and radiomic signature (radscore) construction. Multivariable logistic regression analysis was applied to identify independent predictors. The performance of the model was evaluated using the area under the receiver operating characteristic curve (AUC), calibration curve and decision curve analysis (DCA). Furthermore, the patients were classified into high- or low-risk ER subgroups according to the optimal cutoff value of the nomogram using X-tile. The recurrence-free survival probability (RFS) of each subgroup was assessed.

Results: ER was noted in 69 patients. The radscore included 8 selected radiomic features. The radscore, T stage and surgical margin were independent predictors. The nomogram showed better performance (AUC = 0.92) than either the radscore or the clinical factors in the training cohort ($P < 0.050$). In the testing cohort, the nomogram showed better performance (AUC = 0.92) than the clinical factors ($P = 0.016$) and tended to show better performance than the radscore ($P = 0.177$). The nomogram demonstrated good calibration and clinical utility. Kaplan-Meier analysis showed that the 2-year RFS rate

for low-risk patients was significantly greater than that for high-risk patients in both the training and testing cohorts ($P < 0.001$).

Conclusions: The ADC-based radiomic nomogram model is potentially useful in predicting the risk of ER in advanced SNSCCs.

Keywords: sinonasal cancer, recurrence, apparent diffusion coefficient, radiomics, nomogram

INTRODUCTION

Malignancies involving the sinonasal tract are uncommon, accounting for approximately 3%–5% of all head and neck malignancies (1). Among the histological varieties of malignancies, the most common primary cancer is sinonasal squamous cell carcinoma (SNSCC) (2). SNSCC typically presents with nonspecific symptoms at an advanced stage with involvement of adjacent structures such as the infratemporal fossa, skull base and orbit (3), potentially resulting in the incomplete resection of the whole tumor and positive surgical margins. Thus, a high frequency of local failure and recurrence is observed (4).

Tumor-node-metastasis (TNM) staging is one of the most important prognostic factors guiding the treatment options for SNSCC patients. However, due to highly heterogeneous tumor biology, clinical outcomes may be completely different even in patients with the same stage of disease. To date, the identification of more reliable markers to facilitate individualized prediction of the risk of early relapse (ER), particularly in advanced SNSCC, is urgently needed.

Over the last few years, radiomics has become a research hotspot. It allows the extraction of a large number of image features of the total tumor, which can highlight the heterogeneity and characteristics of the tumor by acting as a whole tumor virtual biopsy. Recently, a few studies revealed that radiomics based on images combined with clinical factors could aid in improving the accuracy of recurrence prediction in several cancers, such as nasopharyngeal carcinoma (5), gastric cancer (6) and hepatocellular carcinoma (7). However, in these studies, the features were all extracted from computed tomography (CT) images, the soft tissue resolution of which was lower than that of MRI. To date, of the available studies, only a few studies (8–10) have focused on the application of radiomics in sinonasal tumors, and most of them have exclusively focused on its use for differential diagnosis.

Diffusion weighted imaging (DWI) can reflect the random movement of molecules of water at the cellular level. With better characterization of tissues, apparent diffusion coefficient (ADC) values calculated from DWI have been increasingly used in sinonasal lesions and shown to be a promising biomarker to discriminate benign from malignant tumors as well as to identify different histopathological types of sinonasal malignancies (11). However, at present, the usefulness of a clinical-radiomics nomogram based on ADC images for predicting the recurrence and survival state in advanced SNSCC patients preoperatively has not been developed.

Thus, using different MR devices, the current study was conducted to explore whether an ADC-based nomogram combining the radiomic signature (radscore) with clinical factors can predict ER in patients with advanced SNSCC.

PATIENTS AND MATERIALS

Patients

A total of 152 patients (115 male, 37 females; age range, 17-84 years; mean, 55.41±14.59 years) with histologically confirmed SNSCC who visited our hospital between December 2013 and October 2019 were enrolled. The SNSCC patients were at an advanced stage, i.e., American Joint Committee on Cancer (AJCC) stage (7^{th} edition) III-IV. All patients underwent surgical treatment with transnasal endoscopic resection or open surgical resection. A total of 145 patients (95.4%) were treated with radiotherapy, including the 3D conformal radiotherapy (3D-CRT) technique or intensity-modulated radiotherapy (IMRI). Adjuvant chemotherapy prior to or after surgery was performed in 31 patients (20.4%). The patients were divided into two cohorts. The training cohort included patients assessed in the headquarters of our hospital using MR scanner 1, and the independent external testing cohort consisted of patients assessed at a branch of our hospital using MR scanner 2. The follow-up time in all patients was 24 months. The patients who experienced relapse within 2 years were defined as the ER cohort, whereas patients who did not experience relapse within 2 years were classified as the nonearly recurrence (NER) cohort. Recurrence-free survival probability (RFS) was calculated from the day after treatment to the date of relapse, death from any cause, or last follow-up (24 months). The Institutional Review Board of our hospital approved this retrospective study, and informed consent was obtained from all patients.

Image Acquisition, Segmentation and Feature Extraction

Preoperative sinonasal MRI scans including axial DWI within half a month prior to the operation. MR scanner 1 was applied in the training cohort (Magnetom Verio; 3.0 T, Siemens Healthcare, Erlangen, Germany) with a 12-channel head and neck coil, and MR scanner 2 was applied in the testing cohort (Magnetom Prisma; 3.0 T, Siemens Healthcare, Erlangen, Germany) with a 64-channel head and neck coil. DWI was performed using the readout-segmented echo-planar diffusion weighted imaging (RESOLVE-DWI).This high-resolution DWI system can offer a higher image quality than conventional DWI and reduce the

disturbance from surrounding bones and air. The parameters for DWI were as follows: TR/TE = 4700/66 ms (scanner 1), 3000/56 ms (scanner 2), b values = 0, 1000 s/mm^2 (scanner 1 and scanner 2); thickness = 3 mm (scanner 1) and 5mm (scanner 2); number of segments = 5 and field of view (FOV) = 230 × 230 mm^2 (scanner 1 and scanner 2). ADC maps were automatically derived from DWI images. The exclusion criteria were as follows: (a) patients who had received therapy before MRI examination; (b) missing information on clinicopathological variable and (c) insufficient lesion size or image quality for diagnosis.

The radiomics workflow is displayed in **Figure 1**.

Image segmentation was performed independently by 2 diagnostic radiologists with over 10 years of experience in radiology using the "Segment Editor" module of the software program 3D Slicer (version 4.8.1). The 3-dimensional regions of interest (ROIs) were outlined slice by slice on the ADC maps to cover the whole tumor with reference to T2WI and contrast-enhanced images avoiding the obvious necrosis and cystic areas within the tumor. Radiomic features were extracted with the "Radiomics" module and classified as (a) shape features; (b) first-order features; (c) texture features; and (d) wavelet-based features. The texture features included the gray level dependence matrix (GLDM), gray level cooccurrence matrix (GLCM), gray level run length matrix (GLRLM), gray level size zone matrix (GLSZM), and neighboring gray tone difference matrix (NGTDM). The inter-operator variability of the radiomic features was assessed with the intraclass correlation coefficient (ICC). Features with ICCs > 0.75 were included in subsequent analysis.

Radiomics Feature Selection and Construction of the Radiomics Signature

All radiomic features were normalized (Z-score transformation) to improve the comparability of the data. Then, we used the least absolute shrinkage and selection operator (LASSO) logistic regression model and 7-fold cross-validation to select the most valuable features based on the training set and build the Radiomics Signature (radscore). A formula was generated using a linear combination of selected features that were weighted by respective coefficients. The radscore was computed according to the formula.

Construction and Validation of the Nomogram

Multivariable logistic regression analysis was applied in the training group based on the following candidate factors: age, sex, smoking history, origin type, lateral location, maximum diameter, T stage, N stage, M stage, surgical margin and radiomic signature. Factors with P <0.050 were included in the nomogram as clinical predictors of tumor ER.

We compared the predictive performances of the radscore, clinical factors and nomogram model using the area under the curve (AUC) of the receiver operating characteristic curve (ROC). Then, the calibration curve accompanied by the Hosmer-Lemeshow test was used to evaluate the accuracy of the nomogram model. Decision curve analysis (DCA) of the nomogram was applied to summarize the clinical value.

Furthermore, the patients were classified into high- or low-risk ER subgroups according to the optimal cutoff value of the nomogram using X-tile. The RFSs of high- and low-risk ER subgroups were assessed in both the training and testing cohorts using Kaplan-Meier survival analysis.

Statistical Analysis

SPSS (version 23.0), Medcal (version 19.0) and R software (version 4.0) were used to perform the statistical analysis. LASSO regression, nomogram generation, calibration curve calculation, and DCA were conducted with the R packages "glmnet", "rms" and "dca.r" packages, respectively. Student's *t test* and the Mann-Whitney U test were used to compare continuous variables with normal and abnormal distributions, respectively. Categorical variables were assessed using the chi-square (χ^2) test.

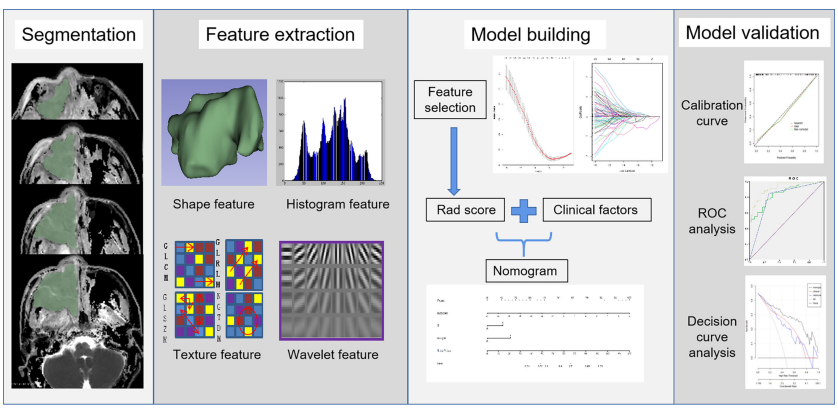

FIGURE 1 | Flowchart of radiomics for predicting the risk of ER in this study.

Here, X-tile software was used (version 3.6.1) to determine the optimal cutoff value of the nomogram and to divide the patients into high- and low-risk subgroups. RFS was calculated using the Kaplan-Meier method. *P* value < 0.050 was considered statistically significant.

RESULTS

In our study, there were 39 cases of AJCC stage III and 113 cases of stage IV (IVa: 75 cases, IVb: 31 cases, IVc: 7 cases). Sixty-nine patients relapsed within 2 years and local recurrence was the main reason among them. **Table 1** shows the characteristics of patients in both cohorts. No significant differences in the presence of ER (P = 0.755), patient age (P = 0.361), sex (P = 0.623), smoking rate (P = 0.703), lesion laterality (P = 0.633), maximum lesion diameter (P = 0.392), origin type (P = 0.118), T stage (P = 0.966), N stage (P = 0.317), M stage (P = 0.459) or surgical margin (P = 0.130) were noted between the two cohorts.

A total of 850 radiomic features were extracted from the ROIs. After the reproducibility analysis, we derived 768 features with ICC>0.75. Based on LASSO regression, these 768 features were reduced to 8 optimal features **(Figure 2)**. Then, we used the 8 radiomic features with nonzero coefficients to construct the radscore as follows:

$$\begin{aligned}\text{Radscore} &= 1.497 \times \text{waveletHLH\_firstorder\_Skewness} - \\ &\quad 0.123 \times \text{waveletHHH\_gldm\_DependenceVariance(DV)} \\ &\quad - 0.001 \times \text{waveletLHH\_firstorder\_90Percentile} \\ &\quad + 0.002 \times \text{waveletLHL\_firstorder\_Maximum} \\ &\quad + 0.195 \times \text{waveletHLL\_firstorder\_Kurtosis} \\ &+ 21.01 \times \text{original\_gldm\_DependenceNonUniformityNormalized(DNUN)} \\ &\quad - 8.176 \times \text{original\_gldm\_SmallDependenceEmphasis(SDE)} \\ &\quad - 4.088 \times \text{original\_shape\_Flatness} - 3.433\end{aligned}$$

ER SNSCC lesions had significantly higher radscore values than NER SNSCCs in both cohorts (P < 0.001).

Based on univariate analysis, the clinical T stage and surgical margin were found to be clinical risk factors for ER in SNSCCs. Based on logistic regression analysis, the radscore and clinical risk factors (including T-stage and surgical margin) were incorporated into the nomogram as independent predictors of ER (**Figure 3**).

Table 2 and **Figure 4** show the differential ability of the clinical factors (T stage and surgical margin), radscore and

TABLE 1 | Characteristics of patients in the training and testing cohorts.

Characteristic	Training Cohort (n = 106)			Testing Cohort (n = 46)		
	NER (n = 57)	ER (n = 49)	*P*	NER (n = 26)	ER (n = 20)	*P*
Age, No. (%)			0.131			0.917
≥55years old	34 (59.6%)	22 (44.9%)		16 (61.5%)	8 (40.0%)	
< 55 years old	23 (40.4%)	27 (55.1%)		10 (38.5%)	12 (60.0%)	
Gender			0.270			0.239
Female	17 (29.8%)	10 (20.4%)		4 (15.4%)	6 (30.0%)	
Male	40 (70.2%)	39 (79.6%)		22 (84.6%)	14 (70.0%)	
Smoking			0.210			0.088
Yes	21 (36.8%)	24 (49.0%)		13 (50.0%)	5 (25.0%)	
No	36 (63.2%)	25 (51.0%)		13 (50.0%)	15 (75.0%)	
Origin type			0.980			0.479
DN-SCC	42 (73.7%)	36 (73.5%)		17 (65.4%)	11 (55.0%)	
IP-SCC	15 (26.3%)	13 (26.5%)		9 (34.6%)	9 (45.0%)	
Lesion laterality			0.185			0.224
Unilateral	49 (86.0%)	46 (93.9%)		24 (92.3%)	16 (80.0%)	
Bilateral	8 (14.0%)	3 (6.1%)		2 (7.7%)	4 (20.0%)	
Maximum diameter			0.938			0.239
< 5cm	33 (57.9%)	28 (57.1%)		15 (57.7%)	8 (40.0%)	
≥ 5cm	24 (42.1%)	21 (42.9%)		11 (42.3%)	12 (60.0%)	
T Stage			0.002*			0.031*
1/2/3	22 (38.6%)	6 (12.2%)		10 (38.5%)	2 (10.0%)	
4a/4b	35 (61.4%)	43 (87.8%)		16 (61.5%)	18 (90.0%)	
N Stage			0.265			0.733
0	48 (84.2%)	37 (75.5%)		23 (88.5%)	17 (85.0%)	
1/2	9 (15.8%)	12 (24.5%)		3 (11.5%)	3 (15.0%)	
M Stage			0.242			0.717
0	56 (98.2%)	46 (93.9%)		24 (92.3%)	19 (95.0%)	
1	1 (1.8%)	3 (6.1%)		2 (7.7%)	1 (5%)	
Surgical Margin			<0.001*			<0.001*
Negative	45 (78.9%)	10 (20.4%)		23 (88.5%)	7 (35.0%)	
Positive	12 (21.1%)	39 (79.6%)		3 (11.5%)	14 (65.0%)	
Radiomics score	-1.04	0.60 (-0.31~ 1.65)	<0.001*	-0.95	0.75	<0.001*
Median, (interquartile range)	(-2.24~ -0.20)			(-2.07~ -0.27)	(-0.71~ 2.29)	

*DN-SNSCC, de-novo SNSCC; IP-SNSCC, inverted papilloma-derived SNSCC; (*P < 0.05) .*

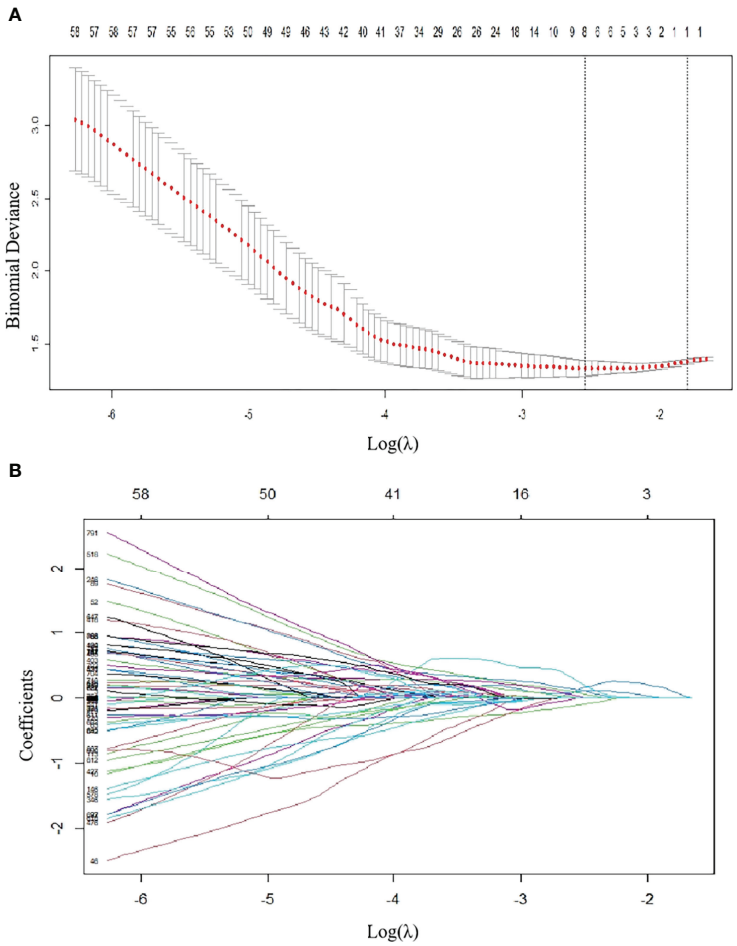

FIGURE 2 | Radiomics feature selection using LASSO regression in the training group. **(A)** *Via* 7-fold cross-validation(CV), the value of λ that gave the minimum average binomial deviance was used to select features. The y-axis shows binomial deviances and the lower x-axis the log(λ). Numbers along the upper x-axis indicate the average number of predictors. Red dots indicate average deviance values for each model with a given λ, and vertical bars through the red dots indicate the upper and lower values of the deviances. By using the minimum criteria and the 1 standard error of the minimum criteria (the 1-SE criteria), the vertical black lines define the optimal λ values = 0.07873. **(B)** The coefficients have been plotted vs. log(λ). The features with nonzero coefficients are shown in the plot.

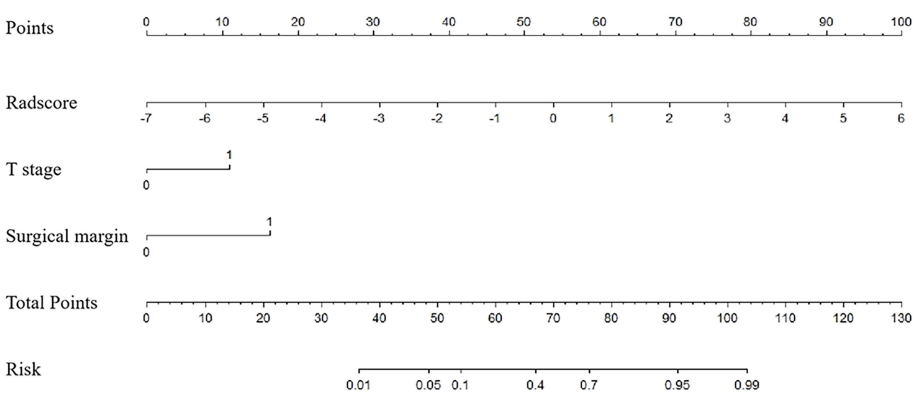

FIGURE 3 | Nomogram for risk prediction of ER with the radiomics signature (Radscore) and clinical factors (T stage and surgical margin) incorporated.

TABLE 2 | AUCs of the Radscore, Clinical model and Nomogram model.

	Training cohort		Testing cohort	
	AUC (95%CI)	***P*-value**	**AUC (95%CI)**	***P*-value**
Radscore	0.84 (0.76-0.91)		0.84 (0.73-0.96)	
Clinical model	0.82 (0.75-0.90)		0.79 (0.66-0.92)	
Nomogram	0.92 (0.87-0.97)		0.92 (0.82-1.00)	
Radscore *vs.* Clinical model		0.831		0.528
Nomogram *vs.* Radscore		0.003*		0.177
Nomogram *vs.* Clinical model		0.004*		0.016*

*(*P < 0.05).*

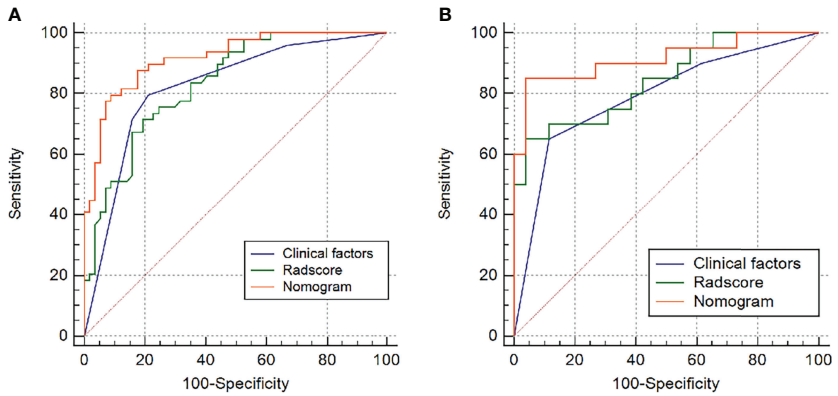

FIGURE 4 | Receiver operating characteristic (ROC) curves of the radiomics model, clinical model and nomogram model in the **(A)** training group and **(B)** testing group.

nomogram model to identify the differentiation grade of SNSCCs. The AUCs for the nomogram, clinical factors and radscore were 0.92, 0.82 and 0.84, respectively, in the training cohort and 0.92, 0.79 and 0.84, respectively, in the testing cohort. When the Hosmer-Lemeshow goodness-of-fit test was applied, the calibration curve of the nomogram (**Figure 5**) demonstrated very good reliability in evaluating ER in the training and testing cohorts ($P > 0.050$).

DCA showed that if the threshold probability was 0.19-1.00, the use of the nomogram to evaluate the ER offered more benefits than either the treat-all scheme (assuming all SNSCCs were ER) or the treat-none scheme (assuming all SNSCCs were NER) (**Figure 6**).

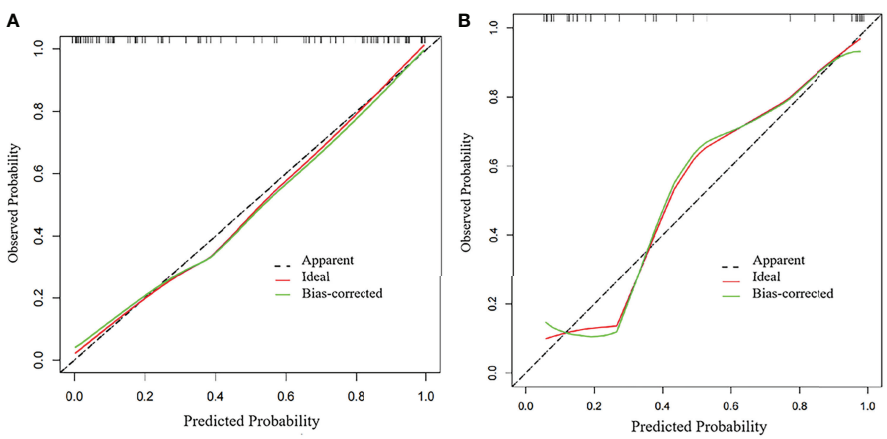

FIGURE 5 | Calibration curves of the radiomics nomogram in the **(A)** training group and **(B)** testing group.

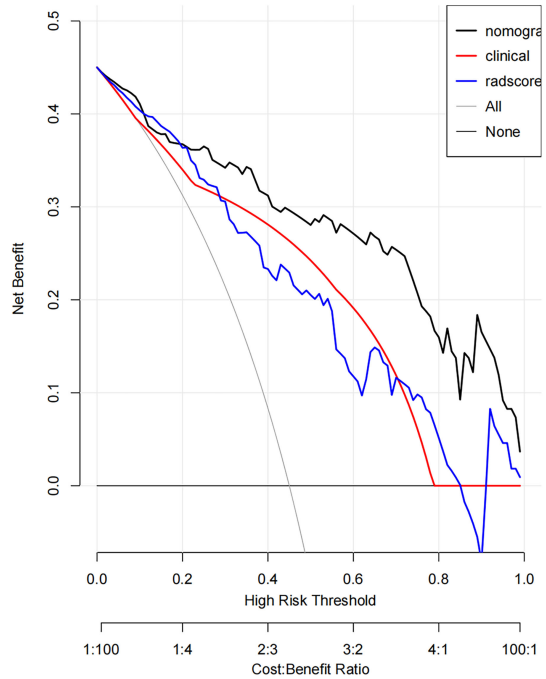

FIGURE 6 | Decision curve analysis (DCA) derived from the testing cohort showed that if the threshold probability was <10% and >20%, the use of the nomogram to evaluate the grade offered more benefits than either the treat-all scheme (assuming all SNSCCs were ER) or the treat-none scheme (assuming all SNSCCs were NER).

In addition, using the same threshold probability, the nomogram could add more benefits than either the strategy involving exclusive use of the radscore or the strategy involving exclusive use of clinical factors.

The optimum cutoff value of the nomogram generated by the X-tile plot was -0.59 on the basis of the training cohort. Accordingly, patients were classified into the high- and low-risk subgroups. Kaplan-Meier analysis showed that in the training cohort, the 2-year RFS rates were 83.4 ± 4.8% for low-risk patients and 13.3 ± 5.1% for high-risk patients ($P < 0.001$). The training cohort showed similar results; the 2-year RFS rates were 78.1 ± 7.3% for low-risk patients and 7.1 ± 6.9% for high-risk patients ($P < 0.001$). (**Figure 7**).

DISCUSSION

In the present study, we developed and validated a combined nomogram model for the prediction of ER in SNSCC patients. A radscore based on eight features was useful for evaluating ER. By incorporating the radscore and clinical factors, the nomogram model achieved higher predictive value. The calibration curve DCA showed the good clinical utility of this easy-to-use nomogram prediction model.

The most common malignant sinonasal tumor is SNSCC, which comprises 50% of all cases (12). Yan et al. (4) reported that a large proportion of SNSCCs diagnosed at an advanced stage showed worse disease-free survival than early stage tumors. In addition, over ten years of follow-up, the researchers found that SNSCC recurrence occurred very early (within 3 years after resection). This finding was also supported by Quan et al. (13), who demonstrated that local relapse was the most important reason for treatment failure in SNSCC patients. Thus, early prediction of the risk of relapse is very important to implement effective individualized treatment.

Radiomics has recently become a research hotspot in oncology. By extracting high-throughput quantitative data characterization algorithms, radiomics provides unprecedented opportunity for improved machine learning powered predictive models of head and neck cancers. These models not only predict survival but also on risk of relapse (14). DWI can reflect the random movement of water molecules at the cellular level, and the apparent diffusion coefficient (ADC) derived from DWI has been shown to be a promising biomarker for characterizing tissues.

In our study, using LASSO, a total of 850 ADC-based features were narrowed to only 8 potential predictors. These 8 radiomic features were divided into 3 types: first-order, texture (GLDM) and shape features. First-order statistics are also known as intensity-based features. Histogram analysis in our study revealed higher signal skewness and kurtosis values in

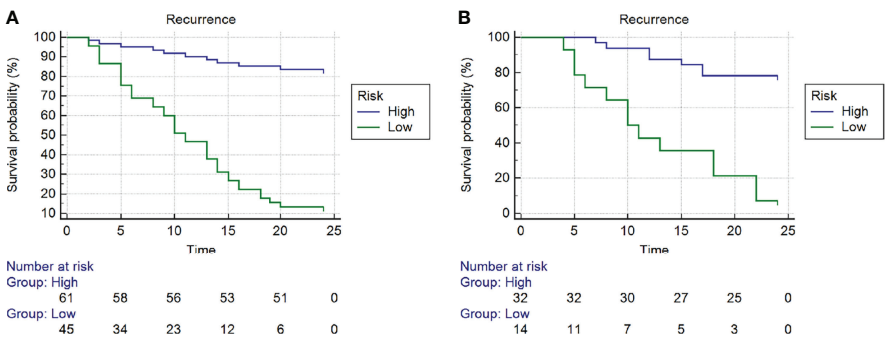

FIGURE 7 | Kaplan-Meier curves of recurrence-free survival (RFS) of high- and low- risk subgroups according to the cut-off value of nomogram in the **(A)** training cohort and **(B)** training cohort.

ER SNSCCs than in NER SNSCCs, explaining the asymmetry of the histogram distribution within tumors (15). Kierans et al. (16) indicated that ADC skewness could reflect the heterogeneity of cellular environments, resulting from a high degree of cellular atypia and nuclear pleomorphism. This information is also useful for the differentiation of high- versus low-grade carcinoma. Hirata1 et al. (17) proposed that ADC histogram-derived parameters of kurtosis were significantly correlated with RFS ($P < 0.001$) in esophageal cancer patients. In the analysis of texture-based features, a higher DV value further elucidated the high heterogeneity in the ER SNSCC group. Another significant radiomic predictor is a shape-based feature, namely, flatness. In our study, SNSCC with ER generated a more irregular shape and lower flatness value. This result is consistent with a recent study by Khodabakhshi et al. (18), which reported a significant correlation between higher values of flatness and better survival outcomes in renal cell carcinoma patients. However, these above features could only reflect one aspect of tumor information. Therefore, by integrating the eight ADC-based radiomic features regarding heterogeneity and shape of the whole tumor, the radscore achieved moderate power in discriminating ER of SNSCCs with AUCs of 0.84 in both of the training and testing cohorts.

The clinical risk factors associated with the ER of advanced SNSCC tumors are seldom addressed in previous literature. Li et al. (19) indicated that in T4 stage SNSCC patients, invasion of the orbit and brain could lead to incomplete resection of tumors and ER. This finding is in agreement with recent studies (6, 13) that reported that the higher the T stage, the greater the probability of recurrence. In addition, the relationship between a positive surgical margin with a higher local recurrence rate and poor survival outcome has been reported in several previous studies (20, 21). However, these clinical factors, which are mainly based on anatomical structures, are not accurate enough due to the highly heterogeneous tumor biology, which can significantly affect patient survival.

Nomogram is a new method to estimate prognosis by incorporating multiple relevant factors and can be readily used in clinical practice. Recent evidence (5) has indicated that a nomogram combining radiomic features and clinical characteristics could be effectively applied in evaluating the recurrence of some types of cancers, such as nasopharyngeal carcinoma, gastric cancer (6) and hepatocellular carcinoma (7). In the present study, multivariate analysis revealed that the radscore and several clinical factors, including T stage (T3 or T4) and surgical margin (negative or positive), were independent predictors of ER in advanced SNSCCs and were included as candidate factors in the nomogram. After comparison, the nomogram showed significantly greater effectiveness (AUC of 0.92) than either the radscore or clinical factors in discriminating ER of SNSCCs in the training cohort. In the testing cohort, the nomogram also tended to show the best performance in predicting ER, which suggested that the nomogram could serve as an important marker for evaluating ER and prognosis. For further study, we identified the optimal cutoff of the nomogram value and divided the patients into different categories of risks using X-tile software. Kaplan-Meier curves revealed a significant difference in RFS between the high- and low-risk SNSCC patients in both the training and testing cohorts. Thus, the nomogram has a significant impact on treatment decisions. Thus, if ER is strongly indicated by the clinical-radiomics nomogram model, clinicians may wish to consider additional or alternate treatment plans.

We also employed DCA to further quantify the clinical utility of this radiomic nomogram model, considering the clinical consequences of decisions. DCA is a new method based on the analysis of threshold probabilities to express the net benefit. In our study, DCA showed the benefit of applying the nomogram as opposed to the clinical factor model or the radscore model for individualized prediction of the probability of ER in advanced SNSCC patients.

Our study has several potential limitations. First, due to the rarity of advanced SNSCC and difficulty in collecting patient data, the number of samples was limited. Second, our study was conducted in a single institution. Multi-center studies are requisite to increase the effectiveness of the nomogram. Thirdly, it is a major challenge to select the most valuable features from high-dimensional and small-sample data; thus, other machine-learning algorithms need to be investigated in the future to yield preferable outcomes. In addition, the ADC values were derived from a monoexponential model of DWI features, whereas biexponential [e.g., intravoxel incoherent motion (IVIM)] and non-Gaussian distribution-based DWI features could yield more robust parameters to characterize tumor heterogeneity.

To our knowledge, the current study is the first report to indicate the utility of a radiomics monogram incorporating both quantitative ADC-based radiomic features and clinical factors in advanced SNSCC patients. Our preliminary study demonstrated that the nomogram represents a promising tool in the prediction of ER in SNSCC and can be conveniently applied to facilitate individualized treatment.

DATA AVAILABILITY STATEMENT

The original contributions presented in the study are included in the article/**Supplementary Material**. Further inquiries can be directed to the corresponding author.

ETHICS STATEMENT

The studies involving human participants were reviewed and approved by Eye and ENT Hospital of Fudan University. The patients/participants provided their written informed consent to participate in this study. Written informed consent was obtained from the individual(s) for

the publication of any potentially identifiable images or data included in this article.

AUTHOR CONTRIBUTIONS

NL, SY, and ML designed the research. NL, SY, ML, YShi, ZX, and WC collected the data. NL, SY, ML, and YShi contributed data analysis tools and performed the analysis. NL wrote the paper. YSha and YC supervised the study. All authors contributed to the article and approved the submitted version.

ACKNOWLEDGMENTS

The entire manuscript has been revised and edited by American Journal Experts (AJE) Language Editing Services.

SUPPLEMENTARY MATERIAL

The Supplementary Material for this article can be found online at: https://www.frontiersin.org/articles/10.3389/fonc.2022.870935/full#supplementary-material

REFERENCES

1. Cracchiolo JR, Patel K, Migliacci JC, Morris LT, Ganly I, Roman BR, et al. Factors Associated With a Primary Surgical Approach for Sinonasal Squamous Cell Carcinoma. *J Surg Oncol* (2018) 117:756–64. doi: 10.1002/jso.24923
2. Al-Qurayshi Z, Smith R, Walsh JE. Sinonasal Squamous Cell Carcinoma Presentation and Outcome: A National Perspective. *Ann Otol Rhinol Laryngol.* (2020) 129:1049–55. doi: 10.1177/0003489420929048
3. Saba NF. Preoperative Chemotherapy for Sinonasal Squamous Cell Carcinoma (SNSCC): Time to Move Closer to a Definitive Answer. *Cancer* (2021) 127:1734–5. doi: 10.1002/cncr.33450
4. Yan CH, Newman JG, Kennedy DW, Palmer JN, Adappa ND. Clinical Outcomes of Sinonasal Squamous Cell Carcinomas Based on Tumor Etiology. *Int Forum Allergy Rhinol* (2017) 7:508–13. doi: 10.1002/alr.21899
5. Zhu C, Huang H, Liu X, Chen H, Jiang H, Liao C, et al. A Clinical-Radiomics Nomogram Based on Computed Tomography for Predicting Risk of Local Recurrence After Radiotherapy in Nasopharyngeal Carcinoma. *Front Oncol* (2021) 11:637687. doi: 10.3389/fonc.2021.637687
6. Huang L, Feng B, Li Y, Liu Y, Chen Y, Chen Q, et al. Computed Tomography-Based Radiomics Nomogram: Potential to Predict Local Recurrence of Gastric Cancer After Radical Resection. *Front Oncol* (2021) 11:638362. doi: 10.3389/fonc.2021.638362
7. Zhu HB, Zheng ZY, Zhao H, Zhang J, Zhu H, Li YH, et al. Radiomics-Based Nomogram Using CT Imaging for Noninvasive Preoperative Prediction of Early Recurrence in Patients With Hepatocellular Carcinoma. *Diagn Interv Radiol* (2020) 26:411–9. doi: 10.5152/dir.2020.19623
8. Wang X, Dai S, Wang Q, Chai X, Xian J. Investigation of MRI-Based Radiomics Model in Differentiation Between Sinonasal Primary Lymphomas and Squamous Cell Carcinomas. *Jpn J Radiol* (2021) 39:755–62. doi: 10.1007/s11604-021-01116-6
9. Bi SC, Zhang H, Wang HX, Ge YQ, Zhang P, Wang ZC, et al. Radiomics Nomograms Based on Multi-Parametric MRI for Preoperative Differential Diagnosis of Malignant and Benign Sinonasal Tumors: A Two-Centre Study. *Front Oncol* (2021) 11:659905. doi: 10.3389/fonc.2021.659905
10. Zhang H, Wang H, Hao D, Ge Y, Wan G, Zhang J, et al. An MRI-Based Radiomic Nomogram for Discrimination Between Malignant and Benign Sinonasal Tumors. *J Magn Reson Imag* (2021) 53(1):141–51. doi: 10.1002/jmri.27298
11. Gencturk M, Ozturk K, Caicedo-Granados E, Li F, Cayci Z. Application of Diffusion-Weighted MR Imaging With ADC Measurement for Distinguishing Between the Histopathological Types of Sinonasal Neoplasms. *Clin Imag* (2019) 55:76–82. doi: 10.1016/j.clinimag.2019.02.004
12. Dulguerov P, Jacobsen MS, Allal AS, Lehmann W, Calcaterra T. Nasal and Paranasal Sinus Carcinoma: Are We Making Progress? A Series of 220 Patients and a Systematic Review. *Cancer* (2001) 92:3012–29. doi: 10.1002/1097-0142(20011215)92:12<3012::aid-cncr10131>3.0.co;2-e
13. Quan H, Zhang H, Zou L, Yuan W, Wang S. Comparison of Outcomes Between Patients With De-Novo Sinonasal Squamous Cell Carcinoma vs Malignant Transformations From Inverted Papillomas. *Int Forum Allergy Rhinol* (2020) 10:762–7. doi: 10.1002/alr.22556
14. Giraud P, Giraud P, Gasnier A, El Ayachy R, Kreps S, Foy J-P, et al. Radiomics and Machine Learning for Radiotherapy in Head and Neck Cancers. *Front Oncol* (2019) 9:174. doi: 10.3389/fonc.2019.00174
15. Kierans AS, Doshi AM, Dunst D, Popiolek D, Blank SV, Rosenkrantz AB, et al. Retrospective Assessment of Histogram-Based Diffusion Metrics for Differentiating Benign and Malignant Endometrial Lesions. *J Comput Assist Tomogr.* (2016) 40:723–9. doi: 10.1097/RCT.0000000000000430
16. Kierans AS, Rusinek H, Lee A, Shaikh MB, Triolo M, Huang WC. Textural Differences in Apparent Diffusion Coefficient Between Low- and High-Stage Clear Cell Renal Cell Carcinoma. *AJR Am JRoentgenol.* (2014) 203:W637–644. doi: 10.2214/AJR.14.12570
17. Hirata A, Hayano K, Ohira G, Imanishi S, Hanaoka T, Toyozumi T, et al. Volumetric Histogram Analysis of Apparent Diffusion Coefficient as a Biomarker to Predict Survival of Esophageal Cancer Patients. *Ann Surg Oncol* (2020) 27:3083–9. doi: 10.1245/s10434-020-08270-7
18. Khodabakhshi Z, Amini M, Mostafaei S, Avval AH, Nazari M, Oveisi M, et al. Overall Survival Prediction in Renal Cell Carcinoma Patients Using Computed Tomography Radiomic and Clinical Information. *J Dig Imag* (2021) 34:1086–98. doi: 10.1007/s10278-021-00500-y
19. Li Y, Wang C, Wang R, He S, Feng L, Ma H, et al. Survival Outcomes and Prognostic Factors of Squamous Cell Carcinomas Arising From Sinonasal Inverted Papillomas: A Retrospective Analysis of 120 Patients. *Int Forum Allergy Rhinol* (2019) 9:1367–73. doi: 10.1002/alr.22400
20. Li W, Lu H, Zhang H, Sun X, Hu L, Wang D. Squamous Cell Carcinoma Associated With Inverted Papilloma: Recurrence and Prognostic Factors. *Oncol Lett* (2020) 19:1082–8. doi: 10.3892/ol.2019.11185
21. Nomura H, Omi M, Netsu S, Aoki Y, Tanigawa T, Kurita T, et al. Positive Surgical Margin is an Independent Predictor of Overall Survival of Patients With Vulvar Squamous Cell Carcinoma. *J Obstet Gynaecol Res* (2021) 47:3990–7. doi: 10.1111/jog.14962

Conflict of Interest: The authors declare that the research was conducted in the absence of any commercial or financial relationships that could be construed as a potential conflict of interest.

frontiers | Frontiers in Oncology

ORIGINAL RESEARCH
published: 31 May 2022
doi: 10.3389/fonc.2022.879054

p63 Directs Subtype-Specific Gene Expression in HPV+ Head and Neck Squamous Cell Carcinoma

Alexandra Ruth Glathar, Akinsola Oyelakin, Christian Gluck, Jonathan Bard and Satrajit Sinha *

Jacobs School of Medicine and Biomedical Sciences, Department of Biochemistry, University at Buffalo, Buffalo, NY, United States

The complex heterogeneity of head and neck squamous cell carcinoma (HNSCC) reflects a diverse underlying etiology. This heterogeneity is also apparent within Human Papillomavirus-positive (HPV+) HNSCC subtypes, which have distinct gene expression profiles and patient outcomes. One aggressive HPV+ HNSCC subtype is characterized by elevated expression of genes involved in keratinization, a process regulated by the oncogenic transcription factor ΔNp63. Furthermore, the human *TP63* gene locus is a frequent HPV integration site and HPV oncoproteins drive ΔNp63 expression, suggesting an unexplored functional link between ΔNp63 and HPV+ HNSCC. Here we show that HPV+ HNSCCs can be molecularly stratified according to ΔNp63 expression levels and derive a ΔNp63-associated gene signature profile for such tumors. We leveraged RNA-seq data from p63 knockdown cells and ChIP-seq data for p63 and histone marks from two $\Delta Np63^{high}$ HPV+ HNSCC cell lines to identify an epigenetically refined ΔNp63 cistrome. Our integrated analyses reveal crucial ΔNp63-bound super-enhancers likely to mediate HPV+ HNSCC subtype-specific gene expression that is anchored, in part, by the PI3K-mTOR pathway. These findings implicate ΔNp63 as a key regulator of essential oncogenic pathways in a subtype of HPV+ HNSCC that can be exploited as a biomarker for patient stratification and treatment choices.

Keywords: p63, HPV, HNSCC, gene expression profiling, biomarker

OPEN ACCESS

Edited by:
Marcela Lizano, National Institute of Cancerology (INCAN), Mexico

Reviewed by:
J. Omar Muñoz-Bello, National Institute of Cancerology (INCAN), Mexico
Francisco Aguayo, University of Chile, Chile

***Correspondence:**
Satrajit Sinha
ssinha2@buffalo.edu

Specialty section:
This article was submitted to Head and Neck Cancer, a section of the journal Frontiers in Oncology

Received: *18 February 2022*
Accepted: *19 April 2022*
Published: *31 May 2022*

Citation:
Glathar AR, Oyelakin A, Gluck C, Bard J and Sinha S (2022) p63 Directs Subtype-Specific Gene Expression in HPV+ Head and Neck Squamous Cell Carcinoma. Front. Oncol. 12:879054. doi: 10.3389/fonc.2022.879054

INTRODUCTION

Head and neck squamous cell carcinoma (HNSCC) is the sixth most common cancer worldwide and has a 5 year-mortality rate of nearly 50%, making it a leading cause of cancer-related death (1). HPV infection has overtaken alcohol and tobacco consumption as the predominant risk factor in the majority of newly diagnosed HNSCC cases (2–4). Intriguingly, patients with HPV+ HNSCC have better overall survival and progression-free survival than those with HPV− HNSCC. However, current treatment options for both HPV+ and HPV− HNSCCs consist of standard care regimens of chemoradiotherapy concurrent with cisplatin (2, 5). More attention has been given toward de-escalation of therapy for HPV+ HNSCC, and a clearer understanding of the underlying biology may aid in identifying patients who would benefit from new treatment modalities (6).

HPV infection of epithelial cells, primarily in the oropharynx, can result in the integration of the viral genome into the host genome, leading to dysregulated expression of viral and cellular oncoproteins and carcinogenesis (7). HPV E6 and E7 oncoproteins are the primary drivers of the pathogenesis of HPV and function by degrading tumor suppressor p53 and retinoblastoma protein (pRb), respectively, leading to activation of the cell cycle-promoting E2F family of transcription factors (TFs) (8, 9). Integration of the HPV genome alters the expression and DNA methylation profiles of a broad range of host genes (10). Although the HPV genome can integrate throughout the human genome, it occurs with a higher incidence in some regions, including the 3q region surrounding *TP63* (11–14). *TP63* encodes p63, a member of the p53 family of transcription factors, which plays an essential role in the development and maintenance of the stratified squamous epithelium (15–18). ΔNp63α is the most prevalent p63 isoform in tissues of epithelial origin and acts predominantly as an oncogene in several cancers, including HNSCC, while TAp63 has much more restricted expression and shows tumor-suppressor features (18–22). Ectopic expression of HPV oncoproteins in human keratinocytes leads to upregulation of p63 at both the mRNA and protein levels (23). Conversely, silencing of E6/E7 expression in HPV+ cell lines leads to a loss of p63 expression (23). Despite these known functional interactions between p63 and HPV, very few studies have examined the specific role of p63 in modulating gene expression in HPV+ HNSCC.

Hierarchical clustering analyses of HPV+ HNSCCs revealed two distinct subtypes based on gene expression profiles, copy number alterations, mutational profiles, and patient outcomes (11, 14). One subtype characterized by the amplification of the 3q chromosomal region, including the *TP63* locus, was shown by two independent studies to be enriched in pathways involved in keratinization and cell adhesion (11, 14). Interestingly, patients with this subtype tend to have worse outcomes and respond more poorly to treatment compared to patients with tumors belonging to the other HPV+ subtype (11, 14). These studies suggest that there are HPV-dependent mechanisms that affect p63 function in HPV+ HNSCC and the pathology of this disease.

To explore the oncogenic role of p63 in HPV+ HNSCC, we established a p63-driven gene regulatory network based on both preclinical cell culture models and tumor datasets. Our in-depth examination of p63 in the broader transcriptomic and genomic context revealed that p63 regulates critical sets of genes and pathways in the HPV infection pathway and HPV-associated malignancy, including PI3K signaling, WNT signaling, and cell cycle control which may inform the clinical differences between the HPV+ HNSCC subtypes. Importantly, we found that p63 expression correlates with the more aggressive HPV+ HNSCC subtype and that it directs the associated gene expression programs. Finally, we identified a potentially important role for p63 in regulating PI3K signaling and mTOR signaling in HPV+ HNSCC, which may have implications for future treatment choices. Our studies suggest that p63 is an important driver of the subtype-specific gene expression program in HPV+ HNSCC, and can serve as a biomarker to identify patients with more aggressive disease.

MATERIAL AND METHODS

Cell Culture Studies

The UM-SCC-104 (referred to as SCC104) cell line was obtained from Sigma-Aldrich, and the UPCI : SCC152 cell line (referred to as SCC152) was obtained from ATCC. Both SCC104 and SCC152 cell lines have been reported to be HPV-16 positive (24, 25). SCC25 and SCC47 cell lines were purchased from ATCC and Millipore Sigma, respectively. Cell lines UM-SCC-11B, UM-SCC-74A, UM-SCC-29, UM-SCC-23, and UM-SCC-103 were obtained from Dr. Thomas Carey (University of Michigan). HSC-3 and CAL-27 cell lines were generously provided by Dr. Manish Bais (Boston University). All cell lines were grown and maintained in high-glutamine DMEM or DMED/F12 as recommended, with the following supplements: 10% FBS, 1% nonessential amino acids, and antibiotics. Other cell lines used in this study have been described before in Gluck et al. 2019 (26). The identities of the cell lines utilized in this study were confirmed *via* short tandem repeat profiling through services offered by Genetica. All cell lines were tested by the eMycoPlus Mycoplasma PCR Detection Kit (BulldogBio) to ensure that they were bereft of any mycoplasma infection.

Knockdown of p63

Lentivirus-mediated depletion of p63 in SCC104 and SCC152 cells was performed using the pGIPZ system. GIPZ lentiviral shRNAs (clone IDs V2LHS_24248 [sh1] and V2LHS_24250 [sh2]) targeting *TP63* were obtained from and virus was generated with the help of Gene Modulation Services Shared Core at Roswell Park Comprehensive Cancer Center. Viral infection and selection with Puromycin was performed as described before (27).

Western Blot Analysis

Protein extracts were prepared according to previously published protocol (27). Briefly 5 μL of protein lysates were loaded onto SDS-polyacrylamide gels and transferred to Immun-Blot PVDF membranes (Bio-Rad Laboratories). After blocking in 5% milk, the membranes were incubated in primary antibodies against the following: p63 (4A4, 1:20,000), ΔNp63 (E6Q3O; Cell Signaling Technology, 1:5000), ITGB1 (Proteintech, 1:10,000), ITGB4 (Proteintech, 1:10,000), cMYC (Santa Cruz Biotechnology, 1:5000), AKT1 (Proteintech, 1:10,000), mTOR (Proteintech, 1:10,000), Raptor (Proteintech, 1:10,000), S6 (Cell Signaling Technology, 1:5000), and p-S6 (Cell Signaling Technology, 1:5000). The MAB374 antibody (EMD Millipore) was used to detect GAPDH as a loading control at 1:20,000 dilution. HRP-conjugated secondary antibodies corresponding to the primary antibody host were incubated with each blot. Unbound antibodies were washed off in 0.05% Tween-20 in Tris-buffered saline. The LumiGLO peroxidase chemiluminescent substrate kit (SeraCare) was used to detect antibody-labeled proteins, and membranes were imaged using the Bio-Rad ChemiDoc imaging system.

ChIP of p63 and Histone Marks

The iDeal ChIP-seq kit for transcription factors (C01010055; Diagenode) or for histones (C01010051; Diagenode) and the

associated protocols were used to perform ChIP-seq. SCC104 and SCC152 cells were grown to ~90% confluency and cross-linked in the supplied fixation buffer supplemented with 0.5% formaldehyde for 10 min. Lysates from the fixed cells were subsequently sonicated with a Diagenode Bioruptor to obtain sheared chromatin with an approximate fragment length of 150–400 bp. The ChIPs for p63 were carried out using 2 μg of p63 4A4 antibody (Santa Cruz Biotechnology) and 2 μg of ΔNp63-1.1 antibody (28). After cross-link reversal, proteinase-K/RNase A treatment, and DNA purification, libraries were prepared using the ThruPLEX DNA-seq kit (Rubicon Genomics). ChIP DNA and input controls were then subjected to 50-bp single-end sequencing on an Illumina HiSeq 2500, which resulted in 15–25 million reads per sample.

ChIP-Seq Analysis

The raw ChIP-seq reads from all experiments were mapped to the *Homo sapiens* genome (hg19 build) using Bowtie v1.1.1 with the parameter m=1 to remove all reads mapping to multiple genomic loci (29). Peak calling was then performed using MACS2 v2.1.0 with a minimum FDR cutoff of 0.05 and sequenced Input used as control for each experiment, and resultant peaks were matched to the nearest gene using GREAT analysis with default settings (30, 31). For visualization of ChIP peaks, the package deeptools v3.3.2 was used to preprocess bam files to generate bigwig files which were then uploaded to IGV (32). Adobe illustrator was used for final image processing. Peak summits determined by MACS2 v2.1.0 were used as input to HOMER's findMotifsGenome.pl program with the parameter "-size 200" (33).

RNA Isolation and Library Preparation for RNA-Seq

Total RNA from cell lines was extracted using a Direct-zol RNA miniprep kit (Zymo Research). The extracted RNA was snap-frozen on dry ice and stored at −80°CC until library preparation. For each RNA sample, cDNA libraries were prepared using the TrueSeq RNA sample preparation kit (Illumina) and were then 50-bp single-end sequenced or paired-end sequenced on an Illumina HiSeq 2500. Quality control metrics were performed on raw sequencing reads using the FASTQC v0.11.9 application.

RNA-Seq Analysis

Reads were mapped to the appropriate reference genome, GRCh38/hg19 build, with HISAT2 v2.1.0 (34). Reads aligning to the reference genome were quantified with featureCounts v1.5.3 to generate a matrix of raw counts, which was then processed in R, to generate normalized expression values in transcripts per million according to the method proposed by Wagner et al. (35). Differential gene expression analysis comparing control to p63 knockdown was carried out using DESeq2 v1.24.0 (26). DEGS with an FDR value of ≤ 0.1 were considered statistically significant.

qRT-PCR Analysis

Total RNA from SCC104 and SCC152 knockdown cell lines was extracted using a Direct-zol RNA miniprep kit (Zymo Research). RNA was reverse transcribed with the Bio-Rad iScript cDNA synthesis kit according to the manufacturer's instructions. The resulting cDNA was used for qPCR with Bio-Rad iQ SYBR green Supermix. A list of the qRT-PCR primers can be found in **Supplementary Table 7**.

HNSCC Dataset Analysis

RNA-seq data from patient samples were obtained from GEO (GSE122512, GSE112026, GSE74927, and GSE72536) (11, 36–38). HPV+ tumors were assigned based on data presented in the original paper of each dataset. Alignment and quantification of counts for each dataset were performed as indicated by the original study. TCGA RNA-seq expression and CNA datasets were downloaded from cBioPortal (39, 40). Briefly, RNA-seq counts were extracted and normalized using the median-ratio method (DESeq2 v.1.24.0 [75]) and subsequently transformed to transcript per million values (35). For GSE112026, RSEM values were utilized for transcript quantification. HPV+ tumors were segregated into high and low p63 expression groups based on the median p63 expression level calculated from the RNA-seq data.

Determination of Enhancers and SEs According to H3K27Ac Marks

H3K27Ac ChIP-seq data from SCC104 and SCC152 cells were aligned to the human genome as described above. Narrow peaks were called using MACS2 v2.1.0 using the following parameters: -p 0.01, -nomodel, -extsize 150. The resulting narrowPeaks files were converted to gff format and used as inputs for the ROSE (rank order of super-enhancers) algorithm, which was run using default parameters along with appropriate input controls to generate typical enhancer and SE lists (41, 42).

Histone Modification Enrichment at p63 Binding Sites

The deepTools package was utilized to generate a signal matrix of histone modifications H3K27Ac, H3K4Me1, and H3K4Me3. The fluff python package was then utilized to generate heat maps showing the resulting signal of the histone modifications around a 2-kb window centered at each p63 ChIP-seq peak summit. The resulting histone signal enrichment was subjected to k-means clustering (k=3) (43).

Genomic Feature Assignment

The CEAS tool was used to annotate p63 ChIP-seq peaks to the nearest genomic feature of the hg19 genome assembly (44). The promoter region was considered up to 1,000 bp from a transcriptional start site, and the proximal enhancer was considered from 1,000 to 3,000 bp away. Any binding within a gene was considered intragenic, whereas any binding site greater than 3,000 bp upstream or downstream was considered distal intergenic.

Motif Enrichment Analysis of Enhancers

To determine the top enriched DNA binding motifs of TFs found within nucleosome-free regions of SCC104 and SCC152 SEs, nucleosome-free regions were first determined using the HOMER findPeaks tool with the -nfr flag (33). The AME tool

was used to determine enriched motifs found within the HOCOMOCO Human (v11 CORE) database. Motifs were ranked according to *p* value.

Gene Ontology/Pathway Enrichment Analysis

The GREAT tool was used to annotate binding loci to the nearest gene (31). Identified genes were then subjected to KEGG pathway analysis utilizing the DAVID functional annotation tool (45–47). For RNA-seq data, DEGs were subjected to both KEGG analysis utilizing the DAVID functional annotation tool and canonical pathway analysis by gene set enrichment analysis (48).

Statistics

Statistical analyses were performed using R, a free software environment for statistical computing and graphics. A Shapiro-Wilk test was performed to check the normality of data, and then either a student's *t* test or Wilcoxon signed-rank test was performed according to whether the data were normally distributed. A *p* value lower than 0.05 was considered significant.

RESULTS

Generation of a p63 Gene Signature From the HPV+ HNSCC TCGA Tumor Dataset

Although a broad oncogenic role of p63 in HNSCC has been reported (21, 49, 50), its specific role in the HPV+ subtypes has not been fully explored. Thus, we first examined three independent RNA-seq datasets of HPV+ HNSCC tumors (GEO datasets GSE112026, GSE74927, and GSE72536) and observed a gradient in the pattern of p63 mRNA expression (**Supplementary Figures 1A–C**). Segregation of HPV+ HNSCC tumors according to median p63 expression revealed distinct $p63^{high}$ and $p63^{low}$ subtypes. This distinction was in agreement with previous unsupervised gene expression clustering analyses performed on HPV+ HNSCC tumors that had identified subtypes with distinct gene expression patterns, including different p63 levels (11, 14, 51).

To investigate the functional relevance of p63 in HPV+ HNSCC, we next focused on data from 67 HPV+ tumors that are available in The Cancer Genome Atlas (TCGA) patient datasets. Exploration of p63 expression across the HPV+ HNSCC tumors in this dataset revealed a similar pattern of p63 expression as observed in the GEO dataset (**Figure 1A**). Using the RNA-seq data from the TCGA datasets to segregate the HPV+ tumors according to $p63^{high}$ and $p63^{low}$ expression, we identified 6,459 differentially expressed genes (DEGs) between these two populations (**Figures 1B, C** and **Supplementary Table 1**). We next examined GO biological processes that were enriched with upregulated and downregulated DEGs to identify pathways that are likely influenced by p63. Downregulated DEGs were significantly enriched in pathways involved in viral transcription and inflammatory immune responses, such as NF-κB and tumor necrosis factor signaling (**Figure 1D**). Upregulated DEGs were significantly enriched in pathways associated with cell adhesion and keratinization—processes linked to p63 (**Figure 1E**). These findings were of particular interest in lieu of prior HPV+ subtype studies in which gene expression-driven clustering analysis showed differential enrichment of immune response and cell adhesion pathways. Notably, the clustering of tumors according to p63 expression recapitulated the molecularly defined distinct subtypes of HPV + HNSCC.

Mapping the Genomic Targets of p63 in Representative HPV+ HNSCC Cell Lines

To verify that the pattern of p63 expression in tumors matches that in HNSCC cell lines to serve as suitable models for follow-up studies, we examined RNA-seq data generated from 9 HPV+ and 55 HPV− HNSCC cell lines (**Supplementary Figure 2A**) (38). Several of the HPV+ HNSCC cell lines had high p63 expression, and we verified this expression at the protein level by Western blotting with two anti-p63 antibodies. Similar to previous reports (23), four of the five HPV+ HNSCC cell lines consistently showed high levels of p63 protein expression, specifically the ΔNp63 isoform (**Supplementary Figure 2B**). Of these, we chose the SCC104 and SCC152 cell lines for follow-up mechanistic studies. These two well-characterized cell lines have been confirmed for HPV-positivity and shown to express viral factors and oncogenes E6 and E7, making them suitable for studies of HPV+ HNSCC *in vitro* (25). The SCC104 cell line was the primary choice for most of our experiments because of its robust growth and detailed phenotypic characterization compared to that for SCC152 (24); data from the SCC152 cell line were used to corroborate and/or validate the findings.

To identify the global network of p63 target genes, we performed ChIP-seq experiments in SCC104 cells with two anti-p63 antibodies. ChIP-seq of p63 with the widely used 4A4 antibody that recognizes all p63 isoforms identified 18,085 genomic sites, whereas ChIP-seq with a ΔNp63-specific antibody, ΔNp63-1.1, identified 10,028 p63-bound sites (**Figure 2A**); 9,724 sites were identified by both antibodies, which were deemed high-confidence p63 targets and utilized for subsequent analysis (**Supplementary Table 2**). As expected, analysis of the p63 ChIP-seq peaks using HOMER revealed the consensus p63 motif (p = 1e-7867) as the most highly enriched motif, followed by the p53 motif (p = 1e-5462), which was independently confirmed by using MEME-ChIP (**Figure 2B** and **Supplementary Figure 3B**). Other enriched motifs were for TFs belonging to the AP-1 family, which cooperates with p63 to regulate target gene expression (**Figure 2B**) (52). The distribution of p63 peaks relative to the transcriptional start sites revealed that, in both cell lines, p63 preferentially targets intragenic and distal regulatory regions, which are likely to act as enhancer sites (**Figure 2C** and **Supplementary Figure 3C**). A DAVID-based pathway analysis of the genes associated with the top 2,500 p63 ChIP-seq peaks revealed several important pathways, including those deemed important in HPV-associated cancers, such as focal adhesion, p53, and Rap1 signaling pathways (**Figure 2D**) (53, 54). Interestingly, focal

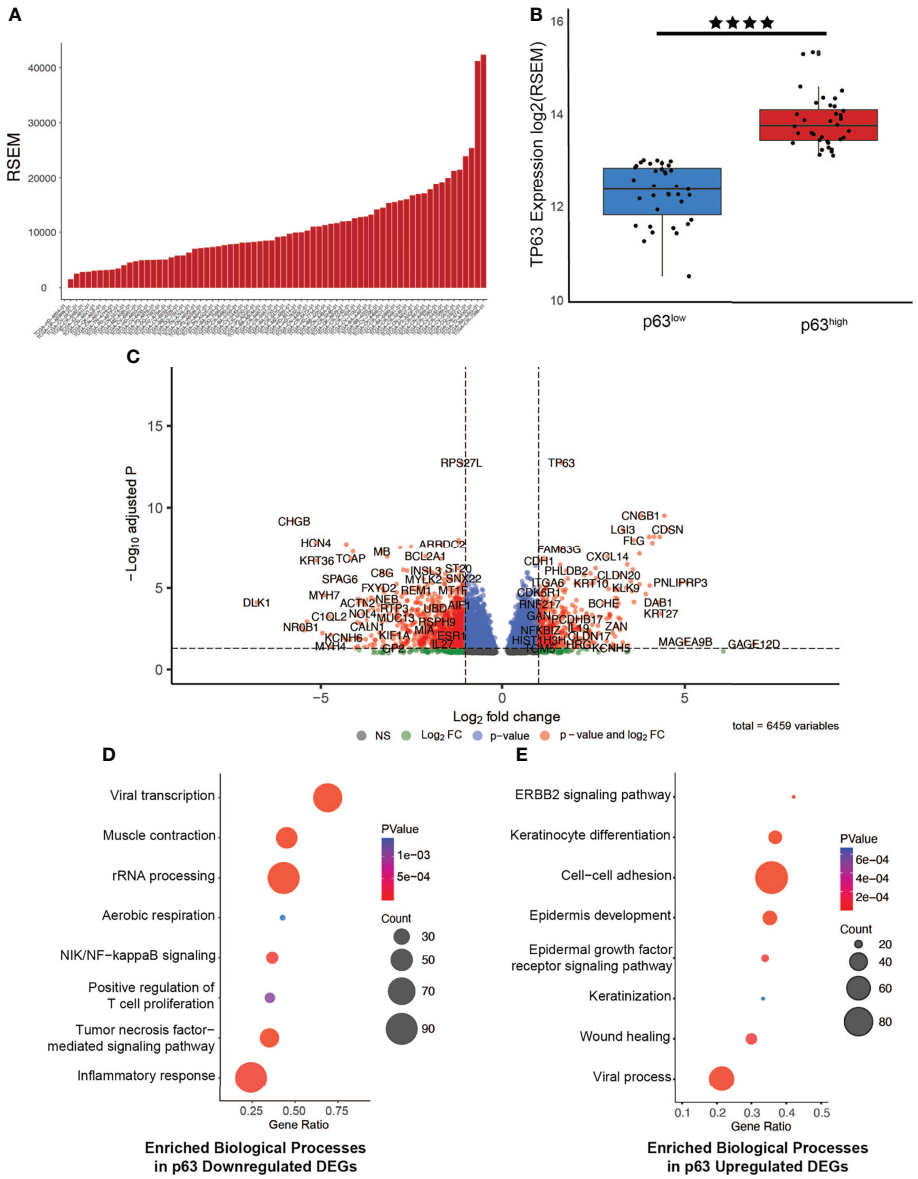

FIGURE 1 | Generation of a p63-driven gene signature in HPV+ HNSCC TCGA tumors. **(A)** Bar chart of p63 expression across tumors in the TCGA HPV+ HNSCC dataset. **(B)** Boxplots displaying the significant difference in expression of *TP63* between the groups (*p* value = 2.472e-6). Tumors were segregated into $p63^{low}$ and $p63^{high}$ groups on the basis of median p63 expression. **(C)** Volcano plot of identified DEGs between $p63^{low}$ and $p63^{high}$ samples. *TP63* is shown as one of the most significant DEGs. **(D)** Gene Ontology (GO) based biological pathway analysis of DEGs whose expression was downregulated according to p63 expression. **(E)** GO biological pathway analysis of DEGs whose expression was upregulated according to p63 expression. **** symbol means a *p*-value of ≤ 0.0001.

adhesion pathways are enriched in the subtype of HPV+ HNSCC tumors with high p63 expression levels (11, 14, 51). In parallel, we performed ChIP-seq of p63 in SCC152 utilizing the 4A4 antibody and identified 26,255 genomic peaks, with the p63 motif as the most enriched (**Supplementary Figures 3A, B** and **Supplementary Table 2**). p63 binding-associated genes in SCC152 were enriched in pathways involving MAPK signaling, cell adhesion molecules, and Rap1, which all play a role in HPV infection (**Supplementary Figure 3D**). Of the 9,724 high-confidence p63 binding sites (identified with both antibodies), 5,933 sites were shared between SCC104 and SCC152 cell lines, providing a strong list of bona-fide p63 targets in HPV+ HNSCC.

Characterizing the Enhancer Landscape of $p63^{high}$ HPV+ Cells

We next explored the epigenomic landscape of SCC104 and SCC152 by ChIP-seq using histone marks H3K27Ac, H3K4Me1, and H3K4Me3 (**Supplementary Figures 4A**, **5A**) (55), which

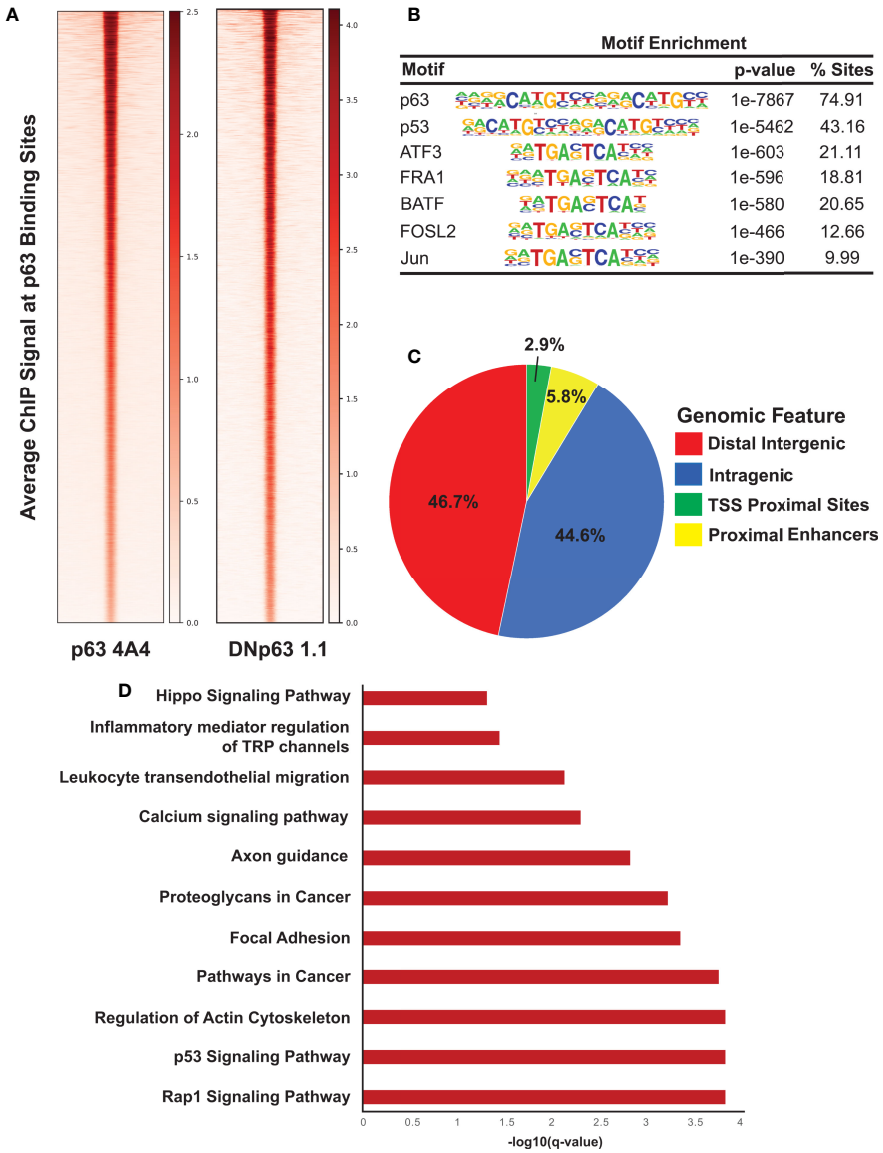

FIGURE 2 | ChIP-seq analysis reveals direct p63 targets in SCC104 cells. **(A)** Heatmap of the average ChIP-seq signals from p63 binding sites for two p63 antibodies across the genome. **(B)** Top transcription factor motifs derived from HOMER's motif analysis on SCC104 consensus p63 ChIP peaks. **(C)** Distribution pattern of genomic features associated with p63 binding sites across the genome. **(D)** Bar graphs displaying selected top enriched KEGG pathways associated with genes identified through GREAT analysis of the top 2,500 p63 ChIP-seq peaks.

identify gene regulatory features such as active enhancers ($H3K27Ac^{high}$ and $H3K4Me1^{high}$), active promoters ($H3K27Ac^{high}$ and $H3K4Me3^{high}$), and poised enhancers ($H3K27Ac^{low}$ and $H3K4Me1^{high}$) (56).We performed k-means clustering on the histone marks centering around each H3K27Ac peak as described in Gluck et al. (27), which identified three distinct clusters of regulatory elements. In SCC104 cells, clusters 1 and 3 represented active enhancers, and associated genes were enriched in pathways such as mRNA processing, differentiation, and focal adhesion (**Supplementary Figures 4B**). Cluster 2 represented active promoters, and associated genes were enriched in viral processes and cell motility (**Supplementary Figures 4A, B**). To identify which TFs may regulate enhancer expression in these clusters, we performed a motif analysis and found enrichment of ZNF, IRF, KLF, and Ets family motifs as well as E2F motifs (**Supplementary Figure 4C**).

Similar results were obtained in clustering analysis of SCC152 cells, where clusters 1 and 3 also represented active enhancers, and genes associated with these sites were enriched in focal adhesion, cell junction assembly, and Notch signaling pathways (**Supplementary Figure 5B**). Cluster 2 was similarly associated with active promoters, and associated genes were enriched in

mRNA processing and cell-cell adhesion pathways (**Supplementary Figures 5A, B**). Motif analysis of these regions in SCC152 also showed enrichment of E2F motifs within all identified clusters (**Supplementary Figure 5C**). The enrichment of E2F motifs across various gene regulatory elements in both HPV + HNSCC cell lines is interesting and likely to be relevant given the known interaction of E2F TFs and HPV E7 and its effects on downstream pathways in HPV+ disease.

p63 Is Super-Enhancer Marked and Regulates Expression of Super-Enhancer-Associated Genes in HPV+ HNSCC

Multi-cluster enhancers, often referred to as super-enhancers (SEs), are associated with H3K27Ac^{high} marks and are densely occupied by key TFs (42, 57). These SEs are often associated with cell identity and lineage-driving genes and oncogenes, and in the context of HPV, viral oncoproteins have been found to play a central role in their activation (58, 59). It is postulated that SEs at the site of HPV integration likely upregulate the expression of HPV E6/E7, leading to activation of other SEs that facilitate disease progression (60). By applying the ROSE algorithm to the H3K27Ac ChIP-seq data, we identified 528 SEs in SCC104 and 317 SEs in SCC152 (**Figure 3A** and **Supplementary Figure 6A**, **Supplementary Table 3**) (42, 61). As expected, several SEs were associated with master TFs, including p63, but we also observed SEs associated with genes important to HPV infection and HPV-induced carcinogenesis, such as *WNT7A*, *ITGA2*, and *NOTCH1*. (**Figure 3B** and **Supplementary Figure 6B**; **Supplementary Table 3**) (62, 63). Motifs for TFs with known roles in HNSCC, including FOSL1, E2F1, and E2F7 (10, 64), were also enriched at SCC104 SEs (**Figure 3C** and **Supplementary Figure 6C**). We found significant enrichment of the p63 motif in SCC104 SEs, suggesting p63 regulates the transcription of many SE-associated genes in HPV+ HNSCC (**Figure 3C** and **Supplementary Figure 6C**). The enrichment of the p63 motif in SEs is functionally relevant, because most (369/540) were occupied by p63 according to the ChIP-seq results from SCC104 cells.

Analysis of SE-marked genes revealed notable enrichment of pathways associated with cancer, including those for focal adhesion and those involving proteoglycans (**Figure 3D**). Interestingly, we found that *SDC1*, which encodes protein syndecan-1 and is a direct p63 target, was associated with SEs (**Supplementary Table 3**). This is notable because syndecan-1 is the most abundant heparan sulfate proteoglycan in keratinocytes and serves as the primary HPV attachment receptor (65). HPV infection is known to affect the expression of genes involved with cell adhesion and cell motility, and several of the implicated genes were found in our data, including *LAMA5*, *ITGA3*, *ITGA6*, and *LAMC2* (11, 36, 54, 66). SE-marked genes in SCC152 were similarly enriched in pathways important for cancer, including the Hippo signaling pathway, implicated in HPV-associated oropharyngeal SCC (**Supplementary Figure 6D**) (67).

We next explored the epigenomic state (as defined by histone marks) of the gene regulatory regions bound by p63 that were identified by ChIP-seq. For this purpose, we performed k-means clustering of the three histone marks, which again identified three distinct clusters (**Supplementary Figures 7A**, **8A**). In SCC104 cells, cluster 1 represented active promoters, and genes associated with these sites were enriched in pathways for apoptosis, cell adhesion, and motility (**Supplementary Figure 7B**). Clusters 2 and 3 represented active enhancers, and the corresponding genes were associated with Notch, protein kinase B, and Rho signaling (**Supplementary Figures 7A, B**). Unsurprisingly, we observed enrichment of AP-1 motifs in p63-bound enhancer regions regulating such processes as signaling and differentiation, which has been reported in keratinocytes and breast cancer (68). Interestingly, we observed enrichment of E2F motifs in cluster 1, suggesting the interaction between p63 and E2F at active promoter regions regulates cellular movement and apoptosis (**Supplementary Figure 7C**).

Similar analyses in SCC152 cells showed identical patterns of clustering of gene regulatory elements, with cluster 1 representing active promoters and clusters 2 and 3 representing active enhancers (**Supplementary Figure 8A**). Cluster 1 showed enrichment of pathways associated with apoptosis and cellular organization (**Supplementary Figure 8B**). Unlike that in SCC104 cells, we did not find enrichment of E2F motifs in these regions but instead saw enrichment of FOX motifs (**Supplementary Figure 8C**). Genes found in clusters 2 and 3 were associated with tissue development, Notch signaling, and cell adhesion pathways (**Supplementary Figure 8B**). Similar to that for SCC104 cells, there was enrichment of ZNF, IRF, and ETS family motifs; however, there was no enrichment of AP-1 motifs (**Supplementary Figure 8C**). These findings suggest that p63 actively regulates genes and pathways considered important in HPV-induced carcinogenesis and that p63 may interact with cellular E2Fs at gene regulatory regions.

Loss of p63 Expression Dysregulates Signaling Pathways Involved in HPV-Associated Carcinogenesis

To identify p63 targets, we performed RNA-seq to profile the global transcriptomic changes resulting from loss of p63 expression. For these experiments, we stably knocked down p63 in SCC104 and SCC152 cells with two independent lentiviral mediated shRNAs. Western blotting confirmed that both shRNAs significantly reduced p63 expression, with sh2 showing markedly greater knockdown (**Figure 4A**). Loss of p63 substantially altered the transcriptomic landscape, with 6,607 and 5,809 genes exhibiting statistically meaningful changes in expression in SCC104 and SCC152 cells, respectively (**Supplementary Table 4**). Of these, 2,189 and 1,461 DEGs showed statistically meaningful ($p_{adj} < 0.1$) changes with both p63 shRNAs in SCC104 and SCC152 cells, respectively (**Figure 4B** and **Supplementary Figure 9A**; **Supplementary Table 4**).

To explore pathways affected by loss of p63, we focused on a select group of 615 DEGs (≥log2 fold change of 1) common to both shRNA knockdowns in SCC104 cells. KEGG analysis of these DEGs showed enrichment of many pathways important in HPV-associated carcinogenesis, such as WNT, MAPK, and PI3K-Akt signaling (**Figure 4C** and **Supplementary Figure 9B**) (21, 53, 62, 69, 70). We also performed gene set

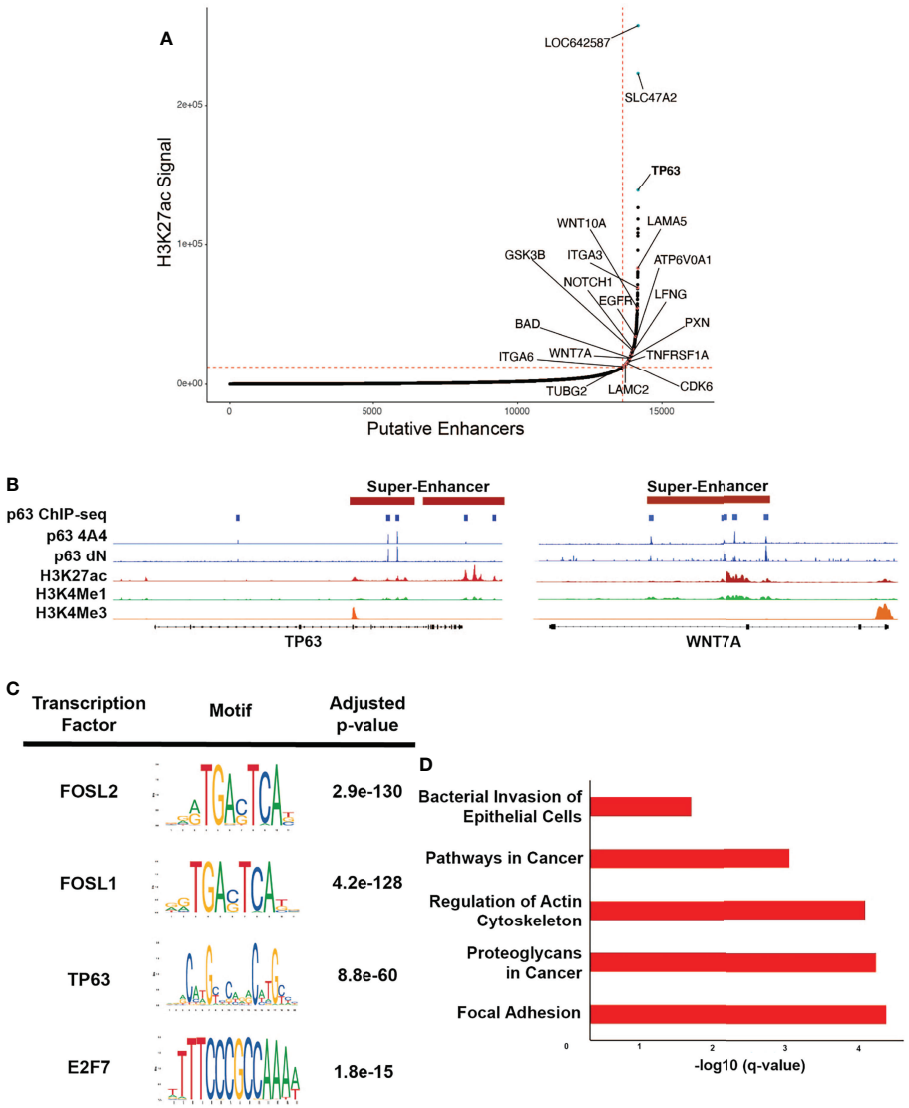

FIGURE 3 | p63 binding enriched at SEs in SCC104. **(A)** Hockey plot displaying the ranked H3K27Ac ChIP-seq signal in SCC104 cells. Representative genes marked by super-enhancers (SE) are shown. *TP63* is highlighted in blue as one of the top SE-associated genes in SCC104. Other labeled points represent genes that have been found in previous literature to be associated with HPV infection. **(B)** Integrative Genomics Viewer (IGV) based representation of Histone and p63 ChIP-seq data from SCC104 cells showcasing peaks of binding around the *TP63* and *WNT7A* loci. **(C)** Top enriched transcription factor motifs found in SE regions in SCC104 cells. **(D)** Bar graphs displaying selected top enriched KEGG pathways associated with genes identified through ROSE analysis of the SE landscape in SCC104 cells.

enrichment analysis of canonical pathways associated with these DEGs, which identified cell cycle and retinoblastoma gene in cancer categories (**Figure 4D**). Genes involved in the pRb signaling pathway, including *E2F1* and *CCNA2*, were significantly upregulated by the loss of p63, suggesting that p63 suppresses E2F-induced transcription and cell cycle activation.

The enrichment of pathways associated with HPV after p63 knockdown prompted us to look closer into the known HPV infection pathway. Of the 324 genes in the KEGG "human papillomavirus infection" pathway, 62 were differentially expressed upon p63 knockdown (**Supplementary Figure 10A**). HPV infection affects cell cycle regulation, which was also the case with p63 knockdown. Several factors involved in the cell cycle, including E2F1, RBL1, and cyclin A2, were upregulated upon loss of p63 (**Supplementary Figure 10A**). We also observed high enrichment of genes involved in focal adhesion and WNT and PI3K signaling (**Supplementary Figure 10B**).

Generation of an Overall p63-Driven Gene Signature in HPV+ HNSCC

To delineate our high-stringency p63-driven gene signature, we combined the gene signatures we identified from TCGA tumor

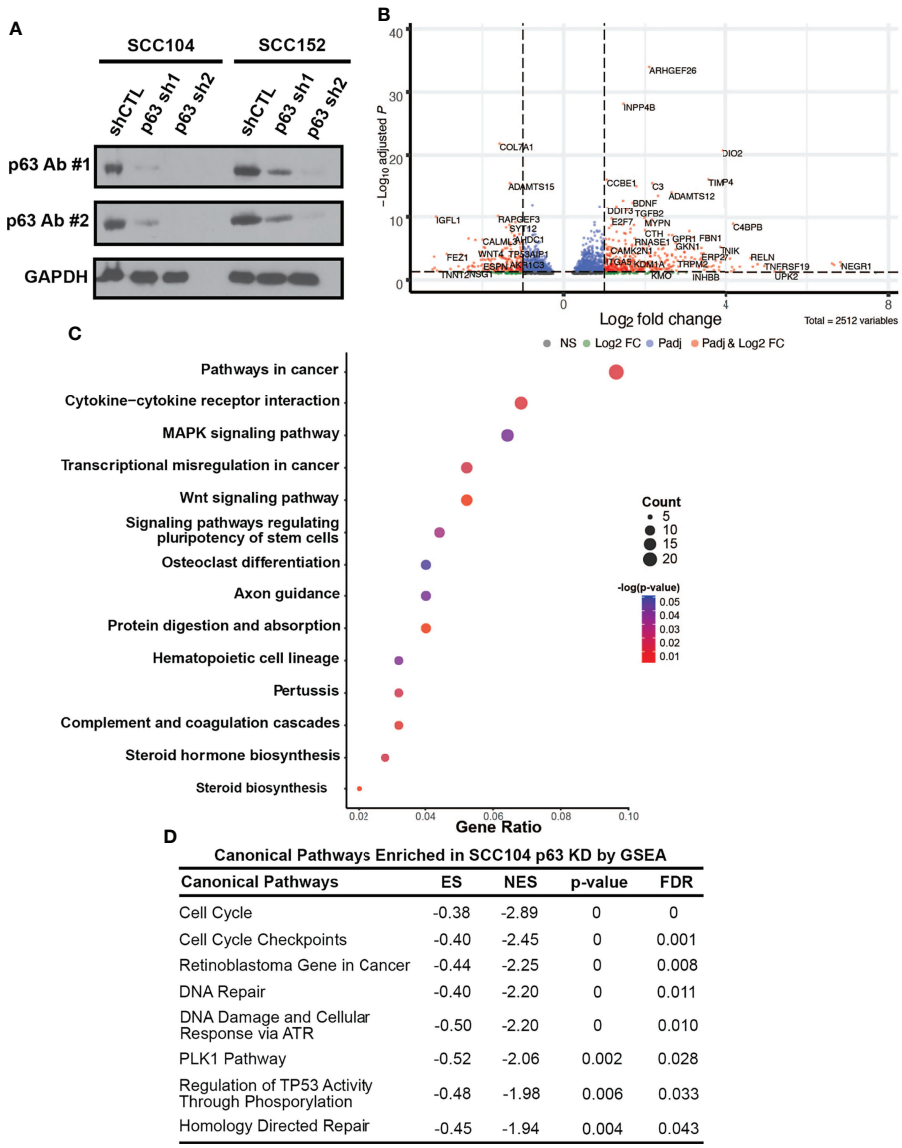

D

Canonical Pathways Enriched in SCC104 p63 KD by GSEA

Canonical Pathways	ES	NES	p-value	FDR
Cell Cycle	-0.38	-2.89	0	0
Cell Cycle Checkpoints	-0.40	-2.45	0	0.001
Retinoblastoma Gene in Cancer	-0.44	-2.25	0	0.008
DNA Repair	-0.40	-2.20	0	0.011
DNA Damage and Cellular Response via ATR	-0.50	-2.20	0	0.010
PLK1 Pathway	-0.52	-2.06	0.002	0.028
Regulation of TP53 Activity Through Phosporylation	-0.48	-1.98	0.006	0.033
Homology Directed Repair	-0.45	-1.94	0.004	0.043

FIGURE 4 | p63 knockdown in SCC104 shows enrichment of HPV-associated signaling pathways. **(A)** Western blot analysis of p63 expression in SCC104 and SCC152 cells expressing either p63-targeting shRNAs or a nontargeting shRNA (shCTL). GAPDH: loading control. **(B)** Volcano plot of DEGs resulting from p63 knockdown in SCC104 cells. **(C)** KEGG pathway analysis of SCC104 DEGs whose expression showed ≥log2 fold change of 1. **(D)** Gene set enrichment analysis (GSEA) of DEGs from p63 knockdown in SCC104 cells.

data and from the p63 expression-defined cell lines (**Supplementary Figure 11A** and **Supplementary Table 1**). To identify which genes are most reliant on p63 expression, we utilized our sh2 data from both cell lines to generate our HPV+ cell line-based signatures (**Supplementary Figure 11A** and **Supplementary Table 5**). These analyses identified 1,052 genes shared between the TCGA and SCC104 datasets and 827 genes shared between the TCGA and SCC152 datasets (**Supplementary Figure 11B**). Then, to identify genes which were directly regulated by p63, we incorporated our p63 ChIP-seq data, which revealed 498 and 574 genes that were directly bound by p63 in SCC104 and SCC152 cells, respectively (**Supplementary Figure 11B**). We filtered all genes that were common between analyses to generate our combined p63 signature of 420 genes (**Supplementary Table 5** and **Supplementary Figure 11B**). Finally, to identify genes of potential importance, we merged this gene signature with our super-enhancer landscape, which revealed 55 super-enhancer-associated genes (**Supplementary Figure 11B** and **Supplementary Table 5**). These analyses provided a p63-driven gene expression signature in HPV+ HNSCC that is relevant in both cancer and HPV contexts for follow-up studies.

p63 May Be a Key Player in Subtype-Specific HPV+ HNSCC Gene Expression

To explore how p63 regulates subtype-specific gene expression in HPV+ HNSCC, we compared our combined p63-driven signature of 420 genes with the aforementioned subtype-specific signatures. Our previous analyses of transcriptomic changes upon p63 knockdown revealed enrichment of cell adhesion and keratinization pathways, like the HPV-KRT subtype defined by Keck et al. (14) and Zhang et al. (11). Keck et al. (14) found HPV-KRT tumors upregulate genes involved in hypoxia, cell adhesion, and HER signaling as well as epithelial-associated genes, whereas genes involved in immune response and mesenchymal-associated genes are downregulated. Our $p63^{high}$ signature displayed a similar pattern of upregulated gene expression (compared to expression in $p63^{low}$ samples), supporting the notion that high p63 expression is a defining aspect of the HPV-KRT subtype (**Figure 5A**). Interestingly, we also found that 36 of our 420 p63 signature genes, including *MAOA, SLC2A1, COL17A1*, and *KRT16*, were associated with the reported HPV-KRT subtype signature (**Supplementary Table 6**). Conversely, the $p63^{low}$ expression signature was enriched with genes associated with the immune response and mesenchymal tissues (**Figure 5A**).

The HPV-KRT signature defined by Zhang et al. (11) had patterns of expression and pathway enrichment similar to the signature defined by Keck et al. (14). Accordingly, the gene signatures within our $p63^{high}$ subgroups also showed comparable upregulation of genes associated with keratinization, redox processes, and cell adhesion previously seen by Zhang et al. (11) (relative to expression in the $p63^{low}$ samples) (**Figure 5B**). The HPV-KRT-like subtype signature defined by Zhang et al. (11) was apparent in our p63-based DEGs (49 DEGs, including *TP63, MAOA, PPARD*, and *KRT16*) (**Figure 5B** and **Supplementary Table 6**), whereas the $p63^{low}$ samples had upregulated genes associated with the immune response and mesenchymal differentiation (**Figure 5B**). To validate the differences in expression observed between the $p63^{high}$ and $p63^{low}$ groups and in our p63-driven signature, we performed qRT-PCR for several genes identified in each subtype signature, including *KRT16*, *SLC2A1*, and *MAOA*, in the HPV+ cell line with p63 knockdowns, confirming our RNA-seq findings (**Figure 5C**). Altogether, these findings support a role for p63 in subtype-specific gene expression within HPV+ HNSCC and suggest that p63 directs the specific gene

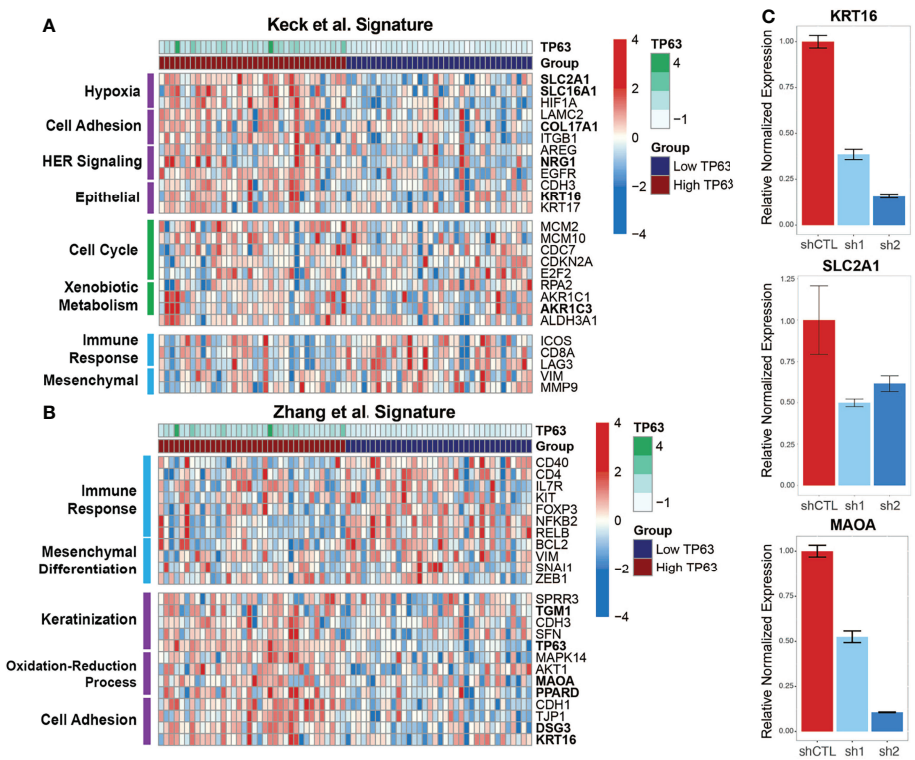

FIGURE 5 | $p63^{high}$ and $p63^{low}$ groups recapitulate published HPV+ HNSCC subtype gene signatures. **(A)** Heatmap representation of expression of genes from the Keck et al. (14) signature within the $p63^{high}$ and $p63^{low}$ HPV+ HNSCC TCGA samples. DEGs are separated based on distinct patterns of expression between the $p63^{high}$ and $p63^{low}$ groups. Specific biological and signaling pathways associated with the DEGs are indicated. Bolded genes represent those that were included in the consensus p63-derived gene signature. **(B)** Heatmap representation of expression of genes from the Zhang et al. (11) signature within our $p63^{high}$ and $p63^{low}$ HPV+ HNSCC TCGA samples. DEGs are divided up by patterns of expression between the $p63^{high}$ and $p63^{low}$ groups. Specific biological and signaling pathways associated with the DEGs are indicated. Bolded genes represent those that were included in the consensus p63-derived gene signature. **(C)** Graph showing qRT-PCR results for normalized expression of 3 key genes in SCC104 cells expressing shCTL and p63 shRNAs.

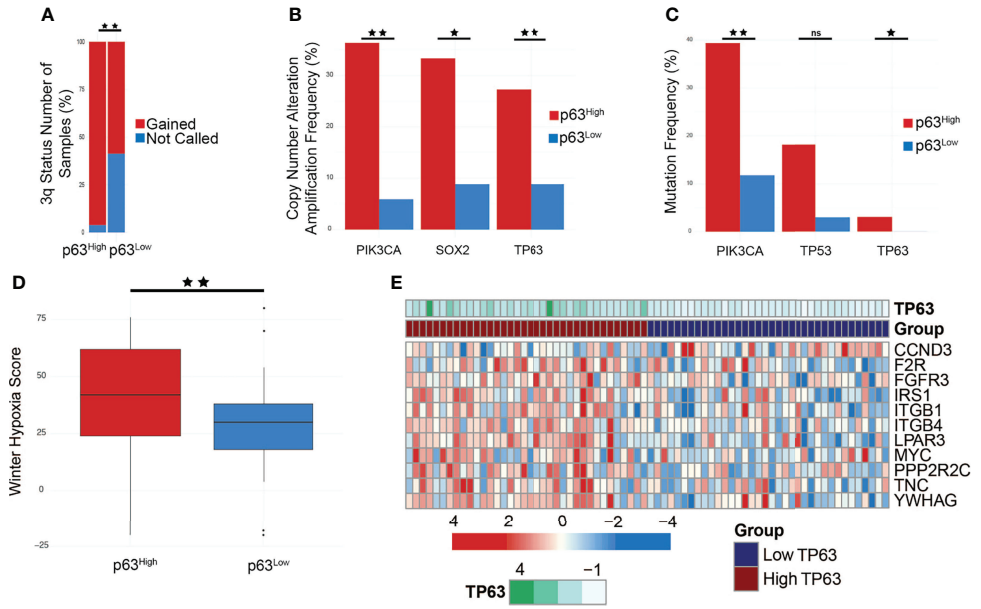

FIGURE 6 | *PIK3CA* is amplified and mutated in p63^{high} tumors and affects PI3K signaling. **(A)** Bar graph comparing chromosome 3q status between p63^{high} and p63^{low} TCGA samples ($p < 0.01$). **(B)** Copy number alteration (CNA) frequencies in p63^{high} and p63^{low} TCGA samples (*PIK3CA*, $p = 2.242e\text{-}3$; *SOX2*, $p = 0.0141$; *TP63*, $p = 0.0483$). **(C)** Mutation frequencies in p63^{high} and p63^{low} TCGA samples (*PIK3CA*, $p = 9.522e\text{-}3$; *TP53*, $p = 0.0482$; *TP63*, $p = 0.493$). **(D)** Boxplot of the Winter hypoxia scores for p63^{high} and p63^{low} TCGA samples ($p = 0.0121$). **(E)** Heatmap of genes involved in PI3K signaling that were present in the combined cell line/TCGA based p63 signature. *p-value of ≤ 0.05, **p-value of ≤ 0.01, ns, non-significant.

expression profiles that were discovered by hierarchal clustering of global gene expression in HPV+ HNSCC.

p63 Exerts Broad Control of the PI3K-Signaling Pathway

HPV+ HNSCC subtypes also have differences in copy number alteration (CNA) patterns and mutation frequencies, specifically in *PIK3CA*. Furthermore, HPV E6 and E7 oncoproteins are implicated in regulating the PI3K/AKT/mTOR network in cancer cells under both normoxic and hypoxic conditions, specifically by regulating AKT, a main effector of both PI3K and mTORC1 signaling (71). We utilized cBioPortal to examine the genomic properties of our p63 subgroups within the TCGA HNSCC tumor dataset, and compared our findings with those by Keck et al. (14) and Zhang et al. (11). Zhang et al. (11) found that HPV-KRT tumors had more amplifications in chr3q than HPV-IMU, the subtype with a strong immune response. Notably, *TP63* is located on chr3q, providing more evidence toward p63 as a driver of this subtype. In accordance, p63^{high} samples had significantly more gains in chr3q than p63^{low} samples (**Figure 6A**). We also explored the frequency of Copy Number Alterations (CNA), specifically amplification events, of genes found within chr3q and found that *TP63*, *SOX2*, and *PIK3CA* had significantly more amplification events in the p63^{high} group ($p = 0.0483$, 0.0141, and 2.242e-3, respectively) (**Figure 6B**).

PI3K signaling plays a role in tumorigenesis, and activating mutations in *PIK3CA* have been found in various cancer types (72). Given the relationship between p63 and activated PIK3CA, we sought to explore if a p63/PI3K signaling axis is active within HPV+ HNSCC (73). First, we examined the mutational status of *PIK3CA* in the p63^{high}/p63^{low} TCGA samples. Strikingly, we found that *PIK3CA* was one of the most highly mutated genes ($p = 9.522e\text{-}3$) in p63^{high} samples, with 40% of tumors harboring *PIK3CA* mutations (**Figure 6C**), similar to what has been reported for the HPV-KRT subtype. Combined with the increased copy number for *PIK3CA* in p63^{high} samples, these data strongly suggest that PI3K activity is upregulated in p63^{high} tumors. The clinical data associated with these p63^{high} and p63^{low} groups revealed a significant difference in the Winter hypoxia score, with the p63^{high} tumors having significantly higher hypoxia scores ($p = 0.0121$) (**Figure 6D**). Hypoxia stimulates AKT signaling and downregulates E6/E7 expression, inducing reversible growth arrest that is a potential pathway by which HPV+ cancers, such as HPV-KRT tumors, evade the immune response and become resistant to therapy (9, 74). The p63 signature included several PI3K pathway members that were affected by p63 knockdown in HPV+ HNSCC cell lines and were part of the p63 expression-based DEGs from the TCGA datasets (**Figure 6E**). These data point to a likely role of p63 in regulating the PI3K signaling pathway within HPV+ HNSCC.

To systematically follow up on the p63-PI3K link, we examined the p63 knockdown datasets and found that many of the DEGs in the KEGG PI3K signaling pathway are known p63 targets, and importantly, some of these DEGs were associated with SEs (**Figure 7A**). Although the expression of many of the genes associated with PI3K signaling was decreased by p63

knockdown, the expression of *AKT1* was modestly increased. We suspect this is due to the loss of repressive effects of other p63 targets. In support of this, qRT-PCR analysis showed that expression of *PTEN*, a negative regulator of phosphorylation and activation of AKT1, is decreased upon p63 knockdown in SCC104 and SCC152 cells (**Figure 7B**). By contrast, the expression of *PIK3CA*, the gene encoding the catalytic subunit of the PI3K complex, was decreased upon knockdown of p63 (**Figure 7B**). We also examined the mTOR pathway, which is downstream of PI3K, not only because it is dysregulated in HPV+ HNSCC but also because mTOR inhibitors show promising anticancer effects in HPV+ HNSCC mouse models (75). Similar to what we found for the PI3K pathway, we saw a general loss of downstream expression of mTORC1 targets upon p63 knockdown, suggesting a downregulation of mTORC1 signaling.

Finally, we performed Western blotting for some of the proteins involved in PI3K and mTORC1 signaling to confirm the transcriptomic findings. We found that the protein levels of

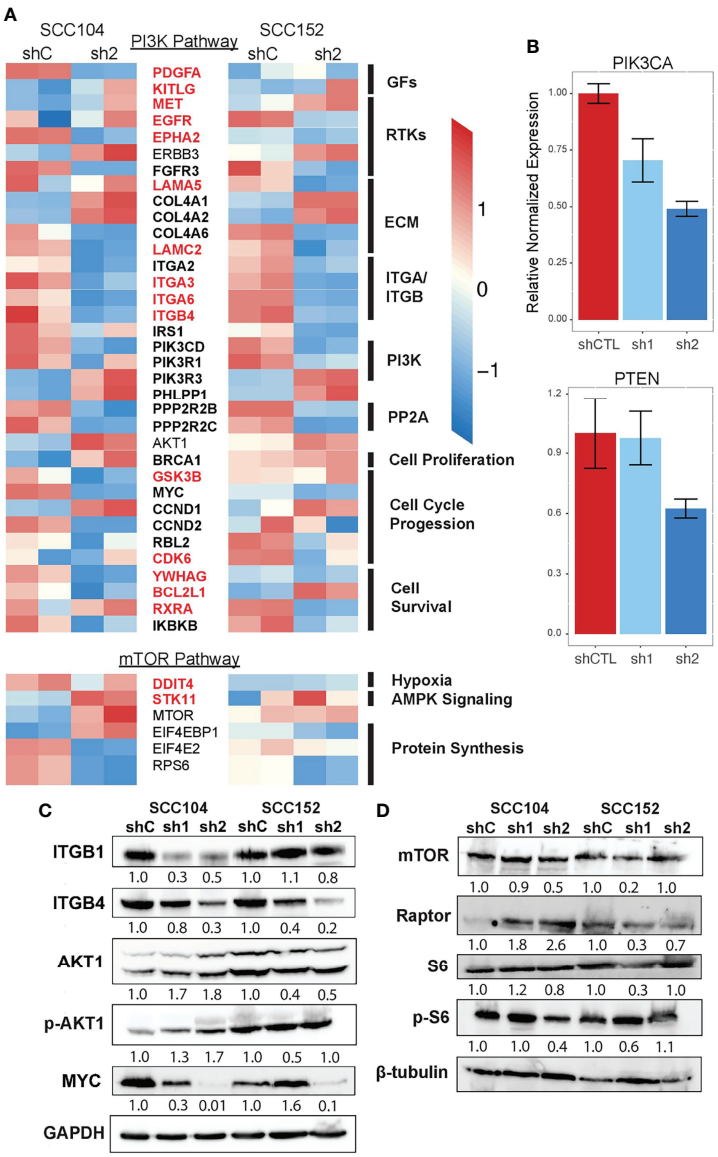

FIGURE 7 | PI3K and mTOR signaling is downregulated upon loss of p63 expression. **(A)** Heatmap of select DEGs shared between SCC104 and SCC152 cells after p63 knockdown that are associated with activation and regulation of the PI3K signaling pathway. Red-labeled genes are SE marked, and bolded genes are direct p63 targets. **(B)** qRT-PCR of SCC104 shCTL and p63 shRNA cell lines. Graphs show the relative normalized expression of the catalytic subunit of PI3K as well as the PI3K phosphatase PTEN. **(C, D)** Western blot results for representative key members of the PI3K pathway **(C)** and mTOR pathway **(D)** upon p63 knockdown in SCC104 and SCC152. Densitometric analysis of protein abundance between control (shC) and knockdown (sh1 and sh2) conditions is displayed below each blot.

upstream regulators of PI3K (ITGB1 and ITGB4) were decreased in SCC104 and SCC152 cells with p63 knockdown (**Figure 7C**), in line with the RNA-seq results. A downstream target of PI3K signaling, MYC, was also downregulated by p63 knockdown, suggesting a broader dampening of PI3K signaling upon loss of p63. However, the levels of phosphorylated AKT1 (pAKT1) were elevated in SCC104 cells with p63 knockdown, suggesting the PI3K pathway is activated despite the downregulated mRNA expression of some of the key signaling components. This suggests that a complex regulatory network controls AKT activation and that other regulators (aside from p63) indirectly play a role. Western blotting also revealed mixed results for components in the mTORC1 pathway (**Figure 7D**). Whereas mTOR expression was decreased in SCC104 cells with p63 knockdown, protein levels of Raptor, a key mTOR-interacting partner, was increased (**Figure 7D**), suggesting a more complex regulatory network for mTOR activation. However, the phosphorylation of S6 ribosomal protein (pS6), a key downstream mediator of mTOR activation was reduced in SCC104, indicating that overall mTORC1 signaling was dampened by the loss of p63 (**Figure 7D**). Taken together, these results point to a complex signaling network by which p63 regulates the PI3K and mTORC1 signaling pathway in HPV+ HNSCC, which may have implications for potential therapeutics.

DISCUSSION

HNSCC associated with high-risk human HPV infection is a growing problem that is clinically and biologically distinct from HPV- HNSCC. Molecular studies of HPV+ HNSCC in the past focused primarily on tumor suppressor pathways that are targeted by viral oncoproteins such as E6, which inactivates the p53 tumor suppressor protein by instigating its degradation (9). However, the operation of oncogenic drivers in the underlying complex genomic and epigenomic milieu of HPV+ HNSCC remains unclear. Studies of p63, especially oncogenic ΔNp63, have established its role in directing broad transcriptional programs in SCCs in various anatomical sites, including the oral cavity (21, 49, 76). However, the specific role of p63 in modulating the transcriptomic landscape of HPV+ HNSCC has received less attention. To address this shortcoming, we leveraged genomic, transcriptomic, and epigenomic data from HPV+ HNSCC tumors and preclinical cell line models and identified p63 as a critical regulator that affects multiple facets of HPV+ HNSCC biology, including pathways essential in HPV-mediated carcinogenesis, and HNSCC subtype-specific gene expression.

One notable finding is the wide range of p63 expression levels across the HPV+ tumors, which is clearly evident in several independent datasets. This reinforces results from previously defined subtypes of HPV+ HNSCC based on hierarchical clustering of gene expression (11, 13, 14, 51). We provide evidence that the molecular and phenotypic attributes of the more aggressive $p63^{high}$ HPV-KRT subtype, such as keratinization and cell adhesion, are likely controlled by a p63-driven direct transcriptional program. Indeed, this is well supported by our integrated analysis of several complementary models that include HPV+ patient tumors and by an epigenetically refined ΔNp63 cistrome assembled from RNA-seq after p63 knockdown and ChIP-seq of p63 and histone marks in SCC104 and SCC152 cell lines. We suspect that the heterogeneity of HPV+ tumors is shaped not only by the expression and the transcriptional output of p63 in the tumor epithelium but also by the enhanced influence of p63 in the tumor microenvironment, as evidenced in triple-negative breast cancer (77). This notion is supported by our identification of enriched immune pathways and immune-related genes as p63 targets, some of which were associated with SEs in SCC104 and SCC152 cells.

The tumor microenvironment of HPV+ HNSCC is distinct from that of its HPV- counterpart, with greater immune infiltration, T-cell activation, and immunoregulation (51). Furthermore, two recent landmark single-cell-based studies indicated that HPV-specific infiltrating lymphocytes may mount an immune-based response to HPV+ HNSCC (78, 79). In these studies, HPV oncoprotein E2 was a target of particular interest, as E2 expression is often maintained in HPV+ HNSCC unlike in HPV+ cervical cancer. Interestingly, E2 expression is lower in the $p63^{high}$ HPV-KRT subtype, most likely because of higher levels of HPV genomic integration, which disrupts HPV early gene expression (11, 51). We suspect that the relatively lower immune cell infiltration and activation in HPV-KRT tumors may be attributable to their $p63^{high}$ and $E2^{low}$ state. Taken together, these studies suggest that more attention should be paid to HPV+ subtypes, because their inherent differences, especially in their tumor microenvironments, likely affect their clinical outcomes.

Our integrated analysis revealed many interesting insights into p63 and its link to specific aspects of HPV biology. One novel potential regulatory mechanism of p63 involves E2F family members, notably E2F1 and E2F7, which regulate cell cycle gene expression in HPV infection and HPV-associated cancers (10, 80). Indeed, E2F7 was consistently enriched throughout our analyses as a direct target of p63 and as a TF whose motif was enriched around many p63-bound genomic sites and in SEs. E2F7 is an atypical E2F factor and a transcriptional repressor of genes involved in genomic stability, cell proliferation, and migration (80, 81). Knockdown of p63 in HPV+ HNSCC cell lines upregulated E2F7 expression, leading us to speculate that the increased p63 expression in HPV+ HNSCC negates the repressive function of E2F7. It is possible that p63 and E2F7 physically interact and coregulate genes that have joint p63/E2F motifs in their regulatory elements, an interesting notion that could be experimentally tested pending the availability of ChIP-grade E2F7 antibodies. Further investigation into the p63-E2F network is needed given the p63-dependent enrichment of pathways related to pRB, the cell cycle, and cell cycle checkpoints that are relevant for HPV+ HNSCC. Along the same line, it is likely that p63-p53 interactions are a key component in the cell cycle circuitry given p63's ability to regulate some p53 targets in the presence or absence of p53 (15, 82, 83).

The results from our studies reemphasize the need to further characterize the drivers and molecular attributes of HPV+ HNSCC subtypes given the potential differences in overall patient survival between the subtypes. This is particularly important in light of recent efforts to identify treatment de-escalation strategies for HPV+ HNSCC to reduce adverse events while maintaining better oncologic outcomes. Unfortunately, two large phase III clinical trials have shown inferior overall survival and progression-free survival as well as increased rates of locoregional failure (6, 84, 85), prompting reevaluation of ongoing deintensification trials for HNSCC. Although current HNSCC treatment options take HPV status into account, we posit that a personalized genomics approach that considers HPV+ subtypes would better inform treatment options and prevent failure of treatment de-escalation. The activated PI3K signaling that we uncovered in the $p63^{high}$ HPV-KRT subtype also suggests a potential avenue for therapeutic intervention. Compensatory activation of downstream signaling pathways, including PI3K, has been suggested as one of the major mechanisms of resistance to EGFR inhibitors, including cetuximab (86). The addition of a mTOR/PI3K inhibitor effectively controls cell growth in EGFR inhibitor-resistant HNSCC, suggesting that combination therapy may increase treatment efficacy (87, 88). In addition, mTOR inhibitors show promising anticancer effects in HPV+ HNSCC xenograft mouse models (75). We suspect that patients with the $p63^{high}$ tumor subtype would benefit from a combination of EGFR and PI3K inhibitor treatment and radiotherapy.

Altogether, the results from our studies suggest p63 and its key downstream effectors can be used as stratification markers for HPV+ HNSCC patients. However, this requires validation of our preclinical genomic and epigenomic data in tumors from HPV+ HNSCC patients.

DATA AVAILABILITY STATEMENT

The datasets presented in this study can be found in online repositories. The names of the repository/repositories and accession number(s) can be found below: https://www.ncbi.nlm.nih.gov/geo/query/acc.cgi?acc=GSE182133.

AUTHOR CONTRIBUTIONS

AG designed and performed experiments, acquired and analyzed data, prepared the figures, and wrote the manuscript. AO and CG performed experiments and acquired data. JB analyzed data. SS supervised the project and experimental design and wrote the manuscript. All authors contributed to the article and approved the submitted version.

FUNDING

AG was supported partly by NYSTEM contract no. C30290GG.

ACKNOWLEDGMENTS

We thank Kirsten Smalley for her excellent technical help. We also thank the UB Genomics and Bioinformatics Core for their next-generation sequencing services.

SUPPLEMENTARY MATERIAL

The Supplementary Material for this article can be found online at: https://www.frontiersin.org/articles/10.3389/fonc.2022.879054/full#supplementary-material

REFERENCES

1. Ferlay J, Shin HR, Bray F, Forman D, Mathers C, Parkin DM. Estimates of Worldwide Burden of Cancer in 2008: GLOBOCAN 2008. *Int J Cancer* (2010) 127(12):2893–917. doi: 10.1002/ijc.25516
2. Marur S, D'Souza G, Westra WH, Forastiere AA. HPV-Associated Head and Neck Cancer: A Virus-Related Cancer Epidemic – A Review of Epidemiology, Biology, Virus Detection and Issues in Management. *Lancet Oncol* (2020) 11 (3):781–9. doi: 10.1016/S1470-2045(10)70017-6
3. Seiwert TY, Zuo Z, Keck MK, Khattri A, Pedamallu CS, Stricker T, et al. Integrative and Comparative Genomic Analysis of HPV-Positive and HPV-Negative Head and Neck Squamous Cell Carcinomas. *Clin Cancer Res* (2015) 21(3):632–41. doi: 10.1158/1078-0432.CCR-13-3310
4. Leemans CR, Snijders PJF, Brakenhoff RH. The Molecular Landscape of Head and Neck Cancer. *Nat Rev Cancer* (2018) 18(5):269–82. doi: 10.1038/nrc.2018.11
5. Dok R, Nuyts S. HPV Positive Head and Neck Cancers: Molecular Pathogenesis and Evolving Treatment Strategies. *Cancers (Basel)* (2016) 8 (41):1–16. doi: 10.3390/cancers8040041
6. Ventz S, Trippa L, Schoenfeld JD. Lessons Learned From Deescalation Trials in Favorable Risk HPV-Associated Squamous Cell Head and Neck Cancer–A Perspective on Future Trial Designs. *Clin Cancer Res* (2019) 25(24):7281–6. doi: 10.1158/1078-0432.CCR-19-0945
7. Groves IJ, Coleman N. Human Papillomavirus Genome Integration in Squamous Carcinogenesis: What Have Next-Generation Sequencing Studies Taught Us? *J Pathol* (2018) 245(1):9–18. doi: 10.1002/path.5058
8. Viarisio D, Gissmann L, Tommasino M. Human Papillomaviruses and Carcinogenesis: Well-Established and Novel Models. *Curr Opin Virol* (2017) 26:56–62. doi: 10.1016/j.coviro.2017.07.014
9. Hoppe-Seyler K, Bossler F, Braun JA, Herrmann AL, Hoppe-Seyler F. The HPV E6/E7 Oncogenes: Key Factors for Viral Carcinogenesis and Therapeutic Targets. *Trends Microbiol* (2018) 26(2):158–68. doi: 10.1016/j.tim.2017.07.007
10. Faraji F, Zaidi M, Fakhry C, Gaykalova DA. Molecular Mechanisms of Human Papillomavirus-Related Carcinogenesis in Head and Neck Cancer. *Microbes Infect* (2017) 19(9–10):464–75. doi: 10.1016/j.micinf.2017.06.001
11. Zhang Y, Koneva LA, Virani S, Arthur AE, Virani A, Hall PB, et al. Subtypes of HPV-Positive Head and Neck Cancers Are Associated With HPV Characteristics, Copy Number Alterations, PIK3CA Mutation, and Pathway Signatures. *Clin Cancer Res* (2016) 22(18):4735–45. doi: 10.1158/1078-0432.CCR-16-0323
12. Walline HM, Goudsmit CM, McHugh JB, Tang AL, Owen JH, Teh BT, et al. Integration of High-Risk Human Papillomavirus Into Cellular Cancer-Related Genes in Head and Neck Cancer Cell Lines. *Head Neck* (2017) 39(5):840–52. doi: 10.1002/hed.24729
13. Walter V, Yin X, Wilkerson MD, Cabanski CR, Zhao N, Du Y, et al. Molecular Subtypes in Head and Neck Cancer Exhibit Distinct Patterns of Chromosomal Gain and Loss of Canonical Cancer Genes. *PloS One* (2013) 8(2):e56823. doi: 10.1371/journal.pone.0056823
14. Keck MK, Zuo Z, Khattri A, Stricker TP, Brown CD, Imanguli M, et al. Integrative Analysis of Head and Neck Cancer Identifies Two Biologically Distinct HPV and Three Non-HPV Subtypes. *Clin Cancer Res* (2015) 21 (4):870–81. doi: 10.1158/1078-0432.CCR-14-2481

15. Botchkarev V, Flores E. P53/P63/P73 in the Epidermis in Health and Disease. *Cold Spring Harb Perspect Med* (2014) 4(8):1260–6. doi: 10.1101/cshperspect.a015248
16. Romano R, Smalley K, Magraw C, Serna VA, Kurita T, Raghavan S, et al. Np63 Knockout Mice Reveal Its Indispensable Role as a Master Regulator of Epithelial Development and Differentiation. *Development* (2012) 139 (4):772–82. doi: 10.1242/dev.071191
17. Romano R, Ortt K, Birkaya B, Smalley K, Sinha S. An Active Role of the D N Isoform of P63 in Regulating Basal Keratin Genes K5 and K14 and Directing Epidermal Cell Fate. *PloS One* (2009) 4(5):e5623. doi: 10.1371/journal.pone.0005623
18. Soares E, Zhou H. Master Regulatory Role of P63 in Epidermal Development and Disease. *Cell Mol Life Sci* (2018) 75(7):1179–90. doi: 10.1007/s00018-017-2701-z
19. Sethi I, Romano RA, Gluck C, Smalley K, Vojtesek B, Buck MJ, et al. A Global Analysis of the Complex Landscape of Isoforms and Regulatory Networks of P63 in Human Cells and Tissues. *BMC Genomics* (2015) 16(1):1–15. doi: 10.1186/s12864-015-1793-9
20. Abbas HA, Bui NHB, Rajapakshe K, Wong J, Gunaratne P, Tsai KY, et al. Distinct TP63 Isoform-Driven Transcriptional Signatures Predict Tumor Progression and Clinical Outcomes. *Cancer Res* (2018) 78(2):451–62. doi: 10.1158/0008-5472.CAN-17-1803
21. Moses MA, George AL, Sakakibara N, Mahmood K, Ponnamperuma RM, King KE, et al. Molecular Mechanisms of P63-Mediated Squamous Cancer Pathogenesis. *Int J Mol Sci* (2019) 20:1–21. doi: 10.3390/ijms20143590
22. Rocco JW, Leong CO, Kuperwasser N, DeYoung MP, Ellisen LW. P63 Mediates Survival in Squamous Cell Carcinoma By Suppression of P73-Dependent Apoptosis. *Cancer Cell* (2006) 9(1):45–56. doi: 10.1016/j.ccr.2005.12.013
23. Citro S, Bellini A, Medda A, Sabatini ME, Tagliabue M, Chu F, et al. Human Papilloma Virus Increases Δnp63α Expression in Head and Neck Squamous Cell Carcinoma. *Front Cell Infect Microbiol* (2020) 10(April):1–6. doi: 10.3389/fcimb.2020.00143
24. Tang AL, Hauff SJ, Owen JH, Graham MP, Czerwinkski MJ, Park JJ, et al. UM-SCC-104: A New Human Papillomavirus-16–Positive Cancer Stem Cell–Containing Head and Neck Squamous Cell Carcinoma Cell Line. *Head Neck* (2011) 34(10):1480–91. doi: 10.1002/hed.21962
25. Greaney-Davies FST, Risk JM, Robinson M, Liloglou T, Shaw RJ, Schache AG. Essential Characterisation of Human Papillomavirus Positive Head and Neck Cancer Cell Lines. *Oral Oncol* (2020) 103:104613. doi: 10.1016/j.oraloncology.2020.104613
26. Love MI, Huber W, Anders S. Moderated Estimation of Fold Change and Dispersion for RNA-Seq Data With Deseq2. *Genome Biol* (2014) 15(12):1–21. doi: 10.1186/s13059-014-0550-8
27. Gluck C, Glathar A, Tsompana M, Nowak N, Garrett-Sinha LA, Buck MJ, et al. Molecular Dissection of the Oncogenic Role of ETS1 in the Mesenchymal Subtypes of Head and Neck Squamous Cell Carcinoma. *PloS Genet* (2019) 15(7):1–31. doi: 10.1371/journal.pgen.1008250
28. Nekulova M, Holcakova J, Nenutil R, Stratmann R, Bouchalova P, Müller P, et al. Characterization of Specific P63 and P63-N-Terminal Isoform Antibodies and Their Application for Immunohistochemistry. *Virchows Arch* (2013) 463(3):415–25. doi: 10.1007/s00428-013-1459-4
29. Langmead B, Trapnell C, Pop M, Salzberg SL. Ultrafast and Memory-Efficient Alignment of Short DNA Sequences to the Human Genome. *Genome Biol* (2009) 10(3):1–10. doi: 10.1186/gb-2009-10-3-r25
30. Zhang Y, Liu T, Meyer CA, Eeckhoute J, Johnson DS, Bernstein BE, et al. Model-Based Analysis of ChIP-Seq (MACS). *Genome Biol* (2008) 9(9):1–9. doi: 10.1186/gb-2008-9-9-r137
31. Mclean CY, Bristor D, Hiller M, Clarke SL, Schaar BT, Wenger AM, et al. GREAT Improves Functional Interpretation of Cis-Regulatory Regions. *Nat Biotechnol* (2010) 28(5):495–501. doi: 10.1038/nbt.1630
32. Ramírez F, Ryan DP, Grüning B, Bhardwaj V, Kilpert F, Richter AS, et al. Deeptools2: A Next Generation Web Server for Deep-Sequencing Data Analysis. *Nucleic Acids Res* (2016) 44(W1):W160–5. doi: 10.1093/nar/gkw257
33. Heinz S, Benner C, Spann N, Bertolino E, Lin YC, Laslo P, et al. Simple Combinations of Lineage-Determining Transcription Factors Prime Cis-Regulatory Elements Required for Macrophage and B Cell Identities. *Mol Cell* (2010) 38(4):576–89. doi: 10.1016/j.molcel.2010.05.004
34. Kim D, Paggi JM, Park C, Bennett C, Salzberg SL. Graph-Based Genome Alignment and Genotyping With HISAT2 and HISAT-Genotype. *Nat Biotechnol* (2019) 37(8):907–15. doi: 10.1038/s41587-019-0201-4
35. Wagner GP, Kin K, Lynch VJ. Measurement of mRNA Abundance Using RNA-Seq Data: RPKM Measure Is Inconsistent Among Samples. *Theory Biosci* (2012) 131(4):281–5. doi: 10.1007/s12064-012-0162-3
36. Ando M, Saito Y, Xu G, Bui NQ, Medetgul-Ernar K, Pu M, et al. Chromatin Dysregulation and DNA Methylation at Transcription Start Sites Associated With Transcriptional Repression in Cancers. *Nat Commun* (2019) 10(1):1–15. doi: 10.1038/s41467-019-09937-w
37. Wood O, Woo J, Seumois G, Savelyeva N, McCann KJ, Singh D, et al. Gene Expression Analysis of TIL Rich HPV-Driven Head and Neck Tumors Reveals a Distinct B-Cell Signature When Compared to HPV Independent Tumors. *Oncotarget* (2016) 7(35):56781–97. doi: 10.18632/oncotarget.10788
38. Gleber-netto FO, Skinner HD, Curtis R, Gleber-netto FO, Rao X, Guo T, et al. Variations in HPV Function are Associated With Survival in Squamous Cell Carcinoma. *JCI Insight* (2019) 4(1):e124762. doi: 10.1172/jci.insight.124762
39. Cerami E, Gao J, Dogrusoz U, Gross BE, Sumer SO, Aksoy BA, et al. The CBio Cancer Genomics. *Cancer Discovery* (2017) 32(7):736–40. doi: 10.1158/2159-8290.CD-12-0095
40. Gao J, Aksoy BA, Dogrusoz U, Dresdner G, Gross B, Sumer SO, et al. Integrative Analysis of Complex Cancer Genomics and Clinical Profiles Using the Cbioportal Complementary Data Sources and Analysis Options. *Sci Signal* (2014) 6(269):1–20. doi: 10.1126/scisignal.2004088
41. Whyte WA, Orlando DA, Hnisz D, Abraham BJ, Lin CY, Kagey MH, et al. Master Transcription Factors and Mediator Establish Super- Enhancers at Key Cell Identity Genes. *Cell* (2013) 153(2):307–19. doi: 10.1016/j.cell.2013.03.035
42. Loven J, Hoke HA, Lin CY, Lau A, Orlando DA, Vakoc CR, et al. Selective Inhibition of Tumor Oncogenes by Disruption of Super-Enhancers. *Cell* (2013) 153:320–34. doi: 10.1016/j.cell.2013.03.036
43. Georgiou G, van Heeringen SJ. Fluff: Exploratory Analysis and Visualization of High-Throughput Sequencing Data. *PeerJ* (2016) 2016(7):1–10. doi: 10.1101/045526
44. Shin H, Liu T, Manrai AK, Liu SX. CEAS: Cis-Regulatory Element Annotation System. *Bioinformatics* (2009) 25(19):2605–6. doi: 10.1093/bioinformatics/btp479
45. Kanehisa M, Furumichi M, Sato Y, Ishiguro-Watanabe M, Tanabe M. KEGG: Integrating Viruses and Cellular Organisms. *Nucleic Acids Res* (2021) 49(D1): D545–51. doi: 10.1093/nar/gkaa970
46. Huang DW, Sherman BT, Lempicki RA. Systematic and Integrative Analysis of Large Gene Lists Using DAVID Bioinformatics Resources. *Nat Protoc* (2009) 4(1):44–57. doi: 10.1038/nprot.2008.211
47. Huang DW, Sherman BT, Lempicki RA. Bioinformatics Enrichment Tools: Paths Toward the Comprehensive Functional Analysis of Large Gene Lists. *Nucleic Acids Res* (2009) 37(1):1–13. doi: 10.1093/nar/gkn923
48. Subramanian A, Tamayo P, Mootha VK, Mukherjee S, Ebert BL, Gillette MA, et al. Gene Set Enrichment Analysis: A Knowledge-Based Approach for Interpreting Genome-Wide Expression Profiles. *Proc Natl Acad Sci USA* (2005) 102(43):15545–50. doi: 10.1073/pnas.0506580102
49. Gatti V, Fierro C, Annicchiarico-Petruzzelli M, Melino G, Peschiaroli A. Δnp63 in Squamous Cell Carcinoma: Defining the Oncogenic Routes Affecting Epigenetic Landscape and Tumour Microenvironment. *Mol Oncol* (2019) 13(5):981–1001. doi: 10.1002/1878-0261.12473
50. Lo Muzio L, Santarelli A, Caltabiano R, Rubini C, Pieramici T, Trevisiol L, et al. P63 Overexpression Associates With Poor Prognosis in Head and Neck Squamous Cell Carcinoma. *Hum Pathol* (2005) 36(2):187–94. doi: 10.1016/j.humpath.2004.12.003
51. Qin T, Li S, Henry LE, Liu S, Sartor MA. Molecular Tumor Subtypes of Hpv-Positive Head and Neck Cancers: Biological Characteristics and Implications for Clinical Outcomes. *Cancers (Basel)* (2021) 13(11):1–21. doi: 10.3390/cancers13112721
52. Si H, Lu H, Yang X, Mattox A, Jang M, Bian Y, et al. TNF-α Modulates Genome-Wide Redistribution of Np63α/TAp73 and NF-κb C-REL Interactive Binding on TP53 and AP-1 Motifs to Promote an Oncogenic Gene Program in Squamous Cancer. *Oncogene* (2016) 35(44):5781–94. doi: 10.1038/onc.2016.112
53. Budhwani M, Lukowski SW, Porceddu SV, Frazer IH, Chandra J. Dysregulation of Stemness Pathways in HPV Mediated Cervical Malignant

Transformation Identifies Potential Oncotherapy Targets. *Front Cell Infect Microbiol* (2020) 10(June):1–9. doi: 10.3389/fcimb.2020.00307
54. Kivi N, Greco D, Auvinen P, Auvinen E. Genes Involved in Cell Adhesion, Cell Motility and Mitogenic Signaling Are Altered Due to HPV 16 E5 Protein Expression. *Oncogene* (2008) 27(18):2532–41. doi: 10.1038/sj.onc.1210916
55. Poreba E, Broniarczyk JK, Gozdzicka-Jozefiak A. Epigenetic Mechanisms in Virus-Induced Tumorigenesis. *Clin Epigenet* (2011) 2(2):233–47. doi: 10.1007/s13148-011-0026-6
56. Heinz S, Romanoski CE, Benner C, Glass CK. The Selection and Function of Cell Type-Specific Enhancers. *Nat Rev Mol Cell Biol* (2015) 16(3):144–54. doi: 10.1038/nrm3949
57. Sigova AA, Hnisz D, Abraham BJ, Lee TI, Lau A, Saint-andre V, et al. Super-Enhancers in the Control of Cell Identity and Disease. *Cell* (2013) 155:934–47. doi: 10.1016/j.cell.2013.09.053
58. Patel D, Huang SM, Baglia LA, McCance DJ. The E6 Protein of Human Papillomavirus Type 16 Binds to and Inhibits Co-Activation by CBP and P300. *EMBO J* (1999) 18(18):5061–72. doi: 10.1093/emboj/18.18.5061
59. Veldman T, Liu X, Yuan H, Schlegel R. Human Papillomavirus E6 and Myc Proteins Associate *In Vivo* and Bind to and Cooperatively Activate the Telomerase Reverse Transcriptase Promoter. *Proc Natl Acad Sci USA* (2003) 100(14):8211–6. doi: 10.1073/pnas.1435900100
60. Dooley KE, Warburton A, McBride AA. Tandemly Integrated HPV16 can Form a Brd4-Dependent Super-Enhancer-Like Element That Drives Transcription of Viral Oncogenes. *MBio* (2016) 7(5):1–10. doi: 10.1128/mBio.01446-16
61. Whyte WA, Orlando DA, Hnisz D, Abraham BJ, Lin CY, Kagey MH, et al. Master Transcription Factors and Mediator Establish Super-Enhancers at Key Cell Identity Genes. *Cell* (2013) 153(2):307–19. doi: 10.1016/j.cell.2013.03.035
62. Bello JOM, Nieva LO, Paredes AC, Gonzalez AMF, Zavaleta LR, Lizano M. Regulation of the Wntβ-Catenin Signaling Pathway by Human Papillomavirus E6 and E7 Oncoproteins. *Viruses* (2015) 7(8):4734–55. doi: 10.3390/v7082842
63. Khelil M, Griffin H, Bleeker MCG, Steenbergen RDM, Zheng K, Saunders-Wood T, et al. Delta-Like Ligand-Notch1 Signalling Is Selectively Modulated by HPV16 E6 to Promote Squamous Cell Proliferation and Correlates With Cervical Cancer Prognosis. *Cancer Res* (2021) 81(7):1909–21. doi: 10.1158/0008-5472.CAN-20-1996
64. Zhang X, Wu J, Luo S, Lechler T, Zhang JY. FRA1 Promotes Squamous Cell Carcinoma Growth and Metastasis Through Distinct AKT and C-Jun Dependent Mechanisms. *Oncotarget* (2016) 7(23):34371–83. doi: 10.18632/oncotarget.9110
65. Surviladze Z, Sterkand RT, Ozbun MA. Interaction of Human Papillomavirus Type 16 Particles With Heparan Sulfate and Syndecan-1 Molecules in the Keratinocyte Extracellular Matrix Plays an Active Role in Infection. *J Gen Virol* (2015) 96(8):2232–41. doi: 10.1099/vir.0.000147
66. D'Costa ZJ, Jolly C, Androphy EJ, Mercer A, Matthews CM, Hibma MH. Transcriptional Repression of E-Cadherin by Human Papillomavirus Type 16 E6. *PloS One* (2012) 7(11):e48954. doi: 10.1371/journal.pone.0048954
67. Alzahrani F, Clattenburg L, Murugananda S, Bullock M, MacIsaac K, Wigerius M, et al. The Hippo Component YAP Localizes in the Nucleus of Human Papilloma Virus Positive Oropharyngeal Squamous Cell Carcinoma. *J Otolaryngol Head Neck Surg* (2017) 46(1):1–7. doi: 10.1186/s40463-017-0187-1
68. Sundqvist A, Vasilaki E, Voytyuk O, Bai Y, Morikawa M, Moustakas A, et al. Tgfβ and EGF Signaling Orchestrates the AP-1- and P63 Transcriptional Regulation of Breast Cancer Invasiveness. *Oncogene* (2020) 39(22):4436–49. doi: 10.1038/s41388-020-1299-z
69. Lakshmanachetty S, Balaiya V, High WA, Koster MI. Loss of TP63 Promotes the Metastasis of Head and Neck Squamous Cell Carcinoma by Activating MAPK and STAT3 Signaling. *Mol Cancer Res* (2019) 17(6):1–16. doi: 10.1158/1541-7786.MCR-18-1355
70. Chakrabarti R, Romano R-A, Kannan N, Amadori D, Choudhury A, Hang X, et al. Δnp63 Promotes Stem Cell Activity in Mammary Gland Development and Basal-Like Breast Cancer by Enhancing Fzd7 Expression and Wnt Signaling. *Nat Cell Biol* (2014) 16(10):1004–15. doi: 10.1038/ncb3040
71. Bossler F, Hoppe-Seyler K, Hoppe-Seyler F. PI3K/AKT/mTOR Signaling Regulates the Virus/Host Cell Crosstalk in HPV-Positive Cervical Cancer Cells. *Int J Mol Sci* (2019) 20(9):1–13. doi: 10.3390/ijms20092188
72. Yuan TL , Cantley LC. PI3K Pathway Alterations in Cancer: Variations on a Theme. *Oncogene* (2008) 27(41):5497–510. doi: 10.1038/onc.2008.245
73. Hu L, Liang S, Chen H, Lv T, Wu J, Chen D, et al. δnp63α is a Common Inhibitory Target in Oncogenic PI3K/Ras/Her2-Induced Cell Motility and Tumor Metastasis. *Proc Natl Acad Sci* (2017) 114(20):E3964–73. doi: 10.1073/pnas.1617816114
74. Bossler F, Kuhn BJ, Gunther T, Kraemer SJ, Khalkar P, Adrian S, et al. Repression of Human Papillomavirus Oncogene Expression Under Hypoxia Is Mediated by PI3K/mTORC2/AKT Signaling. *MBio* (2019) 10(1):1–16. doi: 10.1128/mBio.02323-18
75. Molinolo AA, Marsh C, El-Dinali M, Gangane N, Jennison K, Hewitt S, et al. mTOR as a Molecular Target in HPV-Associated Oral and Cervical Squamous Carcinomas. *Clin Cancer Res* (2012) 18(9):2558–68. doi: 10.1158/1078-0432.CCR-11-2824
76. Ramsey MR, Wilson C, Ory B, Rothenberg SM, Faquin W, Mills AA, et al. FGFR2 Signaling Underlies P63 Oncogenic Function in Squamous Cell Carcinoma. *J Clin Invest* (2013) 123(8):3525–38. doi: 10.1172/JCI68899
77. Kumar S, Gabrilovich D, Chakrabarti R, Kumar S, Wilkes DW, Samuel N, et al. Δnp63-Driven Recruitment of Myeloid-Derived Suppressor Cells Promotes Metastasis in Triple- Negative Breast Cancer. *J Clin Invest* (2018) 128(11):5095–109. doi: 10.1172/JCI99673
78. Wieland A, Patel MR, Cardenas MA, Eberhardt CS, Hudson WH, Obeng RC, et al. Defining HPV-Specific B Cell Responses in Patients With Head and Neck Cancer. *Nature* (2021) 597:274–8. doi: 10.1038/s41586-020-2931-3
79. Eberhardt CS, Kissick HT, Patel MR, Cardenas MA, Prokhnevska N, Obeng RC, et al. Functional HPV-Specific PD-1+ Stem-Like CD8 T Cells in Head and Neck Cancer. *Nature* (2021) 597(7875):279–84. doi: 10.1038/s41586-021-03862-z
80. Mitxelena J, Apraiz A, Vallejo-Rodríguez J, García-Santisteban I, Fullaondo A, Alvarez-Fernández M, et al. An E2F7-Dependent Transcriptional Program Modulates DNA Damage Repair and Genomic Stability. *Nucleic Acids Res* (2018) 46(9):4546–59. doi: 10.1093/nar/gky218
81. Yang C, Zhang ZC, Liu TB, Xu Y, Xia BR, Lou G. E2F1/2/7/8 as Independent Indicators of Survival in Patients With Cervical Squamous Cell Carcinoma. *Cancer Cell Int* (2020) 20(1):1–17. doi: 10.1186/s12935-020-01594-0
82. Mighty KK, Laimins LA. P63 Is Necessary for the Activation of Human Papillomavirus Late Viral Functions Upon Epithelial Differentiation. *J Virol* (2011) 85(17):8863–9. doi: 10.1128/JVI.00750-11
83. Dohn M, Zhang S, Chen X. P63α and Δnp63α can Induce Cell Cycle Arrest and Apoptosis and Differentially Regulate P53 Target Genes. *Oncogene* (2001) 20(25):3193–205. doi: 10.1038/sj.onc.1204427
84. Gillison ML, Trotti AM, Harris J, Eisbruch A, Harari PM, Adelstein DJ, et al. Radiotherapy Plus Cetuximab or Cisplatin for Human Papillomavirus (HPV)-Positive Oropharyngeal Cancer: A Randomized, Multicenter, non-Inferiority Clinical Trial. *Lancet* (2019) 393(10166):40–50. doi: 10.1016/S0140-6736(18)32779-X
85. Mehanna H, Robinson M, Hartley A, Kong A, Foran B, Fulton-Lieuw T, et al. Radiotherapy Plus Cisplatin or Cetuximab in Low-Risk Human Papillomavirus-Positive Oropharyngeal Cancer (De-ESCALaTE HPV): An Open-Label Randomised Controlled Phase 3 Trial. *Lancet* (2019) 393(10166):51–60. doi: https://doi.org/10.1016/S0140-6736(18)32752-1
86. Keysar SB, Astling DP, Anderson RT, Vogler BW, Bowles DW, Morton JJ, et al. A Patient Tumor Transplant Model of Squamous Cell Cancer Identifies PI3K Inhibitors as Candidate Therapeutics in Defined Molecular Bins. *Mol Oncol* (2013) 7(4):776–90. doi: 10.1016/j.molonc.2013.03.004
87. Wang Z, Martin D, Molinolo AA, Patel V, Iglesias-Bartolome R, Degese MS, et al. mTOR Co-Targeting in Cetuximab Resistance in Head and Neck Cancers Harboring PIK3CA and RAS Mutations. *J Natl Cancer Inst* (2014) 106(9):1–11. doi: 10.1093/jnci/dju215
88. D'Amato V, Rosa R, D'Amato C, Formisano L, Marciano R, Nappi L, et al. The Dual PI3K/mTOR Inhibitor PKI-587 Enhances Sensitivity to Cetuximab in EGFR-Resistant Human Head and Neck Cancer Models. *Br J Cancer* (2014) 110(12):2887–95. doi: 10.1038/bjc.2014.241

Conflict of Interest: The authors declare that the research was conducted in the absence of any commercial or financial relationships that could be construed as a potential conflict of interest.

this article, or claim that may be made by its manufacturer, is not guaranteed or endorsed by the publisher.

frontiers | Frontiers in Oncology

ORIGINAL RESEARCH
published: 08 June 2022
doi: 10.3389/fonc.2022.870319

18F-Fluorodeoxyglucose Positron Emission Tomography of Head and Neck Cancer: Location and HPV Specific Parameters for Potential Treatment Individualization

*Sebastian Zschaeck[1,2,3,4,5], Julian Weingärtner[1,2], Elia Lombardo[6], Sebastian Marschner[6,7], Marina Hajiyianni[1], Marcus Beck[1], Daniel Zips[1,8,9], Yimin Li[10], Qin Lin[10], Holger Amthauer[11], Esther G. C. Troost[3,4,5,12,13,14,15], Jörg van den Hoff[16], Volker Budach[1], Jörg Kotzerke[4,5,17], Konstantinos Ferentinos[18], Efstratios Karagiannis[18], David Kaul[1], Vincent Gregoire[19], Adrien Holzgreve[20], Nathalie L. Albert[20], Pavel Nikulin[16], Michael Bachmann[16], Klaus Kopka[16], Mechthild Krause[3,4,5,12,13,14,15], Michael Baumann[3,4,5,12,21], Joanna Kazmierska[22,23], Paulina Cegla[24], Witold Cholewinski[22,24], Iosif Strouthos[18], Klaus Zöphel[4,5,17,25], Ewa Majchrzak[26], Guillaume Landry[6], Claus Belka[6,7], Carmen Stromberger[1] and Frank Hofheinz[16]**

[1] Department of Radiation Oncology, Berlin Institute of Health, Charité – Universitätsmedizin Berlin, Corporate Member of Freie Universität Berlin, Humboldt-Universität zu Berlin, Berlin, Germany, [2] Berlin Institute of Health (BIH), Berlin, Germany, [3] Department of Radiotherapy and Radiation Oncology, Faculty of Medicine and University Hospital Carl Gustav Carus, Technische Universität Dresden, Dresden, Germany, [4] German Cancer Consortium (DKTK), Partner Site Dresden, and German Cancer Research Center (DKFZ) Heidelberg, Germany, Germany, [5] OncoRay – National Center for Radiation Research in Oncology, Faculty of Medicine and University Hospital Carl Gustav Carus, Technische Universität Dresden, Helmholtz-Zentrum Dresden – Rossendorf, Dresden, Germany, [6] Department of Radiation Oncology, University Hospital, Ludwig-Maximilians-University (LMU) Munich, Munich, Germany, [7] German Cancer Consortium (DKTK), Partner Site Munich, Munich, Germany, [8] German Cancer Consortium (DKTK), Partner Site Tübingen, and German Cancer Research Center (DKFZ) Heidelberg, Germany, Germany, [9] Department of Radiation Oncology, University Hospital and Medical Faculty, Eberhard Karls University Tübingen, Tübingen, Germany, [10] Department of Radiation Oncology, Xiamen Cancer Center, The First Affiliated Hospital of Xiamen University, Xiamen, China, [11] Department of Nuclear Medicine, Berlin Institute of Health, Charité – Universitätsmedizin Berlin, Corporate Member of Freie Universität Berlin, Humboldt-Universität zu Berlin, Berlin, Germany, [12] Institute of Radiooncology – OncoRay, Helmholtz-Zentrum Dresden - Rossendorf, Dresden, Germany, [13] National Center for Tumor Diseases (NCT), Partner Site Dresden, Germany: German Cancer Research Center (DKFZ), Heidelberg, Germany, [14] Faculty of Medicine and University Hospital Carl Gustav Carus, Technische Universität Dresden, Dresden, Germany, [15] Helmholtz Association/Helmholtz-Zentrum Dresden - Rossendorf (HZDR), Dresden, Germany, [16] Institute of Radiopharmaceutical Cancer Research, Helmholtz-Zentrum Dresden-Rossendorf, Dresden, Germany, [17] Department of Nuclear Medicine, Faculty of Medicine and University Hospital Carl Gustav Carus, Dresden, Germany, [18] Department of Radiation Oncology, German Oncology Center, European University Cyprus, Limassol, Cyprus, [19] Radiation Oncology Department, Leon Bérard Cancer Center, Lyon, France, [20] Department of Nuclear Medicine, University Hospital, Ludwig-Maximilians-University (LMU) Munich, Germany, [21] German Cancer Research Center (DKFZ), Heidelberg, Germany, [22] Electroradiology Department, University of Medical Sciences, Poznan, Poland, [23] Radiotherapy Department II, Greater Poland Cancer Centre, Poznan, Poland, [24] Department of Nuclear Medicine, Greater Poland Cancer Centre, Poznan, Poland, [25] Department of Nuclear Medicine, Klinikum Chemnitz gGmbH, Chemnitz, Germany, [26] Department of Head and Neck Surgery, Poznan University of Medical Sciences, Greater Poland Cancer Centre, Poznan, Poland

Purpose: 18F-fluorodeoxyglucose positron emission tomography (FDG-PET) is utilized for staging and treatment planning of head and neck squamous cell carcinomas (HNSCC). Some older publications on the prognostic relevance showed inconclusive results, most probably due to small study sizes. This study evaluates the prognostic and potentially predictive value of FDG-PET in a large multi-center analysis.

OPEN ACCESS

Edited by:
Shao Hui Huang, University Health Network, Canada

Reviewed by:
Patrick Veit Haibach, University Health Network (UHN), Canada
Frank Hoebers, Maastricht University Medical Centre, Netherlands

***Correspondence:**
Frank Hofheinz
f.hofheinz@hzdr.de

Specialty section:
This article was submitted to Head and Neck Cancer, a section of the journal Frontiers in Oncology

Received: *06 February 2022*
Accepted: *29 April 2022*
Published: *08 June 2022*

Citation:
Zschaeck S, Weingärtner J, Lombardo E, Marschner S, Hajiyianni M, Beck M, Zips D, Li Y, Lin Q, Amthauer H, Troost EGC, van den Hoff J, Budach V, Kotzerke J, Ferentinos K, Karagiannis E, Kaul D, Gregoire V, Holzgreve A, Albert NL, Nikulin P, Bachmann M, Kopka K, Krause M, Baumann M, Kazmierska J, Cegla P, Cholewinski W, Strouthos I, Zöphel K, Majchrzak E, Landry G, Belka C, Stromberger C and Hofheinz F (2022) 18F-Fluorodeoxyglucose Positron Emission Tomography of Head and Neck Cancer: Location and HPV Specific Parameters for Potential Treatment Individualization. Front. Oncol. 12:870319. doi: 10.3389/fonc.2022.870319

Methods: Original analysis of individual FDG-PET and patient data from 16 international centers (8 institutional datasets, 8 public repositories) with 1104 patients. All patients received curative intent radiotherapy/chemoradiation (CRT) and pre-treatment FDG-PET imaging. Primary tumors were semi-automatically delineated for calculation of SUV_{max}, SUV_{mean}, metabolic tumor volume (MTV) and total lesion glycolysis (TLG). Cox regression analyses were performed for event-free survival (EFS), overall survival (OS), loco-regional control (LRC) and freedom from distant metastases (FFDM).

Results: FDG-PET parameters were associated with patient outcome in the whole cohort regarding clinical endpoints (EFS, OS, LRC, FFDM), in uni- and multivariate Cox regression analyses. Several previously published cut-off values were successfully validated. Subgroup analyses identified tumor- and human papillomavirus (HPV) specific parameters. In HPV positive oropharynx cancer (OPC) SUV_{max} was well suited to identify patients with excellent LRC for organ preservation. Patients with SUV_{max} of 14 or less were unlikely to develop loco-regional recurrence after definitive CRT. In contrast FDG PET parameters deliver only limited prognostic information in laryngeal cancer.

Conclusion: FDG-PET parameters bear considerable prognostic value in HNSCC and potential predictive value in subgroups of patients, especially regarding treatment de-intensification and organ-preservation. The potential predictive value needs further validation in appropriate control groups. Further research on advanced imaging approaches including radiomics or artificial intelligence methods should implement the identified cut-off values as benchmark routine imaging parameters.

Keywords: head and neck squamous cell carcinoma (HNSCC), fluorodeoxyglucose positron emission tomography (FDG PET), radiotherapy, metabolic tumor volume (MTV), standardized uptake value (SUV)

INTRODUCTION

In head and neck squamous cell carcinomas (HNSCC) beside computed tomography (CT), positron emission tomography (PET) with the radiotracer 18f-fluorodeoxyglucose (FDG) is frequently used for tumor staging and treatment planning in clinical routine (1). Various PET parameters have been investigated regarding their prognostic value in HNSCC. One requirement of imaging parameters is that these parameters bear independent prognostic value compared to established clinical parameters. In FDG-PET, metabolic tumor volume (MTV), maximum and mean standardized uptake value (SUV_{max} and SUV_{mean}), and the derived parameter total lesion glycolysis TLG (defined as $MTV \times SUV_{mean}$) can be seen as standard parameters that can be easily evaluated in clinical routine. Currently, the prognostic impact of these parameters is not well defined, especially in biologically heterogeneous sub-groups of HNSCC. A meta-analysis of studies investigating the prognostic value of pre-therapeutic FDG-PET in patients treated with definitive chemoradiation (CRT) reported that only MTV has significant prognostic impact on patients´ outcome (2). However, outcome parameters were only available for a minority of patients. Especially concerning the important endpoint loco-regional control (LRC), only four out of 25 studies included sufficient information. Additionally, the included studies used different tumor segmentation methods, therefore MTV delineation can differ considerably and the MTV values cannot be directly compared between studies. These limitations hamper any valid conclusions regarding the prognostic value of FDG-PET in HNSCC treated with definitive CRT. The aim of this study was to perform a multicenter analysis of original FDG-PET data from HNSCC patients treated with definitive CRT. All images were centrally analyzed by the same observer with the same software and semi-automatic delineation methods. Results of a small subgroup of patients with nasopharyngeal cancer (NPC) have already been published, here we report a larger cohort with additional NPC patients and all other tumor locations (3).

PATIENTS AND METHODS

Patients

Inclusion criteria for this study were: histologically confirmed HNSCC without evidence of distant metastases, definitive radiotherapy or CRT with curative intent, and availability of pre-treatment FDG-PET. We analyzed PET images and patient

data from one Chinese and seven European centers plus additional images and patient data from the cancer imaging archive (4), in particular: Head-Neck-PET-CT, QIN-HEADNECK, HNSCC, TCGA-HNSC, Head-Neck-Radiomics-HN1 (5–12). TNM classification was bases on American Joint Committee on cancer staging manual version number seven.

Imaging

Details on the imaging of the patients from public databases can be found in the original publications cited above. Patients from Berlin, Xiamen, Dresden, Brussels, Tuebingen, Limassol, Poznan and Munich received hybrid-imaging (usually PET-CT) with the following equipment: Gemini TF 16 (Philips Medical Systems, Cleveland, OH, USA), Discovery STE (General Electric Medical Systems, Milwaukee, WI, USA), Biograph 16 PET/CT scanner (Siemens Medical Solutions Inc., Knoxville, TN), Gemini TF PET-CT (Philips Medical Systems, Cleveland, OH, USA), Biograph mCT (Siemens Healthineers), Discovery IQ (General Electric Medical Systems, Milwaukee, WI, USA), Gemini TF TOF 16 (Philips Healthcare Inc., Andover, MA) and Discovery (General Electric Medical Systems, Milwaukee, WI, USA)/ Biograph (Siemens Medical Solutions Inc., Knoxville, TN), respectively.

Treatment

All patients received primary radiotherapy with curative intent. Radiotherapy was performed as three-dimensional, intensity modulated or volumetric modulated treatment. Prescribed radiation doses ranged between 66 and 77 Gray (Gy). In most cases radiotherapy was combined with simultaneous chemotherapy or cetuximab. 804 patients received concomitant systemic therapy. Most patients with individual data on chemotherapy received platinum-based CRT regimes (371 of 439 patients; 85%), 165 patients received radiotherapy only (15%) and 135 patients (12%) had no information available on concomitant therapy. Commonly only patients with early stage disease were treated by radiotherapy only, while CRT was prescribed in locally advanced stages.

Image Analysis

The metabolically active part of the primary tumor was delineated in the PET data by a semi-automatic algorithm based on adaptive thresholding considering the local background (13, 14).

Manual delineation was only performed in case of low or diffuse tracer accumulation. In case of lacking tracer accumulation the voxel with highest activity within the primary tumor site (i.e. with the highest SUV_{max} uptake) was contoured as a single voxel for further analyses, this was the case in 30 patients (2.7%). This approach was chosen to avoid bias by excluding all patients without significant FDG uptake from the analyses. For the resulting regions of interest (ROIs), the metabolic active tumor volume (MTV), maximum and mean standardized uptake value (SUV_{max} and SUV_{mean}), and the total lesion glycolysis (MTV × SUV_{mean}, TLG) were computed. Delineation was performed by an experienced radiation oncologist (SZ) and verified by an experienced Nuclear Medicine physician (KZ). ROI definition and ROI analyses were performed using the software ROVER version 3.0.41 (ABX GmbH, Radeberg, Germany).

Statistical Analyses

Survival analysis was performed with respect to event free survival (EFS), overall survival (OS), locoregional control (LRC), and freedom from distant metastases (FFDM). The association of endpoints with clinical and quantitative PET parameters was analyzed using univariate and multivariate Cox proportional hazard regression in which the PET parameters were included as metric parameters. Parameters were further analyzed in univariate Cox regression using binarized PET parameters. The cut-off values were calculated by minimizing the p-value in univariate Cox regression as described in (15). The optimal cut-off was determined separately for EFS, OS, LRC, and FFDM. Cut-off values leading to $p<0.05$ were tested for stability (i.e., sensibility of the prognostic value against variation of the cut-off value). In this test, the range of cut-off values still leading to a significant effect in univariate analysis was computed by successively decreasing/increasing the cut-off value (starting at the optimal value) and repeating univariate Cox regression. Probability of event occurrence was computed and rendered as Kaplan–Meier curves. Statistical significance was defined as a p-value of less than 0.05. Statistical analysis was performed with the R language and environment for statistical computing version 4.0.5 (16).

For validation of previously published cut-off values, all 25 studies included in the meta-analysis were searched for reported significant cut-off values, published endpoints, and tumor locations (2). **Supplementary Table 1** summarizes these data (only analyses of the primary tumor parameters were considered).

RESULTS

1104 patients with individual patient and outcome data and original PET images for analysis were included in this study. **Supplementary Table 2** summarizes available clinical data of all 16 cohorts. Median age of patients was 60 years and 79% of patients were male. The vast majority of patients presented locally advanced stages of HNSCC (87% > UICC stage II) and oropharynx (OPC) was the most frequent primary tumor location (51%). Detailed patient characteristics are reported in **Supplementary Table 3**. In the whole cohort, median MTV, TLG, SUV_{max} and SUV_{mean} were 7.0 ml, 61.6 ml, 13.0 and 8.4, respectively. Details and distribution of the parameters are reported in **Supplementary Table 4**. There were significant differences of PET parameters depending on tumor location. Broadly speaking, tumors located within the oral cavity (OCC) had higher values and larynx carcinomas (LC) showed lower values of some parameters. Details on the distribution can be found in **Supplementary Figure 1** and comparison between groups is shown in **Supplementary Table 5**. Since tumor location is a known prognostic factor in HNSCC, we checked for prognostic relevance of this parameter in this cohort (see

Supplementary Figure 2) and added the information in uni- and multivariate cox regression analyses. When analyzing oncological outcome of the whole cohort, all PET parameters showed a significant association with all investigated clinical endpoints (EFS, OS, LRC and FFDM). Details are reported in **Table 1**. Note that not all parameters/endpoints were available for all patients. Patients with missing information were excluded in the respective analysis. The number of included patients is listed in column 'N' in **Table 1**. The results are more or less unchanged when patients with missing information are exclude completely (see **Supplementary Table 6**). Upon multivariate testing, MTV showed a robust association with EFS, OS and LRC, while SUV_{max} showed the highest association with FFDM. Details are reported in **Table 2**. Only those patients were included for which all information on all analyzed parameters/endpoints was available. The number of included patients is indicated at the top of the corresponding part of **Table 2**. Binarization and cutoff-stability testing of PET parameters revealed that MTV, TLG, and, in some cases, SUV_{max} are able to significantly discriminate between risk groups across a broad range of values (**Supplementary Tables 7**, **8**). Several previously published cut-off values were successfully validated (**Supplementary Table 9**). **Figures 1**, **2** show Kaplan-Meier estimates for patients stratified according to PET parameters with the endpoints OS and LRC. Figures for EFS and FFDM are shown in **Supplementary Figures 3, 4**. Since tumor location and HPV status have a strong influence on the outcome of patients, PET parameters were optimized for each tumor subtype. **Figures 3**, **4** show Forest plots of the prognostic significance of PET parameters in different subgroups including primary tumor site for PET parameters MTV and SUV_{max}. MTV seems to bear the highest prognostic value especially in younger patients and in patients with NPC, which is partly correlated (average age of NPC patients in this cohort 52.4 years versus 61.1 years for non-NPC HNSCC, $p < 0.001$). Additionally, NPC did show a different behavior regarding FFDM compared to other locations (the only location with decreased risk of FFDM with increased MTV or SUV_{max} although not reaching statistical significance). A surprising finding was the very strong association of SUV_{max} with LRC in HPV-positive (HPV+) OPC. **Figure 5** shows Kaplan-Meier estimates for HPV-positive OPC stratified according to the investigated PET parameters. The SUV_{max} cut-off of 14 was able to identify patients with excellent LRC after CRT/radiotherapy. While in general MTV seems to be an important risk factor regarding LRC, this does not seem to be the case in LC. Also other PET parameters did not show a convincing association in LC (**Supplementary Figure 5**).

DISCUSSION

Based on a plethora of mostly retrospective single-center studies, FDG-PET parameters are considered significant prognostic and potentially predictive parameters for response to CRT in HNSCC. This is reflected by the use of high FDG uptake volumes for dose escalation in several trials (17–20). In a recent review article Clausen and colleagues argued that regarding its prognostic value FDG is beyond the exploratory

TABLE 1 | Univariate cox regression analyses with respect to EFS, OS, LRC and FFDM.

Parameter	EFS				OS			
	N	HR	95% CI	p-value	N	HR	95% CI	p-value
Sex male	1078	1.17	0.93 – 1.47	0.18	1094	1.17	0.91 – 1.51	0.22
Age > 60y	1078	1.51	1.26 – 1.81	<0.001	1078	1.57	1.28 – 1.93	<0.001
T-stage > 2	1074	1.93	1.58 – 2.36	<0.001	1090	2.17	1.72 – 2.75	<0.001
N-stage > 0	1074	1.3	1.03 – 1.64	0.025	1090	1.74	1.31 – 2.31	<0.001
UICC-stage > III	1047	1.48	1.2 – 1.82	<0.001	1063	1.92	1.49 – 2.46	<0.001
HPC+oral cavity	1078	2.48	2.02 – 3.05	<0.001	1094	2.98	2.39 – 3.72	<0.001
Chemotherapy NO	965	1.15	0.92 – 1.44	0.22	969	1.24	0.96 – 1.61	0.099
MTV	1078	1.02	1.02 – 1.02	<0.001	1094	1.02	1.02 – 1.02	<0.001
TLG	986	1.002	1.001 – 1.002	<0.001	1002	1.002	1.001 – 1.002	<0.001
SUV_{max}	986	1.02	1.01 – 1.03	<0.001	1002	1.02	1.01 – 1.04	<0.001
SUV_{mean}	986	1.03	1.01 – 1.05	0.0075	1002	1.03	1.01 – 1.06	0.005
Parameter	**LRC**				**FFDM**			
	N	**HR**	**95% CI**	**p-value**	**N**	**HR**	**95% CI**	**p-value**
Sex male	1094	1.005	0.728 – 1.388	0.97	1061	1.35	0.87 – 2.09	0.18
Age > 60y	1073	1.24	0.95 – 1.62	0.11	1060	1.4	1.01 – 1.96	0.047
T-stage > 2	1087	1.98	1.46 – 2.68	<0.001	1057	1.82	1.26 – 2.63	0.002
N-stage > 0	1087	1.02	0.74 – 1.42	0.89	1057	3.41	1.84 – 6.3	<0.001
UICC-stage > III	1060	1.36	1.01 – 1.83	0.046	1030	2.24	1.47 – 3.41	<0.001
HPC+oral cavity	1094	2.34	1.73 – 3.18	<0.001	1061	2.19	1.48 – 3.24	<0.001
Chemotherapy NO	960	0.994	0.713 – 1.386	0.97	961	2.01	1.25 – 3.23	0.004
MTV	1094	1.02	1.02 – 1.03	<0.001	1061	1.02	1.01 – 1.02	<0.001
TLG	992	1.002	1.001 – 1.002	<0.001	969	1.001	1.001 – 1.002	<0.001
SUV_{max}	992	1.03	1.01 – 1.04	0.011	969	1.03	1.01 – 1.05	0.015
SUV_{mean}	992	1.03	1 – 1.06	0.027	969	1.04	1 – 1.07	0.05

PET parameters were included as metric parameters. Column 'N' shows the number of included patients in the respective analysis.

TABLE 2 | Multivariate cox regression analyses with respect to EFS, OS, LRC and FFDM.

Parameter	EFS (n=955)			OS (n=971)		
	HR	**95% CI**	**P-value**	**HR**	**95% CI**	**P-value**
Age	1.5	1.23 –1.82	<0.001	1.66	1.34–2.07	<0.001
T stage		–			–	
UICC stage	1.2	0.957– 1.51	0.11	1.54	1.17–2.03	0.002
Chemotherapy		–			–	
HPC + Oral Cavity	2.55	2.06 –3.16	<0.001	3.1	2.46–3.92	<0.001
MTV	1.86	1.51 –2.29	<0.001	2.27	1.8 –2.87	<0.001
SUV_{max}	1.31	0.996 – 1.73	0.053	1.14	0.91–1.42	0.26
Parameter	**LRC (n=988)**			**FFDM (n=911)**		
	HR	**95% CI**	**P-value**	**HR**	**95% CI**	**P-value**
Age		–		1.4	0.985– 1.98	0.061
T stage	1.24	0.858 – 1.79	0.25		–	
UICC stage		–		1.6	1.02–2.51	0.041
Chemotherapy		–		1.48	0.904–2.43	0.12
HPC + Oral Cavity	2.31	1.68 – 3.18	<0.001	1.78	1.17–2.71	0.007
MTV	1.79	1.3 –2.45	<0.001	1.83	1.25–2.68	0.002
SUV_{max}	1.56	1.01–2.41	0.043	1.44	1.01–2.07	0.047

PET parameters were included as metric parameters. The number of included patients is shown at the top of the corresponding part of the table.

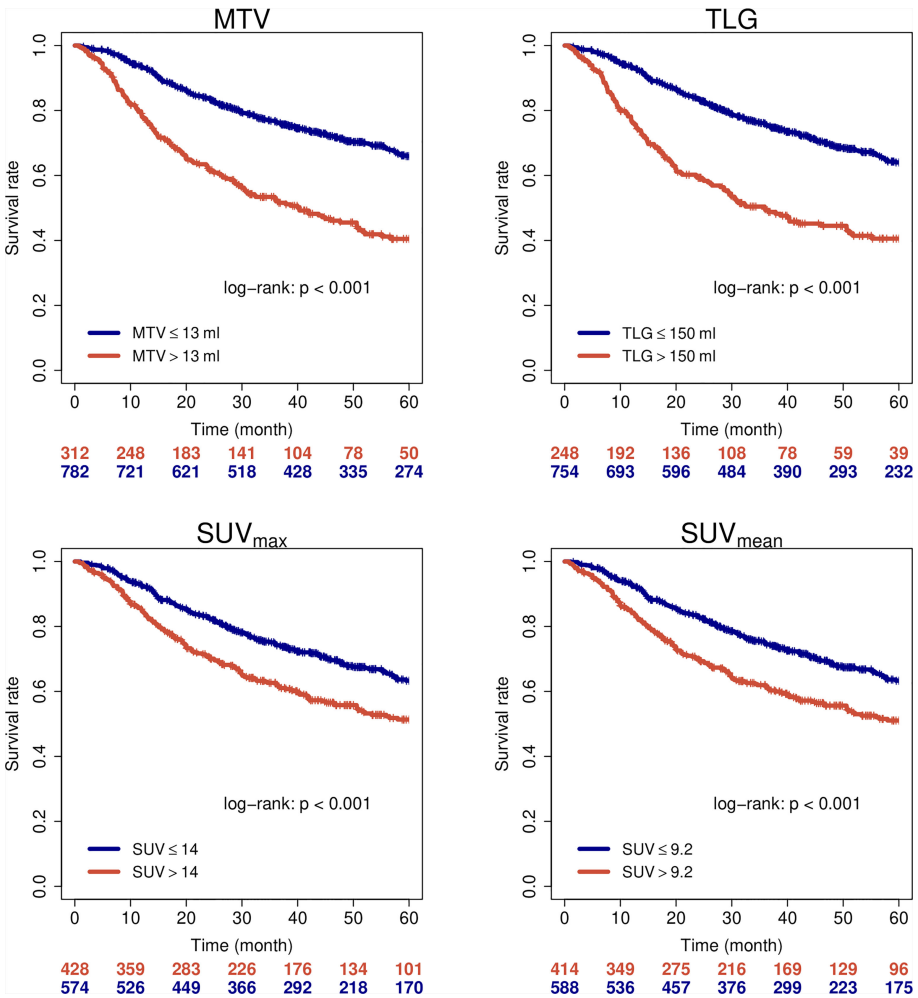

FIGURE 1 | Overall survival of all patients when stratified by PET parameters.

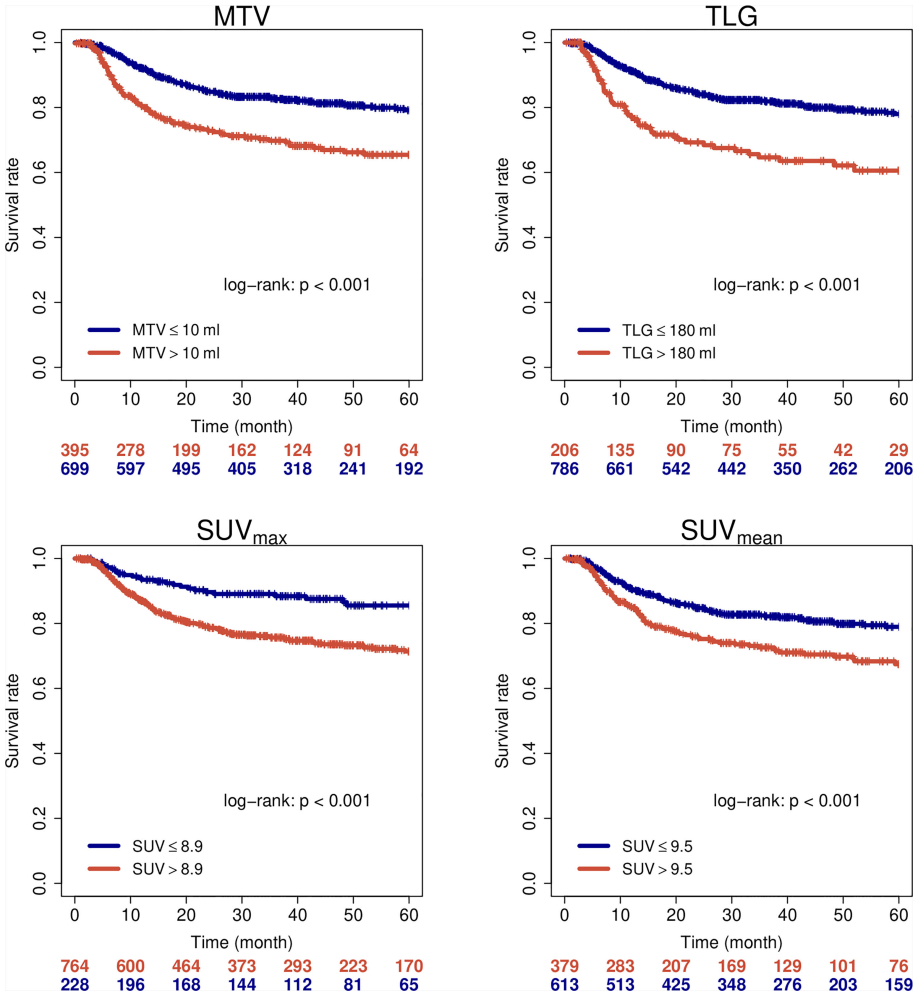

FIGURE 2 | Loco-regional control of all patients when stratified by PET parameters.

phase; at the same time they found evidence for publication bias with potential overestimation of the prognostic effect size of FDG parameters in HNSCC (21). Their analysis, which was not based on individual patient data, included 1704 HNSCC patients from 20 studies with a median sample size of only 58 patients. Given the distinct biological features and prognosis of HNSCC subtypes, this implies that subgroup analyses are not useful in the majority of small sample size publications.

Here we report the, to our knowledge, largest individual patient and imaging based analyses of HNSCC with pre-treatment FDG-PET and primary CRT/radiotherapy. Our analyses confirm a moderate association of several PET parameters with clinical outcome of patients in the whole cohort. At the same time, considerable differences regarding primary tumor location and HPV status were found. This is an important observation for future aims to personalize radio-oncological treatment by the implementation of PET parameters. In early stage OPC, radiotherapy and transoral robotic surgery showed comparable quality of life and outcome, but with different toxicity profiles in a randomized phase-II study (22, 23). Although high-level evidence is lacking for other and more advanced HNSCC, CRT and primary surgery are often considered similar efficient primary treatment approaches. Since toxicity and late side effects are considerable in the head and neck region, biomarkers to individualize treatment are urgently needed for these patients.

LC and HPV positive OPC are probably two of the tumor locations with the strongest need for parameters to individualize treatment, i.e. schedule patients for primary surgery or CRT depending on the probability of LRC. Our analyses revealed that FDG-PET does not deliver convincing information in LC, however in HPV positive OPC, several PET parameters show a very high discriminatory ability. Even the most easily obtainable parameter SUV_{max}, assessed during every clinical routine PET scan, seems to be very well suited to select low-risk patients that could potentially be treated within dose de-escalation trials. To our opinion this is an unexpected finding especially in a multi-center analysis, since SUV parameters are known to be prone to several potential errors. They are uptake-time-dependent and time after injection differs considerably in routine care patients.

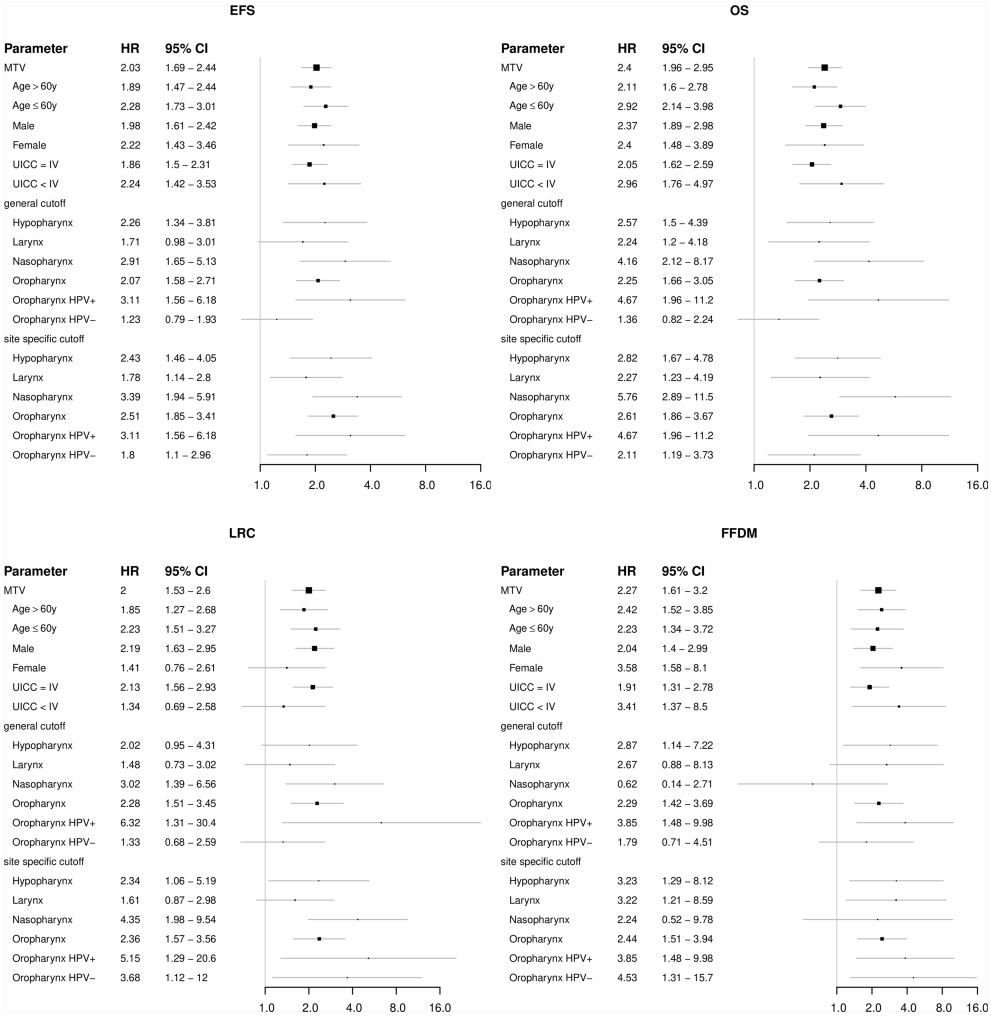

FIGURE 3 | Forest plots showing the prognostic value of the FDG-PET parameter metabolic tumor volume (MTV) in subgroups of patients regarding the clinical endpoints EFS, OS, LRC and FFDM.

Furthermore SUV is susceptible to scanner calibration errors and the correlation between systemic tracer distribution and body weight is only weak, adding additional variability in common SUV calculations. Especially in multicenter analyses, this can make quantitative comparison of SUV difficult and our group was able to show that the uptake time normalized ratio of tumor SUV and blood SUV (SUR) is superior to tumor SUV alone regarding correlation with glucose uptake of lesions, but also regarding outcome discrimination (24–27). However, determination of blood SUV requires a PET/CT scan of the thorax. Some of the included patients had missing corresponding CT scans or PET examination limited to the upper thorax and head and neck region. Therefore, calculation of SUR was not possible in the whole cohort, but is subject of ongoing research in a subgroup of patients with available imaging information. The strong prognostic value of SUV_{max} in this cohort of HPV positive OPC despite its methodological limitations, might be due to the relatively high cutoff value. Given the increasing incidence of HPV positive OPC in combination with the relatively good prognosis, further individually tailored treatment is an urgent medical need (28). Several phase-II studies reported promising outcome results with CRT dose de-escalation to 60 Gy (29, 30). Another phase-II study was able to show that normo-fractionated dose de-escalation down to 50 Gy is feasible after prior selection of patients with favorable biology using induction chemotherapy (31). However, current evidence does not suggest any benefit by induction chemotherapy for OPC patients (32). Therefore, other biomarkers, as our identified PET parameter, would be ideal candidates to guide future treatment de-escalation.

Our study has several limitations such as the retrospective nature of the data and partly missing information, especially in data from public repositories. Most obviously, this affects the HPV status of oropharyngeal carcinomas, which was not available for a relevant number of patients. Furthermore, the TNM staging classification was not according to the most current

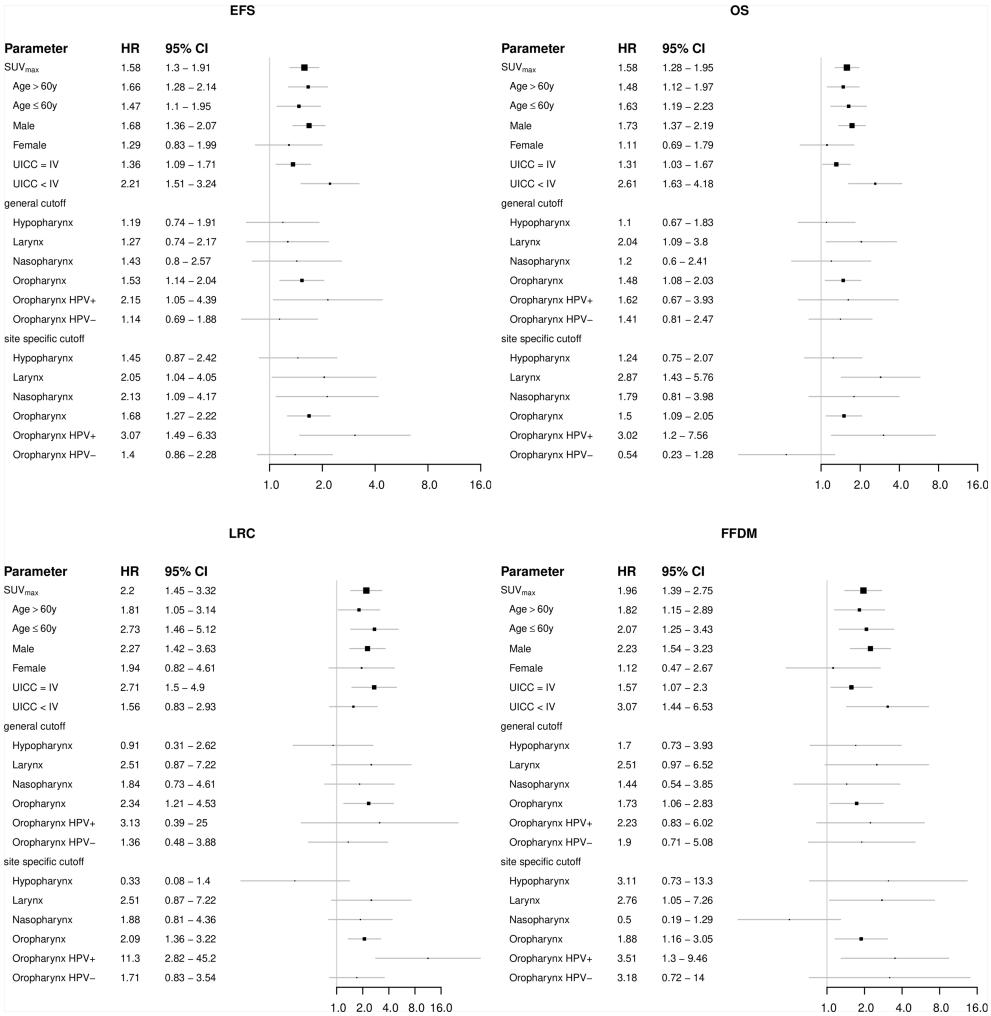

FIGURE 4 | Forest plots showing the prognostic value of the FDG-PET parameter maximum standardized uptake value (SUV_{max}) in subgroups of patients regarding the clinical endpoints EFS, OS, LRC and FFDM.

version number eight. There were substantial modifications from version seven to version eight, with emphasis on HPV positive oropharynx carcinomas (33). This is a major drawback when comparing the data with other current HNSCC data and should be considered when interpreting the data. Nonetheless, most of the basic parameters, including the important endpoints LRC and OS were available and the current analysis includes by far the largest dataset of FDG-PET from HNSCC patients. Therefore, our analysis can be regarded as reference benchmark for future research on the prognostic value of imaging parameters, i.e. the identified parameters should be considered when establishing novel radiomics and/or AI models for prognostication of HNSCC patients and novel signatures should outperform these parameters regarding patient stratification. This seems to be highly important as a recent analysis has shown that one of the most popular radiomics signatures, that has been independently validated, is highly correlated with tumor volume (34). Our analysis does not only identify promising future applications for standard parameters, but also shows for which tumor subtypes and outcome parameters further research on optimal stratification and treatment personalization is warranted. For example, standard PET parameters of primary tumors have not shown convincing results regarding the prediction of distant metastases. Analysis of affected lymph nodes and/or more sophisticated image analyses by convolutional neural networks have shown promising results and should probably be further developed to address this important issue (35–37). The same holds true for laryngeal carcinomas, for which some early radiomic analyses reported encouraging results (38, 39).

CONCLUSION

Standard FDG-PET parameters bear significant prognostic value in HNSCC treated with radiotherapy/CRT but moderate effect

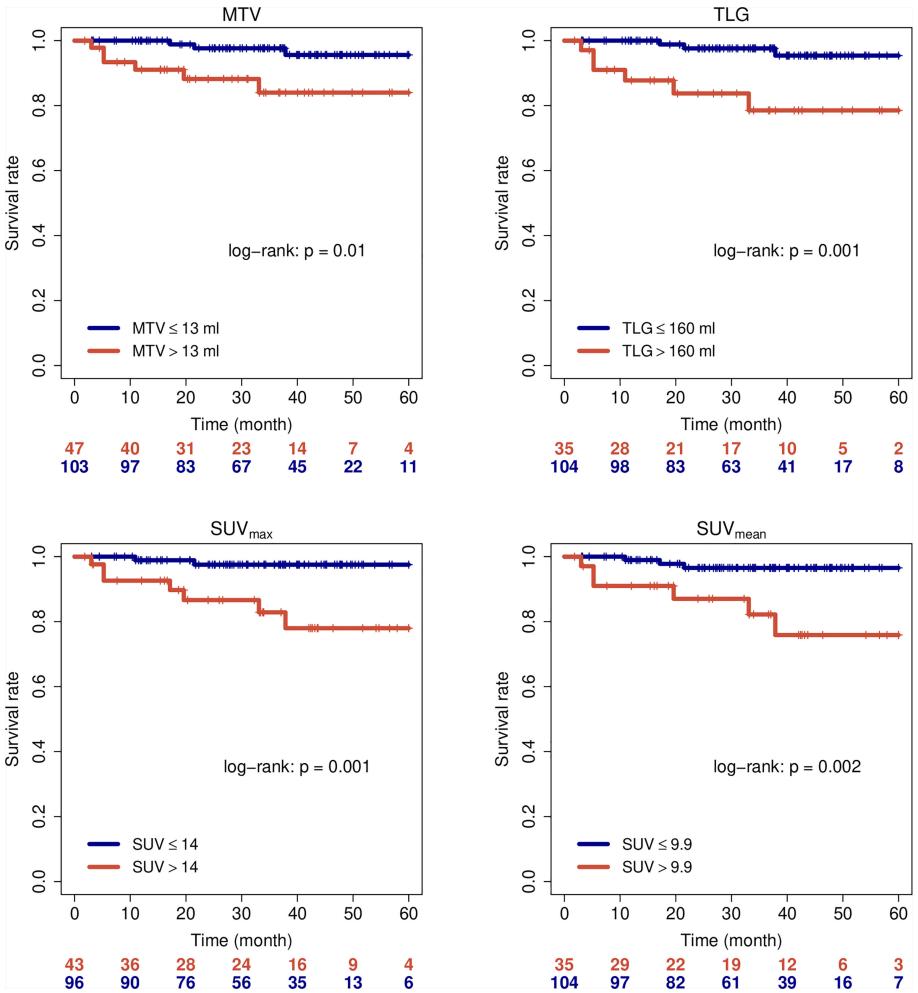

FIGURE 5 | Loco-regional control of HPV-positive oropharyngeal carcinomas when stratified by PET parameters.

size regarding LRC and FFDM in the entire cohort. Subgroup specific analyses revealed SUV_{max} as a promising parameter to select HPV-positive OPC with excellent outcome after CRT/radiotherapy.

DATA AVAILABILITY STATEMENT

The original contributions presented in the study are included in the article/**Supplementary Material**. Further inquiries can be directed to the corresponding author.

ETHICS STATEMENT

The studies involving human participants were reviewed and approved by Ethikkomission der Charité, Charité Universitätsmedizin Berlin, Berlin, Germany. The patients/participants provided their written informed consent to participate in this study.

AUTHOR CONTRIBUTIONS

Study conception and design: SZ and FH; Drafting of manuscript: SZ and FH; Image processing and analysis: SZ, JW, EL, SM, MH, YL, JKo, KF, EK, VG, AH, PN, JKa, PC, KZ, and FH; Study Investigators: SZ, DZ, QL, HA, ET, JvdH, VB, JKo, VG, NA, MK, MBau, WC, KZ, GL, CB, CS, and FH; Interpretation of data: all authors; Final approval of manuscript: all authors.

FUNDING

This work was partly supported by the Berliner Krebsgesellschaft (ZSF201720) and by the German Federal

Ministry of Education and Research (BMBF contract 03ZIK42/OncoRay). The funders had no role in the design of the study; the collection, analysis, and interpretation of the data; the writing of the manuscript; and the decision to submit the manuscript for publication.

SUPPLEMENTARY MATERIAL

The Supplementary Material for this article can be found online at: https://www.frontiersin.org/articles/10.3389/fonc.2022.870319/full#supplementary-material

REFERENCES

1. Cook GJR, Azad G, Owczarczyk K, Siddique M, Goh V. Challenges and Promises of PET Radiomics. *Int J Radiat Oncol Biol Phys* (2018) 102:1083–9. doi: 10.1016/j.ijrobp.2017.12.268
2. Bonomo P, Merlotti A, Olmetto E, Bianchi A, Desideri I, Bacigalupo A, et al. What Is the Prognostic Impact of FDG PET in Locally Advanced Head and Neck Squamous Cell Carcinoma Treated With Concomitant Chemo-Radiotherapy? A Systematic Review and Meta-Analysis. *Eur J Nucl Med Mol Imaging* (2018) 45:2122–38. doi: 10.1007/s00259-018-4065-5
3. Zschaeck S, Li Y, Lin Q, Beck M, Amthauer H, Bauersachs L, et al. Prognostic Value of Baseline [18F]-Fluorodeoxyglucose Positron Emission Tomography Parameters MTV, TLG and Asphericity in an International Multicenter Cohort of Nasopharyngeal Carcinoma Patients. *PloS One* (2020) 15: e0236841. doi: 10.1371/journal.pone.0236841
4. Clark K, Vendt B, Smith K, Freymann J, Kirby J, Koppel P, et al. The Cancer Imaging Archive (TCIA): Maintaining and Operating a Public Information Repository. *J Digit Imaging* (2013) 26:1045–57. doi: 10.1007/s10278-013-9622-7
5. Vallières M, Kay-Rivest E, Perrin L, Liem X, Furstoss C, Khaouam N, et al. *Data From Head-Neck-PET-Ct*. (2017). doi: 10.7937/K9/TCIA.2017.8OJE5Q00.
6. Beichel RR, Ulrich EJ, Bauer C, Wahle A, Brown B, Chang T, et al. *Data From QIN-HEADNECK*. (2015). doi: 10.7937/K9/TCIA.2015.K0F5CGLI.
7. Grossberg AJ, Mohamed ASR, Elhalawani H, Bennett WC, Smith KE, Nolan TS, et al. Imaging and Clinical Data Archive for Head and Neck Squamous Cell Carcinoma Patients Treated With Radiotherapy. *Sci Data* (2018) 5:180173. doi: 10.1038/sdata.2018.173
8. Vallières M, Kay-Rivest E, Perrin LJ, Liem X, Furstoss C, Aerts HJWL, et al. Radiomics Strategies for Risk Assessment of Tumour Failure in Head-and-Neck Cancer. *Sci Rep* (2017) 7:10117. doi: 10.1038/s41598-017-10371-5
9. Fedorov A, Clunie D, Ulrich E, Bauer C, Wahle A, Brown B, et al. DICOM for Quantitative Imaging Biomarker Development: A Standards Based Approach to Sharing Clinical Data and Structured PET/CT Analysis Results in Head and Neck Cancer Research. *PeerJ* (2016) 4:e2057. doi: 10.7717/peerj.2057
10. Grossberg A, Elhalawani H, Mohamed A, Mulder S, Williams B, White A, et al. HNSCC. *Cancer Imaging Archive* doi: 10.7937/k9/tcia.2020.a8sh-7363
11. Wee L, Dekker A. *Data From Head-Neck-Radiomics-Hn1*. (2019). doi: 10.7937/TCIA.2019.8KAP372N.
12. Zuley ML, Jarosz R, Kirk S, Lee Y, Colen R, Garcia K, et al. *Radiology Data From The Cancer Genome Atlas Head-Neck Squamous Cell Carcinoma [TCGA-HNSC] Collection*. (2016). doi: 10.7937/K9/TCIA.2016.LXKQ47MS.
13. Hofheinz F, Pötzsch C, Oehme L, Beuthien-Baumann B, Steinbach J, Kotzerke J, et al. Automatic Volume Delineation in Oncological PET. Evaluation of a Dedicated Software Tool and Comparison With Manual Delineation in Clinical Data Sets. *Nuklearmedizin* (2012) 51:9–16. doi: 10.3413/Nukmed-0419-11-07
14. Hofheinz F, Langner J, Petr J, Beuthien-Baumann B, Steinbach J, Kotzerke J, et al. An Automatic Method for Accurate Volume Delineation of Heterogeneous Tumors in PET. *Med Phys* (2013) 40:082503. doi: 10.1118/1.4812892
15. Bütof R, Hofheinz F, Zöphel K, Stadelmann T, Schmollack J, Jentsch C, et al. Prognostic Value of Pretherapeutic Tumor-To-Blood Standardized Uptake Ratio in Patients With Esophageal Carcinoma. *J Nucl Med* (2015) 56:1150–6. doi: 10.2967/jnumed.115.155309
16. R Core Team. R: A Language and Environment for Statistical Computing. In: *R Foundation for Statistical Computing*. Vienna, Austria (2001).
17. Gouw ZAR, La Fontaine MD, Vogel WV, van de Kamer JB, Sonke J-J, Al-Mamgani A. Single-Center Prospective Trial Investigating the Feasibility of Serial FDG-PET Guided Adaptive Radiation Therapy for Head and Neck Cancer. *Int J Radiat Oncol Biol Phys* (2020) 108:960–8. doi: 10.1016/j.ijrobp.2020.04.030
18. Berwouts D, Madani I, Duprez F, Olteanu AL, Vercauteren T, Boterberg T, et al. Long-Term Outcome of 18 F-Fluorodeoxyglucose-Positron Emission Tomography-Guided Dose Painting for Head and Neck Cancer: Matched Case-Control Study. *Head Neck* (2017) 39:2264–75. doi: 10.1002/hed.24892
19. Duprez F, De Neve W, De Gersem W, Coghe M, Madani I. Adaptive Dose Painting by Numbers for Head-and-Neck Cancer. *Int J Radiat Oncol Biol Phys* (2011) 80:1045–55. doi: 10.1016/j.ijrobp.2010.03.028
20. Rasmussen JH, Håkansson K, Vogelius IR, Aznar MC, Fischer BM, Friborg J, et al. Phase I Trial of 18F-Fludeoxyglucose Based Radiation Dose Painting With Concomitant Cisplatin in Head and Neck Cancer. *Radiother Oncol* (2016) 120:76–80. doi: 10.1016/j.radonc.2016.03.005
21. Clausen MM, Vogelius IR, Kjær A, Bentzen SM. Multiple Testing, Cut-Point Optimization, and Signs of Publication Bias in Prognostic FDG-PET Imaging Studies of Head and Neck and Lung Cancer: A Review and Meta-Analysis. *Diagnostics (Basel)* (2020) 10. doi: 10.3390/diagnostics10121030
22. Nichols AC, Theurer J, Prisman E, Read N, Berthelet E, Tran E, et al. Radiotherapy Versus Transoral Robotic Surgery and Neck Dissection for Oropharyngeal Squamous Cell Carcinoma (ORATOR): An Open-Label, Phase 2, Randomised Trial. *Lancet Oncol* (2019) 20:1349–59. doi: 10.1016/S1470-2045(19)30410-3
23. Nichols AC, Theurer J, Prisman E, Read N, Berthelet E, Tran E, et al. Randomized Trial of Radiotherapy Versus Transoral Robotic Surgery for Oropharyngeal Squamous Cell Carcinoma: Long-Term Results of the ORATOR Trial. *J Clin Oncol* (2022) 40:866–75. doi: 10.1200/JCO.21.01961
24. van den Hoff J, Oehme L, Schramm G, Maus J, Lougovski A, Petr J, et al. The PET-Derived Tumor-to-Blood Standard Uptake Ratio (SUR) Is Superior to Tumor SUV as a Surrogate Parameter of the Metabolic Rate of FDG. *EJNMMI Res* (2013) 3:77. doi: 10.1186/2191-219X-3-77
25. Bütof R, Hofheinz F, Zöphel K, Schmollack J, Jentsch C, Zschaeck S, et al. Prognostic Value of SUR in Patients With Trimodality Treatment of Locally Advanced Esophageal Carcinoma. *J Nucl Med* (2018) 56:1150–6. doi: 10.2967/jnumed.117.207670
26. Hofheinz F, van den HJ, IG S, Lougovski A, Ego K, Amthauer H, et al. Comparative Evaluation of SUV, Tumor-to-Blood Standard Uptake Ratio (SUR), and Dual Time Point Measurements for Assessment of the Metabolic Uptake Rate in FDG PET. *EJNMMI Res* (2016) 6:53. doi: 10.1186/s13550-016-0208-5
27. Hofheinz F, Li Y, Steffen IG, Lin Q, Lili C, Hua W, et al. Confirmation of the Prognostic Value of Pretherapeutic Tumor SUR and MTV in Patients With Esophageal Squamous Cell Carcinoma. *Eur J Nucl Med Mol Imaging* (2019) 46:1485–94. doi: 10.1007/s00259-019-04307-6
28. Mahal BA, Catalano PJ, Haddad RI, Hanna GJ, Kass JI, Schoenfeld JD, et al. Incidence and Demographic Burden of HPV-Associated Oropharyngeal Head and Neck Cancers in the United States. *Cancer Epidemiol Biomarkers Prev* (2019) 28:1660–7. doi: 10.1158/1055-9965.EPI-19-0038
29. Chera BS, Amdur RJ, Green R, Shen C, Gupta G, Tan X, et al. Phase II Trial of De-Intensified Chemoradiotherapy for Human Papillomavirus-Associated Oropharyngeal Squamous Cell Carcinoma. *J Clin Oncol* (2019) 37:2661–9. doi: 10.1200/JCO.19.01007
30. Yom SS, Torres-Saavedra P, Caudell JJ, Waldron JN, Gillison ML, Xia P, et al. Reduced-Dose Radiation Therapy for HPV-Associated Oropharyngeal Carcinoma (NRG Oncology Hn002). *J Clin Oncol* (2021) 39:956–65. doi: 10.1200/JCO.20.03128
31. Seiwert TY, Foster CC, Blair EA, Karrison TG, Agrawal N, Melotek JM, et al. OPTIMA: A Phase II Dose and Volume De-Escalation Trial for Human Papillomavirus-Positive Oropharyngeal Cancer. *Ann Oncol* (2019) 30:297–302. doi: 10.1093/annonc/mdy522

32. Blanchard P, Baujat B, Holostenco V, Bourredjem A, Baey C, Bourhis J, et al. MACH-CH Collaborative Group. Meta-Analysis of Chemotherapy in Head and Neck Cancer (MACH-NC): A Comprehensive Analysis by Tumour Site. *Radiother Oncol* (2011) 100:33–40. doi: 10.1016/j.radonc.2011.05.036
33. Lydiatt WM, Patel SG, O'Sullivan B, Brandwein MS, Ridge JA, Migliacci JC, et al. Head and Neck Cancers-Major Changes in the American Joint Committee on Cancer Eighth Edition Cancer Staging Manual. *CA Cancer J Clin* (2017) 67:122–37. doi: 10.3322/caac.21389
34. Welch ML, McIntosh C, Haibe-Kains B, Milosevic MF, Wee L, Dekker A, et al. Vulnerabilities of Radiomic Signature Development: The Need for Safeguards. *Radiother Oncol* (2019) 130:2–9. doi: 10.1016/j.radonc.2018.10.027
35. Cacicedo J, Fernandez I, Del Hoyo O, Navarro A, Gomez-Iturriaga A, Pijoan JI, et al. Prognostic Value of Maximum Standardized Uptake Value Measured by Pretreatment 18F-FDG PET/CT in Locally Advanced Head and Neck Squamous Cell Carcinoma. *Clin Transl Oncol* (2017) 19:1337–49. doi: 10.1007/s12094-017-1674-6
36. Lombardo E, Kurz C, Marschner S, Avanzo M, Gagliardi V, Fanetti G, et al. Distant Metastasis Time to Event Analysis With CNNs in Independent Head and Neck Cancer Cohorts. *Sci Rep* (2021) 11:6418. doi: 10.1038/s41598-021-85671-y
37. Cheng N-M, Yao J, Cai J, Ye X, Zhao S, Zhao K, et al. Deep Learning for Fully Automated Prediction of Overall Survival in Patients With Oropharyngeal Cancer Using FDG-PET Imaging. *Clin Cancer Res* (2021) 27:3948–59. doi: 10.1158/1078-0432.CCR-20-4935
38. Chen L, Wang H, Zeng H, Zhang Y, Ma X. Evaluation of CT-Based Radiomics Signature and Nomogram as Prognostic Markers in Patients With Laryngeal Squamous Cell Carcinoma. *Cancer Imaging* (2020) 20:28. doi: 10.1186/s40644-020-00310-5
39. Agarwal JP, Sinha S, Goda JS, Joshi K, Mhatre R, Kannan S, et al. Tumor Radiomic Features Complement Clinico-Radiological Factors in Predicting Long-Term Local Control and Laryngectomy Free Survival in Locally Advanced Laryngo-Pharyngeal Cancers. *Br J Radiol* (2020) 93:20190857. doi: 10.1259/bjr.20190857

Conflict of Interest: In the past 5 years, MBau received funding for his research projects and for educational grants to the University of Dresden by Bayer AG (2016–2018), Merck KGaA (2014-open) and Medipan GmbH (2014–2018). He is on the supervisory board of HI-STEM gGmbH (Heidelberg) for the German Cancer Research Center (DKFZ, Heidelberg) and also member of the supervisory body of the Charité University Hospital, Berlin. As former chair of OncoRay (Dresden) and present CEO and Scientific Chair of the German Cancer Research Center (DKFZ, Heidelberg), he has been or is responsible for collaborations with a multitude of companies and institutions, worldwide. In this capacity, he has discussed potential projects and signed contracts for research funding and/or collaborations with industry and academia for his institute(s) and staff, including but not limited to pharmaceutical companies such as Bayer, Boehringer Ingelheim, Bosch, Roche and other companies such as Siemens, IBA, Varian, Elekta, Bruker, etc. In this role, he was/is also responsible for the commercial technology transfer activities of his institute(s), including the creation of start-ups and licensing. This includes the DKFZ-PSMA617 related patent portfolio [WO2015055318 (A1), ANTIGEN (PSMA)] and similar IP portfolios. MBau confirms that, to the best of his knowledge, none of the above funding sources were involved in the preparation of this paper. In the past 5 years, MK received funding for her research projects by IBA (2016), Merck KGaA (2014-2018 for preclinical study; 2018-2020 for clinical study), Medipan GmbH (2014–2018). She is involved in an ongoing publicly funded (German Federal Ministry of Education and Research) project with the companies Medipan, Attomol GmbH, GA Generic Assays GmbH, Gesellschaft für medizinische und wissenschaftliche genetische Analysen, Lipotype GmbH and PolyAn GmbH (2019–2021). For the present manuscript, MK confirms that none of the above funding sources were involved in the preparation of this paper.

HA declares research grants, travel grants, and lecture fees from Sirtex Medical Europe; HA confirms that none of the above funding sources were involved in the preparation of this paper.

The remaining authors declare that the research was conducted in the absence of any commercial or financial relationships that could be construed as a potential conflict of interest.

The reviewer FH declared a past co-authorship with one of the authors ET to the handling Editor.

Publisher's Note: All claims expressed in this article are solely those of the authors and do not necessarily represent those of their affiliated organizations, or those of the publisher, the editors and the reviewers. Any product that may be evaluated in this article, or claim that may be made by its manufacturer, is not guaranteed or endorsed by the publisher.

frontiers | Frontiers in Oncology

ORIGINAL RESEARCH
published: 23 June 2022
doi: 10.3389/fonc.2022.881262

High CBX8 Expression Leads to Poor Prognosis in Laryngeal Squamous Cell Carcinoma by Inducing EMT by Activating the Wnt/β-Catenin Signaling Pathway

Qingchao Meng[1], *Lei Li*[2] *and Liping Wang*[1]*

[1] Department of Otolaryngology, Shengjing Hospital of China Medical University, Shenyang, China, [2] Department of Urology, ShengJing Hospital of China Medical University, Shenyang, China

OPEN ACCESS

Edited by:
Yubing Zhou,
First Affiliated Hospital of Zhengzhou University, China

Reviewed by:
Franz Rödel,
University Hospital Frankfurt, Germany
Mojgan Alaeddini,
Tehran University of Medical Sciences, Iran
Marcos Santos,
University of Brasilia, Brazil

***Correspondence:**
Liping Wang
wanglp@sj-hospital.org

Specialty section:
This article was submitted to Head and Neck Cancer, a section of the journal Frontiers in Oncology

Received: 22 February 2022
Accepted: 25 May 2022
Published: 23 June 2022

Citation:
Meng Q, Li L and Wang L (2022) High CBX8 Expression Leads to Poor Prognosis in Laryngeal Squamous Cell Carcinoma by Inducing EMT by Activating the Wnt/β-Catenin Signaling Pathway. Front. Oncol. 12:881262. doi: 10.3389/fonc.2022.881262

Background: In this study, we detected the expression of chromobox protein homolog 8 (CBX8) in laryngeal squamous cell carcinoma (LSCC) and its influence on the occurrence and progression of LSCC.

Methods: Pancancer analysis of CBX8 was analyzed by TCGA database and its expression in LSCC.The expression of CBX8 in 30 pairs of LSCC and adjacent tissues was analyzed by quantitative real-time PCR(qRT-PCR)and immunohistochemical assays, and its association with the prognosis and clinicopathological features of LSCC was further evaluated. A CBX8 knockdown model was constructed in AMC-HN-8 and Hep2 cell lines. The effects of CBX8 on LSCC cell proliferation, migration, invasion and apoptosis were detected by CCK8,EdU,wound healing, Transwell and flow cytometry assays. Levels of apoptosis-related protein, WNT/β-catenin signaling pathway and epithelial to mesenchymal transition (EMT) proteins, including Bax, Bcl2, β-catenin, DKK1, GSK3β, N-cadherin, E-cadherin and Snail1, in LSCC cells were detected by Western blotting.

Results: CBX8 was overexpressed in LSCC. High expression of CBX8 in LSCC patients led to shorter overall survival and correlated with tumor stage and lymphatic metastasis. After CBX8 knockdown, the proliferation of AMC-HN-8 and Hep2 cells slowed, and the number of EdU-positive cells decreased. Wound healing slowed down, and the number of Transwell invading cells decreased. The percentage of apoptotic cells increased. The expression levels of Bcl2, β-catenin, N-cadherin and Snail11 proteins were significantly reduced in the CBX8 knockdown cells, while Bax, DKK1, GSK3β and E-cadherin significantly increased with their corresponding controls.

Conclusion: CBX8 is highly expressed in LSCC and induces the EMT process by activating the Wnt/β-catenin signaling pathway to promote LSCC cell proliferation and migration and inhibit apoptosis, resulting in poor prognosis.

Keywords: CBX8, LSCC, Wnt/β-catenin, EMT, TCGA

INTRODUCTION

LSCC accounts for 85%-95% of all laryngeal cancers and is an important component of head and neck squamous cell carcinoma (HNSCC), which is also one of the most common tumors in the respiratory system and is highly invasive (1). There were 184,615 new laryngeal cancer cases, and 99,840 deaths were counted worldwide in 2020 according to a recent study from the International Agency for Research on Cancer (IARC) (2). The statistics in 2015 show that the number of new cases and deaths was 26,400 and 14,500 in China (3). Although the incidence of LSCC is relatively low compared with other types of cancer, it has been considered one of the leading causes of cancer-related deaths worldwide in recent years, especially in China (4). LSCC is treated with surgery, radiotherapy, chemotherapy or biological therapy, but the prognosis and survival did not improve significantly (5, 6). Therefore, searching for new therapeutic targets is crucial to LSCC patients.

Chromobox protein homolog 8 (CBX8), a core component of the polycomb group protein (PcG) PRC1 complex, can modify chromatin to inhibit the transcription of target genes. It plays a vital role in regulating cell proliferation, differentiation, senescence, death, tumorigenesis and metastasis (7, 8). The expression of CBX8 is closely related to the progression of a variety of cancers. Studies have shown that CBX8 is overexpressed in esophageal cancer, colorectal cancer, and breast cancer, resulting in a poor prognosis (9–12). Wnt/β-catenin signaling is a highly conserved signaling pathway that is overactivated in tongue squamous carcinoma, cervical cancer, lung cancer, gastric cancer and many other cancers (13–16). The imbalance of Wnt/β-catenin signaling in LSCC is one of the main reasons for the occurrence and progression of laryngeal cancer, and downstream proliferation signals are directly involved in tumor deterioration and metastasis (17). However, the expression of CBX8 in LSCC, its mechanism of action and its relationship with the Wnt/β-catenin signaling pathway have not been systematically elucidated. In our study, the expression of CBX8 in LSCC tissues and paired normal tissues was detected. By constructing LSCC cell lines with CBX8 knockdown, the impacts of CBX8 on cell proliferation, migration and apoptosis were observed, as well as changes in Wnt/β-catenin signaling and EMT-related proteins, to further explore the role of CBX8 in LSCC and its potential mechanism.

MATERIALS AND METHODS

Integrative Analysis of TCGA and GESA

Pancancer analysis of CBX8 can be downloaded from cBioPortal (www.cbioportal.org). Transcriptome data (FPKM) of LSCC samples were downloaded from The Cancer Genome Atlas (TCGA) (https://portal.gdc.cancer.gov). GSE27020 was downloaded from the Gene Expression Omnibus (GEO) (https://www.ncbi.nlm.nih.gov/geo/). The CBX8 expression of tumor tissues in all LSCC patients was compared with that of paired normal tissues. The correlation between CBX8 and CTNNB1 in the TCGA COAD dataset was analyzed in the GEPIA database (http://gepia.cancer-pku.cn/). Gene set enrichment analysis (GSEA) was performed by GSEA 3.0 software.

Clinical Specimens

A total of 30 patients with LSCC who underwent surgical resection in our hospital from August 2020 to March 2021 were enrolled and pathologically diagnosed with squamous cell carcinoma. The surgically removed cancer tissue samples were taken as the observation group, and the tissues 2 cm adjacent to the cancer were taken as the control group. All patients were primary cases and did not undergo preoperative radiotherapy or chemotherapy. Some specimens were placed in EP tubes filled with 4% paraformaldehyde and labeled for the preparation of paraffin sections. The remaining specimens were brought back to the laboratory and stored at -80°C. Another 10 pairs of LSCC and paracancer sections stored in the Department of Pathology of our hospital were collected. This study has been approved by the Ethics Committee of Shengjing Hospital affiliated to China Medical University (Ethics Number: 2017PS31K).

Cell Culture

Two human LSCC cell lines (AMC-HN-8 and Hep2) were purchased from the Cell Bank of the Chinese Academy of Sciences (Shanghai, China). These cell lines were grown in DMEM (HyClone, Beijing, China) and cultured. T25 cell culture bottles were supplemented with 5 ml DMEM complete medium containing 1% penicillin–streptomycin and 10% fetal bovine serum (HAKA, China) and cultured in tin in a humidified chamber at 37°C with 5% CO2. When the cell density reached over 90%, it could be digested for subculture and frozen storage.

Quantitative Real-Time PCR (qRT–PCR)

Thirty pairs of LSCC tissues and their paired adjacent normal tissues were collected during the operation and stored in a refrigerator at -80°C. RNA was extracted and reverse transcribed into cDNA according to Takara instructions. Using GAPDH as an internal reference, the relative expression of CBX8 mRNA in cancer and normal mucosal tissues was detected. CBX8 forward primer 5 '-TTATTTCTGGGTGGGATGTGG-3', reverse primer 5'-GGGAGGAAGGAGGGATGAA-3'; GAPDH forward primer 5'-TTATTTCTGGGTGGGATGTGG-3', reverse primer 5'-GGGAGGAAGGAGGGGAA-3'. Fluorescence quantitative signals were analyzed by the 2^-ΔΔCt method.

Immunohistochemistry

Tissue wax blocks were cut to a thickness of 3.5 μm and hydrated in different concentrations of xylene and ethanol. Then, the antigen was repaired by microwave heating in citrate for 8 min. Next, an SP Kit (SP-9000; Zsgb-bio, Beijing, China) was used according to the manufacturer's instructions. First, endogenous peroxidase blockers were incubated for 30 minutes, phosphate-buffered saline (PBS) was added 3 times, and 10 minutes later,

normal goat serum was added for 30 minutes. All the above operations were carried out at room temperature. Subsequently, the blocked tissue sections were incubated with an anti-CBX8 rabbit polyclonal antibody (1:200, NOVUS Biologicals USA) overnight at 4°C. Binding antibodies were detected by the biotin-streptavidin-peroxidase method and visualized by DAB as a chromogenic agent. Slices were stained with hematoxylin and sealed with neutral resin after dehydration. PBS should be used as a negative control in place of CBX8 antibody.

Cell Transfection

CBX8-siRNA and negative control siRNA were designed by Gima Genomics. AMC-HN-8 and Hep2 cells were inoculated on 6-well plates and transfected 5μl siRNA and 5μl Lipofectamine 3000 (Invitrogen, Carlsbad, CA, USA) to each well when the degree of fusion reached 50%. After culturing for 48 h, the cell RNA and protien samples obtained were tested for siRNA knockdown efficiency by qRT–PCR and Western Blot. The siRNA with the highest knockdown efficiency was selected for the following functional experiments. The siRNA sequences sense:5'-GAAGUACAGCACAUGGGAATT-3', antisense: 5'-UUCCCAUGUGCUGUACUUCTT-3'. Next, *in vitro* experiments were divided into control, si-Negtive Control (si-NC) and si-CBX8 groups.

Cell Counting Kit-8 Assay

Cell Counting Kit-8 (CCK-8) was used to detect cell proliferation in each group. Twenty-four hours after transfection, 100 μL AMC-HN-8 and Hep2 cell suspensions at a density of $3x10^4$ cells/mL were added to each well of the 96-well plate. Three secondary wells were repeated in each group. Then, 100 μL of complete culture medium containing 10% CCK8 reagent was added to each well after the cells returned to normal form and incubated at 37°C for 2 h in the dark. The absorbance at a wavelength of 450 nm was measured with a microplate reader (BioTek Instruments, Winooski, USA). The above operations were repeated at 24 h, 48 h and 72 h.

5-Ethynyl-2'-Deoxyuridine (EdU) Assay

In addition, an EdU proliferation assay can also be used to detect cell proliferation. Twenty-four hours after transfection with 6-well plates, a mixture of 1% EdU (Beyotime, Shanghai, China) and DMEM was added to each well and cultured in a cell incubator for an extra 2 h. Next, 4% formaldehyde fixation, fluorescence staining and other specific procedures were carried out according to the reagent instructions. Five fields were randomly selected under a fluorescence microscope (Olympus, Tokyo, Japan) to analyze the proportion of EdU-positive cells.

Wound Healing Assay

We observed cell migration by wound healing tests. The cells were plated in 6-well plates, and when the degree of cell fusion after transfection reached more than 90%, a straight wound was made with a 100 μL pipette tip under the ruler mark. PBS was gently cleaned to remove suspended cells 3 times and photographed under a microscope. Culture was continued for 24 hours after serum-free medium was added to each well. PBS was also used for cleaning, and wound healing was observed by photographing again.

Transwell Invasion Assay

The day before the experiment, 100μL diluted Matrigel was added to the upper chamber of Transwell chamber and placed in an incubator overnight. Twenty-four hours after transfection, 200 μL serum-free cell suspension containing $3x10^4$ cells was added to the upper chamber, and 500 μL medium containing 10% serum was added to the lower chamber and then incubated at 37°C for 24 h. Next, the chambers were removed from the 24-well plate, and the cells that did not penetrate the upper chamber were gently wiped with cotton swabs after fixation with 4% paraformaldehyde and staining with 0.1% crystal violet. Images were taken by light microscopy, and cells in each experimental group were counted by ImageJ software.

Flow Cytometry Apoptosis Assay

Twenty-four hours after transfection, LSCC cells were digested by trypsin and washed with PBS 3 times. The cells were suspended by flow tube with 1X Binding Buffer density of 1×10^6 cells/ML.100 μL cell mixed suspension was added to each tube, followed by 5 μL Annexin V-FITC and 5 μL PI staining successively. After 15 min of reaction, another 400 μL of 1X binding buffer was added to stop the reaction. Finally, detecting within 1 h. The percentage of apoptotic cells in each group was assessed by calculating the sum of Annexin V +PI+ and Annexin V +PI- cells.

Transmission Electron Microscopy(TEM)

Twenty-four hours after transfection, the cells were digested by trypsin and washed 3 times with PBS. The cells were fixed with 2.5% glutaraldehyde and 1% osmium solution at 4°C for 2 h and then rinsed with sodium dimethoarate 3 times for 5 min each. The cells were dehydrated with ethanol and acetone of different concentration gradients, soaked with a mixed solution of epoxy resin and acetone, and finally embedded, sectioned and photographed under a microscope.

Western Blotting

Forty-eight hours after transfection, the cells were centrifuged at 14000×rpm and 4°C for 15 min for total protein extraction and quantified by the BCA method. Subsequently, 30μg of each protein sample was subjected to SDS-PAGE electrophoresis, and then the samples were transferred to PVDF membranes and blocked with 5% skim milk for 2 h. After blocking, the corresponding primary antibodies CBX8(1:10000), Bcl2 (1:1000), Bax(1:1000), β-catenin(1:1000), DKK1(1:1000), GSK3β(1:1000), N-cadherin(1:1000), E-cadherin(1:1000), Snail1(1:1000), GAPDH(1:5000)were incubated with the membrane overnight at 4°C. On the second day, after

removing the primary antibodies and washing the membranes with Tween-20 tris buffered saline (TBST), the corresponding secondary antibody (1:5000) was incubated for 2 h. Then, the cells were washed with TBST again, and ECL hypersensitive chromogenic solution was added for development and photography. Imaje J software was used to process all the transfer strips, and the gray values of each strip were obtained for statistical analysis.

Statistical Analysis

SPSS 22.0 and GraphPad Prism 9 software were used for experimental data analysis and statistical graph drawing. The data are presented as the mean values ± SEMs. Independent sample *T* tests were used for comparisons between the two samples, and paired samples were used for paired *t* tests. The correlation between CBX8 expression and clinicopathological features was estimated by Pearson's X^2 test. The Kaplan–Meier method was used to draw the survival curve, and the log-rank method was used to test the difference. Cox regression analysis was used to analyze univariate and multivariate factors affecting the prognosis of patients. $P < 0.05$ was statistically significant.

RESULTS

CBX8 Is Overexpressed in Various Cancers and LSCC Tissues

The expression of the CBX8 gene in various common tumors and LSCC was compared and analyzed in the TCGA database. The CBX8 gene is highly expressed in 30 types of malignant tumors, including HNSCC, and expressed at low levels in 4 types of tumors (**Figure 1A**). According to the transcriptomic data of TCGA, the expression of CBX8 mRNA in LSCC was significantly higher than that in para-cancer tissues by using the "limma" package (P<0.001)(**Figure 1B**). Meanwhile, cancer tissues of 30 LSCC patients who underwent total laryngeal surgery in Shengjing Hospital affiliated with China Medical University and their paired para-cancer tissues were collected to detect the expression of CBX8 mRNA by qRT–PCR. Consequently, the results obtained were consistent with TCGA database analysis, and the difference was significant (P<0.001) (**Figure 1C**). Furthermore, IHC revealed that CBX8 is mainly expressed in the tumor nucleus and cytoplasm, and its expression in LSCC (**Figure 1D, E**) was significantly higher than that in paracancer tissues (**Figure 1F**), positive rate in cancer tissues and paracancer

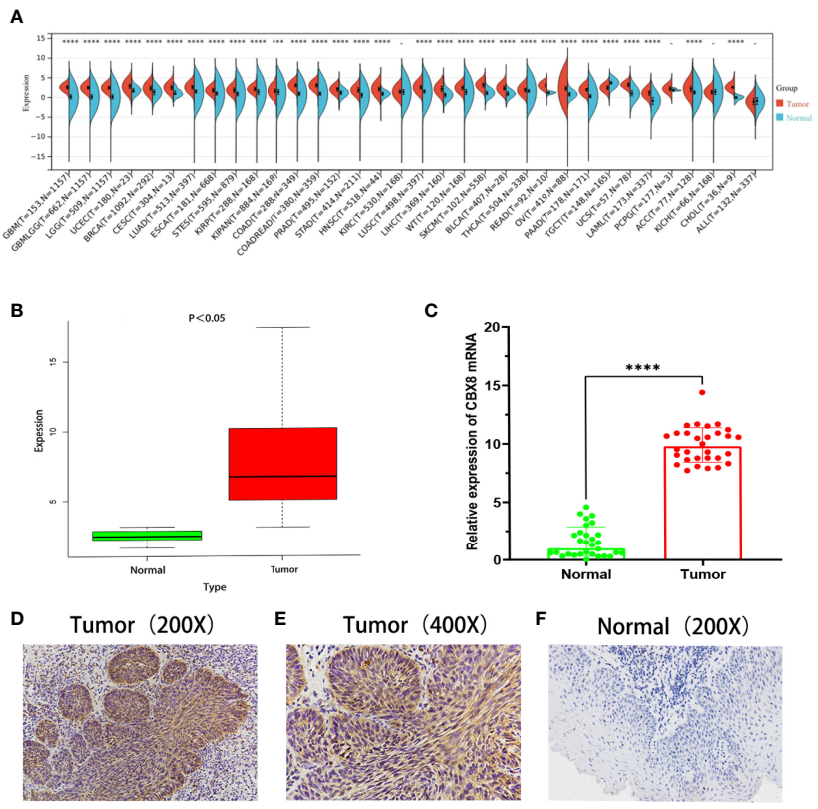

FIGURE 1 | CBX8 was highly expressed in LSCC tissues. **(A)** Expression of CBX8 mRNA in different cancer types according to TCGA and GTEx data. **(B)** Expression of CBX8 in laryngeal squamous cell carcinoma in TCGA database. **(C)** Real-time quantitative PCR was used to detect the relative expression of CBX8 mRNA in laryngeal squamous cell carcinoma and paired normal tissues. **(D–F)** IHC detected the expression of CBX8 protein in laryngeal carcinoma and paired normal tissues. (*P < 0.05, ***P < 0.001, ****P < 0.0001).

tissues were respectively 67.5%(27/40)and 22.5% (9/40) (**Table 1**). These data suggest that CBX8 was overexpressed in LSCC.

High Expression of CBX8 Leads to Poor Prognosis in Patients With LSCC

We divided the expression level of CBX8 in 111 TCGA tumor samples into high expression and low expression groups according to the median(6.690479164). The overall survival rate of CBX8 obtained by the "survival" package showed that the survival time of patients with high CBX8 expression was shorter than that of patients with low CBX8 expression (**Figure 2A**). Next, we used the GEO database for verification, and the conclusion was consistent with the previous analysis (**Figure 2B**). Meanwhile, a total of 92 patients with definite lymph node typing were screened from TCGA database, our bioassay results showed that its expression level was also associated with lymph node metastasis, and survival rates were higher in early-stage patients than in advanced-stage patients (**Figure 2C**). IHC came to the same conclusion, the positive expression rate was 92.31% (12/13) in patients with lymph node metastasis and 55.56% (15/27) in patients without lymph node metastasis. The expression level of CBX8 protein in LSCC tissues was also correlated with the clinical stage of patients. The positive expression rates of STAGE I & II and III & IV patients were 18.18% (2/11), 86.21% (25/29), respectively, with statistically significant differences. At the same time, there was no correlation between CBX8 protein expression level and sex, age, smoking, drinking, site of disease or differentiation degree of patients (**Table 2**).

Promotive Effect of CBX8 on the Proliferative, Migrative and Invasive Ability of LSCC

To observe the effect of CBX8 on the biological behavior of LSCC cells, we synthesized CBX8 siRNA and transfected AMC-HN-8 and Hep2 cells with the highest knockdown efficiency. Finally, we observed that after CBX8 knockdown, the expression of CBX8 mRNA in AMC-HN-8 and Hep2 cells was significantly decreased. The CCK-8 results showed that the proliferation ability of AMC-HN-8 and Hep2 cells was significantly weakened after CBX8 knockdown (**Figures 3A, B**). EdU experiments further verified the above findings, and the number of EdU-positive cells in the CBX8-siRNA group was significantly reduced, which also indicated that cell proliferation was weakened (**Figures 3C, D**). In the wound healing test, the migration distance of the CBX8-siRNA group to the wound was significantly shorter (**Figures 3E, F**). Transwell invasion assay showed that the number of cell invasion was significantly reduced after CBX8 knockdown (**Figures 3G, H**).

Knockdown of CBX8 Can Promote Apoptosis in LSCC Cells

A CBX8 knockdown model was constructed by siRNA transfection, and apoptosis was detected by flow cytometry (Annexin V/PI method). The results showed that the apoptosis rate of the two LSCC cell lines increased significantly in the si-CBX8 groups (**Figures 4A, B**). Meanwhile, total protein of each group was extracted, and Western blotting confirmed that the expression of the apoptotic protein Bax increased and Bcl2

TABLE 1 | Expression of CBX8 protein in LSCC.

Group	n	Positive	Negative	Positive rate (%)	X^2	*P*
LSCC tissue	40	27	13	67.5	16.364	0.000
Normal paracancer tissue	40	9	31	22.5		

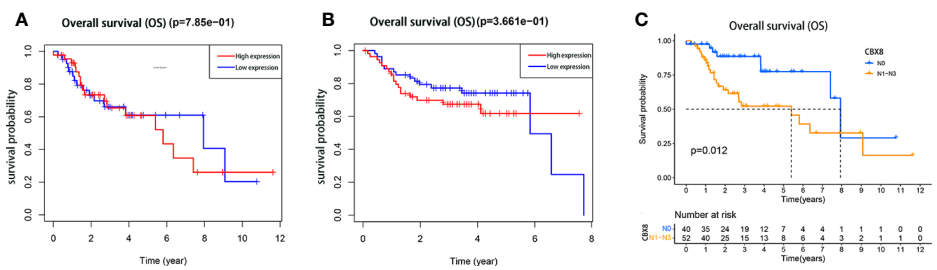

FIGURE 2 | The relationship between the expression of CBX8 protein and the prognosis of patients with LSCC. Kaplan–Meier survival curve comparison of high and low expression of CBX8. **(A)** Kaplan–Meier analysis of TCGA samples. **(B)** The Kaplan–Meier analysis of the GEO (GSE27020)samples. **(C)** The Kaplan–Meier analysis of the TCGA samples with or without lymph node metastasis.

TABLE 2 | The relationship between CBX8 protein expression and clinicopathological features.

Clinical features		n (40)	CBX8		X^2	P-value
			positive (n)	negative (n)		
Gender	Male	34	24	10	0.985	0.321
	Female	6	3	3		
Age	≥60	27	18	9	0.026	0.871
	<60	13	9	4		
Smoking	Yes	38	26	12	0.294	0.588
	No	2	1	1		
Drinking	Yes	30	19	11	0.950	0.330
	No	10	8	2		
Location	Supraglott	14	11	3	2.664	0.264
	Vocal	24	14	10		
	Infraglott	2	2	0		
The degree of differentiation	Low	7	2	5	5.875	0.053
	Medium	20	15	5		
	High	13	10	3		
T stage	I/II	11	2	9	16.822	0.000
	III/IV	29	25	4		
N stage	N0	27	15	12	5.403	0.020
	N1/N2	13	12	1		
M stage	M0	38	26	12	0.294	0.588
	M1	2	1	1		

decreased with the decline of CBX8 (**Figures 4C, D**). Furthermore, transmission electron microscopy showed that after the knockdown of CBX8 expression, the nuclei of AMC-HN-8 and Hep2 cells were deformed, mitochondria were obviously damaged, normal morphology disappeared, and large vacuolar structures were formed (**Figures 4E, F**).

Knockdown CBX8 Regulates Wnt/β-Catenin Signaling Pathway

The CTNNB1 gene encodes the β-catenin protein, which is an important regulatory protein of the Wnt/β-catenin signaling pathway (18). Correlation analysis between CBX8 and CTNNB1 in the TCGA CO-AD dataset showed that CBX8 was positively correlated with CTNNB1 gene expression (**Figure 5A**). To elucidate the mechanism by which CBX8 promotes cell proliferation, we searched for pathways through which CBX8 might be involved *via* KEGG enrichment analysis, and the results showed that CBX8 was associated with the Wnt signaling pathway (**Figure 5B**). Based on this, we detected changes in Wnt/β-catenin signaling pathway-related proteins in CBX8 knockdown cells. The results showed that the expression of β-catenin protein in AMC-HN-8 and Hep2 cells decreased, while the expression of DKK1 and GSK3β increased after transfection (**Figures 5C, D**). These results suggest that CBX8 may positively regulate the Wnt/β-catenin signaling pathway to promote LSCC cell proliferation and migration and inhibit apoptosis.

Knockdown CBX8 Regulates EMT-Related Protein Expression

Relevant studies have confirmed that CBX8 can induce tumor cell proliferation and migration by regulating EMT (19). We detected changes in the EMT-related proteins Snail1, E-catherine and N-cadherin after transfection. Western blotting analysis clearly showed that E-Catherine (epithelial marker) significantly increased while N-cadherin and Snail1 protein levels decreased in CBX8-knockdown cellss (**Figures 6A, B**).

DISCUSSION

The incidence of LSCC is the second highest among all types of HNSCC, and the overall survival rate is still low (20, 21). Therefore, it is of great significance to explore the molecular mechanism of LSCC disease progression. The PcG protein family is a family of proteins that inhibit gene expression epigenetics through chromatin remodeling and histone modification (22) and is involved in stem cell differentiation and tumorigenesis and metastasis (23, 24). CBX8 belongs to the PcG protein family and can jointly induce and maintain the inhibition state of the gene with PRC2 by combining with RING1a/B, BMI1 and other protein molecules to form PRC1 (8). Recent studies have shown that CBX8 interacts with chromatin PTEN to regulate mitosis (25). High expression of CBX8 in HCC enhances proliferation and migration by activating the AKT/β-catenin signaling pathway (26), while in glioblastoma cells, breast cancer cells and lung cancer cells, CBX8 can strengthen proliferation and invasion capacity by activating the WNK2/MMP2 signaling pathway, ultimately leading to metastasis (12). In this study, through the analysis of TCGA database, we can clearly see that CBX8 is highly expressed in a large number of common malignant tumors, including HNSCC, so we speculate that CBX8 may also be involved in the progression of LSCC. Subsequently, through R language analysis in TCGA database,

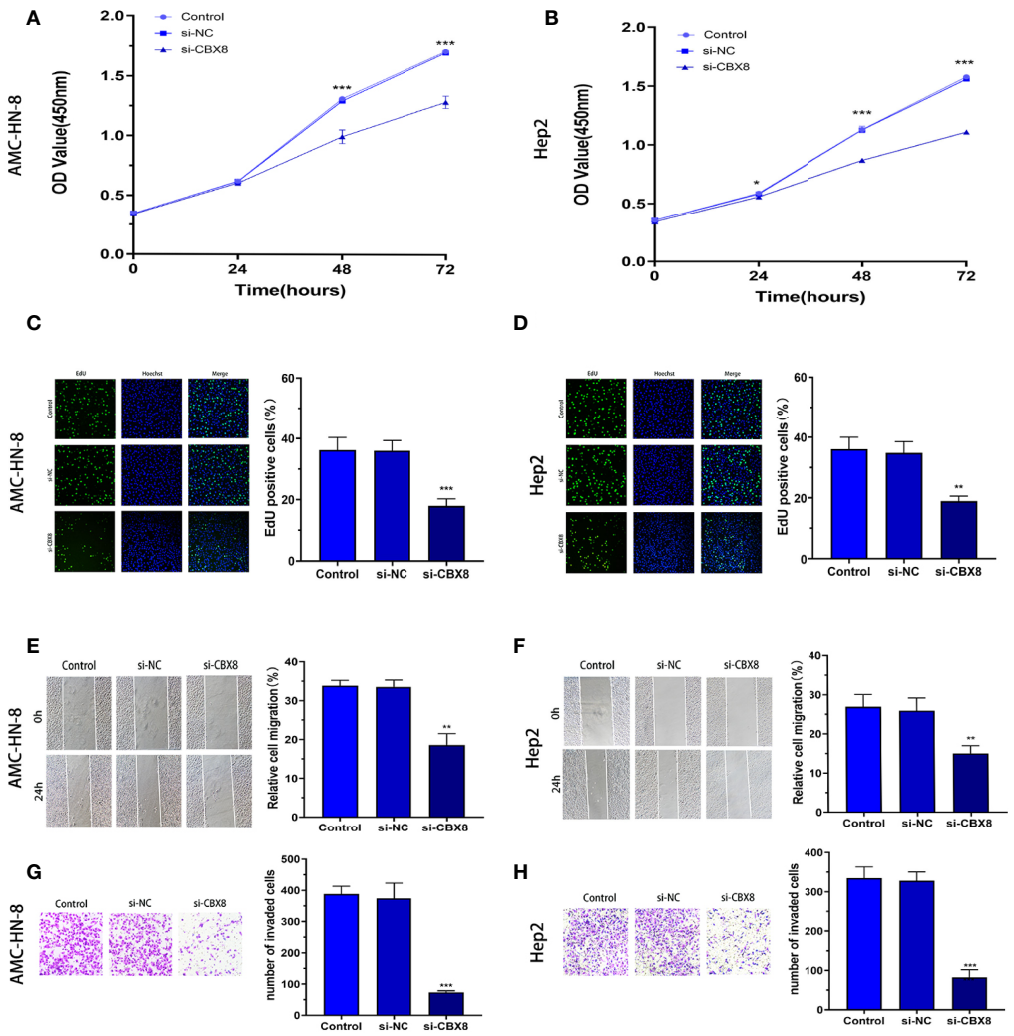

FIGURE 3 | Knockdown of CBX8 inhibited LSCC cell proliferation, migration and invasion. **(A, B)** A CCK-8 assay was used to detect the effect of CBX8 on the proliferation of LSCC cells. **(C, D)** The effect of CBX8 on the proliferation of LSCC was detected by EdU assay. **(E, F)** The effect of CBX8 on the migration of LSCC cells was detected by wound healing assay. **(G, H)** Transwell assays were used to detect the effect of CBX8 on the invasion of LSCC cells (crystal violet staining ×200). Each assay was repeated at least three times. Data from one representative experiment is presented as Mean ± SEM (**P < 0.01, ***P < 0.001).

CBX8 mRNA was highly expressed in LSCC tissues. This result was confirmed in our clinical patient tissue collection. TAGA and GEO database analysis showed that the survival rate of patients with high expression of CBX8 tumors was lower.TCGA database analysis further showed that the survival rate of patients with lymph node metastasis was shorter than that of patients without lymph node metastasis. In addition, Zeng et al. (27) also confirmed that the expression of CBX8 was inversely proportional to the survival rate of patients with bladder cancer and was highly expressed in patients with stage III and IV advanced tumors and lymph node metastasis, which was consistent with the results obtained in our analysis of CBX8 and clinicopathological features.These results suggested that high expression of CBX8 leads to poor prognosis in LSCC patients.

By constructing a CBX8 knockdown model in LSCC cell lines, cell phenotype tests suggested that CBX8 silencing can inhibit cell proliferation, migration,invasion and promote apoptosis. Transmission electron microscopy showed that the nucleus was deformed, mitochondria disappeared and autophagosomes formed. Many studies have proven that autophagy may promote apoptosis (28), further demonstrating that CBX8 can inhibit cell apoptosis. These studies suggested that CBX8 may be inextricably linked to the progression of LSCC.

The occurrence and progression of LSCC are regulated by a variety of signaling pathways. Abnormally activated Wnt/β-catenin signaling pathway regulates the occurrence and development of a variety of tumors, promoting progression, metastasis, and poor prognosis (29, 30). For example, Yu et al.

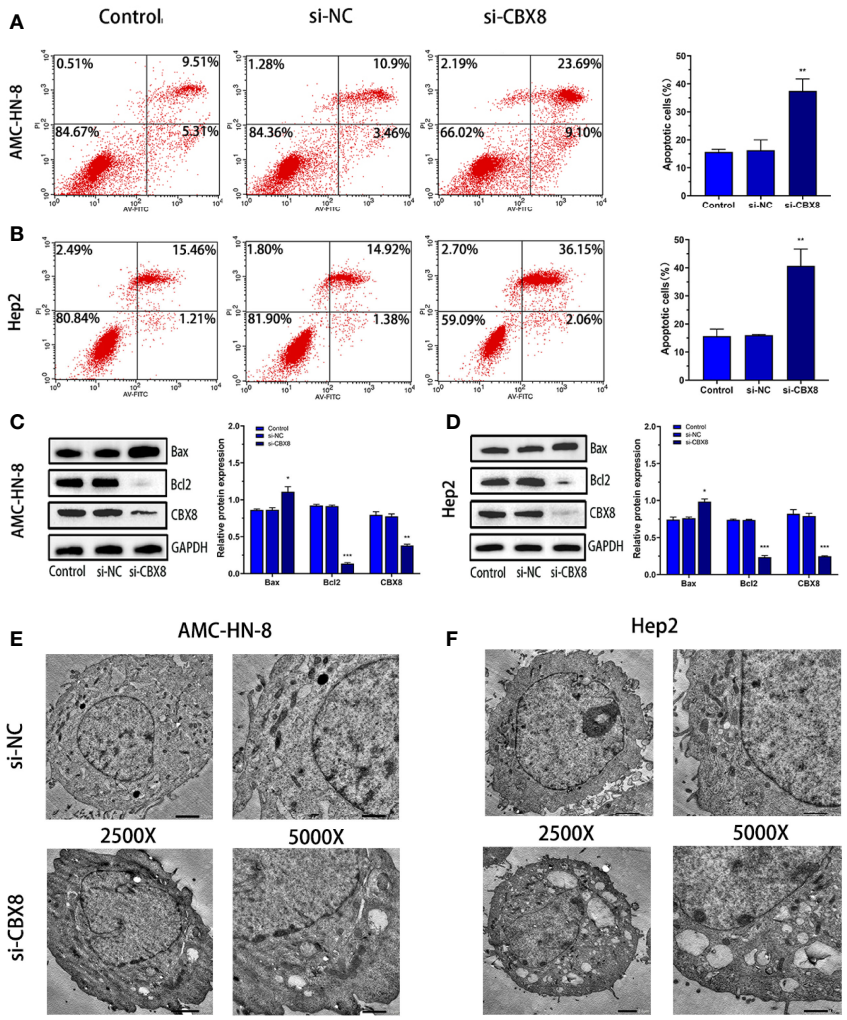

FIGURE 4 | Knockdown of CBX8 can promote apoptosis and autophagy in LSCC cells. **(A, B)** After knockdown of CBX8, cell apoptosis in each group was detected by flow cytometry. **(C, D)** Western blotting was used to detect the protein expression of CBX8, Bax and Bcl2 in AMC-HN-8 and Hep2 cells. **(E, F)** Morphological changes in CBX8 cells were observed by transmission electron microscopy.Each assay was repeated at least three times. Data from one representative experiment is presented as Mean ± SEM (*P < 0.05, **P < 0.01, ***P < 0.001).

(31) identified a novel UBE2T inhibitor, M435-1279, and showed that M435-1279 inhibits overactivation of the Wnt/β-catenin signaling pathway by blocking UBE2T-mediated RACK1 degradation, thereby inhibiting gastric cancer progression and reducing cytotoxicity. Abnormal regulatory transcription factor β-catenin is the key to initiating the Wnt/β-catenin pathway, which can lead to early carcinogenesis (32). In addition, Wnt ligand inhibits ubiquitination and degradation of β-catenin, which is a downstream target gene of the costimulator activation signal of TCF/LEF family transcription factors (33). DKK1 and GSK3β are important components involved in the Wnt/β-catenin signaling pathway. High expression of DKK1 can reduce intracellular β-catenin expression and promote apoptosis of WB-F344 cells (34). Active GSK3β binds to CK1 (Casein Kinase 1), APC (Adenomatous Polyposis Coli), AXIN1 and other members of the destruction complex to inhibit tumor development by phosphorylation and subsequent degradation of the oncogenic β-catenin protein (35). In this study, Western blotting data showed that the expression of β-catenin was also decreased after the expression of CBX8 was downregulated, while the expression of DKK1 and GSK3β was increased, suggesting that the high expression of CBX8 in LSCC may positively regulate the Wnt/β-catenin signaling pathway.

EMT is a reversible developmental process in which cancer cells reversibly transition from an epithelial phenotype of apex-basal polarity and cell adhesion to a fusiform and more active mesenchymal state, enabling cell migration and invasion (36, 37); the result is multiple tumor metastases and poor prognosis (38). EMT transformation in LSCC has been reported. For example, Sun et al. (39) found that DHA could inhibit EMT induced by IL-6

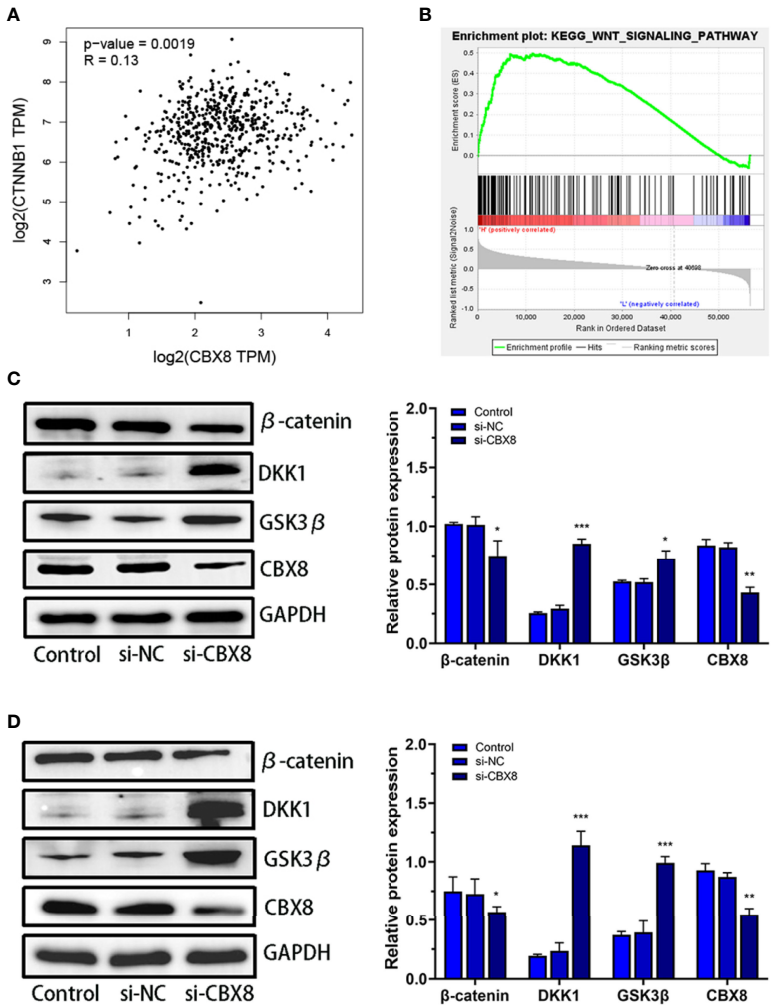

FIGURE 5 | Effect of CBX8 knockdown on the Wnt/β-catenin signaling pathway. **(A)** Correlation analysis between CBX8 and CTNNB1 in the TCGA CO-AD dataset. **(B)** GSEA showed that CBX8 was enriched in the Wnt/β-catenin signaling pathway in LSCC. **(C, D)** The expression levels of β-catenin, DKK1 and GSK3β in AMC-HN-8 and Hep2 cells were detected by Western blotting and semiquantitative analysis. Each assay was repeated at least three times. Data from one representative experiment is presented as Mean ± SEM (*P < 0.05, **P < 0.01, ***P < 0.001).

in LSCC cells through the miR-130B-3p/STAT3/β-catenin pathway, and the interaction between EMT and angiogenesis can improve the invasivity of LSCC (40). We concluded that the expression of E-cadherin increased after CBX8 knockdown, while the expression of N-cadherin and Snail1 decreased, suggesting that CBX8 may participate in the EMT process in LSCC. Many studies have proven that activation of the Wnt/β-catenin signaling pathway can lead to deterioration by inducing EMT in many different types of cancer (41). In other studies, reduced levels of E-cadherin and its complexes were inversely associated with tumor histological grade and were directly associated with intrahepatic metastasis and liver capsule invasion (42). Other studies also found that Galectin-3 could directly increase the expression of N-cadherin by promoting the accumulation of β-catenin in the nucleus, which activated the transcription of TCF/LEF-responsive genes (43). In ovarian cancer tissues and cell lines, GOLPH3 (high phosphoprotein 3) is a gene that encodes an oncoprotein, and Snail1 and other EMT transcription factors have been shown to regulate its expression by activating the Wnt/β-catenin signaling pathway (44). The occurrence of EMT in LSCC is also associated with the signal. Li et al. (45) found that CDK8 was involved in the progression of EMT through β-catenin of Wnt signaling. Therefore, combined with the above results, it can be speculated that high expression of CBX8 may induce the occurrence of LSCC EMT by regulating the Wnt/β-catenin signaling pathway.

Our study analyzed the expression of CBX8 in LSCC and adjacent normal mucosal tissues and its relationship with the Wnt/β-catenin signaling pathway and EMT. CBX8 may regulate the expression of β-catenin, DKK1, GSK3β and EMT-related proteins by activating the Wnt/β-catenin signaling pathway in

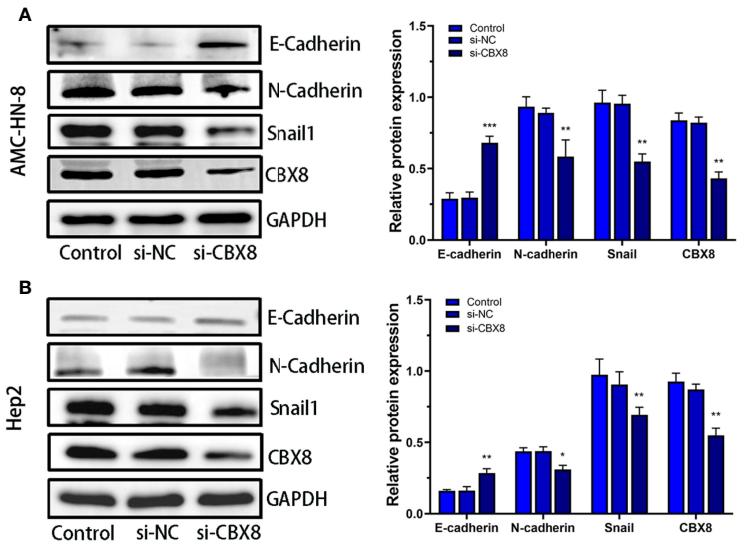

FIGURE 6 | Effect of CBX8 knockdown on EMT-related proteins. Western blotting was used to detect the expression of E-cadherin, N-cadherin and Snail1 in AMC-HN-8 cells **(A)** and Hep2 cells **(B)** and semiquantitative analysis.Each assay was repeated at least three times. Data from one representative experiment is presented as Mean ± SEM (*P < 0.05, **P < 0.01, ***P < 0.001).

LSCC, thus enhancing LSCC cell proliferation, migration and invasion, inhibiting apoptosis, and ultimately leading to poor prognosis of patients. Overall, CBX8 may be intimately involved in the diagnosis and treatment of LSCC, but the specific action and mechanism need to be further studied.

DATA AVAILABILITY STATEMENT

The original contributions presented in the study are included in the article/supplementary material. Further inquiries can be directed to the corresponding author.

ETHICS STATEMENT

The studies involving human participants were reviewed and approved by the ethics committee of Shengjing Hospital Affiliated to China Medical University (ethics No.: 2017ps31k). Written informed consent for participation was not required for this study in accordance with the national legislation and the institutional requirements. Written informed consent was not obtained from the individual(s) for the publication of any potentially identifiable images or data included in this article.

AUTHOR CONTRIBUTIONS

QM conceived structure, authored, or reviewed drafts of the paper, approved the final draft, writing - Review and Editing, prepared figures and/or tables, and approved the final draft. LL: assisting to search related literature. LW authored or reviewed drafts of the paper, and approved the final draft.

REFERENCES

1. Steuer C E, El Deiry M, Parks JR, Higgins KA, Saba NF. An Update on Larynx Cancer[J]. *CA: Cancer J Clin* (2017) 67(1):31–50. doi: 10.3322/caac.21386
2. Steuer CE, El Deiry M, Parks JR, Higgins KA, Saba NF. Global Cancer Statistics 2020: GLOBOCAN Estimates of Incidence and Mortality Worldwide for 36 Cancers in 185 Countries[J]. *CA: Cancer J Clin* (2021) 71 (3):209–49. doi: 10.3322/caac.21660
3. Chen W, Zheng R, Baade PD, Zhang S, Zeng H, Bray F, et al. Cancer Statistics in China, 2015. *CA: Cancer J Clin* (2016) 66(2):115–32. doi: 10.3322/caac.21338
4. Wei Q, Yu D, Liu M, Wang M, Zhao M, Liu M, et al. Genome-Wide Association Study Identifies Three Susceptibility Loci for Laryngeal Squamous Cell Carcinoma in the Chinese Population[J]. *Nat Genet* (2014) 46(10):1110–4. doi: 10.1038/ng.3090
5. Alagkiozidis I. Commentary on 'Development and Validation of Nomograms to Accurately Predict Risk of Recurrence for Patients With Laryngeal Squamous Cell Carcinoma: Cohort Study'[J]. *Int J Surg (London England)* (2020) 78:26–7. doi: 10.1016/j.ijsu.2020.03.076
6. Lo NC, Denaro N, Merlotti A, Merlano M. Head and Neck Cancer: Improving Outcomes With a Multidisciplinary Approach[J]. *Cancer Manag Res* (2017) 9:363–71. doi: 10.2147/CMAR.S115761
7. Morey L, Helin K. Polycomb Group Protein-Mediated Repression of Transcription[J]. *Trends Biochem Sci (Amsterdam Regular ed.)* (2010) 35 (6):323–32. doi: 10.1016/j.tibs.2010.02.009
8. Gao Z, Zhang J, Bonasio R, Strino F, Sawai A, Parisi F, et al. PCGF Homologs, CBX Proteins, and RYBP Define Functionally Distinct PRC1 Family Complexes [J]. *Mol Cell* (2012) 45(3):344–56. doi: 10.1016/j.molcel.2012.01.002
9. Lee SH, Um S, Kim E. CBX8 Suppresses Sirtinol-Induced Premature Senescence in Human Breast Cancer Cells *via* Cooperation With SIRT1[J]. *Cancer Lett* (2013) 335(2):397–403. doi: 10.1016/j.canlet.2013.02.051
10. Xiao WF, Ou C, Qin J, Xing F, Sun Y, Li Z, et al. CBX8, a Novel DNA Repair Protein, Promotes Tumorigenesis in Human Esophageal Carcinoma[J]. *Int J Clin Exp Pathol* (2014) 7(8):4817–26.

11. Zhang Y, Kang M, Zhang B, Meng F, Song J, Kaneko H, et al. M6a Modification-Mediated CBX8 Induction Regulates Stemness and Chemosensitivity of Colon Cancer *via* Upregulation of LGR5[J]. *Mol Cancer* (2019) 18(1):185. doi: 10.1186/s12943-019-1116-x
12. Jia Y, Wang YJ, Zhang CC, Mike Y. Upregulated CBX8 Promotes Cancer Metastasis *via* the WNK2/MMP2 Pathway[J]. *Mol Ther Oncolytics* (2020) 19:188–96. doi: 10.1016/j.omto.2020.09.012
13. Rath G, Jawanjal P, Salhan S, Nalliah M, Dhawan I. Clinical Significance of Inactivated Glycogen Synthase Kinase 3β in HPV-Associated Cervical Cancer: Relationship With Wnt/β-Catenin Pathway Activation[J]. *Am J Reprod Immunol (1989)* (2015) 73(5):460–78. doi: 10.1111/aji.12346
14. Zhang B, Yang Y, Shi XT, Liao W, Chen M, Cheng A S-L, et al. Proton Pump Inhibitor Pantoprazole Abrogates Adriamycin-Resistant Gastric Cancer Cell Invasiveness *via* Suppression of Akt/GSK-β/β-Catenin Signaling and Epithelial–Mesenchymal Transition[J]. *Cancer Lett* (2014) 356(2):704–12. doi; 10.1016/j.canlet.2014.10.016
15. Yan G, Yan GX, Zou RH, Fan B, Wang Z, Wang Y, et al. Silencing RhoA Inhibits Migration and Invasion Through Wnt/β-Catenin Pathway and Growth Through Cell Cycle Regulation in Human Tongue Cancer[J]. *Acta Biochim Biophys Sin* (2014) 46(8):682–90. doi: 10.1093/abbs/gmu051
16. Pan J, Fang S, Tian HH, Zhou C, Zhao X, Tian H, et al. lncRNA JPX/miR-33a-5p/Twist1 Axis Regulates Tumorigenesis and Metastasis of Lung Cancer by Activating Wnt/β-Catenin Signaling[J]. *Mol Cancer* (2020) 19(1):9–9. doi: 10.1186/s12943-020-1133-9
17. Sun S, Gong C, Yuan K. LncRNA UCA1 Promotes Cell Proliferation, Invasion and Migration of Laryngeal Squamous Cell Carcinoma Cells by Activating Wnt/β-Catenin Signaling Pathway[J]. *Exp Ther Med* (2019) 17(2):1182–9. doi; 10.3892/etm.2018.7097
18. Kim G, Kurnit KC, Djordjevic B, Singh C, Munsell M F, Wang W-L, et al. Nuclear β-Catenin Localization and Mutation of the CTNNB1 Gene: A Context-Dependent Association[J]. *Modern Pathol* (2018) 31(10):1553–9. doi: 10.1038/s41379-018-0080-0
19. Wang G, Tang JJ, Zhan WX, Zhang R, Zhang M, Liao D, et al. CBX8 Suppresses Tumor Metastasis *via* Repressing Snail in Esophageal Squamous Cell Carcinoma [J]. *Theranostics* (2017) 7(14):3478–88. doi: 10.7150/thno.20717
20. Spector JG, Sessions DG, Haughey BH, Chao K SC, Simpson J E, Mofty S, et al. Delayed Regional Metastases, Distant Metastases, and Second Primary Malignancies in Squamous Cell Carcinomas of the Larynx and Hypopharynx[J]. *Laryngoscope* (2001) 111(6):1079–87. doi: 10.1097/00005537-200106000-00028
21. Marur SM, Forastiere AAM. Head and Neck Squamous Cell Carcinoma: Update on Epidemiology, Diagnosis, and Treatment[J]. *Mayo Clinic Proc* (2016) 91(3):386–96. doi: 10.1016/j.mayocp.2015.12.017
22. Simon JA, Kingston RE. Mechanisms of Polycomb Gene Silencing: Knowns and Unknowns[J]. *Nat Rev Mol Cell Biol* (2009) 10(10):697–708. doi: 10.1038/nrm2763
23. Sauvageau M, Sauvageau G. Polycomb Group Proteins: Multi-Faceted Regulators of Somatic Stem Cells and Cancer[J]. *Cell Stem Cell* (2010) 7 (3):299–313. doi: 10.1016/j.stem.2010.08.002
24. Zhang Y, Wang HB, Wang LJ, Erdjument-Bromage H, Vidal M, Tempst P, et al. Role of Histone H2A Ubiquitination in Polycomb Silencing[J]. *Nature* (2004) 431(7010):873–8. doi; 10.1038/nature02985
25. Choi BH, Colon TM, Lee E, Lee E, Kou Z, Dai W, et al. CBX8 Interacts With Chromatin PTEN and is Involved in Regulating Mitotic Progression[J]. *Cell Prolif* (2021) 54(11):e13110. doi: 10.1111/cpr.13110
26. Zhang CZ, Chen SL, Wang CH, He Y-F, Yang X, Xie D, et al. CBX8 Exhibits Oncogenic Activity *via* AKT/β-Catenin Activation in Hepatocellular Carcinoma[J]. *Cancer Res (Chicago Ill.)* (2018) 78(1):51–63. doi: 10.1158/0008-5472.CAN-17-0700
27. Zeng F, Luo L, Li D, Guo J, Guo M, et al. KPNA2 Interaction With CBX8 Contributes to the Development and Progression of Bladder Cancer by Mediating the PRDM1/c-FOS Pathway[J]. *J Transl Med* (2021) 19(1):112. doi: 10.1186/s12967-021-02709-5
28. Kroemer G, Maiuri M C, Zalckvar E, Kimchi A. Self-Eating and Self-Killing: Crosstalk Between Autophagy and Apoptosis. *Nat reviews[J] Mol Cell Biol* (2007) 8(9):741–52. doi; 10.1038/nrm2239
29. Zhan T, Rindtorffand MB. Wnt Signaling in Cancer[J]. *Oncogene* (2017) 36:1461–73. doi: 10.1038/onc.2016.304
30. Nusse R, Clevers H. Wnt/β-Catenin Signaling, Disease, and Emerging Therapeutic Modalities[J]. *Cell* (2017) 169(6):985–99. doi: 10.1016/j.cell.2017.05.016
31. Yu Z, Jiang X, Qin L, Deng H, Wang J, Ren W, et al. A Novel UBE2T Inhibitor Suppresses Wnt/beta-Catenin Signaling Hyperactivation and Gastric Cancer Progression by Blocking RACK1 Ubiquitination[J]. *Oncogene* (2021) 40 (5):1027–42. doi: 10.1038/s41388-020-01572-w
32. Chatterjee A, Paul S, Bisht B, Bhattacharya S, Sivasubramaniam S, Paul M K, et al. Advances in Targeting the WNT/β-Catenin Signaling Pathway in Cancer. *Drug Discovery Today* (2021) 13):165. doi; 10.1016/j.drudis.2021.07.007
33. Sebio A, Kahn M, Lenz H. The Potential of Targeting Wnt/β-Catenin in Colon Cancer[J]. *Expert Opin Ther Targets* (2014) 18(6):611–5. doi: 10.1517/14728222.2014.906580
34. Ye J, Xin L, Liu J, Tang T, Bao X, Yan Y, et al. Dkk1 Inhibits Malignant Transformation Induced by Bmi1 *via* the Beta-Catenin Signaling Axis in WB-F344 Oval Cells[J]. *FEBS Open Bio* (2021) 11(7):1854–66. doi: 10.1002/2211-5463.13132
35. Kafka A, Bukovac A, Brglez E, Jarmek A M, Poljak K, Brlek P, et al. Methylation Patterns of DKK1, DKK3 and GSK3beta Are Accompanied With Different Expression Levels in Human Astrocytoma[J]. *Cancers (Basel)* (2021) 13(11):2530. doi: 10.3390/cancers13112530
36. Nieto MA, Huang R, Jackson RA, Thiery JP. EMT: 2016[J]. *Cell* (2016) 166 (1):21–45. doi: 10.1016/j.cell.2016.06.028
37. Lim J, Thiery JP. Epithelial-Mesenchymal Transitions: Insights From Development [J]. *Dev (Cambridge)* (2012) 139(19):3471–86. doi: 10.1242/dev.071209
38. Babaei G, Aziz, Jaghi N. EMT, Cancer Stem Cells and Autophagy; The Three Main Axes of Metastasis[J]. *BioMed Pharmacother* (2021) 133:110909. doi: 10.1016/j.biopha.2020.110909
39. Sun Y, Lu X, Li H, Li X. Dihydroartemisinin Inhibits IL-6-Induced Epithelial-Mesenchymal Transition in Laryngeal Squamous Cell Carcinoma *via* the miR-130b-3p/STAT3/beta-Catenin Signaling Pathway[J]. *J Int Med Res* (2021) 49(11):3000605211009494. doi: 10.1177/03000605211009494
40. Franz L, Nicolè L, Frigo AC, Ottaviano G, Gaudioso P, Saccardo T, et al. Epithelial-To-Mesenchymal Transition and Neoangiogenesis in Laryngeal Squamous Cell Carcinoma[J]. *Cancers* (2021) 13(13):3339. doi: 10.3390/cancers13133339
41. Tian S, Peng P, Li J, Deng H, Zhan N, Zeng Z, et al. SERPINH1 Regulates EMT and Gastric Cancer Metastasis *via* the Wnt/beta-Catenin Signaling Pathway[J]. *Aging (Albany NY)* (2020) 12(4):3574–93. doi: 10.18632/aging.102831
42. Gurzu S, Kobori L, Fodor D, et al. Epithelial Mesenchymal and Endothelial Mesenchymal Transitions in Hepatocellular Carcinoma: A Review[J]. *BioMed Res Int* (2019) 2019:2962580–12. doi: 10.1155/2019/2962580
43. Cao Z, Wang Z, Leng P. Aberrant N-Cadherin Expression in Cancer[J]. *Biomedicine Pharmacotherapy* (2019) 118:109320. doi: 10.1016/j.biopha.2019.109320
44. Teeuwssen M, Fodde R. Wnt Signaling in Ovarian Cancer Stemness, EMT, and Therapy Resistance[J]. *J Clin Med* (2019) . 8(10). doi: 10.3390/jcm8101658
45. Li M, Zhao X, Liu Y, An J, Xiao H, Wang C, et al. Aberrant Expression of CDK8 Regulates the Malignant Phenotype and Associated With Poor Prognosis in Human Laryngeal Squamous Cell Carcinoma. *Eur Arch Otorhinolaryngol* (2017) 274(5):2205–13. doi: 10.1007/s00405-017-4484-0

Conflict of Interest: The authors declare that the research was conducted in the absence of any commercial or financial relationships that could be construed as a potential conflict of interest.

frontiers | Frontiers in Oncology

ORIGINAL RESEARCH
published: 04 July 2022
doi: 10.3389/fonc.2022.876193

Pattern of Recurrence After Platinum-Containing Definitive Therapy and Efficacy of Salvage Treatment for Recurrence in Patients with Squamous Cell Carcinoma of the Head and Neck

Tetsuro Wakasugi, Thi Nga Nguyen, Shoko Takeuchi, Jun-ichi Ohkubo and Hideaki Suzuki*

Department of Otorhinolaryngology—Head and Neck Surgery, University of Occupational and Environmental Health Japan, Fukuoka, Japan

OPEN ACCESS

Edited by:
Jun Itami, Shinmatsudo Central General Hospital, Japan

Reviewed by:
Jeltje Schulten, Merck, Germany
Steven Powell, Sanford Research, United States

***Correspondence:**
Tetsuro Wakasugi
wakasugi@med.uoeh-u.ac.jp

Specialty section:
This article was submitted to Head and Neck Cancer, a section of the journal Frontiers in Oncology

Received: *15 February 2022*
Accepted: *02 June 2022*
Published: *04 July 2022*

Citation:
Wakasugi T, Nguyen TN, Takeuchi S, Ohkubo J-i and Suzuki H (2022) Pattern of Recurrence After Platinum-Containing Definitive Therapy and Efficacy of Salvage Treatment for Recurrence in Patients with Squamous Cell Carcinoma of the Head and Neck. Front. Oncol. 12:876193. doi: 10.3389/fonc.2022.876193

Background: In first-line systemic therapy for unresectable recurrent and/or metastatic squamous cell carcinoma of the head and neck (R/M SCCHN), regimens are generally selected by time-to-relapse with 6 months cutoff after platinum (Pt)-containing definitive therapy, Pt-refractory or Pt-sensitive recurrence, but clinical characteristics between Pt-refractory and Pt-sensitive recurrence of R/M SCCHN has not been fully investigated. This study aimed to evaluate pattern of recurrence and efficacy for salvage treatment for recurrence after Pt-containing definitive therapy for R/M SCCHN in a real-world setting.

Methods: We retrospectively reviewed 150 patients treated with Pt-containing definitive therapy and analyzed the pattern of recurrence and efficacy of salvage therapy for 63 patients with R/M SCCHN.

Results: Pt-refractory recurrence, Pt-sensitive recurrence, second primary cancer (SPC), and no relapse occurred in 23.3%, 18.7%, 14.7%, and 43.3% of patients, respectively. In the cases with distant metastatic recurrence, symptomatic recurrence was significantly more common in the Pt-refractory recurrence, while asymptomatic recurrence was significantly more common in the Pt-sensitive recurrence. The timing of detection of SPC was after 2 years in 59.0% of cases after the completion of definitive therapy and 63.6% of SPC were asymptomatic. There was a significant difference in ΔNLR2 (NLR after definitive therapy minus NLR at detection recurrence; $p = 0.028$) and in prognosis after the detection of recurrence for the overall population ($p = 0.021$), and for salvage treatment group ($p = 0.023$), and systemic therapy group ($p = 0.003$) between Pt-refractory and Pt-sensitive groups.

Conclusions and Significance: Our analysis revealed the recurrence pattern after Pt-containing definitive therapy and showed the validity of dividing patients into Pt-refractory and Pt-sensitive recurrence with different prognosis in salvage therapy, especially systemic therapy.

Keywords: platinum-refractory recurrence, platinum-sensitive recurrence, platinum chemotherapy, recurrent or metastatic head and neck squamous cell cancer, NLR

INTRODUCTION

Patients with local advanced squamous cell carcinoma of the head and neck (L/A SCCHN) are treated with definitive therapy by surgery or radiotherapy (RT). Additionally, platinum (Pt) agents are key drugs in systemic therapy and are used in induction chemotherapy (ICT), chemoradiotherapy (CRT), or postoperative CRT (POCRT). However, even with these multimodality treatments, more than 50% of patients receiving definitive treatment develop locoregional and/or distant relapse within the first 2 years of initial treatment, and have a poor prognosis (1).

The treatment strategy for recurrent or metastatic (R/M) SCCHN is dictated by the availability of locoregional treatment or sensitivity to Pt agents defined by the time-to-relapse in case of unresectable disease. Currently, two programed cell death-1 (PD-1) inhibitors, pembrolizumab (Pembro) and nivolumab (NIVO), were used as first-line systemic therapy worldwide for patients who are not amenable to local treatment. Pembro is used as a first-line chemotherapy for the Pt-sensitive recurrence or untreated patients without feasibility of local treatment (2), while nivolumab is one of the most widely used regimens in the Pt-refractory patients with unresectable R/M SCCHN (3). In other words, the choice of Pembro and NIVO is determined only by the time-to-relapse, platinum-refractory, or platinum-sensitive recurrence, not based on the biological characteristics of recurrent cancer. Furthermore, to the best of our knowledge, the frequency of Pt-refractory and Pt-sensitive recurrence has not been reported, and also the pattern of recurrence and clinical course limited to only after Pt-containing definitive therapy has not been sufficiently examined.

Here, we retrospectively evaluated the pattern of recurrence after Pt-containing definitive therapy and investigated the efficacy of salvage treatment for recurrence in patients with R/M SCCHN.

MATERIALS AND METHODS

Study Population

We retrospectively reviewed the medical records of patients treated with definitive therapy between January 2010 and December 2019 at the University of Occupational and Environmental Health, Japan. In the present study, the inclusion criteria were as follows: (a) primary tumor site located in the head and neck; (b) histologically proven SCC; (c) stage III or IV according to the American Joint Committee on Cancer Staging System (Seventh edition); (d) treated with Pt-containing definitive therapy by CRT or surgery followed by POCRT; (e) diagnosis of R/M SCCHN. The exclusion criteria were as follows: (a) primary tumor site located in nasopharynx; (b) p16 positive oropharyngeal cancer.

Definitive Therapy and Follow-Up Visit

Pt-containing definitive therapy was performed by surgery followed by POCRT or CRT. In cases, in which ICT with TPF (docetaxel/cisplatin/5-FU) was performed, Pt-containing definitive therapy was subsequently performed. The Pt agent in combination with RT was used daily carboplatin 25 mg/m^2 until August 2015, and weekly cisplatin 40 mg/m^2 or triweekly cisplatin 80–100 mg/m^2 after September 2015. A Pt agent was administered to patients with normal renal function above Cockcroft-Gault 60. The definitive radiotherapy dose was 70–72 Gy and the adjuvant radiotherapy dose was 60–66 Gy. Nutritional support was provided using prophylactic percutaneous endoscopic gastrostomy (PEG) before definitive radiotherapy. In cases without prophylactic PEG, nasogastric tube was used when patients had inadequate oral intake. All patients were supported with nutritional supplements. After the Pt-containing definitive therapy, patients were followed with a medical examination every 1–2 months and imaging examination by computed tomography (CT) including the neck and chest every 3–4 months for the first 2 years and followed with imaging examination by CT every 6 months from the third to the fifth years.

Patient Characteristics

We collected the patients' characteristics at definitive therapy and the detection of recurrence including age, sex, Eastern cooperative Oncology Group (ECOG) performance status (PS), primary tumor site, T and N status, disease stage, definitive therapy for primary tumor, radiotherapy, platinum agent used in definitive therapy, induction chemotherapy, nutrition support, body weight (BW), and neutrophil-to-lymphocyte ratio (NLR), symptoms at the time of detection of recurrence, detection modalities, and extent of recurrent disease.

BW and NLR

BW measurement and peripheral blood test were performed before definitive therapy, after definitive treatment, and at the time of detection of recurrence. NLR was calculated as the total neutrophil count divided by the total lymphocyte count. BW and NLR were defined as pre-BW and pre-NLR before definitive therapy, post-BW and post-NLR after definitive therapy, and

rec-BW and rec-NLR at the detection recurrence, respectively. ΔBW1 and 2 were defined as pre-BW minus post-BW and post-BW minus rec-BW, respectively. ΔBW1% and 2% were calculated as a percentage of pre-BW and post-BW, respectively. ΔNLR1 and 2 were defined as pre-NLR minus post-NLR and post-NLR minus rec-NLR, respectively.

Salvage Treatment

In the salvage treatment, surgery was the first choice if resectable. In the case of unresectable disease, RT was selected if the field was not previously irradiated, and systemic therapy was performed if local treatment was difficult. Systemic therapy includes conventional cytotoxic chemotherapy, molecular targeted agents (cetuximab), and immune checkpoint inhibitors (ICIs) such as nivolumab or pembrolizumab. Nivolumab and pembrolizumab have been used in patients since March 2017 and December 2019, respectively. Best supportive care (BSC) alone was performed when it was difficult to treat with these salvage therapies. Their median follow-up period was 470 days (range 19–3,516 days).

Statistical Analysis

No statistical sample size calculations were conducted. Fischer's exact test, the χ^2-test, independent two-sample *t*-tests, or one-way analysis of variance were used to evaluate differences between two or three independent groups. The overall survival (OS) rate was estimated and plotted using the Kaplan–Meier method and compared using the stratified log-rank test. The data were censored on December 31, 2021. OS was calculated from the date of the start of salvage therapy to the date of death or the last confirmed date of survival. Risk factors of recurrence and of survival for salvage therapy were evaluated by estimating hazard ratios (HRs) and 95% confidence interval (CI) using univariate and multivariate COX proportional hazards models. SPSS version 27 software (SPSS Inc., Chicago, IL, USA) was used for all statistical analyses. Statistical significance was defined as a p value <0.05.

RESULTS

Of the 150 patients with L/A-SCCHN treated with Pt-containing definitive therapy, 65 patients (43.3%) who were free of recurrence, and 22 patients (14.7%) with a second primary cancer (SPC), and 63 patients (37.2%) with locoregional and/or distant metastasis as shown in **Figure 1**. Histogram of the time of detection of recurrence from the completion of the Pt-containing definitive therapy was shown in **Figure 2**. Median time of detection of R/M SCCHN and SPC were 166 days (95% confidence interval [CI]: 117–215) and 894 days (95% CI: 330–1,457), respectively. Thirty-five patients (23.3%) of 150 patients who treated with Pt-containing definitive therapy had relapse within 6 months after Pt-containing definitive therapy (Pt-refractory recurrence) and 28 patients (18.7%) of 150 patients who treated with Pt-containing definitive therapy had relapse more than 6 months after Pt-containing definitive therapy (Pt-sensitive recurrence). Fifty-one patients (81.0%) and 61 patients (96.8%) had a relapse within first 1 year and 2 years, respectively. Thirteen (59.0%) of the 22 patients with SPC occurred after the second year. Primary lesion of the SPCs included esophagus in 9, lung in 6, stomach in 2, prostate in 2, and others in 3 patients. **Table 1** presents the patient characteristics at Pt-containing definitive therapy. There was no significant difference between no relapse, R/M SCCHN, and SPC groups except primary tumor site. In the no relapse group, primary tumor sites were less hypopharynx and more larynx compared to R/M SCCHN and SPC. In contrast, in the R/M SCCHN group, primary tumor sites were less oropharynx.

Patients' characteristics at the detection of R/M SCCHN and SPC (**Table 2**), and BW and NLR (**Table 3** and **Supplementary Data 1**) were analyzed to evaluate potential clinical indicators of recurrence. As shown in **Table 2**, there was no significant difference with respect to PS, examination used for the detection of recurrence, extent of recurrent disease, and symptoms between R/M SCCHN and SPC groups. Recurrence

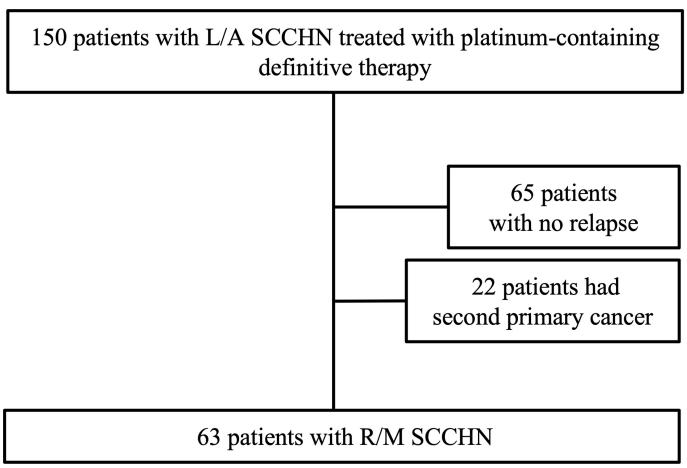

FIGURE 1 | Diagram showing the process of patient selection. L/A SCCHN, local advanced squamous cell carcinoma of head and neck; R/M, recurrent and/or metastatic.

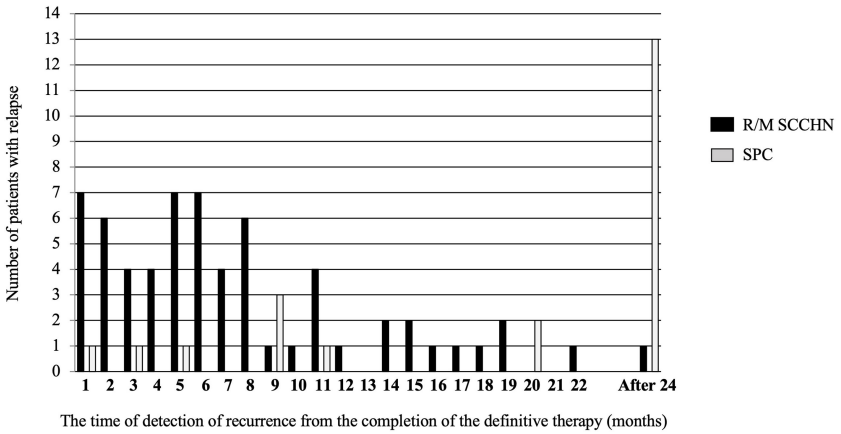

FIGURE 2 | Histogram for the time of the detection of recurrence after definitive therapy.

TABLE 1 | Characteristics at platinum-containing definitive therapy.

	No relapse (n=65), n (%)	R/M SCCHN (n=63), n (%)	SPC (n=22), n (%)	P-value
Median age, years (range)	65 (29–81)	63 (48-78)	63 (47-75)	0.863
Sex				0.467
Male	50 (76.9)	53 (84.1)	19 (86.4)	
Female	15 (23.1)	10 (15.9)	3 (13.6)	
Primary tumor site				0.035*
Oral cavity	10 (15.4)	15 (23.8)	1 (4.5)	
Oropharynx	22 (33.8)	10 (15.9)	7 (31.8)	
Hypopharynx	15 (23.1)	26 (41.3)	11 (50.0)	
Larynx	11 (16.9)	4 (6.3)	1 (4.5)	
Nasal cavity and paranasal sinus	7 (10.8)	8 (12.7)	2 (9.1)	
T status:				0.072
T1	0	4 (6.3)	2 (9.1)	
T2	21 (32.3)	10 (15.9)	8 (36.4)	
T3	18 (27.7)	17 (27.0)	6 (27.3)	
T4	26 (40.0)	32 (50.8)	6 (27.3)	
N status:				0.744
N0	15 (23.1)	15 (23.8)	4 (18.2)	
N1	9 (13.8)	7 (11.1)	6 (27.3)	
N2	38 (58.5)	37 (58.7)	11 (50.0)	
N3	3 (4.6)	4 (6.3)	1 (4.5)	
Disease stage:				0.175
III	17 (26.2)	11 (17.5)	8 (36.4)	
IV	48 (73.8)	52 (82.5)	14 (63.6)	
Definitive therapy for primary tumor:				0.556
Surgery followed by POCRT	22 (33.8)	27 (42.9)	5 (22.7)	
CRT	43 (66.2)	36 (57.1)	17 (77.3)	
Platinum agent used in definitive therapy:				0.764
Cisplatin	32 (49.2)	33 (52.4)	10 (45.5)	
Carboplatin	33 (50.8)	30 (47.6)	12 (54.5)	
Induction chemotherapy:				0.985
Yes	22 (33.8)	21 (33.3)	7 (31.8)	
No	43 (66.2)	42 (66.7)	15 (68.2)	
Prophylactic PEG:				0.898
Yes	12 (19.0)	13 (20.6)	5 (22.7)	
No	53 (81.5)	50 (79.4)	17 (81.8)	

CRT, chemoradiotherapy; POCRT, postoperative chemoradiotherapy; R/M SCCHN, recurrent or metastatic squamous cell carcinoma of head and neck; SPC, second primary cancer; PEG, percutaneous endoscopic gastrostomy.

**, significant difference.*

TABLE 2 | Characteristics of R/M SCCHN and SPC at the detection of recurrence.

	R/M SCCHN (n=63), n (%)	SPC (n=22), n (%)	P-value
PS:			0.376
PS 0	34 (54.0)	8 (36.4)	
PS 1	21 (33.3)	10 (45.5)	
PS 2	7 (11.1)	2 (9.1)	
PS 3	1 (1.6)	2 (9.1)	
Time-to-relapse:			0.001*
Before 6 months	35 (55.6)	3 (13.6)	
After 6 months	28 (44.4)	19 (86.4)	
Examination used for detection of recurrence:			0.254
Imaging examination	48 (76.2)	14 (63.6)	
Medical examination	15 (23.8)	8 (36.4)	
Extent of recurrent disease:			
Locoregional only	29 (46.0)	–	
Distant metastasis	34 (54.0)	–	
Symptoms:			0.052
Asymptomatic	25 (39.7)	14 (63.6)	
Symptomatic	38 (60.3)	8 (36.4)	
Pain	20	1	
Dysphagia	2	1	
Anorexia	5	0	
Cough	3	0	
Dyspnea	2	2	
Others	6	4	

*R/M SCCHN, recurrent and/or metastatic squamous cell carcinoma; SPC, second primary cancer; PS, performance status; *, significant difference.*

was most frequently detected by imaging examination, although 23.8% and 36.4% of recurrences in R/M SCCHN and SPC groups were detected by medical examination, respectively. Asymptomatic recurrence was observed in 39.7% of patients in R/M SCCHN group and 63.6% of those in SPC group. In the cases with distant metastatic recurrence, symptomatic recurrence was significantly more common in the Pt-refractory recurrence, while asymptomatic recurrence was significantly more common in the Pt-sensitive recurrence in **Table 4**. Among patients with symptomatic recurrence, pain was the most common symptom in both cohorts. Time-to-relapse had significant difference between R/M SCCHN and SPC groups, and 86.4% of SPC occurring after 6 months. As shown in **Supplementary Data 1**, there was no significant difference between no relapse, R/M SCCHN, and SPC groups in pre-BW, post-BW, ΔBW1, ΔBW1 (%), pre-NLR, post-NLR, and ΔNLR1. R/M SCCHN group was divided into the Pt-refractory and Pt-sensitive and analyzed adding BW and NLR at the detection of recurrence in **Table 4**. There was a significant difference in ΔNLR2 ($p = 0.028$) between the Pt-refractory and Pt-sensitive cohorts. BW decreased and NLR increased after the completion of definitive treatment. The results indicate the following: at the detection of recurrence, BW tended to decrease slightly in both groups, while NLR decreased in the Pt-sensitive recurrence and remained unchanged in the Pt-refractory recurrence. Clinical indicators of recurrence were analyzed using univariate analysis, but no significant factors were found in **Supplementary Data 2**.

The univariate and multivariate analyses of OS after the detection of recurrence were presented in **Table 5**. In univariate analysis, time-to-relapse (hazard rate [HR] 0.444, 95% CI: 0.219–0.900, $p = 0.024$), extent of recurrent disease (HR 2.228, 95% CI: 1.094–4.457, $p = 0.027$), salvage treatment (HR 0.238, 95% CI: 0.107–0.531, <0.0001), and salvage surgery (HR 0.430, 95% CI: 0.185–0.995, $p = 0.049$) were associated with a low risk of death. In multivariate analysis, time-to-relapse (HR 0.382, 95% CI: 0.184–0.795, $p = 0.010$) and salvage treatment (HR 0.298, 95% CI: 0.130–0.684, $p = 0.004$) were associated with a low risk of death.

Figure 3 shows OS of salvage treatment after the detection of recurrence. In the salvage treatment for recurrence, the longest median OS was 31.0 months (95% CI: 1.7–60.3) for surgery, followed by 21.6 months (95% CI: 3.6–40.0) for systemic therapy, 9.9 months (95% CI: 0–32.1) for RT, and 3.7 months (95%CI: 2.5–4.9) for BSC alone, as shown in **Figure 3A**. Salvage therapy and prognosis of patients were analyzed with stratification by the recurrence detection cutoff time of 6 months (**Figures 3A–C**). There were significant differences between before and after the cutoff time of 6 months for the overall population ($p = 0.021$), and for salvage treatment group ($p = 0.023$), and systemic therapy group ($p = 0.003$). There were no significant differences between

TABLE 3 | BW and NLR before definitive therapy, after definitive therapy, and at the detection of recurrence.

	Pt-refractory Average ± SD	Pt-sensitive Average ± SD	P-value
Pre-BW (kg)	57.8 ± 10.7	57.6 ± 11.9	0.937
Post-BW (kg)	52.3 ± 9.5	53.0 ± 9.3	0.811
Rec-BW (kg)	50.5 ± 10.2	52.6 ± 9.6	0.454
ΔBW1(kg)	5.4 ± 4.1	4.7 ± 4.3	0.456
ΔBW1(%)	9.2 ± 6.4	7.3 ± 7.2	0.262
ΔBW2 (kg)	1.5 ± 4.1	1.1 ± 5.3	0.778
ΔBW2(%)	2.9 ± 8.1	1.9 ± 8.8	0.681
Pre-NLR	4.2 ± 4.2	4.4 ± 4.5	0.878
Post-NLR	9.4 ± 6.1	9.8 ± 7.8	0.867
Rec-NLR	10.1 ± 12.3	6.1 ± 5.0	0.122
ΔNLR1	-5.3 ± 6.9	-5.4 ± 8.2	0.956
ΔNLR2	-1.9 ± .14.1	5.0 ± 7.7	0.028*

*SD, standard deviation; BW, body weight; NLR, Neutrophil to lymphocyte ratio; pre-BW, BW before definitive therapy; post-BW, BW after definitive therapy; rec-BW, BW at the detection of recurrence; ΔBW1, pre-BW minus post-BW; delta-BW2, post-BW minus rec-BW; pre-NLR, NLR before definitive therapy; post-NLR, NLR after definitive therapy; rec-NLR, NLR at the detection of recurrence; ΔNLR1, pre-NLR minus post-NLR; ΔNLR2, post-NLR minus rec-NLR; *Significant difference.*

TABLE 4 | Characteristics of the platinum-refractory and -sensitive recurrence at the detection of recurrence.

	Pt-refractory (n=35), n (%)	Pt-sensitive (n=28), n (%)	P-value
Locoregional only			0.717
Asymptomatic	7	4	
Symptomatic	10	8	
Distant metastasis			0.004*
Asymptomatic	3	11	
Symptomatic	15	5	

*Pt, platinum; *, significant difference.*

the Pt-refractory and Pt-sensitive recurrence for salvage surgery, RT, and BSC alone in **Supplementary Data 3**.

In the Pt-refractory recurrence, first-line systemic therapy was performed by NIVO in 4 (44.4%) of 9 cases, but second-line systemic therapy was performed in 1 case only (**Supplementary Data 4**). In the Pt-sensitive recurrence, all systemic therapies administered were from 2017 onwards. Of 9 cases, ICI therapy was performed 3 (33.3%) as first-line systemic therapy, 2 (22.2%) as second-line systemic therapy, and 1 (11.1%) as third-line systemic therapy. Second-line systemic therapy was performed in 5 (55.6%) of 9 cases, and third-line systemic therapy was performed in 2 (22.2%) in 9 cases (**Supplementary Data 4**).

DISCUSSION

This is the first report on pattern of recurrence and efficacy of salvage treatment for recurrence after Pt-containing definitive therapy by CRT or surgery followed by POCRT for L/A SCCHN. Currently, ICI in first-line systemic therapy for uncurable R/M SCCHN is selected by the time-to-relapse from the completion of Pt-containing therapy. Namely, NIVO is selected for Pt-refractory disease, and Pembro is selected for Pt-sensitive disease in R/M SCCHN (2, 3). In Hodgkin's lymphoma (4–6), small-cell lung carcinoma (7, 8), and ovarian cancer (9–11), it is known that the treatment free survival (TFI) correlates with the response rate to chemotherapy for recurrent disease. The treatment strategies in these malignancies are determined dividing into the refractory or sensitive recurrence stratified the TFI, that is the period between the end of the previous chemotherapy and the start of salvage chemotherapy for relapse, and it differs from the definition of R/M SCCHN. Moreover, the treatment sensitivity and prognosis that are stratified by the time-to-relapse for R/M SCCHN have not been fully investigated. However, recent clinical trials of the ICI therapy have used a time-to-relapse cutoff of 6 months for patient selection (2, 3, 12, 13). Furthermore, the prior treatment of these trials included Pt-containing definitive therapy or no treatment, in addition to chemotherapy treated for uncurable recurrences, and may have included a mix of populations with different biologic characteristics of the target patients. To settle this issue, this study was limited to patients who had relapse after Pt-containing definitive CRT or surgery followed by POCRT.

In this study, 63 patients (42.0%) had locoregional recurrence and/or distant metastasis, and the median time of recurrence was 166 days (95% CI: 117–215). The long-term follow-up data showed that locoregional recurrences developed in 16–25% (14) of patients treated with POCRT for high-risk SCCHN and in 17–52% (15) of patients treated with definitive CRT for unresectable SCCHN. However, these reports did not show the

TABLE 5 | Univariate and multivariate analysis for OS after the detection of recurrence.

Variate	Univariate analysis			Multivariate analysis		
	HR	95% CI	p-value	HR	95% CI	p-value
Time-to-relapse						
Before 6 months	1	0.219-0.900	0.024*	1	0.184-0.795	0.010*
After 6 months	0.444			0.382		
Extent of recurrent disease						
Locoregional only	1	1.094-4.457	0.027*	1	0.641-4.048	0.310
Distant metastasis	2.228			1.611		
PS						
PS 1or 2	1	0.668-3.942	0.285	–	–	–
PS 3 or 4	1.623			–		
Salvage treatment						
No	1	0.107-0.531	<0.0001*	1	0.130-0.684	0.004*
Yes	0.238			0.298		
Salvage surgery						
No	1	0.185-0.995	0.049*	1	0.187-1.894	0.379
Yes	0.430			0.595		
Salvage radiotherapy						
No	1	0.521-2.246	0.833	–	–	–
Yes	1.082			–		
Systemic therapy						
No	1	0.383-1.749	0.605	–	–	–
Yes	0.818			–		

*OS, overall survival; PS, performance status; HR, hazard ratio; CI, confidence interval: *, significant difference.*

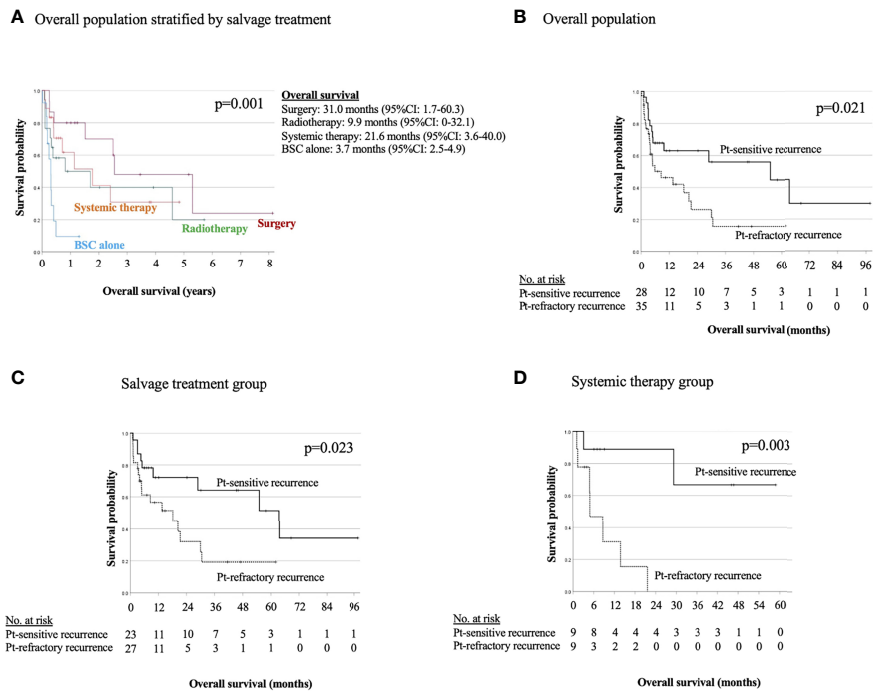

FIGURE 3 | Kaplan–Meier estimates of overall survival in overall population stratified by salvage treatment **(A)** and in overall population **(B)**, salvage treatment group **(C)**, and systemic therapy group **(D)** stratified between the platinum-refractory and platinum-sensitive recurrence.

frequency of Pt-refractory or Pt-sensitive recurrence after definitive therapy. The frequency of recurrence of the present study was similar to those reported in previous reports. One of the new findings of this study was Pt-refractory recurrence occurred in 23.3% of cases and Pt-sensitive recurrence occurred in 18.7% of cases after the completion of Pt-containing definitive therapy. The rate of R/M within 1 year after definitive therapy for L/A SCCHN has been reported to be 44% (16); however, 51patients (81.0%) had a relapse within the first year after Pt-containing definitive therapy in this study. This might suggest that recurrence may occur more quickly after Pt-containing definitive therapy, and it may be advisable to follow-up more carefully after treatment. The National Comprehensive Cancer Network guidelines recommend follow-up HN examinations every 1–3 months for the first year after definitive treatment, but the frequency of Pt-refractory or Pt-sensitive recurrence is not described (17). Therefore, this information might be very important for follow-up. Moreover, the occurrence of second primary cancer was 14.7% and 63.6% of them occurred after 2 years from the completion of definitive treatment in this study, which is a factor that requires attention in the follow-up after definitive therapy of L/A SCCHN. Patients with SCCHN have a high risk of developing other cancers simultaneously or subsequently, and the incidence of multiprimary tumors in this population is reported as 27% (18).

This study showed an important finding of the frequency of asymptomatic recurrence according to pattern of recurrence. Asymptomatic recurrence occurred in 37.9% of locoregional recurrence only, 41.2% of distant metastasis, and 63.6% of SPC. Furthermore, asymptomatic distant metastasis after 6 months after definitive therapy occurred significantly more frequently and might require attention. Moreover, it is important to note that 63.6% of SPCs were asymptomatic recurrences and were found after 2 years in 59.0% of cases from the completion of definitive therapy. These suggest the effectiveness of planned imaging examination for follow-up after 6 months from the completion of definitive therapy to detect asymptomatic recurrence; however, the optimal frequency and modality of routine post-treatment imaging in asymptomatic patients is controversial (17). In this study, post-treatment imaging was performed every 3–4 months for the first 2 years, and salvage therapy was promptly performed after recurrence was detected. This timing of imaging examination might be appropriate for detecting recurrence within first year. In addition, more than half of the patients presented with some symptoms, most commonly pain. It is important to note that 71.4% of the cases with Pt-refractory recurrence were symptomatic and that symptomatic distant metastases occurred significantly frequently. Therefore, for patients presenting with symptoms at a clinical visit, the addition of an imaging examination might help in the early detection of recurrence, especially within 6 months after Pt-containing definitive therapy. On the other hand, for asymptomatic patients, planned imaging examination might be especially useful in detecting Pt-sensitive recurrence with distant metastasis and second primary cancer.

In the present study, ΔNLR2 was significantly different between the two cohorts and might be a useful indicator in

detecting Pt-refractory recurrence. ΔNLR2 is post-NLR minus rec-NLR and was significantly lower in the Pt-refractory cohort. To the best of our knowledge, no study has examined the use of ΔNLR as a marker of recurrence of SCCHN. In the present study, there was no significant difference in rec-NLR between the two cohorts, but there was a higher NLR in the Pt-refractory cohort compared to the Pt-sensitive cohort. Elevated NLR has been reported to be associated with poor prognosis independent of tumor or disease stage in various cancer types, including HNC (19, 20). NLR is an attractive biomarker for systemic inflammatory responses due to its ease of measurement, low cost, and wide clinical use. This finding might suggest that the Pt-refractory cohort would have a worse prognosis compared to the Pt-sensitive cohort. That is, it might be appropriate to perform frequent measurements of the dynamic change in NLR after Pt-containing definitive therapy, and to perform imaging examination if post-NLR does not decrease. Further studies on the prediction of clinical outcome are needed.

ΔBW1 (BW1%) was reduced by 4.8 kg (7.5%) in the no relapse group, and 5.1 kg (8.4%) in R/M SCCHN group, and 4.7 kg (8.3%) in SPC group, but the difference was not significant. In addition, ΔBW2 (BW2%) was further decreased by 1.4 kg (2.5%) in the Pt-sensitive recurrence and 1.6 kg (3.1%) in the Pt-refractory recurrence, but the difference was not significant. In both cohorts that had relapse, it might be important to note that BW was consistently decreasing throughout the treatment and follow-up periods. It has been reported that weight loss during treatment is associated with poor prognosis (21, 22). Persistent weight loss might be a finding suggestive of recurrence. Further studies on the prediction of recurrence by body weight loss are needed.

In R/M SCCHN, there is a history of clinical trial for systemic chemotherapy in which patients were divided into the Pt-refractory and sensitive groups (2, 3, 12, 13) with an empirical "6 months" cutoff in R/M SCCHN, but the differences in their clinical characteristics and the validity of a cutoff of 6 months have not been fully investigated. In addition, drug sensitivity to platinum agents has long been studied molecularly, with intrinsic resistance and acquired resistance, but biomarkers of platinum resistance in clinical practice are unknown (23, 24). In the present study, a new finding is that multivariate analysis of OS after the detection of recurrence shows time-to-relapse with 6 months cutoff and salvage treatment were associated with a low risk of death, and the median OS in overall population and systemic therapy group between the Pt-refractory and Pt-sensitive recurrence were significantly different. In the salvage treatment group, the Pt-refractory recurrence had a significant poor prognosis compared to the Pt-sensitive recurrence ($p = 0.023$). This indicates that Pt-refractory patients have a poor prognosis even with salvage treatment. Furthermore, there was no significant difference in OS by salvage treatment between the Pt-refractory and Pt-sensitive recurrence, except systemic therapy. We believe that this result support the validity of dividing clinical trials in systemic therapy by time-to-relapse with 6 months cutoff. In systemic therapy of the Pt-sensitive recurrence, ICI was used in 66.7% of the cases, and the median OS was not reached because of the presence of long-term survivors by sequential treatment. All of these patients were selected for systemic therapy in April 2017, when ICIs first became covered by insurance in Japan, and no patients had received systemic therapy prior to that date. This suggests the usefulness of systemic therapy as an option when local treatment is not feasible now that ICI is available. However, Pt-refractory recurrence had a poor prognosis despite the use of NIVO in 44.4% of cases, indicating that patients with Pt-refractory relapse are a treatment-resistant population. Although there were no significant differences, the prognosis for the Pt-sensitive recurrence was good for surgery and radiotherapy compared to the Pt-refractory. The better response to salvage therapy might indicate a better prognosis for Pt-sensitive recurrence compared to the Pt-refractory recurrence. The result suggests that the two populations divided by time-to-relapse differ in their sensitivity to systemic therapy, requiring further exploratory studies.

BSC alone had a worse prognosis compared to salvage treatment, and there was no significant difference between the Pt-refractory and Pt-sensitive recurrence. Indeed, these survival times for BSC alone were roughly equivalent to the 3.82 months reported for natural history of untreated head and neck cancer (25). Multivariate analysis of OS after the detection of recurrence shows salvage treatment was associated with a low risk of death, and it is important for survival in R/M SCCHN that we select the salvage treatment. Surgery is the best salvage treatment in terms of cure and long survival. In addition, if local treatment is not an option, it might be better to treat systemic therapy in terms of long survival in cases with the Pt-sensitive resistance.

Several limitations of this study warrant mention. First, the study was conducted using a retrospective design at a single institution and with a small sample size ($n = 150$). However, to the best of our knowledge, this study is the first to investigate R/M SCCHN divided into Pt-refractory and Pt-sensitive recurrence after Pt-containing definitive therapy. The present results should therefore be considered to provide valuable information for selecting the treatment of R/M SCCHN patients. Second, salvage treatment modalities differ according to historical background, and the short duration of ICI resulted in a different prognosis between the two cohorts. Third, only SCCHN patients with recurrence were included with respect to their course after the completion of Pt-containing definitive therapy in this study. Therefore, although the usefulness of BW and NLR as markers of recurrence of SCCHN is unclear, it is useful to clarify the difference between the Pt-sensitive and Pt-refractory recurrence. Fourth, NLR and BW at 6 months after definitive treatment in the Pt-sensitive cohort were not measured, and differences in ΔNLR between the Pt-refractory and Pt-sensitive cohorts at 6 months after definitive therapy were unknown. However, we believe that the characteristics of Pt-refractory recurrence, in which the NLR that increased with definitive therapy did not decrease, might be clinically useful for the monitoring of recurrence. Dynamic changes in NLR during follow-up require further investigation. Fifth, we used time-to-relapse by the empirical "6 months" cutoff. In systemic therapy, regimens are commonly selected according to the Pt-refractory or Pt-sensitive recurrence as defined by time-to-relapse regimens.

Although the biological characteristics of Pt-refractory and Pt-sensitive recurrence have not been clarified, the prognostic difference between the two groups has been revealed, and we consider that this is one of the useful results of this study. However, further investigation of biomarkers of Pt-refractory and Pt-sensitive recurrence is warranted.

CONCLUSION

Our analysis revealed the pattern of recurrence after Pt-containing definitive therapy for L/A SCCHN and the frequency of Pt-refractory and Pt-sensitive recurrence. The clinical differences between Pt-refractory and Pt-sensitive recurrence were that ΔNLR2 was lower in the patients with Pt-refractory recurrence, while prognosis was better in those with Pt-sensitive recurrence in salvage treatment and systemic therapy groups. After Pt-containing definitive therapy, it is especially useful in systemic therapy to detect the recurrence by dividing into the Pt-refractory and Pt-sensitive recurrence, which have different prognosis.

DATA AVAILABILITY STATEMENT

The raw data supporting the conclusions of this article will be made available by the authors, without undue reservation.

ETHICS STATEMENT

Ethical review and approval was not required for the study on human participants in accordance with the local legislation and institutional requirements. The patients/participants provided their written informed consent to participate in this study.

AUTHOR CONTRIBUTIONS

TW designed the study and wrote the initial draft of the manuscript. HS contributed to analysis and interpretation of data and assisted in the preparation of the manuscript. All other authors have contributed to data collection and interpretation, and critically reviewed the manuscript. All authors approved the final version of the manuscript, and agree to be accountable for all aspects of the work in ensuring that questions related to the accuracy or integrity of any part of the work are appropriately investigated and resolved.

SUPPLEMENTARY MATERIAL

The Supplementary Material for this article can be found online at: https://www.frontiersin.org/articles/10.3389/fonc.2022.876193/full#supplementary-material

REFERENCES

1. Argiris A, Karamouzis MV, Raben D, Ferris RL. Head and Neck Cancer. *Lancet* (2008) 371(9625):1695–709. doi: 10.1016/S0140-6736(08)60728-X
2. Burtness B, Harrington KJ, Greil R, Soulières D, Tahara M, de Castro GJr, et al. Pembrolizumab Alone or With Chemotherapy Versus Cetuximab With Chemotherapy for Recurrent or Metastatic Squamous Cell Carcinoma of the Head and Neck (KEYNOTE-048): A Randomised, Open-Label, Phase 3 Study. *Lancet* (2019) 394(10212):1915–28. doi: 10.1016/S0140-6736(19)32591-7
3. Ferris RL, Blumenschein GJr, Fayette J, Guigay J, Colevas AD, Licitra L, et al. Nivolumab for Recurrent Squamous-Cell Carcinoma of the Head and Neck. *N Eng J Med* (2016) 375(19):1856–67. doi: 10.1056/NEJMoa1602252
4. Aparicio J, Segura A, Garcerá S, Oltra A, Santaballa A, Yuste A, et al. ESHAP Is an Active Regimen for Relapsing Hodgkin's Disease. *Ann Oncol* (1999) 10(5):593–5. doi: 10.1023/a:1026454831340
5. Linch DC, Winfield D, Goldstone AH, Moir D, Hancock B, McMillan A, et al. Dose Intensification With Autologous Bone-Marrow Transplantation in Relapsed and Resistant Hodgkin's Disease: Results of a BNLI Randomised Trial. *Lancet* (1993) 341(8852):1051–4. doi: 10.1016/0140-6736(93)92411-l
6. Yuen AR, Rosenberg SA, Hoppe RT, Halpern JD, Horning SJ. Comparison Between Conventional Salvage Therapy and High-Dose Therapy With Autografting for Recurrent or Refractory Hodgkin's Disease. *Blood* (1997) 89(3):814–22. doi: 10.1182/blood.V89.3.814
7. Batist G, Carney DN, Cowan KH, Veach SR, Gilliom M, Bunn PA, et al. Etoposide (VP-16) and Cisplatin in Previously Treated Small-Cell Lung Cancer: Clinical Trial and *In Vitro* Correlates. *J Clin Oncol* (1986) 4(6):982–6. doi: 10.1200/JCO.1986.4.6.982
8. Johnson DH, Greco FA, Strupp J, Hande KR, Hainsworth JD. Prolonged Administration of Oral Etoposide in Patients With Relapsed or Refractory Small-Cell Lung Cancer: A Phase II Trial. *J Clin Oncol* (1990) 8(10):1613–7. doi: 10.1200/JCO.1990.8.10.1613
9. Markman M, Rothman R, Hakes T, Reichman B, Hoskins W, Rubin S, et al. Second-Line Platinum Therapy in Patients With Ovarian Cancer Previously Treated With Cisplatin. *J Clin Oncol* (1991) 9(3):389–93. doi: 10.1200/JCO.1991.9.3.389
10. Harries M, Gore M. Part II: Chemotherapy for Epithelial Ovarian Cancer-Treatment of Recurrent Disease. *Lancet Oncol* (2002) 3(9):537–45. doi: 10.1016/s1470-2045(02)00847-1
11. Pignata S, Cecere S C, Du Bois A, Harter P, Heitz F. Treatment of Recurrent Ovarian Cancer. *Ann Oncol* (2017) 28(suppl_8):viii51–6. doi: 10.1093/annonc/mdx441
12. Zenda S, Onozawa Y, Boku N, Iida Y, Ebihara M, Onitsuka T. Single-Agent Docetaxel in Patients With Platinum-Refractory Metastatic or Recurrent Squamous Cell Carcinoma of the Head and Neck (SCCHN). *Jpn J Clin Oncol* (2007) 37(7):477–81. doi: 10.1093/jjco/hym059
13. Cohen EEW, Soulières D, Le Tourneau C, Dinis J, Licitra L, Ahn MJ, et al. Pembrolizumab Versus Methotrexate, Docetaxel, or Cetuximab for Recurrent or Metastatic Head-and-Neck Squamous Cell Carcinoma (KEYNOTE-040): A Randomised, Open-Label, Phase 3 Study. *Lancet* (2019) 393(10167):156–67. doi: 10.1016/S0140-6736(18)31999-8
14. Cooper JS, Zhang Q, Pajak TF, Forastiere AA, Jacobs J, Saxman SB, et al. Long-Term Follow-Up of the RTOG 9501/Intergroup Phase III Trial: Postoperative Concurrent Radiation Therapy and Chemotherapy in High-Risk Squamous Cell Carcinoma of the Head and Neck. *Int J Radiat Oncol Biol Phys* (2012) 84:1198–205. doi: 10.1016/j.ijrobp.2012.05.008
15. Brockstein B, Haraf DJ, Rademaker AW, Kies MS, Stenson KM, Rosen F, et al. Patterns of Failure, Prognostic Factors and Survival in Locoregionally Advanced Head and Neck Cancer Treated With Concomitant Chemoradiotherapy: A 9-Year, 337-Patient, Multi-Institutional Experience. *Ann Oncol* (2004) 15(8):1179–86. doi: 10.1093/annonc/mdh308
16. Boysen ME, Zätterström UK, Evensen JF. Self-Reported Symptoms to Monitor Recurrent Head and Neck Cancer - Analysis of 1,678 Cases. *Anticancer Res* (2016) 36(6):2849–54.
17. National Comprehensive Cancer Network. *NCCN Clinical Practice Guidelines in Oncology. Head and Neck Cancers. Version 1* (2022). Available at: https://www.nccn.org/professionals/physician_gls/pdf/head-and-neck.pdf (Accessed 2022 February 7).

18. Priante AV, EC C, Kowalski LP. Second Primary Tumors in Patients With Head and Neck Cancer. *Curr Oncol Rep* (2011) 13(2):132–7. doi: 10.1007/s11912-010-0147-7
19. McMillan DC. Systemic Inflammation, Nutritional Status and Survival in Patients With Cancer. *Curr Opin Clin Nutr Metab Care* (2009) 12(3):223–6. doi: 10.1097/MCO.0b013e32832a7902
20. Tham T, Bardash Y, Herman SW, Costantino PD. Neutrophil-To-Lymphocyte Ratio as a Prognostic Indicator in Head and Neck Cancer: A Systematic Review and Meta-Analysis. *Head Neck* (2018) 40(11):2546–57. doi: 10.1002/hed.25324
21. Langius JA, Bakker S, Rietveld DH, Kruizenga HM, Langendijk JA, Weijs PJ, et al. Critical Weight Loss is a Major Prognostic Indicator for Disease-Specific Survival in Patients With Head and Neck Cancer Receiving Radiotherapy. *Br J Cancer* (2013) 109(5):1093–9. doi: 10.1038/bjc.2013.458
22. Capuano G, Grosso A, Gentile PC, Battista M, Bianciardi F, Di Palma A, et al. Influence of Weight Loss on Outcomes in Patients With Head and Neck Cancer Undergoing Concomitant Chemoradiotherapy. *Head Neck* (2008) 30(4):503–8. doi: 10.1002/hed.20737
23. Galluzzi L, Senovilla L, Vitale I, Michels J, Martins I, Kepp O, et al. Molecular Mechanisms of Cisplatin Resistance. *Oncogene* (2012) 31(15):1869–83. doi: 10.1038/onc.2011.384
24. Wakasugi T, Izumi H, Uchiumi T, Suzuki T, Arao T, Nishio K, et al. ZNF143 Interacts With P73 and Is Involved in Cisplatin Resistance Through the Transcriptional Regulation of DNA Repair Genes. *Oncogene* (2007) 26(36):5194–203. doi: 10.1038/sj.onc.1210326
25. Kowalski LP, Carvalho AL. Natural History of Untreated Head and Neck Cancer. *Eur J Cancer* (2000) 36(8):1032–7. doi: 10.1016/s0959-8049(00)00054-x

Conflict of Interest: The authors declare that the research was conducted in the absence of any commercial or financial relationships that could be construed as a potential conflict of interest.

Publisher's Note: All claims expressed in this article are solely those of the authors and do not necessarily represent those of their affiliated organizations, or those of the publisher, the editors and the reviewers. Any product that may be evaluated in this article, or claim that may be made by its manufacturer, is not guaranteed or endorsed by the publisher.

frontiers | Frontiers in Oncology

ORIGINAL RESEARCH
published: 07 July 2022
doi: 10.3389/fonc.2022.836803

Risk Stratification in Oral Cancer: A Novel Approach

Irene Wen-Hui Tu[1‡], Nicholas Brian Shannon[1‡], Krishnakumar Thankappan[2], Deepak Balasubramanian[2], Vijay Pillai[3], Vivek Shetty[3], Vidyabhushan Rangappa[3], Naveen Hedne Chandrasekhar[3†], Vikram Kekatpure[3†], Moni Abraham Kuriakose[3], Arvind Krishnamurthy[4], Arun Mitra[4], Arun Pattatheyil[5], Prateek Jain[5], Subramania Iyer[2], Narayana Subramaniam[3†] and N. Gopalakrishna Iyer[1*] on behalf of the Head and Neck Cooperative Oncology Group*

[1] Department of Head and Neck Surgery Singapore General Hospital and National Cancer Centre Singapore and Duke-National University of Singapore (NUS) Medical School, Singapore, Singapore, [2] Department of Head and Neck Surgical Oncology, Amrita Institute of Medical Sciences, Amrita Vishwa Vidyapeetham, Kochi, India, [3] Department of Head and Neck Surgical Oncology, Mazumdar Shaw Medical Centre, Narayana Health, Bangalore, India, [4] Department of Surgical Oncology, Cancer Institute (WIA), Chennai, India, [5] Department of Head and Neck Surgical Oncology, Tata Medical Centre, Kolkata, India

Background: Oral squamous cell carcinoma (OSCC) is a common head and neck cancer with high morbidity and mortality. Currently, treatment decisions are guided by TNM staging, which omits important negative prognosticators such as lymphovascular invasion, perineural invasion (PNI), and histologic differentiation. We proposed nomogram models based on adverse pathological features to identify candidates suitable for treatment escalation within each risk group according to the National Comprehensive Cancer Network (NCCN) guidelines.

Methods: Anonymized clinicopathologic data of OSCC patients from 5 tertiary healthcare institutions in Asia were divided into 3 risk groups according to the NCCN guidelines. Within each risk group, nomograms were built to predict overall survival based on histologic differentiation, histologic margin involvement, depth of invasion (DOI), extranodal extension, PNI, lymphovascular, and bone invasion. Nomograms were internally validated with precision–recall analysis and the Kaplan–Meier survival analysis.

Results: Low-risk patients with positive pathological nodal involvement and/or positive PNI should be considered for adjuvant radiotherapy. Intermediate-risk patients with gross bone invasion may benefit from concurrent chemotherapy. High-risk patients with positive margins, high DOI, and a high composite score of histologic differentiation, PNI, and the American Joint Committee on Cancer (AJCC) 8th edition T staging should be considered for treatment escalation to experimental therapies in clinical trials.

Conclusion: Nomograms built based on prognostic adverse pathological features can be used within each NCCN risk group to fine-tune treatment decisions for OSCC patients.

Keywords: nomogram, cancer staging, head and neck tumors, oral squamous cell carcinoma (OSCC), pathological prognostic indicators, treatment escalation plan, overall survival

OPEN ACCESS

Edited by:
Wojciech Golusiński, Poznan University of Medical Sciences, Poland

Reviewed by:
Piero Nicolai, University of Padua, Italy
Francesca Gaino, Humanitas University, Italy
Richard Shaw, University of Liverpool, United Kingdom

****Correspondence:***
N. Gopalakrishna Iyer
gmsngi@nus.edu.sg
Narayana Subramaniam
narayana.subramaniam@gmail.com

†Present addresses:
Naveen Hedne Chandrasekhar, Department of Head and Neck Surgical Oncology, Apollo Proton Cancer Centre, Chennai, India
Vikram Kekatpure, Department of Head and Neck Surgical Oncology, Cytecare Hospital, Bangalore, India
Narayana Subramaniam, Department of Head and Neck Surgical Oncology, Sri Shankara Cancer Hospital and Research Centre, Bangalore, India

‡These authors have contributed equally to this work and share first authorship

Specialty section:
This article was submitted to Head and Neck Cancer, a section of the journal Frontiers in Oncology

Received: *15 December 2021*
Accepted: *09 June 2022*
Published: *07 July 2022*

INTRODUCTION

Oral squamous cell carcinoma (OSCC) is the most common histologic subtype of oral cancer (1), and the majority of head and neck squamous cell carcinoma arises from the oral cavity (2). It is associated with high morbidity and mortality, with a 5-year survival rate of only 50% (3). Since 1977, TNM staging guidelines by the American Joint Committee on Cancer (AJCC) and the Union for International Cancer Control (UICC) (1, 4), along with other adverse features, have been used to guide treatment decisions. In oral cancer, however, there has been little modification in the treatment philosophy for these patients over the past decade and a half (5). In spite of modifications in the staging system with the AJCC 8th edition (6), treatment protocols have not changed. It is unclear if prognostic factors such as depth of invasion (DOI) are an independent risk factor that requires adjuvant radiotherapy (7, 8) and if the standard of care for extranodal extension (ENE) continues to be adjuvant chemoradiotherapy (9).

Based on treatments recommended by the National Comprehensive Cancer Network (NCCN) guidelines (10), patients can be divided into three distinct groups: low, intermediate, and high risk. Surgical resection of the tumor with or without neck dissection is offered for low-risk patients, with the addition of radiotherapy for intermediate-risk patients and further addition of chemotherapy for high-risk patients. However, stratification within these groups has remained difficult; locoregional recurrence still occurs in one-third of treated early-stage OSCC despite clear surgical margins (11), while survival for advanced cancers (stages III/IV) is prognosticated solely based on nodal stage (6, 11).

TNM staging, although simple, leaves out multiple adverse pathological features such as lymphovascular invasion (LVI), perineural invasion (PNI), and histologic differentiation, which have been shown to be significant negative prognosticators in literature (12). TNM staging alone may be insufficient to fully address the needs for treatment selection and escalation (3). Models that assess the need for treatment escalation based on objective pathological features are still lacking, making treatment guidance clinically challenging.

Nomograms are user-friendly and effective prognostic models that can integrate a variety of clinical factors to provide improved precision in predicting survival outcomes (13). Current nomogram models described in the literature have attempted to predict prognosis after surgical resection (13), based on biomarkers (3) or only specific cancer types (11, 14). In this study, we looked at predictors of survival in each of the risk groups in order to derive nomograms that would help guide treatment, specifically to identify candidates who would potentially benefit from treatment escalation.

METHODS

Patient Cohort

Demographic and clinicopathologic data of anonymized oral cancer patients were obtained from 5 tertiary healthcare institutions in Asia: Amrita Institute of Medical Sciences, Mazumdar Shaw Medical Centre, Tata Medical Center and Cancer Institute Adyar (India), and the National Cancer Center (Singapore) from 2006 to 2013. All patients were treatment-naive and underwent surgical resection. According to recommendations by an oral cancer multidisciplinary team within the respective institutions, some patients underwent further adjuvant therapy, which includes radiotherapy with or without chemotherapy. Not all patients were recommended adjuvant treatment.

Data collated include patient demographics, clinical and pathological disease features, treatments, and outcomes such as survival and recurrence. Subsites of oral cancer involved include the tongue, buccal, floor of the mouth, alveolus/retromolar, lip, and hard palate. Histologic differentiation was reported based on Broders' grading system (4). PNI and LVI were reported positive when at least 33% of a nerve or vessel was noted to have any degree of tumor cell invasion (5). Histologic margin involvement was described as tumor involvement 0–5 mm from the margin or >5 mm from the margin. A positive margin was defined as tumor involvement 0–5 mm from the margin. ENE was recorded as the presence or absence of tumor spread beyond the tumor capsule, and DOI was measured as a continuous variable in mm. Gross cortical or medullary invasion of the maxilla or mandible was classified as "bone invasion." All pathological reporting was performed by a dedicated head and neck pathologist in each institution and restaged according to the AJCC 8th edition pathological TNM staging for this study. Institutional ethics committee approval was obtained at all centers prior to data collection.

The cohort was retrospectively divided into 3 groups according to treatment received based on the NCCN guidelines: "low-risk" patients were treated with surgery alone. According to NCCN guidelines, this should only be offered to patients with stage I/II (pT1–2) disease with no margin involvement and 0–1 node positive without ENE. However, in real-life medicine, the choice of therapy is confounded by patient factors, financial factors, and social factors. Thus, patients with tumors at the margin and extracapsular spread and AJCC8 T3/4, N2, and M1 patients were excluded, as illustrated in **Figure 1**. "Intermediate-risk" patients included patients who would have been recommended adjuvant radiotherapy after surgical resection according to NCCN guidelines: patients with stage III/IV disease who did not have positive margins or ENE. Patients with surgical resection and radiotherapy but had a tumor at the margin, positive extracapsular spread, and AJCC8 N3 disease were excluded. NCCN recommends that patients with positive margins and/or ENE should have adjuvant chemotherapy on top of surgical resection and adjuvant radiotherapy. Patients with surgery, adjuvant radiotherapy, and chemotherapy who had no (AJCC8) N3 or M1 disease were included in the "high-risk" group. Patients with (AJCC8) N3 or M1 are excluded from this study, as their tumors are not surgically resectable (**Figure 1**).

Statistical Analysis

All statistical analyses were performed using the R program (Version 4.1.0), with the rms package (version 6.2.0) (15). Demographic data were described with univariate analysis. The

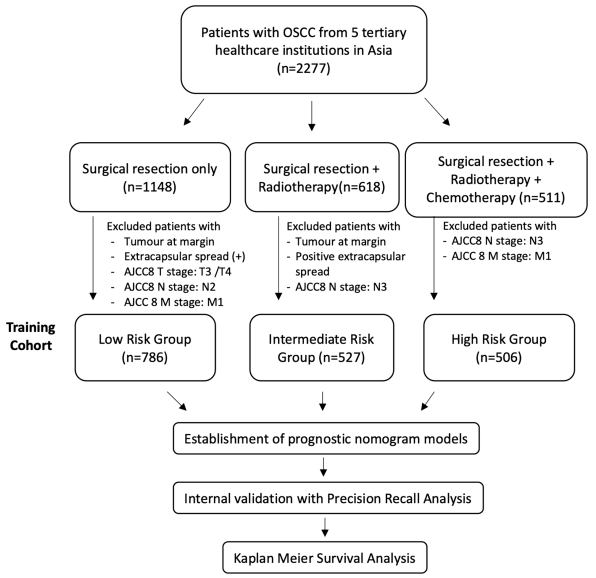

FIGURE 1 | Flowchart of study cohort selection process.

primary end point was overall survival (OS), estimated according to the Kaplan–Meier method, which was defined as the time elapsed from the date of surgery to the date of death or last follow-up. The range of OS was defined as the upper 95% confidence limit minus the lower 95% confidence limit.

To screen for independent prognostic factors, Cox regression bivariate analysis of adverse clinicopathologic factors was performed. Adverse clinicopathologic factors analyzed for each subgroup include sex, age, margin, histologic differentiation, PNI, LVI, ENE, bone invasion, DOI, and AJCC8 TNM staging. p-Value and F-statistic were calculated for each variable. Variables with p-value <0.1 were used to build a Cox multivariable regression model using backward selection, and variables with p-value <0.05 were considered significant in multivariate analysis.

For each risk group, a nomogram was constructed reflecting all variables considered for multivariate analysis. All variables significant on bivariate analysis ($p < 0.1$) were included on the nomogram models if they exhibited a p-value <0.05 for prognosticating OS on the Kaplan–Meier analysis, even if they did not fulfill $p < 0.05$ on multivariate analysis. The Kaplan–Meier curves for OS were plotted for each variable selected for the nomogram. For each variable selected for the nomograms, their effect on OS was studied by Cox regression with a hazard ratio (HR) and p-value and illustrated with the Kaplan–Meier plots for each risk group (See **Supplementary Figures**).

For the high-risk group, in particular, a *post-hoc* analysis was conducted by stratifying high-risk patients based on a cumulative number of adverse histopathological features: a composite score of 1–4 was tabulated for PNI, histologic differentiation, and AJCC8 pathological T (pT) stages according to linear effect size based on variable coefficients (PNI, 0.1997; histologic differentiation, 0.2342; AJCC8 pT stage, 0.1171). Positive PNI and moderate/poorly differentiated cases were given 1 point each. Points were assigned to pT stages (AJCC8 criteria), as follows: T1 = 0, T2 = 1, and T3/4 = 2.

Each nomogram was internally validated with precision–recall analysis, as the size of each group varied widely. The predictive strength of each nomogram model was measured with the precision–recall area under the curve (PR AUC). Predictive performance was visualized using the Kaplan–Meier survival curves comparing modeled data on OS above and below a cutoff prediction score generated by a 5-year prediction model.

RESULTS

A retrospective analysis was performed on the demographic and clinicopathologic characteristics of 1,819 patients with oral cancers collected at 5 tertiary healthcare institutions from 2006 to 2013. Patients were divided into low-risk (n = 786), intermediate-risk (n = 527), and high-risk (n = 506) groups. The mean age was 54.7, 55.8, and 50.2 years for low-risk, intermediate-risk, and high-risk patients, respectively. Gender distribution was similar in the low-risk group (54.7% men), with a slight male predominance in the intermediate-risk (68.1% men) and high-risk (74.1% men) groups. Patients who used tobacco (smoked or chewed) were more prominently featured in the high-risk group (45.7%) compared to the low-risk (32.7%) and intermediate-risk (38.5%) groups. Subsite distribution of oral cancers studied included mostly the tongue, floor of the mouth, alveolus, and retromolar cancers. Clinical, demographic, and histopathological features in each subgroup are summarized in **Table 1**.

Low-Risk Group

For the low-risk group, PNI ($p = 0.062$) and pathological nodal (pN) stage ($p < 0.01$) were negative prognostic factors for OS on bivariate analysis. Interestingly, multivariate Cox regression analysis revealed that only PNI was statistically significant in predicting poor OS ($p < 0.01$) in this group (**Table 2**). The Kaplan–Meier analysis for the pN stage revealed that it was significant in predicting poorer OS (HR = 1.96, $p = 0.0622$). The degree of impact of both PNI (HR = 25, $p < 0.01$) and pN stage was visualized succinctly in the nomogram to predict 12-month and 5-year survival, where a higher score depicted a poorer prognosis (**Figure 2A**). Internal validation of the nomogram model showed significant predictive strength as illustrated by **Figure 2B** (PR AUC = 0.800).

Intermediate-Risk Group

In the intermediate-risk group, only bone invasion ($p < 0.05$) was negatively prognostic for OS on bivariate analysis and remained a significant negative prognosticator on multivariate analysis ($p = 0.0313$). The nomogram for the intermediate-risk group (**Figure 3A**) illustrated the influence of bone invasion in predicting a negative prognosis for OS. Predictive strength was significant, with PR AUC = 0.836, on internal validation (**Figure 3B**).

TABLE 1 | Demographic and clinicopathologic profile of patients (n = 1,819).

	Low risk (n = 786)		Intermediate risk (n = 527)		High risk (n = 506)	
Sex: male, n (%)	422	(53.7)	359	(68.1)	375	(74.1)
Age, mean (SD)	54.7	(13.7)	55.8	(12.3)	50.2	(11.8)
Smoker, n (%)	257	(32.7)	203	(38.5)	231	(45.7)
Subsite, n (%)						
Tongue,	492	(62.6)	208	(39.5)	283	(55.9)
Buccal mucosa	66	(8.40)	75	(14.2)	51	(10.1)
Floor of Mouth	160	(20.4)	132	(25.1)	119	(23.5)
Alveolus/retromolar	47	(5.98)	94	(17.8)	43	(8.50)
Lip	17	(2.16)	5	(0.949)	2	(0.395)
Hard palate	3	(0.382)	11	(2.09)	6	(1.19)
Margin, mm, mean (SD)	0.096	(0.298)	6.562	(3.743)	6.513	(3.512)
<5 mm from margin	136	(17.3)	116	(22.0)	100	(19.8)
>5 mm from margin	605	(77.0)	394	(74.8)	369	(72.9)
At margin	0	(0)	0	(0)	30	(5.93)
Histologic differentiation, n (%)						
G1 (well differentiated)	351	(44.7)	143	(27.1)	110	(21.7)
G2 (moderately differentiated)	344	(43.8)	316	(60.0)	320	(63.2)
G3 (poorly differentiated)	48	(6.11)	54	(10.2)	66	(13.0)
Diameter, mean (SD)	18.2	(7.41)	33.7	(14.7)	1.95	(0.584)
Depth of invasion, mean (SD)	6.45	(2.63)	14.5	(9.38)	18.7	(11.5)
(+) Perineural invasion, n (%)	77	(9.80)	197	(37.4)	319	(63.0)
(+) Lymphovascular invasion, n (%)	28	(3.56)	197	(37.4)	319	(63.0)
(+) Extracapsular spread, n (%)	0	(0)	0	(0)	336	(66.4)
(+) Bone Invasion, n (%)	0	(0)	152	(28.8)	121	(23.9)
Follow up time, mean (SD), years	3.069	(2.594)	3.307	(3.487)	1.43	(1.386)
Death rate, n (%)	14	(26.9)	99	(18.8)	85	(55.9)
Recurrence rate, n (%)	143	(18.2)	135	(25.6)	205	(40.5)
Overall survival[+], months, median (range*)	37.9	(22.9)	17.0	(18.9)	22.7	(23.4)

[+]*Overall survival is defined as duration from date of surgery to last date of follow-up or death.*

**Range is defined as upper 95% confidence limit–lower 95% confidence limit.*

TABLE 2 | Stepwise bivariate and multivariate Cox regression analysis for overall survival (p-value).

	Low risk		Intermediate risk		High risk	
	Bivariate	**Multivariate**	**Bivariate**	**Multivariate**	**Bivariate**	**Multivariate**
Sex	0.927		0.183		0.768	
Age	0.761		0.903		0.271	
Margin	0.685		0.935		0.010*	0.0213**
Histologic differentiation	0.258		0.627		0.033*	0.349
PNI (+)	0.062*	0.00683**	0.555		0.025*	0.0249**
LVI (+)	0.732		0.941		0.774	
ECS	-		-		0.865	
Bone invasion	-		0.031*	0.0313**	0.588	
DOI	0.991		0.640		0.003*	0.234
AJCC8 T stage	0.984		0.119		0.010*	0.351
AJCC8 N stage	0.009*	0.344	0.539		0.639	

PNI, perineural invasion; LVI, lymphovascular invasion; ECS, extracapsular spread; DOI, depth of invasion.

** p-value <0.1 (bivariate analysis).*

*** p-value <0.05 (multivariate analysis).*

High-Risk Group

For the high-risk group, preliminary bivariate and multivariate analyses deemed margin, DOI, PNI, histologic differentiation, and pT staging to be statistically significant for poor prognosis (**Table 2**). However, the absolute impact on poor prognosis for the factors PNI, histologic differentiation, and pT staging was low compared to the factors margin ($p = 0.0213$) and DOI ($p = 0.0249$). A composite score of PNI, histologic differentiation, and pT staging was employed to better illustrate their impact. The Kaplan–Meier analysis showed that the composite score was significant for prognosticating poor OS (HR = 1.43, $p < 0.01$). Other negative prognostic factors reflected on the nomogram for high-risk patients include margin (HR = 2.07, $p = 0.0134$) and DOI (HR = 2.42, $p < 0.01$) (**Figure 4A**). Internal validation revealed significant predictive strength of PR AUC = 0.925 (**Figure 4B**).

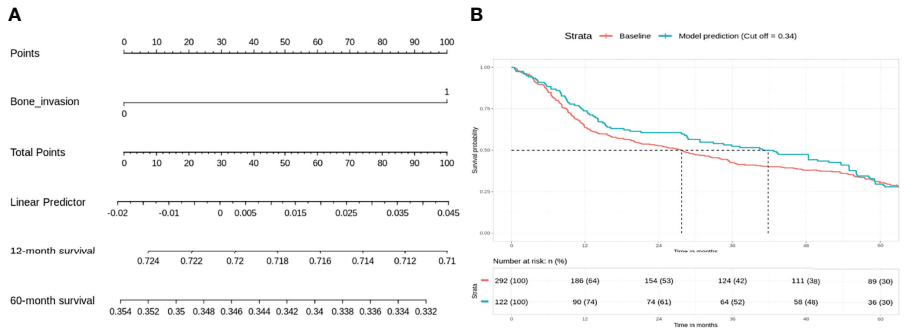

FIGURE 2 | Low risk: nodal stage and perineural invasion (PNI) are negative prognosticators of overall survival. **(A)** Nomogram model. **(B)** Internal validation: prediction of 5-year overall survival with nomogram model as compared to baseline (PR AUC = 0.800). PNI, perineural invasion; PR AUC, precision–recall area under the curve.

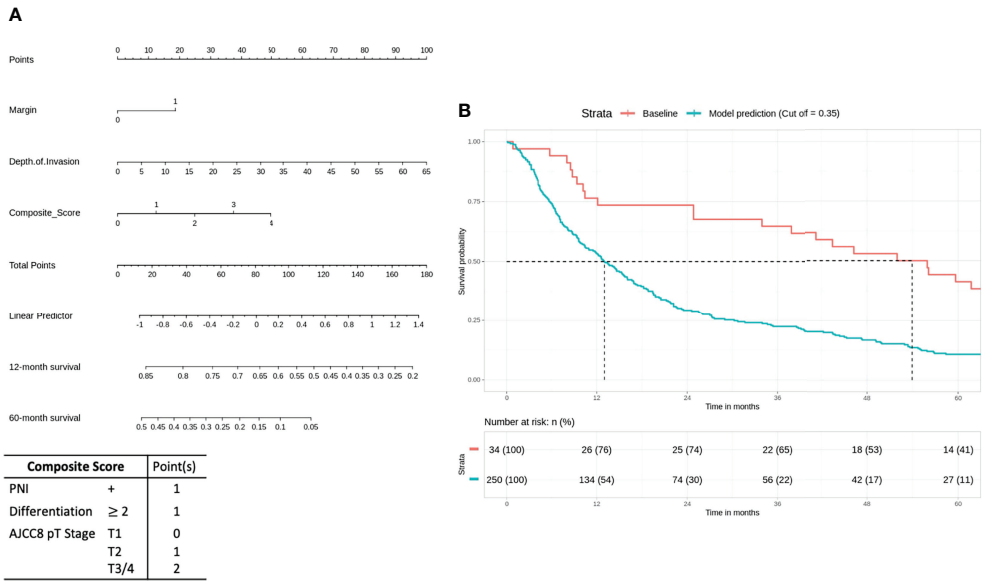

Composite Score		Point(s)
PNI	+	1
Differentiation	≥ 2	1
AJCC8 pT Stage	T1	0
	T2	1
	T3/4	2

FIGURE 3 | Intermediate-risk group: bone invasion is a significant negative prognosticator for overall survival (OS). **(A)** Nomogram model. **(B)** Internal validation: prediction of 5-year overall survival with nomogram model as compared to baseline (PR AUC = 0.836). PR AUC, precision–recall area under the curve.

DISCUSSION

Nomograms have been widely used to predict survival outcomes in a variety of cancers, including OSCC, by reflecting the prognostic strength of relevant variables (13). Previous nomograms designed for OSCC mostly focused on the prognostic effect of genes, biomarkers, or specific subsite and tumor grade of OSCC (3, 11, 13, 16). Recently, Zhou et al. published a nomogram model for risk stratification of OSCC based on clinical and pathological features (17). Montero et al. presented nomograms for preoperative prediction of OS and locoregional recurrence-free probability in OSCC (18). However, as cancer recurrence remained a significant problem after each step of treatment, there remained a need to develop a holistic prognostic model based on adverse pathological features commonly used in multidisciplinary tumor boards (MDTs) to better inform clinicians objectively on indications for treatment escalation.

The current practice for OSCC management is largely directed by multidisciplinary discussions in tumor boards, which take into consideration the cancer stage, adverse pathological factors, individual patient factors, and the likely functional consequences and morbidity of each treatment approach (19). Pathological staging by AJCC8 TNM staging is considered together with adverse pathological variables such as primary tumor site, histologic differentiation, perineural, lymphovascular, and bone invasion, as well as an ENE for prognostic risk stratification. As

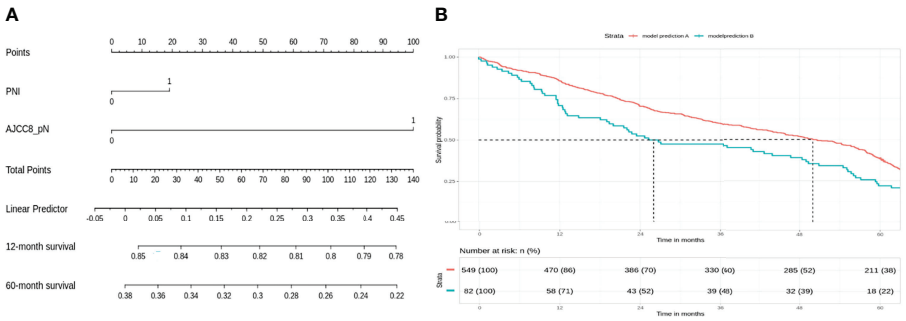

FIGURE 4 | High-risk group: margin, depth of invasion, and a composite score are significant negative prognostic indicators for overall survival (OS). **(A)** Nomogram model. **(B)** Internal validation: prediction of 5-year overall survival with nomogram model as compared to baseline (PR AUC = 0.925). Margin: 0, <5 mm from margin; 1, >5 mm from margin. Histologic differentiation: G1, well differentiated (1); G2, moderately differentiated (2); G3, poorly differentiated (3). PNI, perineural invasion; PR AUC, precision–recall area under the curve.

such, TNM staging alone remains insufficient in directing treatment decisions reliably (17).

In our study, we divided the multicentric patient population into 3 groups (low/intermediate/high) according to the NCCN. Patients were first divided according to the treatments they have been given and subsequently the training cohort was streamlined to ensure its characteristics reflect the prognostic risk profile of the relevant subgroup (**Figure 1**).

Patients in the low-risk group have localized (stage I/II) disease with 60%–80% 5-year OS (20). These patients were not advised of any adjuvant radiotherapy by the intra-institutional MDT. Our nomogram illustrated that positive nodal disease plays a major role in OS, even though the margins were clear post-resection. This was not unexpected and has been shown previously in National Cancer Database (NCDB) and Surveillance, Epidemiology, and End Results (SEER) data (21, 22) (**Figure 1**). However, PNI was unequivocally identified as a negative prognostic factor from Cox regression analysis. The strength of prognostic impact for PNI was marginal for OS (10 points ≤ 5% survival) on the nomogram. Multiple studies have stressed the importance of PNI as an independent negative prognostic factor associated with aggressive tumor behavior, tumor recurrence, and poor outcomes in T2N0 patients (23). However, other studies have suggested that adjuvant radiotherapy may not benefit this cohort of patients (24). LVI may not have been significant for survival in this cohort because a relatively small percentage of patients with LVI received solely surgical management (2.54%). It is likely that LVI was associated with a higher risk of nodal metastases, and these patients received adjuvant therapy as a result.

Patients in the intermediate risk group received adjuvant radiotherapy after surgical resection in view of locoregionally advanced disease and a higher risk of local recurrence (25). Our preliminary Cox regression analysis revealed that bone invasion had a significant impact on survival in this cohort. This is in concordance with existing literature, which identified bone invasion as an important prognostic factor to classify late-stage OSCC. It was associated with the worst quality of life and shorter life expectancy (26, 27) (**Figure 2**). This would suggest that there is likely a subset of patients with equivocal bone invasion who require adjuvant chemoradiotherapy; unfortunately, it was not possible to reclassify bone invasion in our cohort to better understand this. If there are other adverse features in addition to bone invasion, adjuvant chemotherapy use may be considered.

In the high-risk group that already received chemoradiotherapy, our analysis suggests that margins and DOI are important negative prognosticating factors, and the nomogram reflects a high impact on OS (50 points = 30% 2-year survival). The importance of DOI in OSCC is widely recognized, with the latest AJCC TNM classification incorporating DOI as part of the T staging (4). Positive margins are associated with tumor recurrence, diminished disease-specific survival, and poor OS even at 2 years (28). Interestingly, the impact of the ENE seems to be at least partially mitigated by adjuvant chemoradiotherapy. Our results also reveal that histologic differentiation, PNI, and T staging are independent negative prognosticators significant in both bivariate and multivariate Cox regression analysis. However, the prognostic value is weak individually, and a composite score of the 3 variables provides a stronger prognostic value for better visualization on the nomogram: the T stage relates to the anatomical extent of tumor growth and invasion into surrounding tissues and is an important prognostic factor in AJCC8 TNM staging (4). Chen et al. showed that poor tumor differentiation is a negative predictor of subsequent distant metastasis in locoregionally advanced OSCC (29), while Jardim et al. argued for the prognostic impact of PNI in advanced-stage OSCC (30). While literature suggested that each of these 3 factors are important adverse pathological prognosticators, in the context of high-risk OSCC, their impact on predicting poorer prognosis was marginal independently. The prognostic significance of the composite score; however, suggests that their impact should not be overlooked. Therefore, our analysis suggests that positive margin, DOI, and a composite score of histologic differentiation, PNI, and T stage (AJCC8) are important negative prognostic indicators for poor survival.

The limitations of this study include, first, the heterogeneity of OSCC as tumor characteristics differed significantly across

subsites. Yet universal treatment guidelines such as TNM staging had been able to provide sound treatment advice on OSCC as a whole, and our study largely revolved around known adverse pathological parameters common to all subsites of OSCC. Second, we assumed that treatment decisions at each center were based only on the pathology of the disease and did not consider patient factors such as finances. Third, all recommendations were made based on statistical modeling, which was co-relational and hypothesis-generating in nature. Causation relationships between the variables and OS would require further randomized control trials to be firmly established. The inclusion of molecular markers for prognostication in this group may have added value but unfortunately was beyond the scope of this work. Fourth, pathological interpretation of DOI and extracapsular invasion may defer across different pathologists across different nations. In this study, we opted to record these variables objectively without further interpretation: presence or absence of extracapsular invasion(,) and the objective measurement of the DOI in mm directly. Finally, our database was collected postoperatively and had limited preoperative factors to build an Asia-specific preoperative nomogram to supplement our postoperative nomograms. This could be explored in future studies. Further work could also look into prognostication with specifically medullary invasion (31), instead of overall bone invasion.

By constructing these nomograms based on real-world data of patients who received appropriate adjuvant therapy after surgical resection, it was our intention to determine specific cohorts who had a higher risk of death and hence may be candidates for treatment escalation. To our knowledge, this is the first report of its kind. Our findings recommend that low-risk patients with positive pathological nodal involvement and/or positive PNI should consider adjuvant radiotherapy. Intermediate-risk patients with gross bone invasion may benefit from concurrent chemotherapy; however, it is likely that this decision needs to be taken on a patient-by-patient basis after consideration of other adverse features and the extent of bone invasion. Finally, high-risk patients with positive margins, high DOI, and a high composite score of histologic differentiation, PNI, and AJCC8 T staging should be considered for treatment escalation or experimental therapies in the setting of clinical trials.

DATA AVAILABILITY STATEMENT

The data analyzed in this study is subject to the following licenses/restrictions: This dataset was built from information on patient details that have been de-identified. However as these details were originally from patients, they cannot be available publicly. Please direct any request for data to the corresponding author. Requests to access these datasets should be directed to NI, gmsngi@duke.nus.sg.

AUTHOR CONTRIBUTIONS

IT and NS are co first authors contributing equally to the conception, design of study and data analysis. KT, DB, VP, VS, VR, NC, VK, MK, AK, AM, AP, PJ, and SI contributed the dataset of study used for training and internal validation of the proposed nomogram model. NI and NS are both corresponding authors contributing to conception and design of study. All authors contributed to manuscript revision, read, and approved the submitted version.

ACKNOWLEDGMENTS

The authors will like to thank Dr Manraj Singh for his valuable advice in data presentation and management.

SUPPLEMENTARY MATERIAL

The Supplementary Material for this article can be found online at: https://www.frontiersin.org/articles/10.3389/fonc.2022.836803/full#supplementary-material

REFERENCES

1. Almangush A, Pirinen M, Youssef O, Mäkitie AA, Leivo I. Risk Stratification in Oral Squamous Cell Carcinoma Using Staging of the Eighth American Joint Committee on Cancer: Systematic Review and Meta-Analysis. *Head Neck* (2020) 42(10):3002–17. doi: 10.1002/hed.26344
2. Chi AC, Day TA, Neville BW. Oral Cavity and Oropharyngeal Squamous Cell Carcinoma—an Update. *CA: Cancer J Clin* (2015) 65(5):401–21.
3. Huang Z-D, Yao Y-Y, Chen T-Y, Zhao Y-F, Zhang C, Niu Y-M. Construction of Prognostic Risk Prediction Model of Oral Squamous Cell Carcinoma Based on Nine Survival-Associated Metabolic Genes. *Front Physiol* (2021) 12:290. doi: 10.3389/fphys.2021.609770
4. Lydiatt WM, Patel SG, O'Sullivan B, Brandwein MS, Ridge JA, Migliacci JC, et al. Head and Neck Cancers—Major Changes in the American Joint Committee on Cancer Eighth Edition Cancer Staging Manual. *CA: Cancer J Clin* (2017) 67(2):122–37.
5. Almangush A, Mäkitie AA, Triantafyllou A, de Bree R, Strojan P, Rinaldo A, et al. Staging and Grading of Oral Squamous Cell Carcinoma: An Update. *Oral Oncol* (2020) 107:104799. doi: 10.1016/j.oraloncology.2020.104799
6. Mattavelli D, Ferrari M, Taboni S, Morello R, Paderno A, Rampinelli V, et al. The 8th TNM Classification for Oral Squamous Cell Carcinoma: What Is Gained, What is Lost, and What Is Missing. *Oral Oncol* (2020) 111:104937. doi: 10.1016/j.oraloncology.2020.104937
7. Ebrahimi A, Gil Z, Amit M, Yen TC, t. Liao C, Chaturvedi P, et al. Depth of Invasion Alone as an Indication for Postoperative Radiotherapy in Small Oral Squamous Cell Carcinomas: An International Collaborative Study. *Head Neck* (2019) 41(6):1935–42. doi: 10.1002/hed.25633
8. Subramaniam N, Balasubramanian D, Murthy S, Rathod P, Vidhyadharan S, Thankappan K, et al. Impact of Postoperative Radiotherapy on Survival and Loco-Regional Control in Node-Negative Oral Cavity Tumours Classified as T3 Using the AJCC Cancer Staging Manual Eighth Edition. *Int J Oral Maxillofac Surg* (2019) 48(2):152–6. doi: 10.1016/j.ijom.2018.07.009
9. Bernier J, Cooper JS, Pajak T, Van Glabbeke M, Bourhis J, Forastiere A, et al. Defining Risk Levels in Locally Advanced Head and Neck Cancers: A Comparative Analysis of Concurrent Postoperative Radiation Plus Chemotherapy Trials of the EORTC (# 22931) and RTOG (# 9501). *Head Neck: J Sci Specialties Head Neck* (2005) 27(10):843–50. doi: 10.1002/hed.20279

10. Colevas AD, Yom SS, Pfister DG, Spencer S, Adelstein D, Adkins D, et al. NCCN Guidelines Insights: Head and Neck Cancers, Version 1.2018. *J Natl Compr Cancer Netwo* (2018) 16(5):479–90. doi: 10.6004/jnccn.2018.0026
11. Balasubramanian D, Subramaniam N, Missale F, Marchi F, Dokhe Y, Vijayan S, et al. Predictive Nomograms for Oral Tongue Squamous Cell Carcinoma Applying the American Joint Committee on Cancer/Union Internationale Contre Le Cancer 8th Edition Staging System. *Head Neck* (2021) 43(4):1043–55. doi: 10.1002/hed.26554
12. Subramaniam N, Balasubramanian D, Murthy S, Limbachiya S, Thankappan K, Iyer S. Adverse Pathologic Features in Early Oral Squamous Cell Carcinoma and the Role of Postoperative Radiotherapy—A Review. *Oral surg Oral medic Oral Pathol Oral Radiol* (2017) 124(1):24–31. doi: 10.1016/j.oooo.2017.03.002
13. Nie Z, Zhao P, Shang Y, Sun B. Nomograms to Predict the Prognosis in Locally Advanced Oral Squamous Cell Carcinoma After Curative Resection. *BMC Cancer* (2021) 21(1):1–17. doi: 10.1186/s12885-021-08106-x
14. Zheng S, Yang J, Li C, Han D, Xu F, Elishilia Kaaya R, et al. Prognostic Exploration of All-Cause Death in Gingival Squamous Cell Carcinoma: A Retrospective Analysis of 2076 Patients. *J Oncol* 2021(2021). doi: 10.1155/2021/6676587
15. R. C. Team. *R: A Language and Environment for Statistical Computing* (2021). Available at: https://www.R-project.org/.
16. Wang S, Li T, Liu H, Wei W, Yang Y, Wang C, et al. A Combined Prediction Model for Lymph Node Metastasis Based on a Molecular Panel and Clinicopathological Factors in Oral Squamous Cell Carcinoma. *Front Oncol* (2021) 11:1211. doi: 10.3389/fonc.2021.660615
17. Zhou J, Li H, Cheng B, Cao R, Zou F, Yang D, et al. Derivation and Validation of a Prognostic Scoring Model Based on Clinical and Pathological Features for Risk Stratification in Oral Squamous Cell Carcinoma Patients: A Retrospective Multicenter Study. *Front Oncol* (2021) 11:1500. doi: 10.3389/fonc.2021.652553
18. Montero PH, Yu C, Palmer FL, Patel PD, Ganly I, Shah JP, et al. Nomograms for Preoperative Prediction of Prognosis in Patients With Oral Cavity Squamous Cell Carcinoma. *Cancer* (2014) 120(2):214–21. doi: 10.1002/cncr.28407
19. Wheless SA, McKinney KA, Zanation AM. A Prospective Study of the Clinical Impact of a Multidisciplinary Head and Neck Tumor Board. *Otolaryngol—Head Neck Surg* (2010) 143(5):650–4. doi: 10.1016/j.otohns.2010.07.020
20. Viet CT, Yu G, Asam K, Thomas CM, Yoon AJ, Wongworawat YC, et al. The REASON Score: An Epigenetic and Clinicopathologic Score to Predict Risk of Poor Survival in Patients With Early Stage Oral Squamous Cell Carcinoma. *biomark Res* (2021) 9(1):1–13. doi: 10.1186/s40364-021-00292-x
21. Shrime MG, Gullane PJ, Dawson L, Kim J, Gilbert RW, Irish JC, et al. The Impact of Adjuvant Radiotherapy on Survival in T1-2N1 Squamous Cell Carcinoma of the Oral Cavity. *Arch Otolaryngol–Head Neck Surg* (2010) 136(3):225–8. doi: 10.1001/archoto.2010.22
22. Chen MM, Harris JP, Hara W, Sirjani D, Divi V. Association of Postoperative Radiotherapy With Survival in Patients With N1 Oral Cavity and Oropharyngeal Squamous Cell Carcinoma. *JAMA Otolaryngol–Head Neck Surg* (2016) 142(12):1224–30. doi: 10.1001/jamaoto.2016.3519
23. Cheng C-S, Chen C-C, Liu Y-C, Wang C-C, Chou Y-S. *Peri-Neural Invasion is An Important Prognostic Factor of T2N0 Oral Cancer*. (2021). ResearchSquare, Taiwan (ROC).
24. Bur AM, Lin A, Weinstein GS. Adjuvant Radiotherapy for Early Head and Neck Squamous Cell Carcinoma With Perineural Invasion: A Systematic Review. *Head Neck* (2016) 38(S1):E2350–7. doi: 10.1002/hed.24295
25. Stenson KM, Brockstein BE. Shiyu Song: Overview of Treatment for Head and Neck Section: Management of SCC - Localized (Early Stage Disease). In: MP Fried, MR Posner, DM Brizel and S Shah, editors. *UpToDate* (2021). Available at: www.uptodate.com.
26. Brown JS, Lowe D, Kalavrezos N, D'Souza J, Magennis P, Woolgar J. Patterns of Invasion and Routes of Tumor Entry Into the Mandible by Oral Squamous Cell Carcinoma. *Head Neck: J Sci Specialties Head Neck* (2002) 24(4):370–83. doi: 10.1002/hed.10062
27. Yao CM, Chang EI, Lai SY. Contemporary Approach to Locally Advanced Oral Cavity Squamous Cell Carcinoma. *Curr Oncol Rep* (2019) 21(11):1–9. doi: 10.1007/s11912-019-0845-8
28. Jain PV, Sharan R, Manikantan K, Clark GM, Chatterjee S, Mallick I, et al. Redefining Adequate Margins in Oral Squamous Cell Carcinoma: Outcomes From Close and Positive Margins. *Eur Arch Oto-Rhino-Laryngol* (2020) 277(4):1155–65. doi: 10.1007/s00405-019-05779-w
29. Chen T-C, Hsu C-W, Lou P-J, Ko J-Y, Yang T-L, Chen C-N, et al. The Clinical Predictive Factors for Subsequent Distant Metastasis in Patients With Locoregionally Advanced Oral Squamous Cell Carcinoma. *Oral Oncol* (2013) 49(4):367–73. doi: 10.1016/j.oraloncology.2012.10.006
30. Jardim J, Francisco A, Gondak R, Damascena A, Kowalski L. Prognostic Impact of Perineural Invasion and Lymphovascular Invasion in Advanced Stage Oral Squamous Cell Carcinoma. *Int J Oral Maxillofac Surg* (2015) 44(1):23–8. doi: 10.1016/j.ijom.2014.10.006
31. Ebrahimi A, Murali R, Gao K, Elliott MS, Clark JR. The Prognostic and Staging Implications of Bone Invasion in Oral Squamous Cell Carcinoma. *Cancer* (2011) 117(19):4460–7. doi: 10.1002/cncr.26032

Conflict of Interest: The authors declare that the research was conducted in the absence of any commercial or financial relationships that could be construed as a potential conflict of interest.

Publisher's Note: All claims expressed in this article are solely those of the authors and do not necessarily represent those of their affiliated organizations, or those of the publisher, the editors and the reviewers. Any product that may be evaluated in this article, or claim that may be made by its manufacturer, is not guaranteed or endorsed by the publisher.

Citation: *Tu IW, Shannon NB, Thankappan K, Balasubramanian D, Pillai V, Shetty V, Rangappa V, Chandrasekhar NH, Kekatpure V, Kuriakose MA, Krishnamurthy A, Mitra A, Pattatheyil A, Jain P, Iyer S, Subramaniam N and Iyer NG (2022) Risk Stratification in Oral Cancer: A Novel Approach. Front. Oncol. 12:836803. doi: 10.3389/fonc.2022.836803*

Frontiers in Oncology

Advances knowledge of carcinogenesis and tumor progression for better treatment and management

The third most-cited oncology journal, which highlights research in carcinogenesis and tumor progression, bridging the gap between basic research and applications to imrpove diagnosis, therapeutics and management strategies.

Discover the latest Research Topics

See more →

Frontiers

Avenue du Tribunal-Fédéral 34
1005 Lausanne, Switzerland
frontiersin.org

Contact us

+41 (0)21 510 17 00
frontiersin.org/about/contact